

**SINGLE ANTENNA UNIT WITH ROBUST  
NEAR- AND FAR-FIELD FOR  
MULTIBAND APPLICATIONS**

PhD Dissertation by

**ASHWANI SHARMA**

Director

**IGNACIO J. GARCIA ZUAZOLA**



**FACULTY OF ENGINEERING  
UNIVERSITY OF DEUSTO  
BILBAO, SPAIN, 48007  
OCTOBER 2015**











# Single Antenna Unit with Robust Near- and Far-field for Multiband Applications

Dissertation submitted by Ashwani Sharma (Passport: G5401372) enrolled in **Doctoral program in Engineering for the Information Society and Sustainable Development** at the University of Deusto, 48007 Bilbao, Spain.

STUDENT

SUPERVISOR

Signature:

Signature:

\_\_\_\_\_  
**Ashwani Sharma**  
Mobility, DeustoTech,  
Universidad de Deusto  
48007 Bilbao, Spain

\_\_\_\_\_  
**Dr. I. J. Garcia Zuazola**  
School of Electronic, Electrical  
and Systems Engineering,  
Loughborough University  
Leicestershire LE11 3TU, UK

Date  
\_\_\_\_\_





© University of Deusto, Bilbao, Spain, 2015.



# Single Antenna Unit with Robust Near- and Far-field for Multiband Applications

By

Ashwani Sharma

*Submitted in fulfillment of the requirements  
of the degree of Doctor of Philosophy*

*to the*



FACULTY OF ENGINEERING  
UNIVERSITY OF DEUSTO  
BILBAO, SPAIN, 48007  
OCT 2015



*To*  
*My loving Parents*



# Acknowledgements

*It is my pleasure to record deepest gratitude to my supervisor, Dr. Ignacio J. Garcia Zuazola (University of Deusto, Spain) for giving me this opportunity to work under his supervision and for making my research a beautiful journey. I heartily thank to Dr. Ignacio for his consistent encouragement, advice, supervision, and contribution. The kind of energy and motivation he bears is phenomenal and always inspirational to me. His valuable suggestions and guidelines kept me focused in my research. I had very little knowledge about antennas when I first joined him. However, he guided me from the beginning very patiently and exhibited gradually to me the beauty of research work. His mentorship and support is of most importance in completion of this dissertation.*

*In the same way, I wish to thank Dr. Asier Perallos Ruiz (Universidad de Deusto, Spain), Dr. John Batchelor (University of Kent, UK), Prof. Ramon Martinez and Prof. Leandro de-Haro Ariet (Universidad Politecnica de Madrid, Spain), for their contributions towards this thesis.*

*I am grateful to the helpful correspondence with Dr. Anshu Gupta. Discussing with him on antennas is been a pleasure and a great learning experience for me. Thanks to all my colleagues in Mobility Group, DeustoTech (Universidad de Deusto) for their constant support.*

*Most importantly, I would like to express my heart-felt gratitude to my father Sushen Sharma, my mother Madhu Sharma and my sister Poonam. None of this would have been possible without the love and patience of my family.*

*Finally, my greatest regards to the Almighty for bestowing upon me the courage to face the complexities of life and complete this dissertation successfully.*

*Bilbao, Spain  
(Oct. 2015)*

*Ashwani Sharma*



# Abstract

This investigation targets to develop a multi-purpose switched multi-band antenna for Radio Frequency IDentification (RFID) reader applications. Typically, the RFID systems can be categorized depending on the range of the applications, this defines a Near-Field (NF) RFID and a Far-Field (FF) RFID, and depending on that the reader and the tag antennas are developed exclusively. Additionally, the RFID systems can be categorized also depending of the frequency of operation, e.g., HF, UHF, 2.46GHz, and 5.8GHz. Therefore, various combinations of the range and frequency categories are possible, but the objective of this research is to design a reader antenna which can serve both the NF- and the FF-RFIDs and is able to operate at almost all of the adopted frequencies of the RFID applications in a switching manner. To achieve this goal, the RFID reader antenna is optimized first for the desired interrogation zone, and then multiple purposes and frequencies are integrated with optimized design. In this regard, a novel Non-uniformly Distributed Turns coil (NDTC) antenna is designed for HF-RFID reader application operating at 13.56MHz. The multiple turns of the NDTC are optimally distributed in inner area of the coil for a significantly enhanced magnetic field (H-field) in the NF zone. To include FF interrogation along with the NF, a Segmented-Line NDTC (SL-NDTC) antenna for UHF-RFID reader application is developed and presented as a dual-purpose antenna operating at a single-frequency 915MHz. To integrate the dual-purpose (NF and FF) property with multiple bands of RFID applications, a Dual-Band NDTC (DB-NDTC) antenna is proposed operating at switchable frequencies of HF 13.56MHz and UHF 915MHz. The DB-NDTC antenna can interrogate in both NF and FF zones, and when switched to HF persists the robust H-field of the NDTC antenna in the NF zone, and shows a decent gain and radiation efficiency in the FF zone when switched to UHF. Hence, DB-NDTC can be realized as a dual-purpose switchable dual-band antenna. To achieve the ultimate objective of this research work, a multi-purpose switched multiband antenna is designed using RF-switches and having three modes of operations (mode-1-3) depending of states (ON or OFF)

of the switches. In mode-1, 2, and 3, the antenna respectively switches to operating frequencies 915MHz, 2.45GHz, and 5.8GHz, where, for each individual mode, it can perform for both NF and FF RFID applications. This demonstrates a switched antenna for multiband behavior designed to be used as multi-purpose RFID reader.

During the investigation, analytical and numerical methods are used to develop the designs, and parametric studies using simulator are conducted to optimize the performance of the antennas. The designs are fabricated and the measurement results are corroborated with analytical and simulated results.



## Author's publications from this thesis

1. **A. Sharma**, I. J. Garcia Zuazola, A. Gupta, A. Perallos, and J. C. Batchelor, "Non-uniformly distributed-turns coil antenna for enhanced H-field in HF RFID", *IEEE Transaction Antennas Propagation*, vol. 61, no. 10, pp. 4900-4907, Oct 2013.
2. **A. Sharma**, I.J. Garcia Zuazola, A. Gupta, A. Perallos, and J.C. Batchelor, "Enhanced H-field in HF RFID systems by optimizing the loop spacing of antenna coils", *Wiley - Microwave and Optical Technology Letters*, Volume 55, Issue 4, pages 944-948, April 2013.
3. **A. Sharma**, I. J. Garcia Zuazola, A. Gupta, A. Perallos, and J. C. Batchelor, "Fabricated Non-uniformly distributed-turns coil," in *IEEE Antennas and Propagation Society International Symposium*, Memphis, USA, July 2014, pp. 1536-1537.
4. **A. Sharma**, I. J. Garcia Zuazola, A. Gupta, J. C. Batchelor, and A. Perallos, "Influence of Substrate Types and Reflector Proximities Over a NDTC Antenna," in *Loughborough Antennas and Propagation Conference (LAPC)*, Loughborough, UK, Nov 2014, pp. 431-433.
5. **A. Sharma**, I. J. Garcia Zuazola, J. C. Batchelor, and A. Perallos, "Wide-spread near-Field with robust H-field using NDTC antennas in multipurpose Applications," in *Twenty First National Conference on Communication (NCC-2015)*, Mumbai, India, Feb.-Mar. 2015, pp. 1-5.
6. **A. Sharma**, I. J. Garcia Zuazola, A. Gupta, A. Perallos, and J. C. Batchelor, "Dual purpose near- and far-field UHF RFID Coil Antenna with Non-uniformly Distributed-Turns," *IEEE Letters on Antennas and Propagation*, vol. 14 , pp. 1342-1345, Feb. 2015.
7. **A. Sharma**, I. J. Garcia Zuazola, J. C. Batchelor, and A. Perallos, "Switched Non-uniformly Distributed-Turns Coil Antenna for Dual-band operation", in *9th European Conference on Antennas and Propagation (EuCAP)*, Lisbon, Portugal, April 2015, pp. 1-4.
8. **A. Sharma**, I. J. Garcia Zuazola, J. C. Batchelor, and A. Perallos, "Multi-purpose near- far-field switched multiband coil antenna for 915MHz /2.45/ 5.8GHz RFIDs," *shall be communicated in a Journal*, 2015.

9. **A. Sharma**, I. J. Garcia Zuazola, R. Martinez, J. C. Batchelor, A. Perallos, and L. de-Haro Ariet, "Optimal E-field vector for a highly-focused antenna-array", *IEEE Letters on Antennas and Propagation*, vol. 13, pp. 392-395, Feb. 2014.
10. I.J. Garcia Zuazola, **A. Sharma**, J.C. Batchelor, I. Angulo, A. Perallos, W.G. Whittow, J.M.H. Elmirghani, and R. Langley, "Radio frequency Identification miniature interrogator antenna sprayed over an in-vehicle chassis", *IET Microwaves, Antennas and Propagation*, Volume 6, Issue 15, pp. 1674-1680, Dec. 2012.
11. I.J. Garcia Zuazola, **A. Sharma**, J.C. Batchelor, I. Angulo, A. Perallos, and J.M.H. Elmirghani, "Sprayed antenna on cans for WLAN-RFID tags", *Wiley - Microwave and Optical Technology Letters*, Volume 55, Issue 4, pp. 773-775, April 2013.
12. I.J. Garcia Zuazola, L. Azpilicueta, **A. Sharma**, H.Landaluce, F.Falcone, I. Angulo, A.Perallos, W.G.Whittow, J.M.H. Elmirghani, and J.C. Batchelor, "Bandpass filter-like antenna validation in an ultra-wideband in-car wireless channel", *IET Communications*, Volume 9, Issue 4, pp. 532-540, Mar. 2015.
13. **A. Sharma**, I.J. Garcia Zuazola, R. Martinez, A. Perallos, and J. C. Batchelor, "Channel-based Antenna Synthesis for Improved In-vehicle UWB MB-OFDM Communications", *submitted for review in a IEEE Journal*.

## Grants:

1. Predoctoral Research Grant (FPI-Deusto 2011-2015); **A. Sharma**.
2. International Relations Mobility Grant (Deusto 2014) worth ~7500Euros, **A. Sharma**.

## Prizes:

1. A. Perallos, I. Angulo, A. Moreno, I.J. Garca Zuazola, A. Chertudi, H. Landaluce, P. Elejoste, A. San Nicolas, R. Carballedo, **A. Sharma**, U. Hernandez, N. Sainz, P. Fernndez, I. Salaberria, G. Urquiola, A. Sidhik. "UD-Santander Research Prize Euro 7,000 - awarded by the University of Deusto to whom makes the growth and development of new scientific contributions", 5 Feb. 2013.



# Contents

<b>Acknowledgements</b>	<b>ix</b>
<b>Abstract</b>	<b>xi</b>
<b>List of Figures</b>	<b>5</b>
<b>List of Tables</b>	<b>8</b>
<b>1 Introduction and motivation</b>	<b>11</b>
1.1 Background	11
1.1.1 Antennas for RFID Technology	13
1.2 Literature review and motivation	16
1.2.1 Review of Near-Field RFID reader antennas	17
1.2.1.1 NF LF-RFID reader antennas	17
1.2.1.2 NF HF-RFID reader antennas	18
1.2.1.3 NF UHF-RFID Reader antennas	22
1.2.1.4 NF MW-RFID Reader antennas	23
1.2.2 Review of Far-Field RFID reader antennas	24
1.2.2.1 FF RFID single-band antennas	25
1.2.2.2 FF RFID multiband antennas	25
1.2.3 Review of NF-FF and multiband antennas for RFID	26
1.3 Overview of the dissertation	28
1.3.1 Hypothesis	28
1.3.2 Objective of this research	28
1.3.3 Key contributions of the dissertation	29
1.3.4 Scope of the dissertation	30
1.3.5 Organization of the dissertation	31
<b>2 Antenna: Theoretical Background</b>	<b>35</b>
2.1 Antenna System	35
2.2 Part 1: Transmission Line Theory	37
2.2.1 Distributed lumped elements model for transmission line	38
2.2.2 Open circuited transmission line	42
2.2.3 Short circuited transmission line	43
2.3 Part 2: Antenna Theory	45
2.3.1 Radiating elements	45

2.3.2	Antenna parameters and properties . . . . .	46
2.3.2.1	Input impedance . . . . .	47
2.3.2.2	Impedance Bandwidth . . . . .	48
2.3.2.3	Antenna total efficiency . . . . .	48
2.3.2.4	Antenna radiation efficiency . . . . .	48
2.3.2.5	Radiation power . . . . .	49
2.4	Part 3: EM Propagation and Radiation . . . . .	49
2.4.1	Electric and Magnetic fields . . . . .	50
2.4.2	Power in space around antenna . . . . .	51
2.4.3	Directivity and Gain . . . . .	52
2.4.4	Case study: The Magnetic Coil Antenna . . . . .	52
2.4.4.1	Field at the axis of a current carrying small loop . . . . .	53
2.4.4.2	The multi-turn coil . . . . .	54
2.5	Part 4: Matching Network . . . . .	56
2.6	Part 5: Band Pass Filter . . . . .	58
2.7	Summary . . . . .	59
<b>3</b>	<b>Coil Antenna for HF-RFID</b> . . . . .	<b>61</b>
3.1	Introduction . . . . .	61
3.2	Coil design for high power transfer efficiency . . . . .	63
3.2.1	H-field Enhancement . . . . .	65
3.2.2	Distributed-turns coil for H-field enhancement . . . . .	67
3.2.3	Analytical Results . . . . .	68
3.2.3.1	Parametric study of $Q$ and $H$ versus $\Delta$ . . . . .	68
3.2.3.2	Optimum design and performance . . . . .	70
3.2.4	Simulation and Results . . . . .	71
3.3	Coil design for reliable data transfer . . . . .	72
3.3.1	Background . . . . .	73
3.3.2	HF-RFID System: Modeling and Design . . . . .	74
3.3.3	Reader Coil Design . . . . .	75
3.3.3.1	Size . . . . .	75
3.3.3.2	Number of Turns . . . . .	76
3.3.4	H-field Enhancement by Distributed-Turns Coil Design . . . . .	78
3.3.5	Non-uniformly Distributed-Turns Coil antenna . . . . .	80
3.3.5.1	Formulating the optimization problem . . . . .	80
3.3.5.2	Numerical method to find Optimum turn assignment $\mathbf{A}$ . . . . .	81
3.3.6	Analytical results of NDTC antenna . . . . .	83
3.3.7	Simulated Results of NDTC antenna . . . . .	84
3.4	Summary . . . . .	85
3.5	Chapter related publications . . . . .	86
<b>4</b>	<b>Fabrication of NDTC antenna and its applications</b> . . . . .	<b>87</b>
4.1	NDTC Coil antenna Fabrication and Measurements . . . . .	88

4.1.1	Measurement Setup and results . . . . .	89
4.2	NDTC Antenna over different Substrate Types and Reflector Prox- imities . . . . .	93
4.2.1	Various substrates and conductor types under consideration	94
4.2.2	Simulation of NDTC antenna printed over various substrates	95
4.2.3	Influence of Reflector Proximities over NDTC antenna . . . .	98
4.3	Application: Wide-spreading of the near-field . . . . .	100
4.3.1	The NDTC array antenna design . . . . .	102
4.3.2	Simulation and Results . . . . .	103
4.4	Summary . . . . .	105
4.5	Chapter related publications . . . . .	107
<b>5</b>	<b>Coil antenna for UHF-RFID</b>	<b>109</b>
5.1	Introduction . . . . .	109
5.2	Segmented-line coil antenna for UHF-RFID readers . . . . .	111
5.2.1	The STC and the SL-STC antenna design . . . . .	111
5.2.2	The SL-NDTC antenna design . . . . .	112
5.3	Simulations and results . . . . .	115
5.3.1	Far-field simulation results . . . . .	118
5.4	UHF antenna fabrication and measurements . . . . .	119
5.4.1	Measurement results . . . . .	120
5.5	Summary . . . . .	121
5.6	Chapter related publications . . . . .	123
<b>6</b>	<b>Switchable Multiband antennas</b>	<b>125</b>
6.1	Switchable dual-band NDTC antenna . . . . .	126
6.1.1	Design description of dual-band NDTC antenna . . . . .	126
6.1.1.1	State-1: Near-Field HF band . . . . .	128
6.1.1.2	State-2: Far-field UHF band . . . . .	128
6.1.2	RF MEMS switch modeling . . . . .	129
6.1.3	Simulation and measurement: Results . . . . .	129
6.1.3.1	State-1: Near-Field HF band . . . . .	129
6.1.3.2	State-2: Far-field UHF-band . . . . .	131
6.2	Multi-purpose switched multi-band antenna . . . . .	133
6.2.1	Design of a switched multi-band antenna . . . . .	134
6.3	UHF antenna fabrication and measurements . . . . .	136
6.3.1	Results . . . . .	136
6.3.1.1	mode-1: UHF 915 MHz near- and far-field results . . . . .	137
6.3.1.2	mode-2: 2.45GHz near- and far-field results . . . . .	140
6.3.1.3	mode-3: 5.8GHz near- and far-field results . . . . .	142
6.4	Summary . . . . .	144
6.5	Chapter related publications . . . . .	145
<b>7</b>	<b>Applications</b>	<b>147</b>
7.1	Near-field focusing for RFID applications . . . . .	147

7.1.1	The optimization process using vector projections . . . . .	149
7.1.1.1	Customized 3-D vector projection analytical model . . . . .	149
7.1.1.2	Initial NF-FCA antenna design . . . . .	153
7.1.1.3	Final NF-FCA antenna design . . . . .	153
7.1.2	Analytical Results . . . . .	155
7.2	Ink-jet printing of antennas using conductive ink . . . . .	159
7.2.1	Sprayed antenna on cans for WLAN-RFID tags . . . . .	161
7.2.1.1	Sprayed antenna structure . . . . .	161
7.2.1.2	Results . . . . .	162
7.3	Antenna customization for In-vehicle UWB MB-OFDM Communi- cations . . . . .	163
7.3.1	Introduction . . . . .	163
7.3.2	In-vehicle UWB connectivity in the passenger plane: Prob- lem description . . . . .	167
7.3.3	Channel-aware source synthesis process . . . . .	168
7.3.4	Results . . . . .	175
7.4	Summary . . . . .	176
7.5	Chapter related publications . . . . .	177
<b>8</b>	<b>Conclusion and Future Open Problems</b>	<b>179</b>
8.1	Concluding remarks . . . . .	179
8.2	Scope for future research . . . . .	182
	<b>Bibliography</b>	<b>185</b>

# List of Figures

1.1	Defining field regions around the antenna. . . . .	12
1.2	Three entities categorizing a RFID application. . . . .	13
1.3	Various combinations of RFID entities reported in literature. . . . .	15
2.1	Basic antenna system model. . . . .	36
2.2	Distributed lumped elements model for transmission line. . . . .	39
2.3	Transmission line terminated at an arbitrary load. . . . .	41
2.4	Transmission line with open circuit load (a) voltage (b) current (c) impedance. . . . .	43
2.5	Transmission line with short circuit load (a) voltage (b) current (c) impedance. . . . .	44
2.6	Evolution of electric dipole antenna . . . . .	46
2.7	Equivalent antenna circuit in transmitting mode. . . . .	47
2.8	Infinitesimal current carrying element and EM radiation. . . . .	50
2.9	Infinitesimal current carrying element and EM radiation. . . . .	53
2.10	The field at a distance $D$ from a multi-turn coil. . . . .	55
2.11	L-section matching networks . . . . .	57
3.1	(a) Concentrated-turns coil antenna (b) Distributed-turns coil antenna. . . . .	64
3.2	$Q$ -factor versus normalized $\Delta$ for different $N$ ; $a_1 = 0.07$ m; $r = 0.125$ mm; $I = 0.1$ A; $D = 0.05$ m. . . . .	68
3.3	H-field versus normalized $\Delta$ for different $N$ ; $a_1 = 0.07$ m; $r = 0.125$ mm; $I = 0.1$ A; $D = 0.05$ m. . . . .	69
3.4	Simulated $Q$ -factor and H-field versus $\Delta$ and $N$ . . . . .	72
3.5	HF-RFID equivalent network model (a) reader (b) Tag. . . . .	74
3.6	Coil antennas: (i) Single Turn Coil (STC) (ii) Uniformly Distributed-Turns Coil (UDTC) (iii) Non-uniformly Distributed-Turns Coil (NDTC). . . . .	77
3.7	$Q$ -factor of UDTC versus $\Delta$ and various $N$ ; $D = 0.05$ m. . . . .	79
3.8	Revealed NDTC antennas optimized using algorithm for various $N$ ; $D = 0.05$ m; $S_{wire} = 0.05$ mm <sup>2</sup> ; $I_0 = 0.4$ A. . . . .	83
4.1	(a) Fabricated Coil antennas (b) Circuit Model (c) Matching assembly. . . . .	88
4.2	a) The micro probe to measure $R$ , $L$ , and $Q$ b) The test points for the probe c) Near-field probe and setup for $H$ measurement. . . . .	89
4.3	Measured $R$ , $L$ , and $Q$ variation with frequency. . . . .	90
4.4	Measured S11 of the fabricated Coils-1 to -5. . . . .	91

4.5	The NDTC antenna front view printed of various substrates . . . . .	93
4.6	The NDTC antenna bottom view . . . . .	94
4.7	S11 of the loaded NDTC antenna with various substrates. . . . .	96
4.8	H-field comparison of NDTC antenna with various substrates. . . . .	97
4.9	The NDTC antenna working in proximity to a metallic reflector. . . . .	97
4.10	The simulated S11 response of the NDTC antenna (PCB FR4) and nearby reflector situated at $d$ distance. . . . .	98
4.11	The simulated $H$ captured at $z = 5\text{cm}$ of the NDTC antenna lying next to a reflector. . . . .	99
4.12	Applications demanding wide-spreading of the near-field (photos are for representation purpose only) . . . . .	100
4.13	The NDTC array antenna. . . . .	101
4.14	Current distribution in one NDTC element. . . . .	102
4.15	H-field distribution for one NDTC element at $z = 5\text{cm}$ . . . . .	103
4.16	Current distribution in the NDTC array antenna. . . . .	104
4.17	H-field distribution for NDTC array at $z = 5\text{cm}$ . . . . .	105
5.1	a) The STC and b) the SL-STC antennas for UHF-RFID. . . . .	111
5.2	The SL-NDTC antenna for UHF-RFID reader. . . . .	113
5.3	The intermediate design: SL-DTC antenna. . . . .	114
5.4	Assessing the optimal radius $R_2$ of the SL-DTC antenna. . . . .	114
5.5	Simulated S11 of the UHF-RFID coil antennas. . . . .	115
5.6	Simulated (a) currents and (b) $H$ distribution of the coils. . . . .	117
5.7	Simulated H-field distribution along z-axis and percentage $H$ enhancement by the SL-NDTC antenna. . . . .	118
5.8	Simulated radiation pattern of the SL-NDTC antenna . . . . .	119
5.9	Simulated efficiency and gain of the SL-NDTC antenna. . . . .	119
5.10	a) Fabricated antennas b) setup for measurement . . . . .	120
5.11	Measured S11 of the UHF-RFID coil antennas. . . . .	121
5.12	Measured $H$ of the UHF-RFID coil antennas at $z = 50\text{mm}$ . . . . .	122
5.13	SL-NDTC measured normalized radiation pattern. . . . .	123
6.1	The switched DB-NDTC antenna. . . . .	127
6.2	MEMS equivalent circuit model for ON-OFF states. . . . .	128
6.3	Simulated and measured S11 of the switched DB-NDTC antenna. . . . .	130
6.4	Simulated radiation pattern of the switched DB-NDTC antenna. . . . .	131
6.5	Simulated efficiency and gain of the switched DB-NDTC antenna. . . . .	132
6.6	Fabricated switched DB-NDTC antenna in anechoic chamber. . . . .	132
6.7	Measured radiation pattern of the switched DB-NDTC antenna. . . . .	133
6.8	Multipurpose switched multiband antenna. . . . .	135
6.9	Fabricated antenna a) front b) back c) in anechoic chamber . . . . .	136
6.10	S11 of the switched multiband antenna. . . . .	137
6.11	Simulated current at 915MHz in switching mode-1. . . . .	138
6.12	mode-1: (i) simulated $H_z$ in near-field (ii) far-field radiation patterns at 915MHz. . . . .	139

6.13	Simulated current at 2.45GHz in switching mode-2. . . . .	140
6.14	mode-2: (i) simulated $H_z$ in near-field (ii) far-field radiation patterns at 2.45MHz. . . . .	141
6.15	Simulated current at 5.8GHz in switching mode-3. . . . .	142
6.16	mode-3: (i) simulated $H_z$ in near-field (ii) far-field radiation patterns at 5.8GHz. . . . .	143
7.1	(a) The NF-FCA antenna E-field vector projections in a 3-D rectangular coordinate system. (b) A 2-D representation of the array elements (phases $\psi$ ) in regard to the focus and (c) Geometric evaluation of the $\psi^v$ corresponding to a circle $v$ . . . . .	150
7.2	Optimal E-field vectors to adequately direct in a more concentrated fashion at focus and due to (a) radially oriented dipoles (initial design), (b) co-linearly oriented dipoles (final design). . . . .	154
7.3	Normalized $ E $ in the focal plane when $F = z = 1$ m (a) initial design (b) final design. . . . .	156
7.4	The normalized $ E $ (analytical) for two transversal cuts of the main beam, $z = F = 1$ m along the (a)X-axis (b)Y-axis. . . . .	157
7.5	Focus agility comparison of the initial and the final design along the Z-axis ( $x = 0, y = 0$ ) for various $F$ . . . . .	157
7.6	Sprayed Tag antenna on a can. . . . .	162
7.7	The in-vehicle system configuration. . . . .	167
7.8	Steps for the channel-aware process of antenna design for in-vehicle UWB connectivity. . . . .	169
7.9	Measurements of the in-car UWB channel scenario. . . . .	171
7.10	MATLAB Simulink model of UWB MB-OFDM system. . . . .	172
7.11	The geometry of the antenna physical aperture used as AP. . . . .	173
7.12	BER distribution in the passenger plane (a) $BER^0$ for the commercial antenna (b) $BER^{fin}$ for the customized optimum source . . . .	175



# List of Tables

1.1	Various combinations of NF, FF, and Multiband properties for RFID reader antennas . . . . .	27
3.1	Optimum spacing $\Delta_0$ and % H-field enhancement for the Constant-Q design* compared to a constant- $L$ design# . . . . .	70
3.2	Simulated optimum spacing $\Delta_0$ and % H-field enhancement for the proposed design compared to a constant- $L$ design . . . . .	72
3.3	Algorithm to find optimum turn assignment <b>A</b> . . . . .	82
3.4	Analytical results of H-field enhancement for optimal NDTC antenna designs . . . . .	84
3.5	Simulated results of H-field enhancement for optimal NDTC antenna designs . . . . .	84
4.1	The $Q$ of the stand-alone coils. . . . .	90
4.2	Calculated and commercially available capacitance . . . . .	90
4.3	The measured $H$ enhancement of the coils . . . . .	92
4.4	Considered substrates with corresponding conductors. . . . .	95
4.5	R, L, Q of unloaded coils and corresponding matching network elements. . . . .	95
4.6	Recalculated matching network C1 and C2 to preserve matching. . . . .	99
5.1	Simulated bandwidths of the UHF coil antennas. . . . .	116
6.1	The DB-NDTC antenna switching . . . . .	128
6.2	Switching modes of multi-band antenna . . . . .	136
7.1	focus properties of the initial design vs. the final design . . . . .	158
7.2	Performance comparison of the optimized antenna vs. the standard antenna used as AP. . . . .	176



# Chapter 1

## Introduction and motivation

### 1.1 Background

The need for user mobility and communication technology advancements demands to transfer power and information wirelessly between two devices termed as transmitter (Tx) and receiver (Rx). The end entity of a wireless communication system, which is responsible for an efficient exchange of power and information between Tx and Rx, is an antenna. Therefore, it is crucial to design an efficient antenna for an efficient communication between the devices. This exchange of power and information is feasible only when both the devices (hence Tx and Rx antennas) are tuned to a common frequency of operation. There are various frequencies allocated for communication systems, but the choice of a common frequency of operation is governed by many factors e.g., application type and range, device size, system surroundings, etc. According to the chosen frequency, the dimension of antenna is determined.

As far as the range is concerned, from the basics of antenna theory [1, 2] we know that the field around any antenna is divided into regions shown in Fig. 1.1. Typically, it has two: 1) near-field (subdivided into reactive and radiating fields with dominantly magnetic/electric energy ) and 2) far-field (radiating with ElectroMagnetic (EM) waves) regions. Depending on this region/range division, the

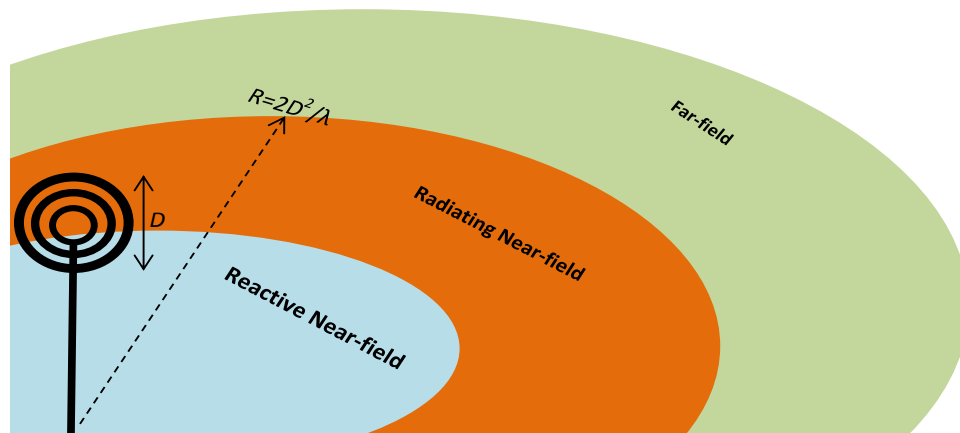


FIGURE 1.1: Defining field regions around the antenna.

communication systems present in the market can be divided into two categories; Near-Field (NF) systems and Far-Field (FF) systems. The NF systems work on the principle of inductive coupling between Tx and Rx [3], where power in the Rx antenna is induced by reactive field (Magnetic Field (H-field) or electric field (E-field)) oscillating near to the Tx antenna. That is why the antennas producing high reactive fields in their NF regions are desirable candidates for NF applications. Whereas, the FF systems utilize real power of propagating EM waves for coupling of two devices [4], and antennas producing high radiation in the FF region are welcomed for FF applications. For instance, the NF systems usually operate at Low Frequency (LF), High Frequency (HF) bands, because, the practical antennas at these frequencies are electrically small and having very low radiation resistance (a measure of FF radiation) which is not suitable for FF applications but can produce a decent NF reactive energy. In contrast, the far-field systems effectively operate in general at higher frequencies e.g., Ultra High Frequency (UHF), MicroWave (MW) bands where the practical antenna can have a size comparable to half wavelength therefore can produce enough far-field radiation. Thus, we can observe that the choice of operating frequency, the kind of antenna selected, and the working field region, all are somewhat interconnected and should be decided cautiously for a particular application.

An example of application where one clearly can realize the categorization of the communication systems based on the operating region, the choice of operating

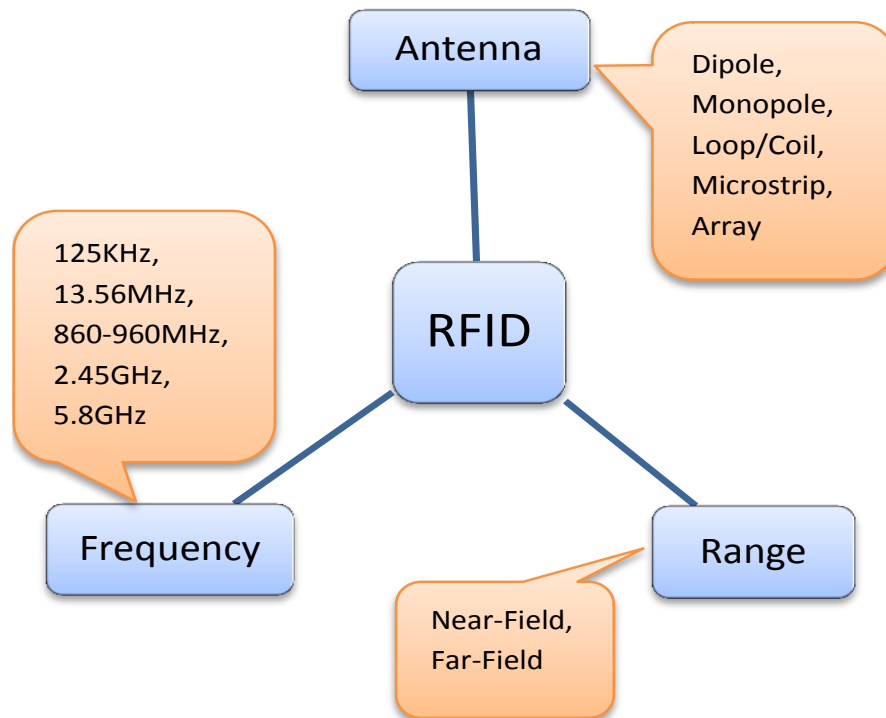


FIGURE 1.2: Three entities categorizing a RFID application.

frequency, and the selection of antenna type, is Radio Frequency IDentification (RFID). Fig. 1.2 shows the related entities defining the RFID application from antenna engineering point of view where various options of antennas, frequencies, and regions/ranges are selected. To investigate how these entities are related to each other the antennas are designed and evaluated in genuine RFID applications. The author first initiates with a background study of RFID systems with emphasis to the antenna perspective and presents it subsequently.

### 1.1.1 Antennas for RFID Technology

Since a few decades, barcoding is widely used in identification of objects, but analogously, the use of radio waves to track and trace the objects is gaining considerable attention. This identification through wireless communication is termed as RFID,

where a digital key associated with the object under the trace works analogous to the barcode. By using digital key, the RFID provides opportunity to uniquely identify and track several objects at a time without line of sight within range (mm to several meters) of the RFID system. It provides a contactless transfer of the information between an Interrogator (Reader) and a Transponder (Tag) tuned at the same frequency of operation. As presented earlier in Fig. 1.2, the RFID can be categorized depending of the frequency of operation, and various frequency bands have been adopted for RFID applications e.g., HF-13.56MHz, UHF-866/915MHz, 2.45 GHz, 5.8GHz. A particular frequency chosen for the RFID application defines the kind of antennas to be used for the reader and the tag.

Apart from the operating frequency, the region of operation defines two categories; NF RFID and FF RFID as defined in Fig. 1.2. The NF RFID systems are used for short range interrogation while employing inductive coupling between the Tag and the Reader antenna [3]. Whereas, the FF RFID is applicable for long range systems using a back-scattering concept and a decent FF radiation is expected from the reader antenna in this case. In general, the RFID antennas are designed for individual applications each having a particular operating frequency and optimized for either NF or FF operation. However, there exist in the literature, several designs of RFID antennas incorporating multiple combinations of NF, FF and frequency responses. Such combinations reported in the literature is tabulated in Fig. 1.3, where the correspondingly adopted antenna techniques are listed.

An overview of Fig. 1.3 suggests that, typically, NF RFID systems operate in LF (125KHz) and HF (13.56MHz), and uses multiturn coil, spiral loop, and distributed-turns coil antennas to generate robust reactive field for a maximum coupling between the reader and the tag. Whereas, it seems challenging to use original coil antennas for NF UHF-RFID systems due to phase inversions posed by electrically large coils at that frequency, segmented-line or capacitive coupler loaded loop antennas are the preferred choices at UHF. In contrast, for MW frequencies, e.g., 5.8GHz, the NF RFID found new applications of focusing the electric/magnetic fields in the NF region using phased array antennas..

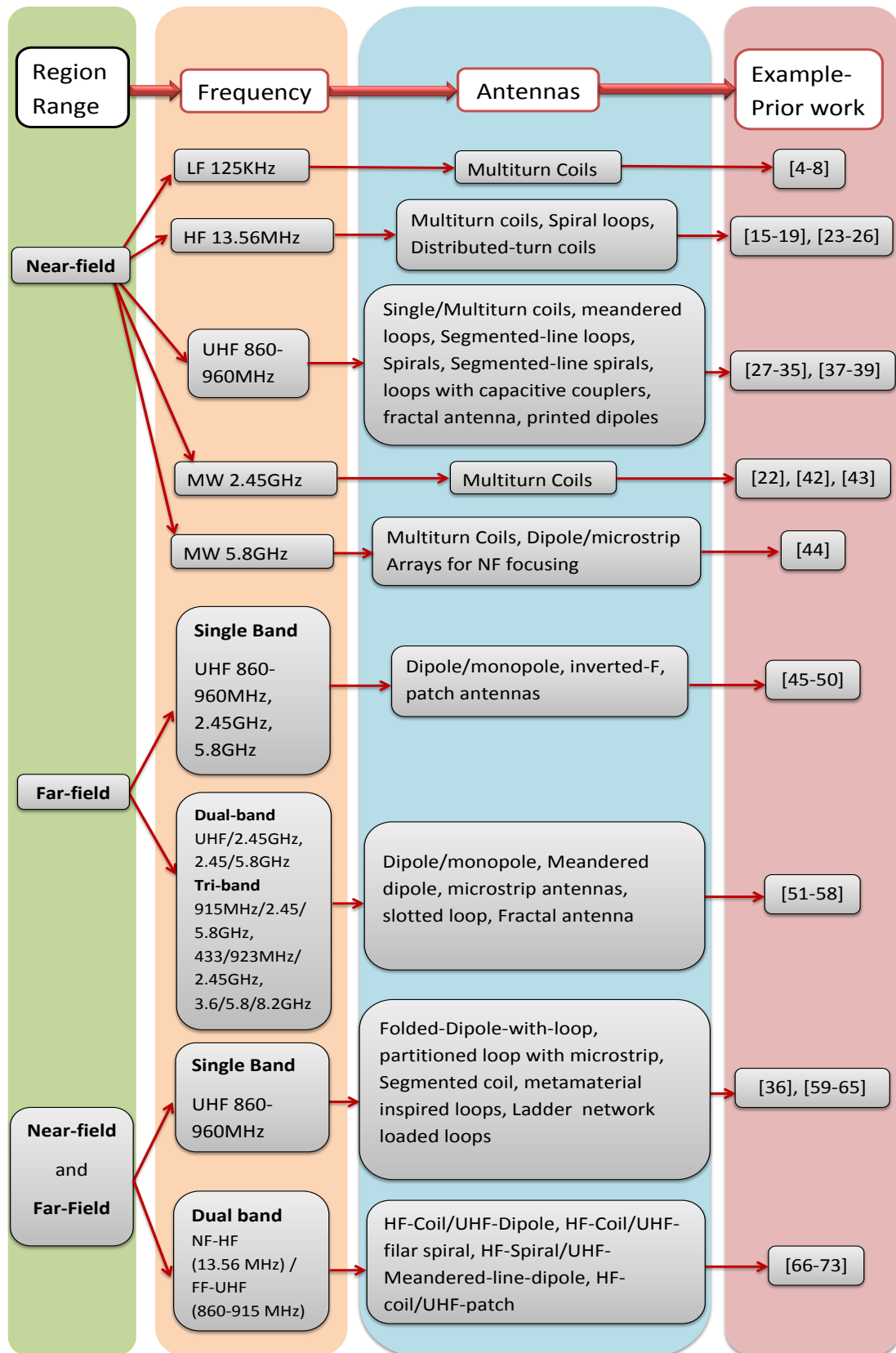


FIGURE 1.3: Various combinations of RFID entities reported in literature.

As shown in Fig. 1.3, the FF RFID systems, typically operating at higher frequencies, use monopole, dipole, and patch antennas for radiations in the FF region. The FF RFIDs are not confined to a single-band operation, but there are multiband antennas reported in the literature designed to work at multiple frequencies of RFIDs. For instance, dual-band (915MHz/2.45GHz, 2.45/5.8GHz) and tri-band (915MHz/2.45/5.8GHz, 433/923MHz/2.45GHz, 3.6/ 5.8/8.2GHz) antennas are reported for multiband FF RFID applications, where the antenna techniques such as meandered dipoles, slotted loops, fractal antennas, etc., are used to facilitate a multi frequency response.

Although RFID antennas designed for a particular application operate at a single frequency and are optimized for either NF or FF, for cost reduction the multipurpose antennas having both NF and FF operations along with multi-band responses are highly desirable. In this regard, Fig. 1.3 includes NF-FF RFID systems designed to operate both in NF and FF regions; this is reported by, some single-band UHF RFIDs using antennas with folded-dipole and loop, segmented-coil, partitioned loop and microstrip, meta-material inspired loop, and ladder network loaded loops, and some dual-band NF-FF RFIDs using dipoles, coils, filar spirals, etc. Fig. 1.3 also includes pertinent prior works reported in the literature for each combination of region and frequency. A detailed review is presented subsequently to detail further the RFID antennas.

## 1.2 Literature review and motivation

In this section, the review of most pertinent prior works is covered including the NF and the FF antennas along with multiband antennas used for RFID applications. Since, this investigation is mostly based on RFID readers, the focus in this section will be to review NF, FF, and multiband reader antennas.

## 1.2.1 Review of Near-Field RFID reader antennas

Initiating the review of LF-RFID antennas, several RFID bands will be detailed subsequently. Since the HF and the UHF bands became quite matured for the use in NF RFID, a detailed review of HF- and UHF-RFID reader antennas is additionally presented.

### 1.2.1.1 NF LF-RFID reader antennas

Since NF RFID applications are intended to operate for a short read range (due to NF communications), the antenna radiator can be electrically small which contributes to a low radiation resistance. Therefore, LF and HF are indeed frequency choices for the NF RFID systems. For the applications, requiring a short range, slow data reading speeds, high penetration of surrounding material, and relatively less stringent design limitations, the NF RFID in LF at 125KHz and 134.2KHz is attractive. Several LF-RFID antennas are reported in the literature. For instance, [5] presented a step-by-step process of designing LF-RFID interrogator/reader antenna and a multi-turn multi-layer coil was developed through this process. In [6], the range of LF-RFID reader antenna was investigated and single-/multi-loop antennas were considered in the study, whereas in [7], a square-shaped loop antenna was developed having 105 turns for maximizing the H-field in the NF zone. RFID antennas designed for some specific applications were also presented, for instance in [8], where a LF-RFID antenna was developed to fit in a fishing net for a cuboid aquarium application using an operating frequency of 134.2KHz. A recent ink-jet printing technology was also utilized to fabricate a LF-RFID antenna in [9] at 125KHz and presented two spiral coils printed on a flexible substrate for cost-effective solution. These LF coils can be re-used for higher frequencies but requires optimization, for instance, the coils developed for HF-RFIDs have to be cautiously optimized for a given read range. This is presented next.

### 1.2.1.2 NF HF-RFID reader antennas

The HF 13.56MHz band is the preferred choice for NF RFID applications which demand relatively low data rate (106 kbps [10]) and a small read range ( $\approx 1\text{m}$ ) [11] and is due to the following two reasons. First, since the unlicensed use of this band is worldwide internationally allowed, therefore, every system designed for this band is applicable any where in the world. Second, the magnetic waves at this frequency is less affected by and able to penetrate very dense surroundings and dielectric materials with high permittivity, e.g., water, the ground, than EM waves at higher frequencies. Therefore, HF-RFID systems are highly appreciated in the literature to be adopted for NF applications.

RFID system architecture and design methodology has been investigated in various reports of the literature. An architecture of RFID system was presented in [12] and Tx and Rx modules were conveniently designed using commercially available circuitry. Whereas, circuit design and related data processing of a transceiver was reported in [13], in [14], the HF-RFID system compatible with multiple standards was analyzed. The Silicon Phosphate (SiP) technology was used to develop the HF-RFID reader in [15] and hereby the RFID module where the antenna integrates is reviewed as to have a clear notion of how to enhance the overall performance of the HF-RFID system. Since antennas are the responsible end entities for an efficient power and data transfer between the reader and the tag, its optimization is crucial to achieve optimum system performance.

Typically, the NF RFID systems at HF (similar to LF) employs inductive coupling between the tag and the reader antennas [3]. Therefore, out of the solutions presented in Fig. 1.3, the coil antennas are widely adopted in this case as a low-cost solution for both Tx and Rx, which becomes analogous to a loosely coupled (magnetically) transformer. By inductive NF coupling, a sufficient power is provided to activate the tag IC from oscillating magnetic field (H-field) around the reader coil antenna [16–18]. This poses the challenge to design the coil antennas of both, the reader and the tag, to produce a robust H-field for the former and to effectively capture this field for the latter. Unlike FF antennas which are characterized

by gain, directivity, radiation pattern, etc., the coil antennas for HF-RFID are characterized by the following performance parameters, the coupling coefficient ( $k$ ) between the reader and tag coils, received H-field ( $H$ ) and induced voltage ( $V_{ind}$ ) in the tag circuit, inductance ( $L$ ) and resistance ( $R$ ) and unloaded quality factor ( $Q$ ) of the coil antennas. These parameters are considered to design a coil for optimal system performance and depend on the geometry of the coils such as the shape, dimension in radius, the section of wire in radian, and the number of turns in the coil [19]. Both the tag and the reader coil antennas were designed in the literature and optimized for a particular property.

Previous studies in the literature dedicated on designing the efficient tag coils for inductive-coupling, largely concentrate on procedures to minimize the size of the tag antenna and to enlarge the read out range [16–18, 20]. In general, these procedures of designing the tag coil antennas were mainly influenced by low cost, low profile, and electrically small size, however, the bandwidth (BW) requirement for the tag coil was not stringent [16] due to applications i.e., tracking and tracing, requiring low data rates. Recent advancements in the antenna fabrication procedure, e.g., ink-jet printing [21], urged to find new applications of RFID by pasting the antennas anywhere, for instance, a car-body [22], food and drink cans, etc. Therefore, the current investigations of the tag coil antennas are focusing towards gaining flexibility to be able to lay the tags over surfaces of any shape and material.

On the other hand, a set of reported works have investigated the overall performance of the HF-RFID system by optimizing the reader coil antennas for a maximum  $V_{ind}$  induced in the tag [23], an increased reading range (read out distance) [24], and the coil size reduction [17, 25]. For instance, [24] reports a design procedure of a RFID reader antenna where coil size was optimized for a given read out distance and a predefined tag. Other than the size, the design parameters for the reader antenna are the coil shape, the section of the wire, and the number of turns. These parameters are also included in optimization, because ultimately they do define relevant system performance quantities,  $k$ ,  $H$ ,  $L$  and  $Q$  of the reader coil antenna. Since the tag chip is powered by the voltage induced in the tag circuit, the  $V_{ind}$  is the ultimate target of optimization whose value is

desired to be as high as possible. The higher  $V_{ind}$  can be translated either into an improved coverage (read-out distance), higher reliability of communication, or antenna size reduction (smaller size of tag antenna captures comparatively low  $H$  which compensates increased  $V_{ind}$ ). For enhancing the  $V_{ind}$  in the tag circuit, typically, two optimization approaches are followed in the literature [17, 23, 25]; 1) by  $k$  enhancement with unconstrained  $L$  and 2) by  $H$  enhancement.

In the first approach of obtaining higher  $V_{ind}$ , the reader coil antenna is optimized to enhance  $k$  between the reader and the tag by keeping the reader  $L$  constant [23, 25]. Any  $k$  improvement is supposed to yield an increased  $V_{ind}$  by following the relation from [23],

$$V_{ind} = j \cdot \omega \cdot k \cdot \sqrt{L \cdot L_{Rx}} \cdot I,$$

where  $L$  and  $L_{Rx}$  are the inductances of the reader and the tag coils, respectively,  $I$  is the current in the reader coil, and  $\omega$  is the operating frequency. Since  $k$  represents intensity of magnetic coupling between the two coils, it depends on and can be altered with a change in reader coil dimensional parameters (e.g., radius, shape, number of turns), and same dependence is true for the  $L$ . Therefore, the  $k$  enhancement by altering reader coil dimensional properties also changes the  $L$ . We note that  $V_{ind}$  depends both on  $k$  and  $L$ , therefore, any approach of enhancing  $k$  value oblivion of  $L$  does not fully reflect a desired enhancement in  $V_{ind}$ , hence this approach may not be the optimal one. However, the approach of  $k$  enhancement while keeping the  $L$  unaltered (to maintain resonance frequency constant) was proposed in [25] that maximization of  $k$  is fully reflected into a  $V_{ind}$  maximization. For example, maximization of  $k$  by optimizing the number of turns and separation between the turns of the reader coil antenna is an attractive approach [17, 25], however, it renders  $Q$  degraded. This is because, when number of turns in the coil increases, the coil resistance  $R$  increases, but if  $L$  is kept unchanged, this definitely lowers the quality followed by [24]

$$Q = \frac{\omega \cdot L}{R}, \quad (1.1)$$

We term this approach as constant- $L$  design where  $L$  is assumed constant therefore  $Q$  reduces. Thus, optimization of  $k$  using constant- $L$  approach has a disadvantage that it results into a 25% reduction in  $Q$ -factor [25], which means increment in antenna losses and reduction in power efficiency.

The second approach of obtaining a higher  $V_{ind}$  by optimizing  $H$  is more appealing and governed by the following relation from faraday's law

$$V_{ind} = \mu_0 \cdot j\omega \cdot N_{Rx} \cdot A_{Rx} \cdot H$$

where coil area  $A_{Rx}$  and number of turn  $N_{Rx}$  both belong to tag coil antenna. By observing this relation, we note that the  $V_{ind}$  is exclusively dependent on a single entity belonging to reader antenna, that is the H-Field  $H$ . Therefore, an enhancement of  $H$  will be exclusively reflected as a greater  $V_{ind}$ . For instance, maximizing  $H$  by optimizing the reader coil antenna's dimensional parameters surely maximizes  $V_{ind}$ . Since several coil parameters are available, e.g., shape, size, number of turns, etc., there can be many approaches to optimize these parameters, one of them is the immediately mentioned constant- $L$  approach. If constant- $L$  is used to maximize  $H$ , it will definitely improve  $V_{ind}$ , but will result into a lower  $Q$  of the reader coil. This leaves a scope to develop a new approach of optimizing multi-turn coil to obtain an enhanced H-field and high  $Q$  of the reader antenna to improve the link-budget of HF-RFID systems. Thus, the target to maximize the propagating H-field while ensuring a unconstrained  $Q$  performance of the reader coil antenna motivates us to design the optimum reader coil prototype for HF-RFID systems.

In recent developments on HF-RFID antennas, there are investigations which focus on developing antennas for some particular applications. For instance, in [26] a semicircular spiral antenna was developed for the applications where tags are surrounded by conducting materials. In [27], HF-RFID reader antenna was developed to monitor gaming chips in a casino by installing synchronized spiral coils under the playing chip tray.

### 1.2.1.3 NF UHF-RFID Reader antennas

As presented in Fig. 1.3, a typical UHF-RFID works in the FF region and correspondingly developed antennas hold a high radiation property implying an ability of efficient FF detection of the UHF tags. In contrast, for applications, e.g., item-level identification in medical instrumentation, health-care (e.g. bio-sensing), and real-time logistics of mobile consumables (e.g. medicines) and patients, the promising NF RFID technology developed recently operates at UHF [28]. The coil antenna (solid-line) are the kind which preferred in the NF applications, as presented in Section 1.2.2.1, they are the conventionally used low-cost solutions at HF for reader and tag antennas. The idea of NF UHF-RFID antenna design is to re-utilize those solid-line coil antennas [24, 25, 29] which are used as reader in the LF- and HF-RFID. This poses a big challenge to adapt conventional HF-RFID coil antenna for the use in UHF-RFID while maintaining the original coil size and hence the large interrogation area. For instance, the solid-line coil antennas used in LF/HF-RFID are electrically small loops ( $C < \lambda/10$ , where  $C$  is the total circumference of the loop and  $\lambda$  is the operating wavelength [1]), the current flowing along the loop is almost in-phase which makes them capable of producing strong H-field in the NF region of the reader antenna [24, 25, 29]. Whereas, at UHF,  $C$  of the same coil antenna becomes comparable to  $\lambda$  [28, 30] (the loop becomes electrically large) and current distribution along the loop is no longer in-phase, moreover, the phase inversions and current nulls are encountered. Therefore, conventional solid-line coil used as UHF-RFID reader antenna suffers with weak and non-uniform H-field in the interrogation zone diminishing the system performance. For near-field operations, a strong magnetic field is required and the electrically large coil at UHF must be modified to compensate current phase variations.

To effectively design the electrically large coil antennas for NF UHF-RFID applications, some ideas have been reported in the literature. To obtain strong and uniform H-field distribution, a coil antenna is proposed in [31] using segmented-line loaded with lumped capacitors. The key of this design is to compensate the

current phases (introduced along the line) at the end of each segment by a capacitor, such that the current in the coil appears to be in-phase. A similar idea is reported in [32–34] where broken-loop antennas were proposed using different coupled lines. Furthermore, to compensate the phases, various configurations of the segmented-line coils were proposed using e.g., dashed-line [30], embedded phase shifters in solid-line coil [35], and distributed capacitors [36]. This way, irrespective of the coil being electrically large at UHF, the current along the perimeter of the coil is forced to be in-phase. The UHF segmented-line coils presented in [37, 38] were composed of multiple segments of a solid-line section intercalated with a fork-shaped capacitor, these segments were distributed along the periphery of the coil. This coil was composed of only a single turn and termed as Segmented-Line Single-Turn Coil (SL-STC). Although, conventional solid-line Single-Turn Coils are widely used in HF-RFID readers, their evolution into multi-turn coils was a major interest for coupling enhancement between the inductively coupled reader and tag HF-RFID antennas. On contrary, segmented-line coils having multiple turns for UHF-RFID have not been attended. This motivates us to investigate the possibility to utilize the segmented-lines in a multiturn manner to maximize H-field in the NF zone of the UHF-RFID.

In recent developments, some novel technologies are adopted to design UHF-RFID reader antenna for NF applications. In [39], fractal antenna technique was used to design a protruded tapered slot antenna for UHF-RFID reader. Whereas, in [40], array technique was applied to develop a UHF-RFID reader antenna consisting multiple layers of printed dipoles arranged in a square geometry to produce a strong H-field in the NF zone.

#### **1.2.1.4 NF MW-RFID Reader antennas**

The typical applications of NF RFID in the market are largely dominated by lower frequencies, e.g., LH and HF, because of their maturity over the time, however, the demand to reduce size and cost of the tags is always motivating researchers to explore other possibilities of cost-effective tag design technologies. One possible

solution for the same was reported in [23], where a on-chip antenna (OCA) technology was developed to design tags with significantly reduced size and price. In OCA technology, since the tag coil is fabricated directly on the Tag chip, the size of the coil is very small, therefore, a higher operating frequency should be used to realize such antenna. The NF RFID system developed in [23] uses frequency 2.45GHz to realize OCA for the tag, and correspondingly a reader antenna was designed to operate at the same frequency.

Among various applications of the NF RFID, for the one which requires energy confinement into a small area, e.g., supply chain, warehouse management, heating of cancerous cells in medical application, item location search, etc., the Near-Field Focusing (NF-F) antennas are demanded. For instance, for assets identification on conveyor belts, the reader antenna is desired to be well focused in the near-field region with low Side-Lobe-Levels (SLL) [41, 42]. A highly focused antenna results in a high gain with increased efficiency of the RFID reader and the low SLLs are welcomed for accuracy and reduced cross-talk systems. In [43, 44], a NF-F planar microstrip array was designed for 2.4GHz RFID readers. A focus agile (tunes/re-configures the focal distance) antenna can empower RFID systems with rapid reconfigurability of the energy confinement of a reader. Following this idea, a NF-F circular array antenna for 5.8GHz RFID reader applications was proposed in [45] and uses planar printed dipoles as radiating array elements.

### **1.2.2 Review of Far-Field RFID reader antennas**

In the previous section, the NF RFIDs with typical frequencies LF, HF, and UHF were reviewed, and the coil antennas were found to be the most suitable candidate for such applications. In contrast, the FF RFIDs find more applications at higher frequencies e.g., UHF, 2.45, and 5.8GHz, as shown in Fig. 1.3, and the antenna with high FF radiation is the preferred choice. In addition, the FF RFID reader antennas in the literature were developed for multiple utilities adopting multiband approach through a single antenna unit, therefore, the review of FF RFIDs is attended individually for single- and multi-band antennas.

### 1.2.2.1 FF RFID single-band antennas

Although, the typical antennas at higher frequencies can be developed using dipole, monopole, microstrip/patch technology, there exist approaches in the literature possessing low cost manufacturing and higher gain designing. For instance, in [46, 47], partitioned circular/square loops were reported to produce robust FF radiation and operate at 5.8GHz, where overlapped/top-layer printed loops were designed. Whereas, in [48] to obtain a higher gain and impedance bandwidth, a coplanar waveguide-taper fed technology was developed for RFID antennas of frequencies 5.8 GHz and 915MHz individually. To reduce interference, beam-forming techniques are useful, and smart antenna/phased-array is adopted to shape the beam of a specific size. A phased array was developed for FF UHF-RFID reader antenna in [49, 50] claiming wider bandwidth in UHF and narrower beam-width to mitigate interference from multiple tag reading. For 2.45 GHz FF RFID reader application, a five element digital beam-forming antenna was reported in [51].

### 1.2.2.2 FF RFID multiband antennas

The antennas with multi-band response and solely FF operation are presented in the following. Dual band antennas combining UHF and MW for FF RFID applications were designed; in [52] using microstrip slot line operating at 915MHz/2.45GHz and in [53] using annular plate with slots operating at 922.5MHz/2.45GHz. In contrast, to combine two MW bands, dual-band 2.45/5.8GHz antennas for FF RFID readers were developed; using folded strip monopole in [54], using a U-shaped feed with rectangular printed ring in [55] providing high gains, and in [56], using a slot loop and a pair of strips for tunability. Some tri-band antennas for FF RFID applications were also reported. For instance, in [57] HF-UHF-MW were combined in one design using microstrip to develop a tri-band antenna for 433/923MHz/2.45GHz RFID reader application. Whereas, a tri-band tag antenna was developed in [58] using meandered dipole antenna for 910 MHz/2.45GHz/5.8GHz. Tri-band antennas were designed using fractal geometry in [59] for both the reader and the tag operating at 3.6/5.8/8.2GHz.

Once we reviewed the antennas which were developed individually either for NF or FF RFIDs, the review of antennas providing both NF and FF functionality through a single design unit is presented next.

### 1.2.3 Review of NF-FF and multiband antennas for RFID

In general, RFID antennas are designed for applications with a particular frequency and optimized individually for either NF or FF. However, if a single antenna unit could be developed to read the tags in NF as well as FF regions, it can significantly reduce the cost of the readers introducing multi-purpose applications of RFIDs. Moreover, rather using a separate antenna for each frequency of RFID operation, if a single antenna unit can be developed to operate for multiple frequencies, this will serve to the ultimate purpose of minimizing system-cost. Therefore, the low-cost multipurpose antennas having both NF and FF operations along with multi-band responses are highly desirable. In the literature, some designs of RFID antennas with limited combinations of NF, FF and multi-band responses were reported.

For instance, antennas functioning at single band UHF having both NF and FF operations were developed by using; loop constructed from folded dipole [60–62], segmented circular-loop with capacitive couplers [37], segmented square loop encompassing patch [63, 64], slotted circularly-polarized Patch [65], and loop loaded by a left-handed ladder network for reconfigurability [66]. Some dual-band RFID antennas to operate in the NF at HF 13.56MHz and in the FF at UHF 866/915MHz were also reported, e.g., tag antennas designed in [67–72], and the reader antennas proposed in [73, 74] made of HF-coil and UHF-dipole/monopole elements.

Although, the multiband antennas serve to cost-effective system design, they can invite extra interference through multiple bands into the operational frequency band. To mitigate such problems, frequency reconfigurability approach is adopted [75], in that case the antenna's operational frequency can be changed to the current desired operation. One kind of frequency reconfigurability is called 'switched

multiband antenna’, where the antenna is able to work at predefined multiple frequencies but behaves like a single-band antenna at a time, this is performed by switching the operational frequency between multiple bands using RF switches. Hence, reconfigurable antennas having multi-band response with switchable operating frequencies are of great interest to reduce interference and improve overall system performance [75] while keeping the cost to a minimum.

TABLE 1.1: Various combinations of NF, FF, and Multiband properties for RFID reader antennas

Region	HF	UHF	2.45GHz	5.8GHz	Reconfig.	Design
NF FF	×	✓	×	×	×	[37, 60–65] (single loop)
NF FF	×	✓	×	×	✓	[66] (single loop)
NF FF	×	✓	×	×	×	Chapter 5 (multi-turn coil)
NF FF	×	×	×	×	×	[52, 53]
NF FF	×	×	×	×	×	[54–56]
NF FF	×	×	×	×	×	[57]
NF FF	✓	×	×	×	×	[73, 74]
NF FF	✓	×	×	×	✓	Section 6.1
NF FF	×	✓	×	×	×	Section 6.2
NF FF	×	✓	✓	✓	✓	Section 6.2

For RFID reader applications, Table 1.1 summarizes the antennas developed with various combination of NF, FF, Multiband, and switching properties. It can be observed that previous designs leave a lot of scope for designing multi-purpose RFID reader antenna with switchable mutiband response. This motivated us to investigate and develop the antennas which can include most of the properties shown in Table 1.1. The current research will try to achieve this goal through the new designs referred in Table 1.1.

## 1.3 Overview of the dissertation

The review of previous designs developed for RFID applications, presented in Section 1.2 showed the limitations of existing antennas, it assisted us to discover a research problem for this dissertation. Currently, as far as the author is aware, there are no antennas that can actually work in both NF and FF along with having multiple operational frequencies to be switched between. It is necessary to design such antennas to achieve a minimal system expenditure and to gain in terms of communication reliability. This study intends to contribute in designing new antenna structures towards addressing the existing limitations, and it forms the hypothesis of this investigation presented as following.

### 1.3.1 Hypothesis

*It is possible to design a switched multi-band antenna that works for both near-field and far-field RFID and whose operating frequency can be switched between multiple bands.*

### 1.3.2 Objective of this research

The main objective of the study is to design a multi-purpose switched multiband RFID reader antenna. The specific objectives of the study are mainly two folds: 1) To enhance the performance of RFID systems by optimizing reader antennas to produce intensive fields in the desired interrogation zone 2) To design RFID reader antenna whose frequency can be switched between multiple bands and for each band the antenna should be able to work in both NF and FF region. To achieve the final goal, this study will proceed by targeting following sub-objectives:

- In single-band NF RFID applications, the reader antenna should be optimally designed to enhance field in the vicinity, because, any enhancement in the field directly translates into an extended reading range and more reliable

communication between reader and tag units. To achieve this, one approach can be by adjusting the geometrical parameters of the reader antenna, but it should not affect negatively on other features like quality and operating frequency of the reader antenna.

- Single-band reader antennas for RFID applications should be designed to serve multiple purposes by able to read the tags in NF as well as FF zones. The intended antenna should be able to produce a robust field in the NF zone and a decent radiation in FF zone. Such multi-purpose NF and FF antennas are needed for range extension and for reducing the cost of the reader system by serving two purposes through a single antenna unit.
- RFID reader antenna should be designed for multi-band operation serving as universally used antenna for all the frequencies of RFID applications. However, the switching must be incorporated to reduce interference and cross-talks by selecting one of the multiple bands at a time for current operation. Furthermore, this intended switched multiband antenna should perform both NF and FF operations for each individually selected frequency band.

### **1.3.3 Key contributions of the dissertation**

The dissertation has the following contributions to the knowledge:

- Proposed a novel geometrically optimized multi-turn coil antenna for RFID application to generate significantly enhanced field intensity in the NF zone of the reader antenna without affecting quality-factor of the coil.
- Proposed an antenna-array for RFID and wireless-power-charging applications to wide-spread the interrogation area of the NF reader. A robust field intensity was achieved throughout the extended interrogation area using novel optimized multi-turn coil as the array element.
- Deployed the optimized multi-turn coil technique into RFID reader antenna to generate an enhanced H-field in the NF zone along with a decent radiation

in the FF zone, as a result, proposed a multi-purpose NF- and FF- antenna for single-band operation.

- Developed a dual-purpose NF and FF reader antenna with dual-band response whose operation can be switched between two RFID frequencies.
- Designed a multi-purpose multi-band reader antenna switchable between three RFID frequencies and at each individually selected band it can work for both NF as well as FF RFID applications.
- Introduced a 3-D vector-projection-model to analyze the RFID array antenna for NF focusing applications, and developed an array antenna for RFID reader with highly focused beam in NF and reduced side-lobes in interrogation zone.
- Designed a novel RFID-WLAN antenna using ink-jet printing process, where the antenna is sprayed directly on metal-based containers like food/beverage cans and useful for hidden antenna applications.

### 1.3.4 Scope of the dissertation

The dissertation study is performed to address the issues which are not covered by previous works and summarized in Table 1.1. It is a big engineering challenge to design a universal antenna which can work efficiently for all the applications covering all the frequency bands assigned to the RFID. This dissertation work investigates the challenge of developing antennas gradually to include as many properties as possible.

For instance, it begins with designing a novel antenna called Non-uniformly Distributed Turns coil (NDTC) optimized for a maximum H-field generation in the NF zone of a HF-RFID reader operating at 13.56MHz. Therefore, a single-band antenna having intensified field intensity in the NF zone is developed for 13.56MHz, however, this NDTC antenna does not serve any FF purpose. For that operation, a multi-purpose antenna serving both NF and FF operations is developed for

UHF-RFID readers functioning at 915MHz, this is termed as SL-NDTC antenna and designed using the novel NDTC approach and a segmented-line technique of obtaining an intensified and wider NF zone. Although, the SL-NDTC antenna can interrogate tags in both NF and FF, however, it operates only at a single RFID frequency 915MHz. Towards the intention of addressing the challenge, a Dual-band reader antenna is developed using the optimized NDTC antenna along with two RF-switches, the antenna can interrogate tags in both NF and FF zone and its operating frequency can be switched between two RFID bands, HF and UHF. Following that, ultimately, a multi-purpose switched multiband antenna is designed to serve in both NF and FF whose operating frequency is switched between three RFID bands 915MHz, 2.45GHz, and 5.8GHz. It will be shown to include two more bands of frequencies 354MHz and 3.72GHz in conjunction with 915MHz and 2.45GHz, respectively, hence, a penta-band antenna is developed. However, since in this study we are concentrating only on reader antennas for RFID applications, only three bands 915MHz, 2.45GHz, and 5.8GHz are chosen for performance evaluation.

Although, there are various RFID frequency bands adopted in the literature, e.g., LH, HF, UHF, 2.45GHz, and 5.8GHz, and each individual band can be utilized for either NF or FF operations, a single antenna unit which incorporates both the operations at all the RFID bands with switching facility is uneasy to design. Therefore, this dissertation limits itself upto three RFID bands in a single antenna unit incorporating multiple purposes of NF and FF RFID applications.

### **1.3.5 Organization of the dissertation**

The rest of the dissertation is organized as follows:

Chap. 2 tours a theoretical overview of the antenna system model to build the basic knowledge of each separate block consisting in the system model. The performance parameters of the antenna system are derived and utilized later to analyze some typical antenna structures.

In Chap. 3, the design process of 13.56MHz HF-RFID reader coil antenna used for NF applications is described. To optimize the HF antenna, a novel NDTC coil approach is proposed which can significantly improve performance of the HF-RFID reader. The NDTC antenna is modeled theoretically and simulated using EM solver, and both the results are compared.

In Chap. 4, the NDTC antenna is fabricated and measured results are compared with the theoretical and the simulated ones. The NDTC antenna's performance is further investigated for various substrate and deposited conductor types and the effect of reflector proximities over NDTC antenna is reported. Moreover, for extended application of NDTC antenna in RFID and wireless power charging, an array is developed using NDTC antenna elements to expand the interrogation area to 4 times while keeping the field intensity to the maximum.

Chap. 5 presents the UHF-RFID reader antenna designed using NDTC approach to maximize field intensity in the NF zone, in addition, to have a decent FF radiation characteristics. Hence, a multi-purpose UHF-RFID reader antenna is developed and presented in this chapter.

In Chap. 6, first, a dual-purpose NF and FF antenna is presented having dual band operation and can be switched between HF and UHF RFID bands. Second, a tri-band antenna is presented holding four properties: 1) serves multi-purpose NF and FF zones 2) has multi-band response to cover UHF and two microwave RFID frequency bands 3) its operating frequency is switchable between these three bands 4) operate in NF and FF for each individually selected frequency band.

Chap. 7 demonstrates some applications of antennas. First, a NF focused array antenna is analyzed for 5.8GHz RFID application. Then a review of ink-jet printing process for current generation antennas is presented, followed by design of a RFID Tag antenna developed using ink-jet printing technology and sprayed over food/beverage can. At the end, an introduction of UWB antennas for in-car communication is presented, and a technique to design highly efficient antenna for in-car communication is demonstrated.

Finally, Chap. 8 concludes the dissertation with indication of some open problems and directions of future research.



# Chapter 2

## Antenna: Theoretical Background

An antenna is a crucial part of wireless communication system and equally important at transmitter and receiver side. The transceiver (transmitter + receiver) system consists of several parts, each having its own attributes and working principles, and a dedicated governing theory of analysis and synthesis for each part. These building blocks can be studied separately and a vast literature is dedicated for each of them. In this chapter, to build the base to understand the overall antenna system principle, a summary of various building blocks of antenna system is presented.

### 2.1 Antenna System

The basic antenna system model [1, 76] for a transmitter or a receiver node is articulated in Fig. 2.1. The system is divided into several different parts each one of them having its own importance and vast pertinent theory established in the literature. To illustrate the model, we take transmitter side as an example, and the receiver side will be analogous. At the transmitter side, the initial block in the chain is a transmission module (Tx). The Radio-Frequency (RF) signal traveling out from the Tx is fed to a Band pass filter, BPF (Part 5 in Fig. 2.1) to confine the energy flow through a desirable frequency band and to reject the leakage of

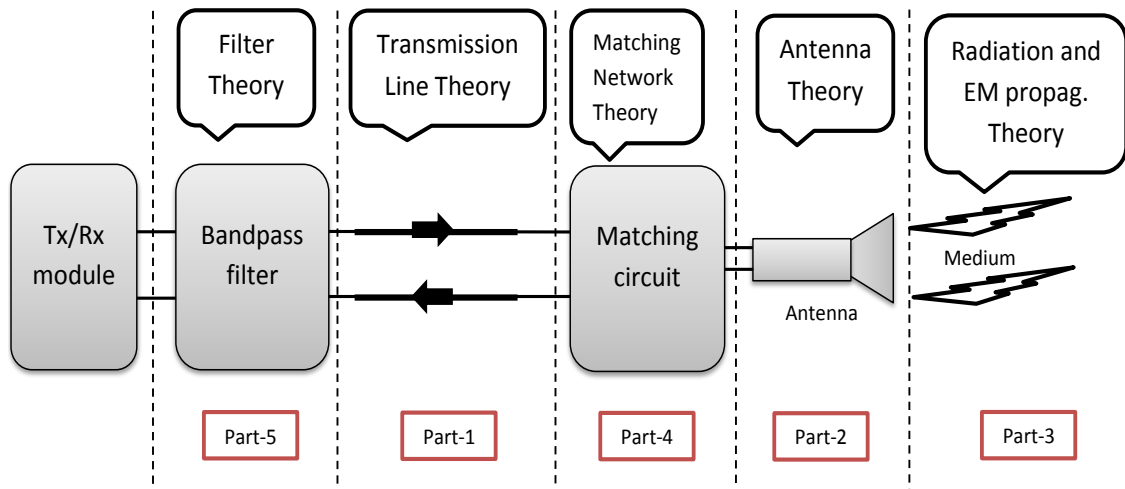


FIGURE 2.1: Basic antenna system model.

unwanted energy into the adjacent bands. The theory of Band pass filter design and its property is studied to get the idea of loss and noise associated with BPF operation, this can be a crucial part for the overall system performance and its efficiency.

The filtered signal from BPF reaches to antenna by traveling through a transmission lines (Part 1 in Fig. 2.1), which may also introduce losses and distortions in the traveling signal. At lower frequencies, length of the transmission line is comparatively smaller than wavelength of the traveling signal, an equivalent lumped elements model can be used to represent and analyze the transmission lines, which is governed by circuit theory. In contrast, at higher frequencies, transmission line can not be represented as lumped elements model, thereby, making the analysis complex. This is because, when the signal's wavelength is smaller than the transmission line's length, it causes a spacial variation in the signal's amplitude along the line length. Hence, the transmission line theory is required when dealing with such a higher frequency signal traveling through the transmission line. At the termination point of the transmission line, if the impedance of the antenna is mismatched with the impedance of the transmission line, it can cause reflections at input junction of the antenna. The impedance mismatching can significantly reduce the efficiency of the system, therefore, a matching network (Part 4 in Fig.

2.1) is required to effectively match the transmission line to the antenna. The art of designing an efficient matching network is covered in matching network theory and will be described in this chapter along with several other parts of Fig. 2.1.

The electrical signal fed to the antenna is launched into the space in the form of Electro-Magnetic (EM) waves. Therefore, the antenna can be perceived as a converter of the electrical energy to the EM energy. This energy conversion should be efficient for a desirable system performance and governed by the characteristics of the antenna (Part 2 in Fig. 2.1). Once released from the antenna, EM waves can travel through the medium (channel) and undergo through different channel phenomenon, e.g, distortion, multipath fading, reflections, etc (Part 3 in Fig. 2.1). The characteristics of the EM waves propagating through a medium are studied under radiation and EM propagation theory.

At the beginning, it is desirable to start with the transmission line theory, so that evolution and working principle of a radiating element or an antenna can be understood. Hence, first we evaluate the basic characteristics of the transmission lines and the theory for its analysis.

## 2.2 Part 1: Transmission Line Theory

In this section, an overview of transmission line theory is presented, and most of the descriptions are fetched from well built chapter on this topic in [76]. For all circuits consisting of lumped elements and connectors, circuit theory is the way to analyze the properties of the circuit elements. The limitation of the circuit theory analysis is that it is useful only for the lower frequency signals having wavelength considerably higher than the spacial extension of the circuit elements. In other words, if a time varying signal is fed to a circuit element then at a given point of time its phase should not vary along the length of that element. Since, the spacial invariance of signal property is not assured for higher frequencies, the circuit element can not be represented by a lumped element network. Therefore,

the circuit theory analysis is not valid and a separate method called field theory is evolved.

In the field theory, the signal is represented as electric and magnetic field waves which travel through the medium, this provides the relationships among various entities of waves, sources, and medium. These relations are derived from the Maxwell's wave equations that provide full solution of wave properties and EM fields at each location of the space. In contrast, at very higher frequency (optical domain) where the wavelength is much shorter than the element's size, the analysis is carried out using geometrical optics theory.

Depending on the complexity of the microwave circuit elements, the field theory analysis possess its own mathematical complexity due to complex Maxwell's field relations. We note that, although, phase and magnitude of the signal vary along the component length, it can still be represented as distributed lumped elements connected in series. The study using distributed elements model is called as transmission line theory, which is a bridge between the standard circuit theory and the field theory, and also an easy method for initial understanding of the component's behavior.

### **2.2.1 Distributed lumped elements model for transmission line**

The transmission line is modeled using distributed lumped elements. A small element of the line is chosen such that its length  $dl$  represents only a small fraction of the wavelength, and the applied voltage and current can be treated constant along the  $dl$ . This small fraction of length  $dl$  can be represented as a lumped elements network as shown in Fig. 2.2 [76], this way the entire transmission line can be represented by a series connections of such lumped networks. The fraction  $dl$  is represented in Fig. 2.2 by series and parallel combinations of lumped resistance, capacitance, and inductance where

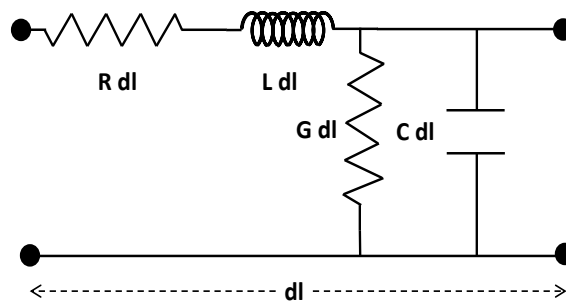


FIGURE 2.2: Distributed lumped elements model for transmission line.

$R$ =series resistance per unit length (representing losses due to finite conductivity of the two conductors in  $dl$ )

$G$ =shunt conductance per unit length (representing dielectric losses of the material between to conductors)

$L$ = inductance per unit length of the two wires

$C$ =capacitance per unit length between two conductors

These are the primary parameters of the transmission line and depends only on the physical characteristics of the line. In terms of primary parameters  $R$ ,  $G$ ,  $L$ , and  $C$ , the voltage  $V(x)$  and the current  $I(x)$  variation along the line length  $x$  is given by:

$$\frac{dV(x)}{dx} = -(R + j\omega L)I(x); \quad \frac{dI(x)}{dx} = -(G + j\omega C)V(x), \quad (2.1)$$

where sinusoidal variation  $e^{j\omega t}$  of signal is assumed in time. The solution sets of differential equations (2.1) are obtained as:

$$V(x) = V_0^+ e^{-\gamma x} + V_0^- e^{\gamma x}; \quad I(x) = \frac{V_0^+}{Z_0} e^{-\gamma x} - \frac{V_0^-}{Z_0} e^{\gamma x} \quad (2.2)$$

where  $\gamma$  is the complex propagation constant given by a combination of attenuation constant  $\alpha$  and phase constant  $\beta$ , and  $Z_0$  is the characteristic impedance of the transmission line. Both  $\gamma$  and  $Z_0$  are the secondary parameters which are defined

in terms of primary parameters as:

$$\gamma = \alpha + j\beta = \sqrt{(R + j\omega L)(G + j\omega C)} \quad (2.3)$$

and

$$Z_0 = \sqrt{\frac{R + j\omega L}{G + j\omega C}}. \quad (2.4)$$

Moreover, for a lossless transmission line with  $R = G = 0$ , the  $\gamma$  is purely imaginary and we have:

$$\alpha = 0; \quad \beta = \omega\sqrt{LC}; \quad Z_0 = \sqrt{\frac{L}{C}}. \quad (2.5)$$

From (2.5) we note that  $\beta$  is frequency dependent, therefore, signals with different frequencies will travel with different velocities through the transmission line. In practice, secondary parameters are widely used to describe the properties of the transmission lines.

By observing  $V(x)$  in (2.2), we note that the voltage is a linear combination of forward and backward traveling waves. This wave behavior corroborates the claim made for the field theory that electric and magnetic fields are a combination of waves traveling along the line in opposite directions. To understand the physical meaning of characteristic impedance  $Z_0$  of a line, we note from (2.2) that  $Z_0$  is the impedance seen by individual traveling waves. In other words, characteristic impedance is the voltage to current ratio in the presence of a single wave traveling in only one direction. But we can see the energy flow in (2.2) occurring in both the directions simultaneously, which means there exists a source of this backward traveling wave at the line termination. This phenomenon can be explained as following.

When transmission line is terminated at an arbitrary load impedance  $Z_L$ , shown in Fig. 2.3 [76], a part of forward traveling wave (incident wave) is reflected back due to mismatch at the load site. This reflected wave serves like a source for the backward traveling wave in (2.2). This reflection phenomenon is characterized by reflection coefficient  $\Gamma$  which is the ratio of reflected and incident voltage wave

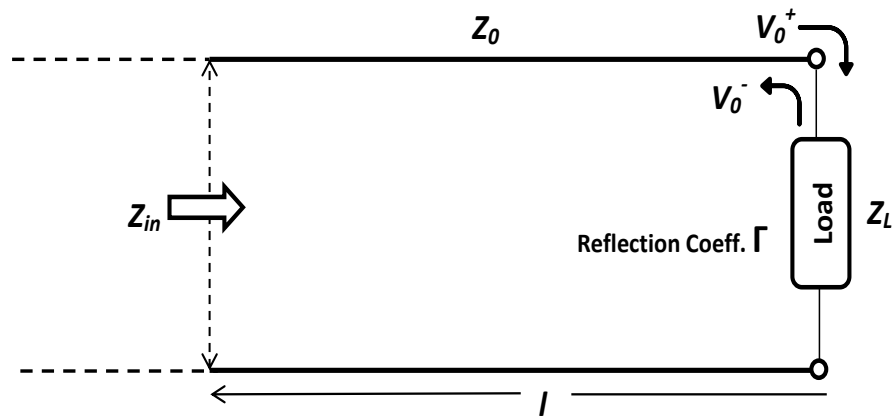


FIGURE 2.3: Transmission line terminated at an arbitrary load.

amplitudes and is given by:

$$\Gamma = \frac{V_0^-}{V_0^+} = \frac{Z_L - Z_0}{Z_L + Z_0}. \quad (2.6)$$

Due to this reflection, the whole power is not getting transferred to the load; this loss is quantified by return loss ( $RL$ ) in dB as:

$$RL = -20 \cdot \log|\Gamma| \quad \text{dB}. \quad (2.7)$$

In practice, to realize  $\Gamma$  of an antenna (which can be seen as a single port network), the scattering parameter  $S_{11}$  is measured.

Arose due to mismatching, the forward and backward waves traveling through the same line interfere and generate standing wave along the transmission line. This standing wave exhibits voltage maxima/minima distributed across the line, and their relative values determine the intensity of the reflected wave and mismatching. Therefore, another measure of mismatch is given by Voltage Standing Wave Ratio (VSWR) and defined as:

$$\text{VSWR} = \frac{V_{max}}{V_{min}} = \frac{1 + |\Gamma|}{1 - |\Gamma|}. \quad (2.8)$$

Since the voltage in (2.2) varies along the length of the line due to reflections, the

input impedance  $Z_{in}$  of the transmission line while looking from source side will also vary along the length. The value of  $Z_{in}(l)$  at a distance  $l$  away from the load site (Fig. 2.3) is given by:

$$Z_{in}(l) = \frac{V(-l)}{I(-l)} = Z_0 \frac{Z_L + jZ_0 \tan \beta l}{Z_0 + jZ_L \tan \beta l}. \quad (2.9)$$

The  $Z_{in}(l)$  relation given in (2.9) is very important to build basic understanding of the antenna theory, shown later in this chapter. As we will see in Section 2.3, it is simpler to understand antennas (e.g., electric dipoles and loops) by realizing antennas as a special case of transmission line terminated with specific loads. For instance, a short electric dipoles (or loop) can be realized as an open (short) circuited transmission line. Therefore, we will now consider these two special cases of load termination of the transmission line.

## 2.2.2 Open circuited transmission line

When a lossless line is terminated with open end, the load impedance  $Z_L = \infty$ , and  $Z_{in}$  in (2.9) reduces to

$$Z_{in}(l) = -jZ_0 \cot \beta l. \quad (2.10)$$

We note that the input impedance of an open circuited lossless transmission line in (2.10) is purely imaginary and capacitive for a short line length  $l$ . The input impedance, voltage, and current variations along the length of the open circuited line is depicted in Fig. 2.4 [76]. As expected, the standing wave voltage is maximum and the current is zero at the end of transmission line. These results are important and utilized in Section 2.3 in understanding small electric dipoles. It is intended that the input impedance of a small electric dipole should have a capacitive imaginary part.

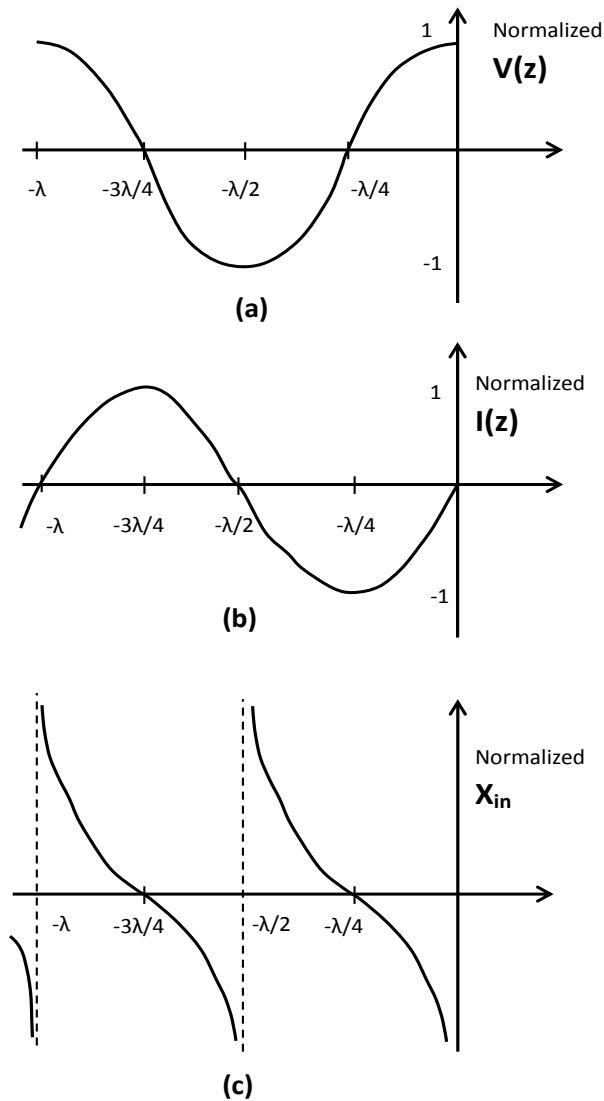


FIGURE 2.4: Transmission line with open circuit load (a) voltage (b) current (c) impedance.

### 2.2.3 Short circuited transmission line

If a lossless line is terminated with short circuited load, the load impedance  $Z_L = 0$ , and  $Z_{in}$  in (2.9) simplifies to

$$Z_{in}(l) = jZ_0 \tan \beta l. \quad (2.11)$$

We note that the input impedance of a short circuited lossless transmission line in (2.11) is purely imaginary and inductive for smaller length  $l$ . The input impedance,

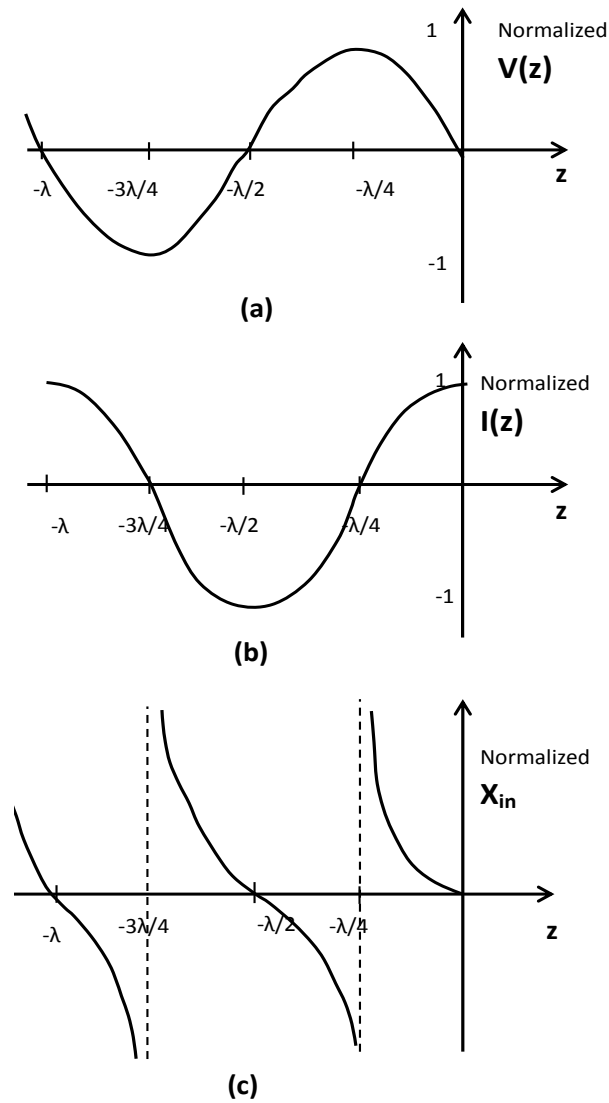


FIGURE 2.5: Transmission line with short circuit load (a) voltage (b) current (c) impedance.

voltage, and current variations along the length of short circuited line is depicted in Fig. 2.5 [76]. The standing wave current is maximum and the voltage is zero at the end of the transmission line. Analogous to the open-circuited transmission line, the short-circuited line can describe small current loops which intended to have input impedance with an inductive imaginary part.

## 2.3 Part 2: Antenna Theory

Once the basic features of a transmission line were covered in Section 2.2, the antenna and its characteristics are now described. The antenna is defined as a unit which emits electro-magnetic radiation. As we will see in this section, a transmission line can also behave like an antenna if the conducting wires of the transmission line are optimized for the purpose. Most of the description and theory in this section is inspired by [1, 77].

### 2.3.1 Radiating elements

The radiation is a property of conductors but not all the conductors radiate electromagnetic energy. The antenna built with a single wire can radiate only when the wire is bent, terminated, truncated, curved or discontinuous, in case the charges in the wire are moving with constant velocity. A single wire without any deformation will radiate if the movement of charges in wire is time varying, this way, even a single wire can be used as an antenna. But the single wire antenna does not support TEM mode, because from the field theory we know that at least two conductors are required for TEM mode to be operational.

The transmission line with two parallel wires seems suitable for the TEM propagation at first sight. But the currents in two wires of the transmission line flow in parallel but in opposite directions, and too close to each other that the total field is canceled in space. Therefore, it eliminates the possibility of EM radiation and can only guide EM waves along the length without any radiation.

Lets consider a two wire transmission line which is open circuited at the load site as shown in Fig. 2.6 [78] with standing waves depicted in Fig. 2.4. Now we gradually bend the two wires from open end in opposite directions to make a vertical dipole as shown in Fig. 2.6. The dipole now has two currents flowing in the same direction in the two vertical wires, and hence it radiates EM waves into the space. This way, we can understand the EM radiation process of a dipole

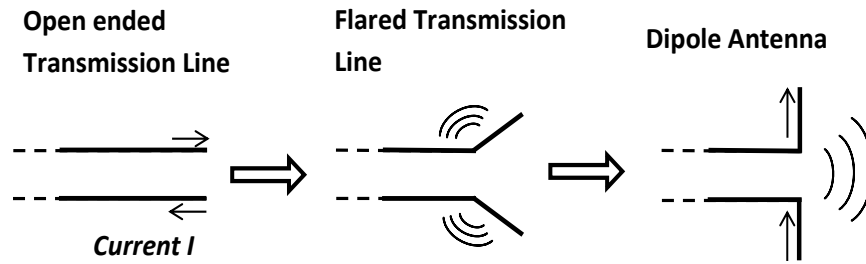


FIGURE 2.6: Evolution of electric dipole antenna

which is a simplest form of the antenna. It is also required to realize the radiation of other complex antennas. For this, we analyze the radiation characteristic of an infinitesimal dipole antenna known as Hertz dipole in Section 2.4, which is nothing but a very small current carrying element. Since any complex antenna can be represented as combination of distributed infinitesimal current carrying elements, the radiation by that complex antenna can be realized as a vector combination of radiation from infinitesimal dipoles.

In general, the antennas do not radiate the whole power supplied to them by the transmission line; this is characterized by the efficiency of the antenna radiation. The antenna system has its own limitations and behavior which should be characterized to know the efficiency of the antenna systems and their properties. We now study some of such parameters associated in general with the antennas.

### 2.3.2 Antenna parameters and properties

Although, the antenna can radiate EM power, but no practical antenna is ideal to radiate all the power fed into it, because, antennas have losses due to finite conductivity of metal and also due to dielectric. Moreover, when the antenna is not matched with feeding transmission line, this adds return loss to the practical antennas systems. To analyze the antenna properties, its transmitting mode equivalent circuit is represented in Fig. 2.7 [1].

The equivalent circuit of the antenna consists of loss resistance  $R_L$ , radiation resistance  $R_r$ , and reactance  $X_a$ . The loss resistance  $R_L$  represents the conduction

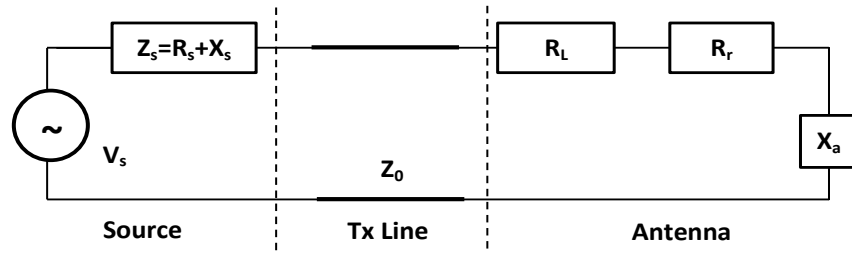


FIGURE 2.7: Equivalent antenna circuit in transmitting mode.

loss  $R_c$  and dielectric loss  $R_d$  of the antenna structure following the relation:

$$R_L = R_c + R_d. \quad (2.12)$$

Hence, the total antenna resistance becomes:

$$R_a = R_L + R_r = R_c + R_d + R_r. \quad (2.13)$$

The antenna is fed by a source  $V_s$  with internal impedance  $Z_s = R_s + jX_s$  through a transmission line with characteristic impedance  $Z_0$ .

### 2.3.2.1 Input impedance

Input impedance,  $Z_a$ , of the antenna is the impedance at input terminal of the antenna and given as,

$$Z_a = R_a + jX_a = (R_L + R_r) + jX_a. \quad (2.14)$$

Once we know  $Z_a$ , the reflection coefficient,  $\Gamma_a$ , at antenna's terminal can be calculated using (2.6) and is given as:

$$\Gamma_a = \frac{Z_a - Z_0}{Z_a + Z_0}. \quad (2.15)$$

### 2.3.2.2 Impedance Bandwidth

The input impedance of the antenna is frequency dependent, and because of that the antenna is not tuned for all the frequencies. Therefore, return loss of the antenna will also depend on the frequency and it will increase with operating frequency deviation from central frequency of operation. The frequency range around central frequency (tuned) where return loss is under tolerable limit (mostly taken as 10 dB) is called as impedance bandwidth. The prefix 'impedance' given for this bandwidth is because the antenna impedance is mismatched if signal frequency is out of this bandwidth around operating frequency of antenna.

### 2.3.2.3 Antenna total efficiency

The antenna total efficiency  $e_a$  takes into account all the losses present in the antenna structure as well as the mismatch loss occurs at the input terminal of the antenna. In terms of conduction efficiency  $e_c$ , dielectric efficiency  $e_d$ , and reflection or mismatch efficiency  $e_r = 1 - |\Gamma_a|^2$ , total efficiency is given by:

$$e_a = e_c e_d e_r = e_{cd}(1 - |\Gamma_a|^2), \quad (2.16)$$

where  $e_{cd}$  represent total loss in antenna structure and  $\Gamma_a$  is given by (2.16).

In practice  $e_c$  and  $e_d$  can not be measured separately, hence the combined  $e_{cd}$  is measured, whereas  $\Gamma_a$  can be measured by  $S_{11}$  as stated earlier for single port network like antenna.

### 2.3.2.4 Antenna radiation efficiency

Antenna radiation efficiency,  $e_{cd}$ , is defined as the ratio of the power delivered to  $R_r$  to the total power entering in to the antenna structure (power delivered to  $R_L$  and  $R_r$ ) and is obtained as:

$$e_{cd} = \frac{R_r}{R_c + R_d + R_r}. \quad (2.17)$$

### 2.3.2.5 Radiation power

The power radiated by antenna is nothing but the power dissipated in  $R_r$  and is given by:

$$P_{rad} = \frac{1}{2}|I|R_r^2. \quad (2.18)$$

In this section, we have analyzed some of the properties of the antennas by representing it by an equivalent circuit. But by doing that we can analyze only the physical losses, reflections etc. of the antenna, but not the spacial radiation characteristics and patterns. The radiated power  $P_{rad}$  detaches from antenna in the form of EM waves. Therefore, to understand the radiation characteristics, we first need to study the properties of EM waves detached from antenna. Moreover, the antenna may not be able to radiate its power uniformly in all the directions. Hence, the directional properties of the antenna radiation are also of interest. Since  $P_{rad}$  represents only the real power radiated by the antenna, there should be some reactive power associated with the antenna represented by  $X_a$ . To know about these mentioned characteristics, e.g., complex power and its distribution in the space around antenna, we study the properties of EM waves emitted from the antenna in Section 2.4.

## 2.4 Part 3: EM Propagation and Radiation

As discussed in Section 2.3, the antenna emits EM radiation into the space. The radiation properties as a function of space in 3-Dimension (3D) is represented by radiation pattern of the antenna where the radiation properties like Electric-field (E-field), H-field, radiated power density, directivity, etc. are presented in graphical or mathematical form. The EM radiation from an antenna can be fully described by knowing E- and H-field values at each location of the space surrounding the antenna. In this regards, the overview of background theory presented in this section are developed from [1, 2].

### 2.4.1 Electric and Magnetic fields

Similar to Section 2.3, an infinitely small current carrying element (Hertz dipole) should be studied to understand the EM behavior of other complex antennas. To evaluate the electric and magnetic fields, we place a Hertz dipole of length  $l \ll \lambda/50$  and a uniform finite current  $I_0$  at the origin and aligned it along z-axis in spherical coordinate system, as shown in Fig. 2.8. The electric and magnetic

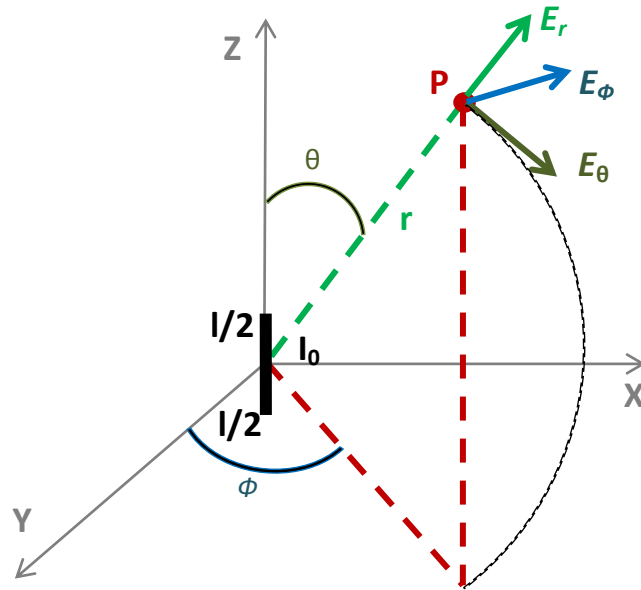


FIGURE 2.8: Infinitesimal current carrying element and EM radiation.

fields at a point P in space having a distance  $r$  from the Hertz dipole are obtained by solving Maxwell equations for EM waves in space with current source at the origin. The field components are calculated as:

$$E_r = \frac{I_0 l \cos\theta}{4\pi\epsilon} e^{j\omega t - j\beta r} \left[ \frac{\beta}{\omega r^2} - \frac{j}{\omega r^3} \right], \quad (2.19)$$

$$E_\theta = \frac{I_0 l \sin\theta}{4\pi\epsilon} e^{j\omega t - j\beta r} \left[ \frac{j\beta^2}{\omega r} + \frac{\beta}{\omega r^2} - \frac{j}{\omega r^3} \right], \quad (2.20)$$

$$E_\phi = 0, \quad H_r = 0, \quad H_\theta = 0, \quad (2.21)$$

$$H_\phi = \frac{I_0 l \sin\theta}{4\pi} e^{j\omega t - j\beta r} \left[ \frac{j\beta}{r} + \frac{1}{r^2} \right]. \quad (2.22)$$

By analyzing these field equations, we observe that there are three different term variations with distance  $r$ . Depending on the degree of decay with  $r$ , the three different terms can be described as:

1.  $\frac{1}{r}$  Radiation field  $\sim \frac{\omega\mu\epsilon}{r} \propto \omega$
2.  $\frac{1}{r^2}$  Induction field  $\sim \frac{\sqrt{\mu\epsilon}}{r^2}$ , independent of  $\omega$
3.  $\frac{1}{r^3}$  Electrostatic field  $\sim \frac{1}{\omega r^3} \propto \frac{1}{\omega}$

These three points are the key and at the core of different properties of the fields at different region of space around antenna element, presented next.

## 2.4.2 Power in space around antenna

Once we know the field distribution around the antenna in space, we can evaluate the power emitted into the space as a function of distance from the antenna. The total power flow in radial direction at a distance  $r$  is given by:

$$P = \frac{\eta\pi}{3} \left| \frac{I_0 l}{\lambda} \right|^2 \left( 1 - j \frac{1}{(kr)^3} \right) = P_{rad}(\text{Real}) + \text{Reactive power (Imaginary)} \quad (2.23)$$

From (2.23), it can be seen that the total power is a complex quantity with real part being radiated power and the imaginary part being reactive power stored in the space, therefore, justifying the reactive element  $X_a$  in circuit model of Fig. 2.7. We note that, the complex power in (2.23) is only the radial component. There exist also the transverse component of the power which is purely imaginary added contribution to  $X_a$ . Depending on the domination of the reactive or the real powers, the region around the Hertz dipole is divided broadly in to two regions. The first region  $r \ll \lambda/2\pi$ , where reactive power dominates the real power, is called as near-field region. The second region  $r \gg \lambda/2\pi$ , where the real power dominates and reactive power (diminishes to zero), is called as far-field region.

After the study of radiated power and near- and far- field region characterization, we realize that the power is assumed to be radiated uniformly in all the direction,

till now there is no clue of directional properties of the antenna radiation pattern. In the next section some directional properties of the antenna are described.

### 2.4.3 Directivity and Gain

The energy flow carried by electric and magnetic fields in radial direction is represented by average pointing vector (power density)  $W$  defined as:

$$W = \frac{1}{2} \text{Re}[E \times H^*] \quad (2.24)$$

and for far-field it is called as radiation density. The radiation intensity  $U$  defined as power radiated per unit solid angle is obtained as

$$U = r^2 W \quad (2.25)$$

Directivity  $D$ : ratio of radiation intensity  $U$  in given direction to radiation intensity  $U_{avg}$  averaged in all the directions, using  $U_{avg} = P_{rad}/4\pi$  is given by

$$D = \frac{U}{U_{avg}} = \frac{4\pi U}{P_{rad}} \quad (2.26)$$

Relative Gain  $G$ : the ratio of power gain in a given direction to the power gain of a reference antenna (e.g., isotropic lossless source) in the referenced direction.

$$G = \frac{4\pi U}{P_{in}(\text{lossless isotropic antenna})} = e_{cd} \frac{4\pi U}{P_{rad}} = e_{cd} D \quad (2.27)$$

### 2.4.4 Case study: The Magnetic Coil Antenna

The coil antennas having one or more loops are suitably adopted in near field applications such as RFID. The principles behind which these systems work is known as near field induction (coupling) between the Tx and the Rx coil antennas. It is widely used in High Frequency RFID (HF-RFID) applications, where the coil antenna is a natural choice and adopted in both a reader and a tag system.

Once the field equations for infinitesimal current carrying element are known from Section 2.4.1, in this section, we utilize them to derive the field distribution of a current carrying loop and extend it later for a multi-turn coil antenna.

#### 2.4.4.1 Field at the axis of a current carrying small loop

Lets consider a small loop of radius  $a$  carrying a constant current  $I_0$  (electrically small loop hence a constant current assumption is valid) as shown in the Fig. 2.9. The electric and magnetic field intensity will be derived at an observation point situated at a distance  $D$  from the center of loop antenna. The loop is divided into several infinitely small current sections of length  $dl$ , each having current  $I_0$ . The field components originating from one such current section at observation point are depicted in Fig. 2.9(a) [24]. By knowing this geometry, it is observed that the

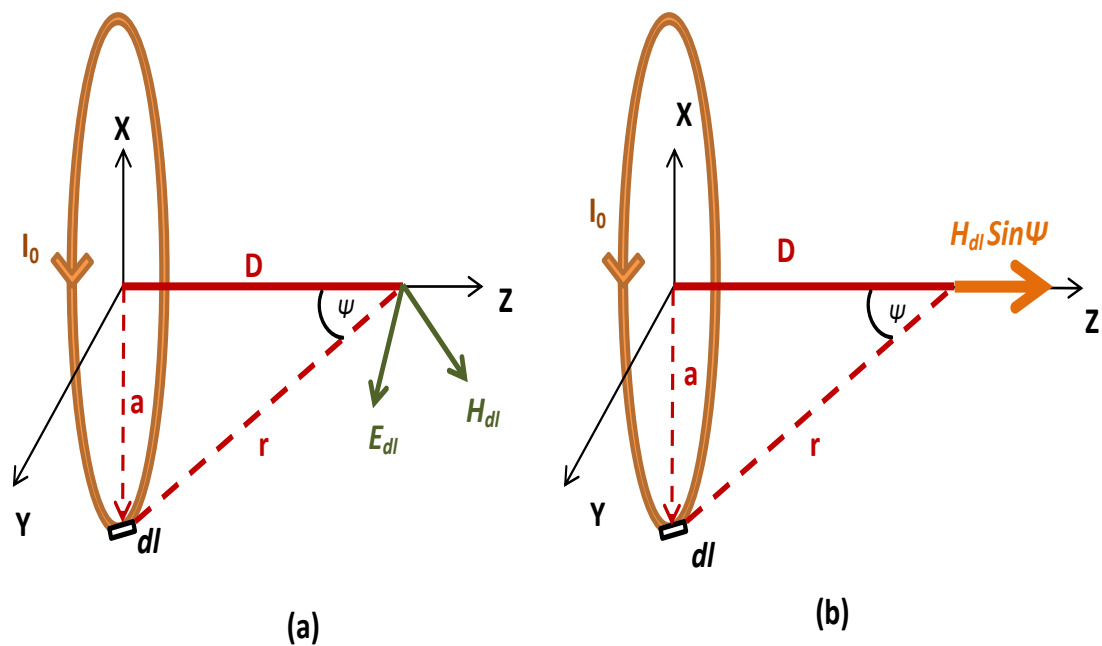


FIGURE 2.9: Infinitesimal current carrying element and EM radiation.

fields due to  $dl$  can be obtained by substituting  $\theta = 90^\circ$  in to the field equations (2.19) - (2.22). This renders all the fields zero except  $E_\theta$  and  $H_\phi$  whose magnitudes

can be obtained from (2.20) and (2.22) as:

$$E_{dl} = \frac{I_0 dl}{4\pi\epsilon} \left[ \frac{\beta}{\omega r^2} \right], \quad (2.28)$$

$$H_{dl} = \frac{I_0 dl}{4\pi} \left[ \frac{1}{r^2} \right]. \quad (2.29)$$

where only the near field reactive parts are considered as explained in Section 2.4.1. The directions of these fields are geometrically shown in Fig. 2.9(a). The total field at distance  $D$  is given by vector summation of field components from all the current elements forming the loop.

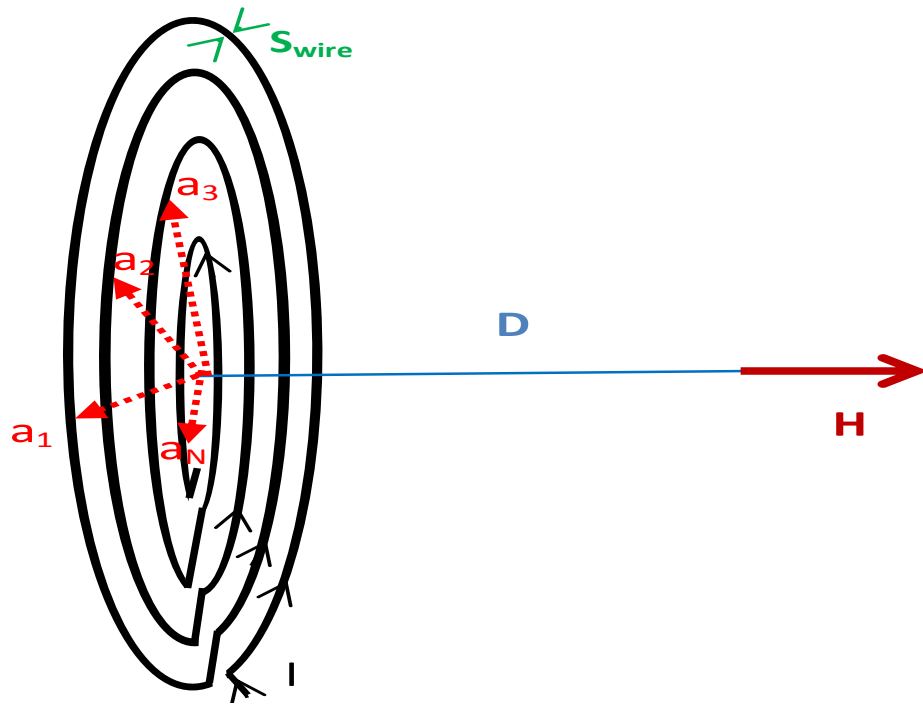
We note that due to symmetry, the E components will cancel each other, and hence, the total E will be zero. The H components ( $H_{dl} \sin\psi$ ) parallel to loop plane will cancel each other, whereas, the H-components ( $H_{dl} \cos\psi$ ) along the axis will add to the total H-field and calculated as [24]:

$$H = \sum_{2\pi a} H_{dl} \sin\psi = \int_0^{2\pi a} \frac{I_0}{4\pi} \left[ \frac{1}{r^2} \right] \cdot \frac{a}{r} dl = \frac{I_0}{2} \left[ \frac{a^2}{r^3} \right] = \frac{I_0 a^2}{2(\sqrt{a^2 + D^2})^3} \quad (2.30)$$

The resultant H-field formulated in equation (2.30) represents the total field at the axis of the loop and has a direction normal to the loop plane. By analyzing this case study, it is proved that any complex antenna can be analyzed by knowing the field distribution of an infinitesimal current carrying element (Hertz dipole).

#### 2.4.4.2 The multi-turn coil

To enhance near-field coupling of the magnetic loops, a coil having multiple turns is utilized. The multi-turn coil antenna, shown in Fig. 2.10, can be expressed by a radius vector  $\mathbf{A}$ , where  $\mathbf{A} = [a_1, a_2, \dots, a_N]$  and  $a_i$  is the radius of  $i^{\text{th}}$  turn (loop), number of turns  $N$ , and current  $I$  in the coil. In this section, we extend the derivation performed in the previous section to find the H-field produced by an electrically small multi-turn coil antenna at a distance  $D$ . The total H-field for a multi-turn coil is given by summation of all fields generated by each of  $N$  turns [17]. Hence, using derived H-field of a single loop in (2.30), the resultant  $H$  of a

FIGURE 2.10: The field at a distance  $D$  from a multi-turn coil.

multi-turn coil antenna is obtained and given by [24]:

$$H(\mathbf{A}) = \sum_{i=1}^N \frac{I \cdot a_i^2}{2 \left[ \sqrt{a_i^2 + D^2} \right]^3}. \quad (2.31)$$

### Inductance and Resistance of a multi-turn coil

To analyze the antenna, an equivalent circuit having lumped elements is used. Therefore, the equivalent circuit parameters of the multi-turn coil antenna is derived and used in later chapters. The multi-turn coil antenna is highly inductive and equivalently represented as an inductance  $L$  and a resistance  $R$ .

The inductance  $L$  of a multi-turn coil with  $N$  turns is given by the sum of self-inductances of individual turns added with mutual inductances between them [25]. For a single turn of radius  $a$ , the self-inductance is calculated as:

$$L(a, S_{wire}) = \mu_0 a \left( \ln \left( \frac{8\sqrt{\pi}a}{\sqrt{S_{wire}}} - 2 \right) \right), \quad (2.32)$$

where  $S_{wire}$  is the cross sectional area of the wire. The mutual inductance between two turns having radius  $a_i$  and  $a_j$  is obtained by [25]:

$$M(a_i, a_j) = \mu_0 \sqrt{a_i a_j} \left[ \left( \frac{2}{\kappa} - \kappa \right) K(\kappa) - \frac{2}{\kappa} E(\kappa) \right], \quad (2.33)$$

where  $\kappa = 2\sqrt{a_i a_j} / (a_i + a_j)$ ,  $K(\kappa)$  and  $E(\kappa)$  are the complete elliptic integrals of the 1<sup>st</sup> and 2<sup>nd</sup> kind respectively. Hence, using (2.32) and (2.33),  $L$  is given by:

$$L(\mathbf{A}) = \sum_{i=1}^N L(a_i, r) + \sum_{i=1}^N \sum_{j=1}^N M(a_i, a_j) (1 - \phi_{ij}), \quad (2.34)$$

where  $\phi_{ij}$  is one for  $i = j$  and zero otherwise.

The resistance  $R$  of the multi-turn coil antenna depends on the conductor length and an approximate value is given by [79]:

$$R(\mathbf{A}) = \frac{1}{\sigma \cdot S_{wire}} \sum_{i=1}^N 2\pi a_i, \quad (2.35)$$

where  $\sigma = 5.9 \times 10^7 / \Omega m$  is the conductivity of the copper. Since,  $L$  and  $R$  are the functions of  $\mathbf{A}$ , they can be calculated using (2.34) and (2.35) if the turn distribution  $\mathbf{A}$  is provided.

## 2.5 Part 4: Matching Network

To maximize the power delivered to the antenna, input impedance of the antenna should be conjugately matched with characteristic impedance of the transmission line; a matching network is used to perform that task. Matching becomes crucial for safety purpose for the systems which are highly sensitive to the reflected powers. The basic feature achieved by the matching is that there should not exist any reflections coming into the source. Various sort of matching networks are present but the choice depends on the complexity, bandwidth, frequency agility, implementation and cost.

For instance, in case of antenna's input impedance has purely real part, a quarter wave transmission line can be used to match the load; this involves a simple analytic solution. But to match a complex input impedance of the antenna, a L-section matching network with lumped elements can be used [76]; this involves either a graphical solution based on smith chart or an analytical solution using formulas to calculate matching network parameters. Fig. 2.11 [76] shows two L-

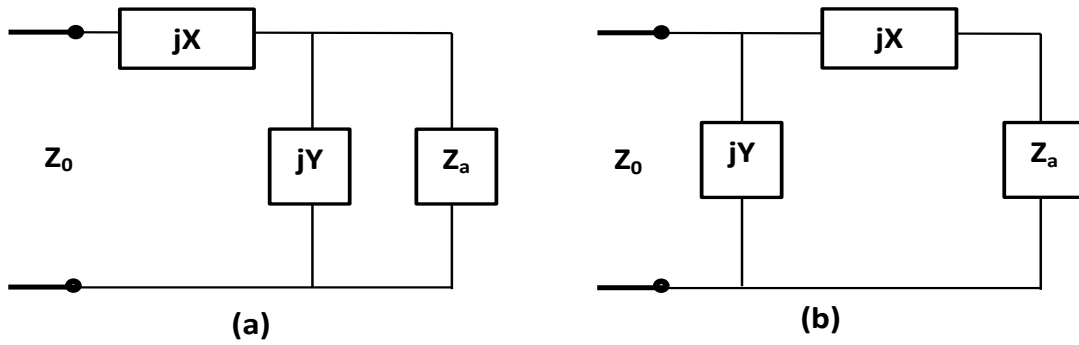


FIGURE 2.11: L-section matching networks

section matching networks attached with antenna impedance  $Z_a = R_a + jX_a$  and having series or parallel combinations of the lumped elements. For designing the matching network shown in Fig. 2.11(a), the analytical solutions are given by:

$$Y = \frac{X_a \pm \sqrt{\frac{R_a}{Z_0} \sqrt{R_a^2 + X_a^2} - Z_0 R_a}}{R_a^2 + X_a^2}, \quad (2.36)$$

$$X = \frac{1}{Y} + \frac{X_a Z_0}{R_a} - \frac{Z_0}{Y R_a}, \quad (2.37)$$

and for matching network of Fig. 2.11(b), the parameters are given by:

$$X = \pm \sqrt{R_a(Z_0 - R_a)} - X_a, \quad (2.38)$$

$$B = \pm \frac{\sqrt{(Z_0 - R_a)/R_a}}{X_a}. \quad (2.39)$$

For antennas, designed to operate at microwave frequencies, e.g., printed, microstrip antennas, a single and double stub matching techniques can be used; this is

done by the lumped elements replaced by open and short circuited printed transmission lines connected in series or parallel with antenna input. Above impedance matching techniques are useful for narrow band antennas and applications. For the antennas demanding high bandwidth, more sophisticated matching units are used for instance Chebyshev multisection matching transformers, etc, [76].

## 2.6 Part 5: Band Pass Filter

A filter is an entity of the system which is used to control the frequency response of the system by controlling transmission of signal depending on frequency. The filter allows transmission of signals of frequencies falling in passband of the filter, whereas, it causes severe attenuation of the signal falling in stop-band of the designed filter [76, 80]. At lower frequencies, the filters are designed using lumped element circuit and various methods such as image parameter method, insertion loss method can be used [76]. Whereas, at higher frequencies lumped element circuits are not effective as the size of element becomes comparable to the wavelength, therefore, distributed element model should be used. The lower frequency methods for BPF designing yield lumped element parameters for equivalent circuit of the filter, but at microwave frequencies, these lumped parameters should be transformed into distributed element parameters of transmission line sections, which can be done using techniques called Richard's transformation or Kuroda identities [76]

A band-pass filter (BPF) is designed to transmit the signal of an specific band while stopping the signal out-side the pass-band to reduce interference from other devices and cross-talk in the system. The ultimate advantage of BPF in a communication system is the improvement of Signal-to-Noise Ratio (SNR) by rejecting unwanted noise from the deemed signal of transmission or reception. The same operation is somewhat done by an antenna which transmits signals falling inside its bandwidth and rejects out of band signals. However, the attenuation at the out-of-band

frequencies is carefully designed by BPF, an antenna can be designed carefully to also work like a BPF [81], therefore, relaxing the front-end BPF requirement.

## 2.7 Summary

This chapter was dedicated to present a theoretical background of antenna systems. Various basic building blocks of the antenna systems were introduced and most important features of each block were described. These building blocks were backed by corresponding theories such as transmission-line, antenna, radiation and EM propagation, matching network, and band-pass filter, where an analogy was presented between these blocks. The focus in this chapter was on introducing the antenna parameters and their relation with antenna's radiation characteristics. The typical antenna equations defining antenna's physical and radiation characteristics were presented and used in later sections to analyze some typical antenna structures, e.g., electric dipole, loop, and multi-turn coil antennas. The analytical knowledge reported through this chapter will serve throughout the remaining of this dissertation.



# Chapter 3

## Coil Antenna for HF-RFID

This chapter explores modeling and designing of near field coil antennas used as reader in HF-RFID applications. The RFID system is optimized for high power transfer efficiency (e.g., wireless power charging) and/or high data rate (for reliable communications) applications. The performance is enhanced by optimally choosing the coil's geometric properties to maximize/provide a significantly enhanced magnetic field as a result.

### 3.1 Introduction

In chap. 1, near-field RFID systems were introduced and concluded that the antennas having a high near-field reactive energy and low radiation resistance are the preferred choices for such applications. It is welcomed to adopt HF 13.56 MHz band for its worldwide unlicensed use and its immunity to water and surrounding dielectric materials. Once frequency is chosen, a suitable antenna is designed and the coil antenna seems to be the preferred choice for its low-cost when used in both Tx and Rx of HF-RFID [3, 16–18, 82].

Since the power and data transfer is performed ultimately through the antennas using near-field coupling, their optimal design is crucial for achieving optimal system performance. In HF-RFID, both the coils (Tx and Rx) can be realized as

loosely coupled (magnetically) transformer, where energy gets transferred because of inductive coupling between the coils. This way, the coil antennas for HF-RFID are characterized by parameters such as the coupling coefficient ( $k$ ) between the Tx and Rx coils, H-field ( $H$ ) at the receiving coil, inductance,  $L$ , and unloaded quality  $Q$  factor of the antenna, etc. Due to the fact that the coil antennas for HF-RFID are designed for maximum reactive field and minimum radiation resistance, the performance characteristics which belong to a usual far-field radiating antenna e.g., gain, directivity, radiation pattern, etc. are of minimal interest for a near-field antenna. To achieve desired performance characteristics, the optimization of geometric parameters such as the coil shape and dimension in radius, the section of the wire in radian, and the number of turns [19] is performed.

Lets consider the Tx coil antenna design to understand the process. It is certain that a maximum  $H$  at Rx coil (to maximize coupling between them) should be achieved and is done by optimally choosing geometric parameters of a Tx coil. On the other hand, what should happen with  $Q$ , should it be maximized along with  $H$ ? It is known that a higher  $Q$  means lower losses and high power transfer efficiency between Tx and Rx. In contrast, the  $Q$  being inversely proportional to the Band Width (BW) influences the design for specific applications demanding higher data rates and hence a lower  $Q$ . Because of this ‘application dependent  $Q$  demand’, subsequently, the coil antenna design can be bifurcated into the following:

1. Coil design for a high power transfer efficiency (high  $Q$  design); for the applications which demand high power transfer but not the data rate, e.g., 1-bit RFID, Biomedical applications, wireless power charging for sensors, etc.
2. Coil design for a reliable data transfer (low  $Q$  design); for the applications demanding some data rate while low power transfer efficiency can be compensated by low communication range, e.g., short range RFID 106 kbps ISO-14443 [83].

## 3.2 Coil design for high power transfer efficiency

In this section, we present the design and H-field enhancement procedure for the power efficient coil antenna. For case study, we choose the reader coil antenna design for a RFID application (1-bit RFID), but the approach is equally valid for other applications demanding power efficient designs with a high  $Q$ . In [24], the design procedure for a RFID reader antenna is presented, where dependency of the reader coil size on the read out distance from a predefined tag is studied. The design parameters for the reader antenna are the coil shape and size, the section of the wire, and the number of loops. These parameters determine relevant system performance quantities,  $H$  at the receiver coil,  $L$ ,  $Q$  of the reader antenna.

Consider  $D$  be the maximum distance a tag can be situated (reading range of interrogation) from the reader coil. Typically, that reader coil should be designed such that the tag collects sufficient  $H$  (the minimum value  $H_{min}$ ) to activate the tag IC. As this system works in near-field only,  $D$  is limited to  $D \ll \lambda/2\pi \approx 4m$  (chap. 5 of [1]) for 13.56 MHz. An electrically small circular coil [1] with a constant current  $I$  flowing along the tracks of the coil is considered as reader antenna. Because of the electrically small size of the coil, the current flowing in the resulting loops are in phase and hence the H-field components adds constructively contributing to the overall H-field for a distance  $D$  [24] as shown in Section 2.4.4. The coil having  $N$  number of turns is called the Concentrated-loops coil Fig. 3.1(a) [29] where all the turns of the coil are concentrated near the outer loop with radius  $a_1$  and hence the spacing between the loops is negligibly small.

The two geometric parameters  $N$  and  $a_1$  are to be found and optimized to get the reader coil designed where it produces maximized  $H$  at predefined  $D$ . In [24],  $a_1$  of Concentrated-loops coil was optimally found to have a maximum  $H$ , which turned out to be a function of  $D$  but independent of  $N$ ; the optimal  $a_1$  was found as  $a_1 = \sqrt{2}D$  for small  $D$  ( $\leq 1$  m) [84]. Whereas, the values of  $N$  and  $I$  were derived in [24] as follows:

$$I \times N = \sqrt{27}H_{min}D. \quad (3.1)$$

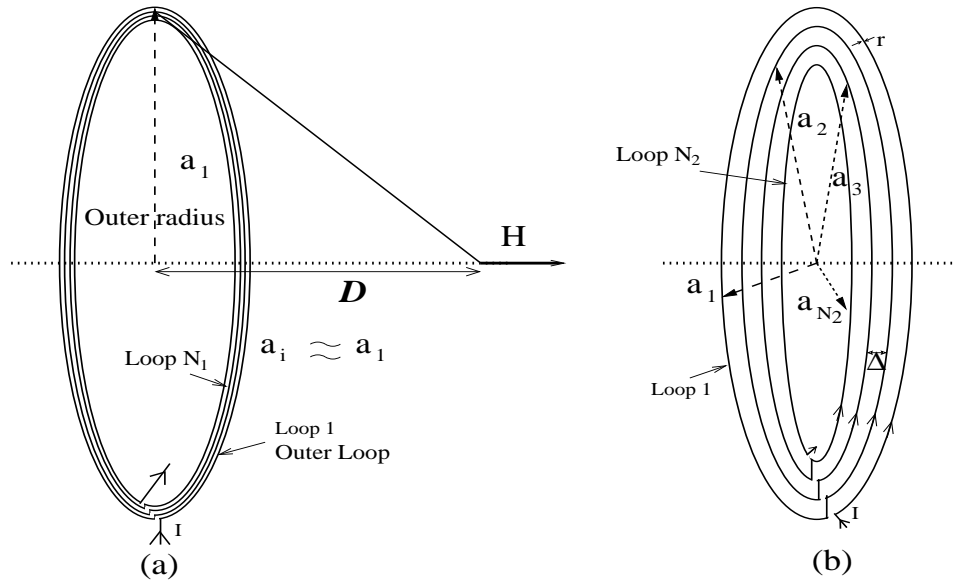


FIGURE 3.1: (a) Concentrated-turns coil antenna (b) Distributed-turns coil antenna.

Using (3.1), the number of loops,  $N$ , can be obtained if the coil is fed with a constant but limited known current source,  $I$ . Hence, for a given  $I$  and  $D$ , the optimized  $a_1$  and  $N$  can be obtain.

However, the obtained  $N$  affects the  $Q$  of the antenna, as both are proportional to each other. The  $Q$  increases with  $N$ , whereas the BW of the antenna reduces with  $N$  because the  $Q$  is inversely proportional to the bandwidth [79, 85]. The BW requirement for the current design is low, but the high  $Q$  is required. Hence, the value of  $N$  is chosen such that the desired  $Q$  is achieved. This design method will lead to an optimum reader coil with radius  $a_1$ , number of loops (turns)  $N_1$ , corresponding inductance  $L_1$ , resistance  $R_1$ , and quality factor  $Q_1$ . Once the input impedance of the coil is known, it is important to match the antenna to  $50\Omega$  by resonating coil at 13.56MHz using a matching series RLC circuit with a lumped capacitance  $C$ , given in [24]. The lumped capacitance  $C$  is chosen to resonate the coil at  $f = 13.56\text{MHz}$  using formula  $f = \frac{1}{2\pi\sqrt{L_1C}}$ .

### 3.2.1 H-field Enhancement

To this end, we notice that, to further improve  $H$  of an antenna of Fig. 3.1(a) without increasing  $I$  (for limited current sources),  $N$  should be increased. However, an indefinite increment of  $N$  in the Concentrated-loops coil, Fig. 3.1(a), causes unacceptable reduction in BW due to an increased  $Q$ . We note that, improving  $H$  ultimately improves induced voltage ( $V_{ind}$ ) in the Rx (Tag) circuit and hence a higher power transfer. Several approaches are adopted in the literature to ultimately increase the  $V_{ind}$  [17, 23, 25] using various geometric optimization and using various performance quantities, one of them is improving  $k$  to improve  $V_{ind}$ .

In this approach, we enhance  $k$  between the reader and the tag to ultimately get an improved  $V_{ind}$  by keeping the reader's inductance  $L$  constant [23, 25]. This  $k$  improvement can be translated into an improved coverage (read-out distance) and Tag antenna size reduction otherwise. The improvement in  $k$  results in increased  $V_{ind}$  by following the relation from [23]

$$V_{ind} = j \cdot \omega \cdot k \cdot \sqrt{L \cdot L_{Rx}} \cdot I \quad (3.2)$$

where  $L$  and  $L_{Rx}$  are the inductances of the reader and the tag coils respectively.  $I$  is the current in the reader coil, and  $\omega$  is the operating frequency. We can observe from (3.2) that the  $V_{ind}$  is not exclusively a function of  $k$  (the reader coil dimension dependent), and is subject to  $L$  of the reader coil which can also be altered (like  $k$ ) with a change in reader coil parameters (e.g., radius). Therefore, changing the reader's geometric parameters to enhance  $k$  (keeping  $L$  constant) may not fully reflect as desired enhancement in  $V_{ind}$ . This is why a 25% reduction in  $Q$ -factor [25, 29] is observed in the constrained optimization of  $k$  while keeping  $L$  constant. A reduced  $Q$  results into an increased loss in the reader circuit, and hence reduces the power efficiency.

Another approach is more appealing with other design consideration, where our focus is to enhance the propagating H-field coverage (distance) between the

reader and the tag following the relation by faraday's law

$$V_{ind} = \mu_0 \cdot j\omega \cdot N_{Rx} \cdot A_{Rx} \cdot H \quad (3.3)$$

The importance of this approach is, as apparent from (3.3),  $H$  is the only parameter depending of reader's geometry and  $V_{ind}$  is exclusively dependent on the  $H$ . Therefore, an enhancement in  $H$  by geometric alteration of the reader coil will fully reflect as desired and greater  $V_{ind}$ . However, some  $H$  enhancement approaches to improve  $V_{ind}$  may result in a degraded  $Q$ , for example, the constant- $L$  approach [23, 25].

For instance, a very attractive approach is adopted to enhance the H-field at a predefined distance of a tag by increasing  $N$  and spacing between the elements that form the coil [17, 25], yet, it results in a lower  $Q$ . This is because of the increment in the reader coil resistance  $R$  (while  $L$  remains unchanged) and as a result, lowers the quality given by

$$Q = \frac{\omega \cdot L}{R}, \quad (3.4)$$

for a series resonator in [24]. That is why this approach is called as constant- $L$  design in [29] where  $L$  is assumed constant, therefore,  $Q$  varies. Moreover, authors in [29], for the first time proposed constant  $Q$  approach to enhance the propagating H-field and got motivated to design the optimum reader coil prototype for HF RFID systems.

Subsequently in Section 3.2.2, the proposed approach in [29] to enhance the H-field of the reader is presented. The parametric study of inner area of the coil to find an optimal loop spacing between the turns is performed; this implies a Distributed-turns coils antenna. For the approach, a final design (*Distributed-turns*) with a  $Q$  equal to that of an initial design (*Concentrated-turns*) is developed, a shown in Fig. 3.1. The Distributed-turns of the coil antenna are given by  $a_N$ , results in a modified  $L$  with no resonance detuning (as antenna is matched back by adjusting the lumped capacitance  $C$  of the matching circuit). The superiority of the

proposed Distributed-turns coil design over the constant- $L$  is now demonstrated subsequently in Section 3.2.2.

### 3.2.2 Distributed-turns coil for H-field enhancement

The H-field of the reader coil shown in Fig. 3.1(a) is now enhanced by the design which is proposed in [29] and represented in Fig. 3.1(b). The Distributed-turns coil has  $N_2$  number of turns ( $N_2 > N_1$ ) but the outer radius of the new design is maintained to  $a_1$ , hence,  $Q$  is expected to rise (shown later in Fig. 3.2). However, to effectively bring the  $Q$  back to the initial value, it is proposed to have a finite and equal spacing  $\Delta$  between the adjacent turns, as shown in the Fig. 3.1(b); the radius of the turn  $i$  is

$$a_i = a_1 - (i - 1) \cdot \Delta, \quad (3.5)$$

where  $i \in [1, N_2]$ . Hence, the turn distribution, set  $\mathbf{A} = [a_1, a_2, \dots, a_{N_2}]$  is defined accordingly. The quality factor  $Q_2$  of the Distributed-turns coil antenna can be obtained from (3.4) using  $L_2$  and  $R_2$ , the inductance and the resistance of the Distributed-turns coil, respectively. The set  $\mathbf{A}$  is substituted in (2.34) and (2.35) to calculate  $L_2$  and  $R_2$ . It can be observed from (2.34), (2.35), and (3.5) that  $L_2$  and  $R_2$  are the functions of  $\Delta$  and  $N_2$ . Therefore, substituting  $L_2$  and  $R_2$  in (3.4), provides  $Q_2$  as a function of  $\Delta$  and  $N_2$ . The parametric study of  $\Delta$  is performed to analyze the change in  $Q_2$ . Similarly, for the Concentrated-turns coil,  $Q_1$  is obtained using  $L_1$  and  $R_1$ , and set  $\mathbf{A}$  is obtained using (3.5) with  $i \in [1, N_1]$  and  $\Delta \approx 2r$  (the minimum possible separation between the turns,  $r$  being the wire radius), following Fig. 3.1(a). By substituting expressions from (2.34) and (2.35) and solving (3.4) for  $Q_2 = Q_1$ , the optimal spacing  $\Delta_0$  was numerically calculated. Subsequently, the parametric study of H-field due to  $\Delta$  variation is shown. By substitution of  $\mathbf{A}$  at  $\Delta_0$  in (2.31), the expected optimum H-field of the proposed prototype, Fig. 3.1(b), is calculated.

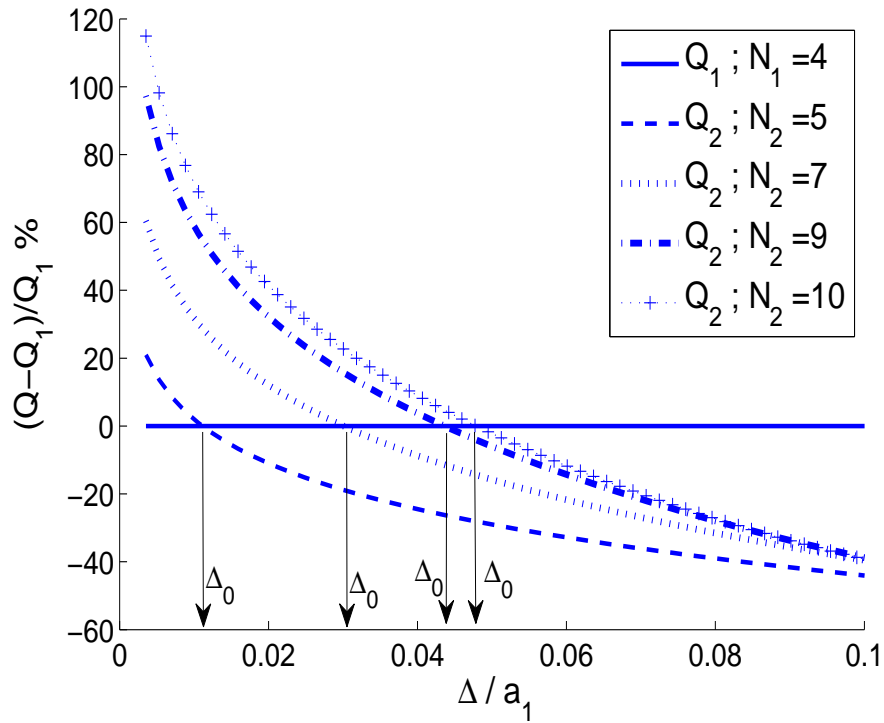


FIGURE 3.2:  $Q$ -factor versus normalized  $\Delta$  for different  $N$ ;  $a_1 = 0.07$  m;  $r = 0.125$  mm;  $I = 0.1$  A;  $D = 0.05$  m.

### 3.2.3 Analytical Results

The designs under investigation are analytically studied using MATLAB. We choose  $D = 0.05$  m,  $r = 0.125$  mm, and  $a_1 = 0.07$  m (using  $a_1 = \sqrt{2}D$  [84]). In (2.31),  $N_1 = 4$  and  $H_1 = H_{min} = 1.5$  A/m (rms value specified in ISO-14443 [83]) led to  $I = 0.1$  A.

#### 3.2.3.1 Parametric study of $Q$ and $H$ versus $\Delta$

In this section, we present the variation of the  $Q$ -factor and produced  $H$  of the Distributed-turns coil versus  $\Delta$ , the percentage variation for different values of  $N_2$  is shown in Fig. 3.2 which includes  $Q_1$  for comparison purposes. Before analyzing this figure, note that  $\Delta = 0$  signifies that there exists no spacing between the turns of Distributed-turns coils, that essentially becomes Concentrated-turns coil. However, as  $\Delta$  value increases, the turns distribute themselves and exploit the inner area of the coil. As apparent from Fig. 3.2, all the curves corresponding to

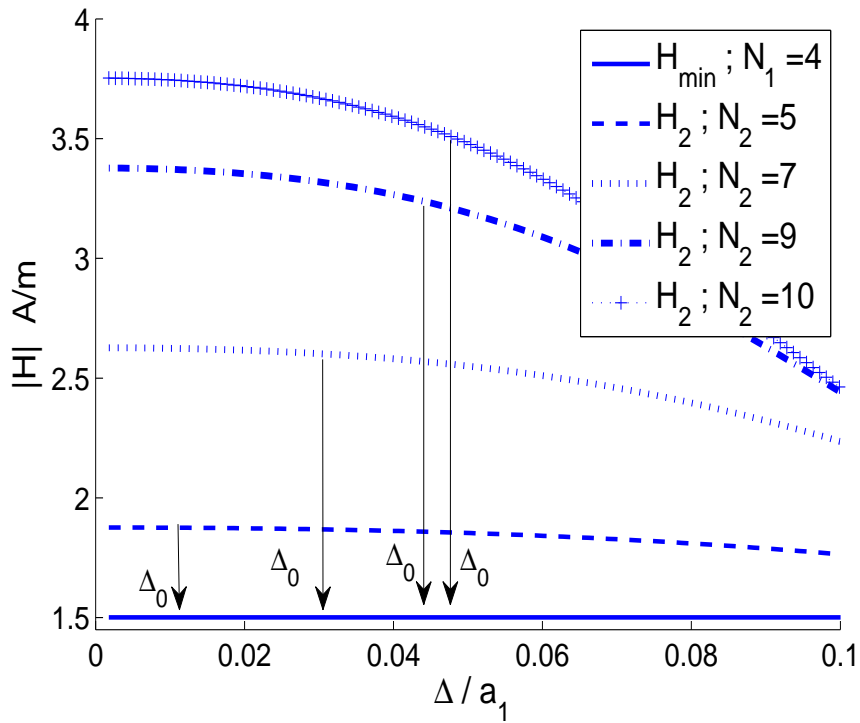


FIGURE 3.3: H-field versus normalized  $\Delta$  for different  $N$ ;  $a_1 = 0.07$  m;  $r = 0.125$  mm;  $I = 0.1$  A;  $D = 0.05$  m.

$Q_2$  cross the horizontal curve reference ( $Q_1$ ), the intersections occur at particular  $\Delta$  points for each curve. This means that there exist  $\Delta$  values for which the  $Q_2$  can be maintained to  $Q_1$ . This concludes that the final prototype (Distributed-turns coil design, Fig. 3.1(b)) has an optimal  $\Delta_0$  which corresponds to a Q-factor equal to that of the initial design (Concentrated-turns coil design, Fig. 3.1(a)), i.e.,  $Q_2 = Q_1$ . Moreover, from Fig. 3.2, it is observed that a higher  $\Delta_0$  is achieved for a correspondingly higher  $N_2$ . This increase in  $N_2$  proves the exploitation of the inner area of the initial coil antenna in an advantageous manner to compensate any possible  $Q_2 > Q_1$ .

The corresponding variation of the  $H_2$  of the Distributed-turns coil antenna, which was calculated using (2.31), is plotted in Fig. 3.3 which includes  $H_1$  of the Concentrated-turns coil having  $N_1$  turns for comparison. We observe from Fig. 3.3 that  $H_2$  reduces if  $\Delta$  increases, however  $H_2$  is always higher than a denoted value  $H_{min}$  which is essentially the  $H_1$  of the Concentrated-turns coil. The optimal  $\Delta_0$  points where  $Q_2 = Q_1$  (Fig. 3.2) are also depicted in Fig. 3.3 where a significant

improvement in the H-field by using the Distributed-turns design is observed. A higher H-field enhancement is observed for higher  $N_2$ , but the rate of improvement reduces for higher  $N_2$  as shown in Fig. 3.3. At this point, It may seem beneficial to use as high  $N_2$  as possible, however, the higher  $N_2$  implies a longer length of the coil tracks, therefore, a constant and in-phase current assumption may not be valid. This results in a lower H-field due to phase variations unless the total coil length can be regarded small compared to the wavelength [24], that's why this approach is only valid for the electrically small coils.

### 3.2.3.2 Optimum design and performance

Once the parametric study of  $H_2$  over  $\Delta$  is performed in Fig. 3.3, for different values of  $N_2$ , the optimized  $\Delta_0$  and corresponding  $H_2$  are presented in Table 3.1 ; the percentage variation over to the Concentrated-turn coil antenna ( $H_1 = 1.5$  A/m;  $N_1 = 4$ ) is listed. One would presumably realize that any improvement in  $H$  will be translated as higher gain. Table 3.1 includes the calculated  $\Delta_0$

TABLE 3.1: Optimum spacing  $\Delta_0$  and % H-field enhancement for the Constant-Q design\* compared to a constant- $L$  design#

$N_2$	* $\Delta_0/a_1$	* $\frac{(H_2-H_1)}{H_1} \%$	# $\frac{(H_L-H_1)}{H_1} \%$	# $\frac{(Q_L-Q_1)}{Q_1} \%$
5	0.011	24.93	24.61	-16.25
6	0.020	49.56	46.50	-23.92
7	0.030	73.35	62.82	-28.18
8	0.037	95.68	72.66	-30.92
9	0.0436	115.9	77.13	-32.83
10	0.0479	133.6	78.32	-34.14

and percentage field improvement given by  $\frac{(H_2-H_1)}{H_1}100\%$ . To compare the gain achieved by the proposed approach, results of the constant- $L$  scheme with H-field  $H_L$ , quality factor  $Q_L$ , and inductance  $L_1$  is also included. The constant-Q scheme provides an significant improvement in H-field, e.g., a minimum of around 24.9 % gain for just one turn increment, but without any loss of quality. It was mentioned in Section 3.2.1 that the antennas prototyped using the constant- $L$  design suffer

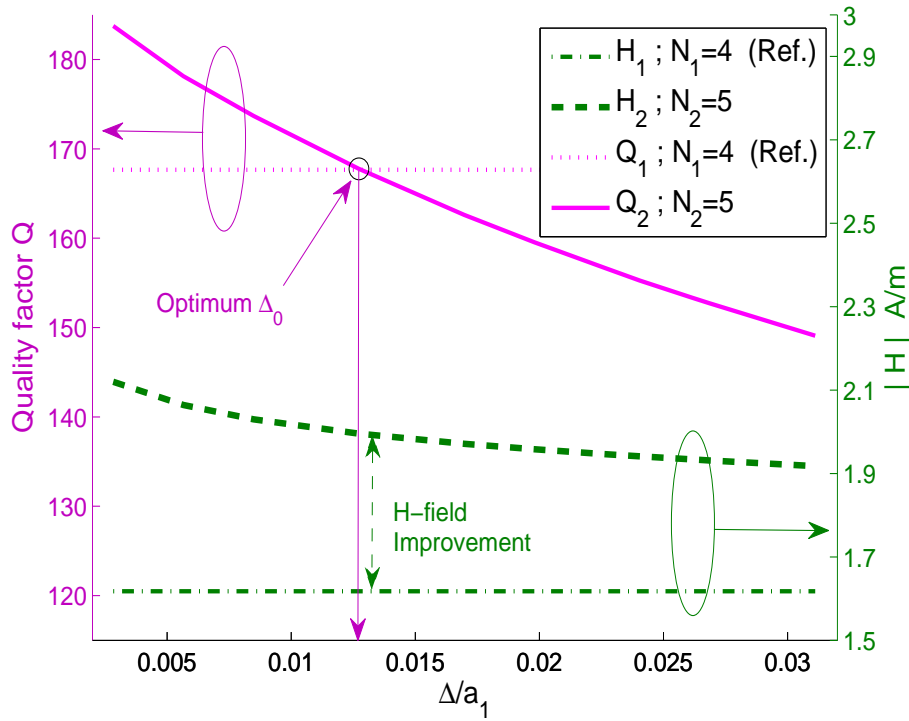
with a lower  $Q$  factor [25] which is now proved here that it has at-least  $\approx 16.25\%$  loss in  $Q$  for  $N_2 = 5$ , moreover, this loss increases for higher  $N_2$  values. In addition, the  $H$  enhancement shown by the constant- $L$  design in Table 3.1 is inferior to that achieved by the constant- $Q$  design. For instance, when  $N$  is doubled (e.g.,  $N_2 = 8$  and  $N_1 = 4$ ), then 72.66%  $H$  enhancement is realized by the constant- $L$  design<sup>#</sup>; this is trivial compared to the 95.68% achieved by the proposed design\*. Hence, observations report a benefit of utilizing intelligently the inner area of a reader coil for H-field enhancement.

### 3.2.4 Simulation and Results

Simulated results shown in [29] are now presented here. Near-field simulations of the coil antennas are carried out using Zeland IE3D. The coils are drawn with outer radius  $a_1 = 70.7$  mm and strip width 0.25 mm for all the designs. The Concentrated-turns coil was simulated with  $N_1 = 4$ ;  $\Delta = 0.2$  mm and used as the reference for the comparison; the simulated results for  $Q_1$  and  $H_1$  were 167.6 and 1.6 A/m, respectively. It was compared to the Distributed-turns with constant- $Q$  (simulated for  $N_2 = 5$  and arbitrary  $\Delta$ ) and the constant- $L$  designs. The simulated  $H_2$  and  $Q_2$  variations with  $\Delta$  of Distributed-turn design are plotted in Fig. 3.4 from [29].

The similar trend as Section 3.2.3.1 was observed in the simulations; 1)  $Q_2$  and  $H_2$  both decreases with higher  $\Delta$ , 2) the optimum  $\Delta$  is found where the  $Q_2$  of the Distributed-turn coil design crosses  $Q_1$  of the reference design. It was found through simulations that  $\Delta_0 = 0.0127$  and the H-field improvement at this  $\Delta_0$  is shown in Fig. 3.4 validating the advantage of using the proposed design.

Furthermore, a comparison with the constant- $L$  design is also provided in Table 3.2. It is indicated that the proposed design had a 3.97% higher  $H$  compared to the constant- $L$  design. Furthermore, the constant- $L$  design had a 8.92% lower  $Q$  compared to the reference design ( $Q_1$ ). This proves that the Distributed-turns coil designed with constant- $Q$  approach accomplished an enhanced H-field with

FIGURE 3.4: Simulated Q-factor and H-field versus  $\Delta$  and  $N$ .TABLE 3.2: Simulated optimum spacing  $\Delta_0$  and % H-field enhancement for the proposed design compared to a constant- $L$  design

$N_2 = 5$	$\Delta_0/a_1$	$\frac{(H-H_1)}{H_1} \%$	$\frac{(Q-Q_1)}{Q_1} \%$	$C(pF)$
Proposed	0.0127	23.34	0	12.97
Constant-L	0.0269	19.37	-8.92	15.98

unconstrained Q-factor, whereas the constant- $L$  design suffers with a reduced  $Q$  and comparatively lower  $H$  enhancement.

To resonate the reader antenna at 13.56 MHz, lumped capacitor  $C$  for the series RLC equivalent circuit was evaluated by simulations using commercially available Agilent ADS software and included in Table 3.2.

### 3.3 Coil design for reliable data transfer

In Section 3.2, we have seen the design and enhancement approach for the near-field coil with high  $Q$  demand. Although, a high  $Q$  implies a higher power efficiency

but at the same time a lower BW. In that case, the attained BW from a high  $Q$  design may be unacceptably low for the system requiring high data transfer, e.g., RFID 106 kbps ISO-14443 [83]. In this section, we will study the coil design for a 13.56-MHz HF RFID reader demanding reliable data transfer, and subsequently, a field enhancement approach is developed analytically.

### 3.3.1 Background

To achieve optimized coupling between the Tag and reader coil antennas, their geometries should be optimized. The Tag coil designing is adopted in various studies of the literature e.g., [16–18, 20, 86, 87]. However, the reader coils should also be optimized to produce maximum reactive energy resulting into a higher read range. The reader coil design procedure for a predefined tag is discussed in [24], where the optimum size of the coil is formulated for a given read range [11]. Whereas, a design study of the RFID system is presented in [79] suggesting that the  $Q$  of a reader coil antenna should be as small as possible for reliable data transfer. Following this observation, [24, 79, 88] proposed the reader coils having only a single turn. Hence, a Single Turn Coil (STC) antenna was evolved having a minimum  $Q$  suitable for the reliable data transmission, and an optimized size for a maximum  $H$ . Once the optimal STC antenna is designed, and if a further H-field enhancement is targeted, the adopted methods work by exploiting the inner area of the reader coil (by using multiple turns) as performed in [17, 19, 23, 25, 89] which having their own limitations.

To further enhance the H-field of the STC, similar approaches of Section 3.2.1 can be adopted. For this case, the constant- $L$  enhancement approach will change the desired  $Q$ , hence, it is not appropriate. Whereas, the one proposed in [29] and detailed in Section 3.2.2 for unconstrained  $Q$  seems suitable at first look.

The investigation presented in this Section is divided into three parts. First, the HF RFID system architecture is discussed in Section 3.3.2. Second, Section 3.3.3 will present a typical optimization of the reader coil antenna for a reliable data

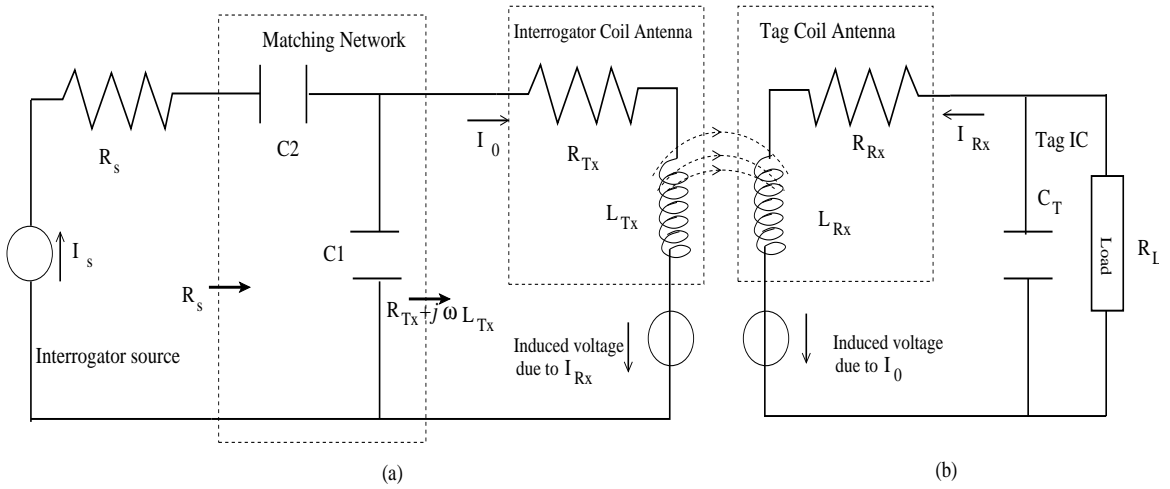


FIGURE 3.5: HF-RFID equivalent network model (a) reader (b) Tag.

transfer. Third, once the coil is optimized using traditional approach, further enhancement of the H-field (proposed in [90]) from the designed coil antenna is elaborated in Section 3.3.4.

### 3.3.2 HF-RFID System: Modeling and Design

The HF-RFID system is modeled in Fig. 3.5 with inductively coupled reader and tag circuits inherited from [79]. The equivalent circuit model of the reader coil antenna consists of coil inductance  $L_{Tx}$  and coil resistance  $R_{Tx}$  (represents ohmic losses of the coil). A current source  $I_s$  is attached to feed the reader coil antenna and having an internal resistance  $R_s$ . To maximize the power transfer and to resonate the reader coil, a matching network is placed between the source and the antenna. An L-match circuit is designed with lumped capacitances  $C1$  and  $C2$  forming a matching network as presented in Fig. 3.5, which is a simple and low cost solution for this purpose [11, 91]. The L-match network matches the antenna impedance with the standard value  $R_s = 50\Omega$ . To achieve the resonance condition of the antenna at frequency  $f = 13.56$  MHz, the lumped capacitances  $C1$  and  $C2$  are chosen such that the coil can resonate at the desired frequency  $f$ .

Similarly, the tag network is represented with  $L_{Rx}$  and  $R_{Rx}$  as inductance and resistance of the tag coil, respectively. The induction effect (mutual coupling) and resulting induced voltages are also shown in Fig. 3.5. The tag is powered by

the induced voltage in tag circuit due to reader coil current  $I_0$  through inductive coupling. On the other hand, the induced current  $I_{Rx}$  in the tag coil induces a voltage in the reader coil. Therefore, the impact of the tag should also be considered while optimizing the RFID system. This influence of the tag is studied in [84] and modeled by entity Transformed Tag Impedance (TTI),  $R_T$  which is simplified in [79] as:

$$R_T = \omega k^2 L_{Tx} Q_{Rx}, \quad (3.6)$$

where  $Q_{Rx}$  is the tag's quality factor. In [84], a rigorous study was conducted and concluded the necessity of maximizing  $R_T$  for an optimized reader and tag design. The maximum  $R_T$  is achieved by maximizing  $Q_{Rx}$  (a tag property) and also by maximizing  $k^2 L_{Tx}$  (an reader property). We only study the reader coils in this chapter and the effect of  $k^2 L_{Tx}$  is now presented in Section 3.3.3).

### 3.3.3 Reader Coil Design

The reader coil is designed following the instructions presented in [24, 79]. Subsequently, we present the overview of how the coil parameters are chosen to provide the optimized reader coil and assuming a predefined interrogating distance  $D$  (read range). Initially, an electrically small circular coil [1] antenna with a constant current  $I_0$  is considered, therefore, the H-field components that originate by the current flowing in the resulting turns are in phase and contribute to the overall H-field for a distance  $D$ . The coil consists of  $N_0$  number of turns where all the windings are concentrated in close proximity to the outer winding (radius  $a_0$ ). In [24, 79], the optimum design parameters are evaluated for this coil and given as follows.

#### 3.3.3.1 Size

The reader is designed by taking care of maximization of the quantity  $k^2 L_{Tx}$  introduced in (3.6). We subsequently show that the quantity  $k^2 L_{Tx}$  can be realized solely as H-field,  $H$ . By equating (3.2) with (3.3), and after manipulation we obtain

the relation:

$$k^2 L_{Tx} = \left( \frac{\mu_0 \cdot N_{Rx} \cdot A_{Rx} H}{\sqrt{L_{Rx}} I_0} \right)^2 \quad (3.7)$$

We observe from (3.7) that the quantity  $k^2 L_{Tx}$  can be realized solely as  $\frac{H}{I_0}$  for a predefined Tag parameters ( $N_{Rx}$ ,  $A_{Rx}$ ,  $L_{Rx}$ ). Therefore, for a given tag, maximization of TTI in (3.6) can be realized as maximization of  $\frac{H}{I_0}$  which is obtained from (2.31) and given as:

$$\frac{H}{I_0} = \frac{N_0 a_0^2}{2 \left[ \sqrt{(a_0^2 + D^2)} \right]^3}. \quad (3.8)$$

From (3.8) it is noted that, the optimization of  $\frac{H}{I_0}$  is independent of  $I_0$  and depends only upon the geometric properties ( $a_0$  and  $N_0$ ) of the reader coil. Therefore, without loss of generality, we consider constant current source  $I_0$  and maximize  $H$  by choosing optimal  $a_0$  and  $N_0$ . The optimum radius  $a_0$  of the reader coil is obtained for a maximized H-field at a predefined  $D$ . The optimum value  $a_0$  was derived in [24] as a function of  $D$ , and was obtained as  $a_0 = \sqrt{2}D$  for small  $D$  ( $\leq 1$  m) [84].

### 3.3.3.2 Number of Turns

For a given tag at an specified  $D$ , the reader antenna is typically designed to at least provide the tag with a minimum required value  $H_{min}$ , so that the tag IC can be activated [29]. The values of  $N_0$  and  $I_0$  are found by  $I_0 \times N_0 = \sqrt{27} H_{min} D$  derived in [24]. In this relation, for a constant but limited current source,  $I_0$ , the number of turns,  $N_0$ , can be obtained, but the use of higher  $N_0$  is limited by the reader antenna quality factor  $Q_0$  given by  $Q_0 = \frac{2\pi f \cdot L_{Tx}}{R_{Tx}}$  [79, 85]. As shown in [79], the  $Q_0$  increases with increment in  $N_0$ , whereas, the BW of the antenna reduces. Hence, the value of  $N_0$  is chosen such that the BW should not fall below a desired value; therefore, the authors in [24, 79] proposed to choose a single turn ( $N_0 = 1$ ) antenna to get  $Q_0$  as low as possible for reliable data transmission.

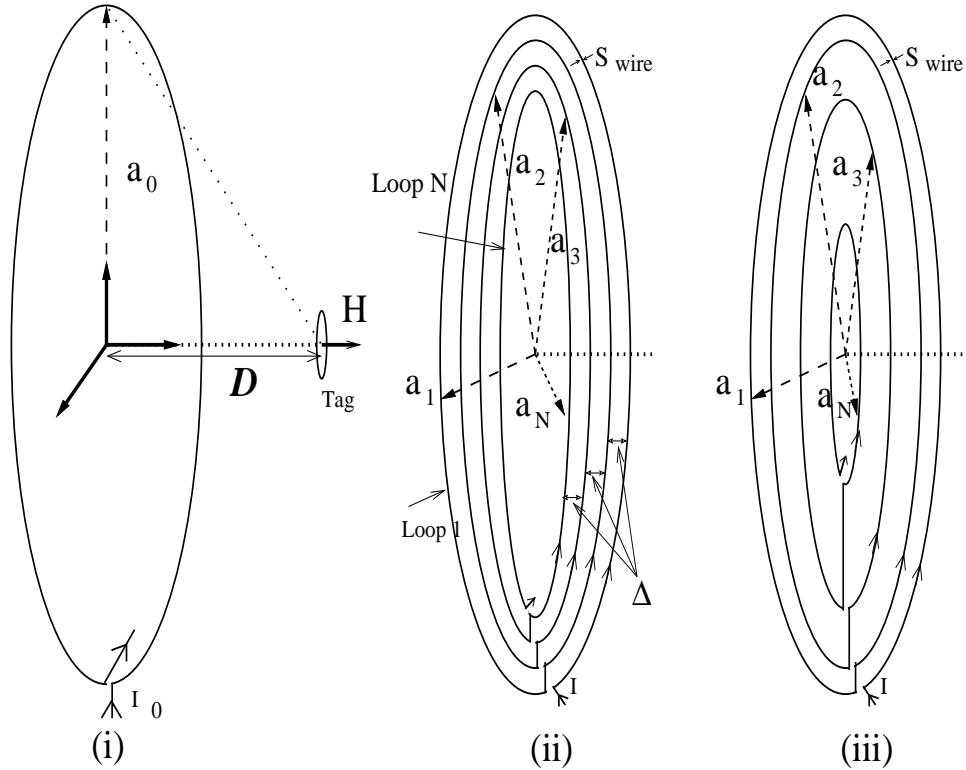


FIGURE 3.6: Coil antennas: (i) Single Turn Coil (STC) (ii) Uniformly Distributed-Turns Coil (UDTC) (iii) Non-uniformly Distributed-Turns Coil (NDTC).

This design method leads to an optimum reader coil with radius  $a_0 = \sqrt{2}D$ , number of turns  $N_0 = 1$  [24, 79]. The corresponding inductance  $L_0$ , resistance  $R_0$ , and the restricted quality factor  $Q_0 = \frac{2\pi f \cdot L_0}{R_0}$  is obtained and the design is called as Single Turn Coil (STC) antenna, shown in Fig. 3.6(i). The lumped capacitances  $C1$  and  $C2$  of the matching network (Fig. 3.5) are chosen so that the STC coil can be resonated at  $f = 13.56$  MHz.

To this end, we notice that while keeping optimal size and feed current unconstrained, a further improvement in  $H$  of the STC antenna in (3.8) is not possible unless a  $N > 1$ ; that is the use of multiturn coil antenna. However, the multiturn coil can have unacceptably reduced BW due to the increment in  $Q$  compare to STC. Therefore, geometric approaches where a multiturn coil can be used to enhance  $H$  but at same time  $Q$  is maintained are desirable. It has been demonstrated in Section 3.2.2, that the use of finite spacing  $\Delta$  between two adjacent turns e.g. Distributed-Turns Coil (DTC) is an attractive approach and can be

equally utilized to improve  $H$  for this case also.

A possible solution of DTC antenna design is Uniformly Distributed-Turns Coil (UDTC), [17, 25, 29] shown in Fig. 3.6(ii) and very well studied in Section 3.2.2, which has an equal spacing  $\Delta$  between the adjacent turns. But, it will be shown subsequently in Section 3.3.4 that there does not exist any optimal solution which can be achieved using UDTC approach, however, a novel approach proposed in [90] will be demonstrated having feasible solution for unconstrained  $Q$ . This novel approach allows turns to have unequal spacing between them, as shown in Fig. 3.6(iii), and termed as Non-uniformly Distributed-Turns Coil (NDTC) antenna design. The distributed turns of the NDTC coil, given by  $a_N$ , are optimally found to obtain unconstrained  $Q$  as STC.

### 3.3.4 H-field Enhancement by Distributed-Turns Coil Design

The geometry of the DTC antennas (both UDTC and NDTC) shown in Fig. 3.6(ii)(iii) are defined by radius vector  $\mathbf{A}$ , where  $\mathbf{A} = [a_1, a_2, \dots, a_N]$  and  $a_i$  is the radius of  $i^{th}$  turn. The DTC antenna contains multiple turns ( $N > 1$ ), therefore, a certain improvement of  $H$  over the STC antenna can be expected. However,  $Q$  will show an increment as presented later in Fig. 3.7), that needs to be effectively controlled back. In this regard, a parametric investigation of the inter turn spacing of the DTC is performed which ultimately produce design having unconstrained  $Q$  and significantly improved  $H$ .

The UDTC design approach, elaborated in Section 3.2.2 and proposed in [29], has an equal spacing  $\Delta$  between two adjacent turns, so that the  $i^{th}$  turn radius is given by  $a_i = a_0 - (i - 1)\Delta$ , Fig. 3.6(ii). The UDTC designs are investigated and will be shown to not have any outstanding solution for the  $H$  enhancement with the unconstrained  $Q$ . Moreover, when the uniform spacing  $\Delta$  is used, it restricts the adjustments between the turns so that the inner area of the coil is only partially exploited, restricting a further scope of maximizing the  $H$  enhancement. All these

claims about failure of the UDTC designs to achieve unconstrained  $Q$  over STC are demonstrated, next.

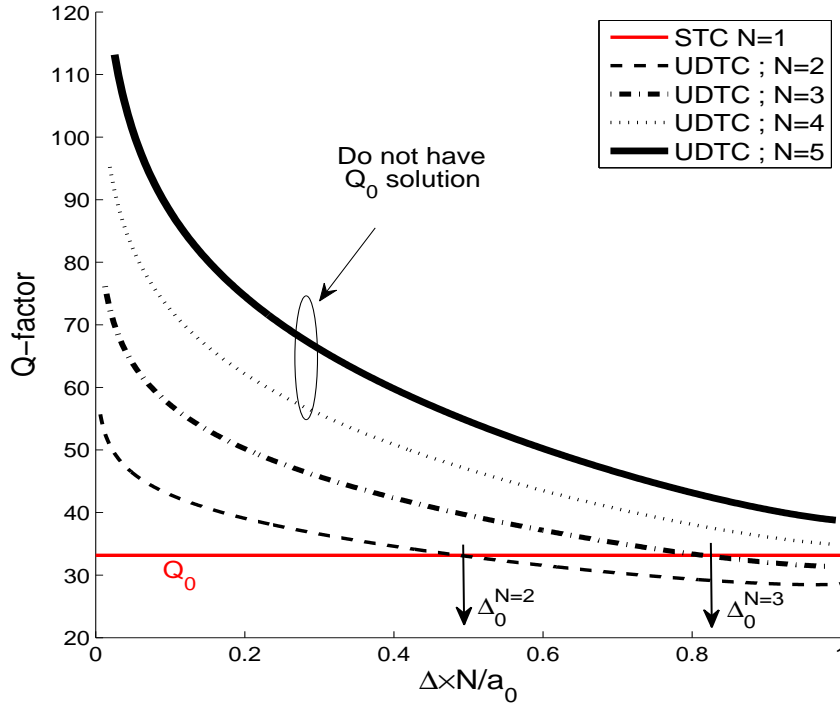


FIGURE 3.7:  $Q$ -factor of UDTC versus  $\Delta$  and various  $N$ ;  $D = 0.05$  m.

For the proof of the claims, parametric study is presented, the  $Q$  of UDTC design is plotted against  $\Delta$  and different  $N$  in Fig. 3.7. The  $Q$  values are obtained using (2.34) and (2.35) in (3.4), and other parameter values are set as  $D = 0.05$  m, wire cross section =  $0.05 \text{ mm}^2$ , and  $a_0 = 0.07 \text{ m}$  calculated in Section 3.2.2. The following are the information extracted from Fig. 3.7. At lower side of  $\Delta$ , the  $Q$  of all the UDTC designs exceeds the  $Q$  of STC ( $Q_0$ , reference) design. However, the  $Q$  reduces to  $Q_0$  at optimum  $\Delta_0^{N=2}$  and  $\Delta_0^{N=3}$ , respectively for  $N = 2$  and  $N = 3$ , it is not possible to obtain the unconstrained  $Q$  solution for  $N \geq 4$ . Essentially, the UDTC design with  $N = 2$  having only two turns can be termed as UDTC as well as NDTC, subsequently we will include it in the NDTC category. All the extracted observations about the use of a UDTC antenna to achieve unconstrained  $Q$  suggest it to be a discouraging approach to enhance  $H$  over STC. Whereas, the NDTC antenna proposed in [90] uses non-uniformly distributed-turns and shows

a promising approach to get unconstrained  $Q$  while maximizing  $H$  enhancement over the STC design, subsequently presented in Section 3.3.5.

### 3.3.5 Non-uniformly Distributed-Turns Coil antenna

Similar to what defined DTC in Section 3.3.4, the NDTC antenna [90] geometry is realized by radius vector  $\mathbf{A} = [a_1, a_2, \dots, a_N]$  with  $N$  number of turns, and current  $I$ , and shown in the Fig. 3.6(iii). For fair comparison, the NDTC antenna is fed with an equal current as of the STC ( $I = I_0$ ). The NDTC antenna has Q-factor  $Q_1$ . The  $\mathbf{A}$  of the NDTC is targeted to be optimized for a predefined tag at a distance  $D$  by maximizing  $H$  while keeping  $Q$  unconstrained as compared to the STC antenna ( $Q_1 = Q_0$ ).

#### 3.3.5.1 Formulating the optimization problem

The optimum coil size for a maximize  $H$  is found to be  $a = \sqrt{2}D$  from Section 3.3.3.1. However, the turns in NDTC antenna are distributed in the inner area, they should be confined to  $0 < a_i \leq \sqrt{2}D$ . The aim is to find an optimum turn set  $\mathbf{A}$  which maximizes  $H$  with unconstrained Q-factor and this optimization problem of NDTC antenna design is defined in [90] as:

$$\begin{aligned} & \underset{\mathbf{A}}{\text{maximize}} && H(\mathbf{A}) \\ & \text{subject to} && Q_1(\mathbf{A}) = Q_0, \\ & && 0 < a_i \leq \sqrt{2}D, \end{aligned} \quad (3.9)$$

where  $H(\mathbf{A})$  is given by (2.31) and  $Q_1(\mathbf{A})$  is obtained by substitution from (2.34) and (2.35) in (3.4) as:

$$Q_1(\mathbf{A}) = \omega \frac{\sum_{i=1}^N L(a_i, r) + \sum_{i=1}^N \sum_{j=1}^N M(a_i, a_j)(1 - \phi_{ij})}{\frac{1}{\sigma \cdot S_{wire}} \sum_{i=1}^N 2\pi a_i}. \quad (3.10)$$

To solve the maximization problem (3.9), its Lagrangian is defined as

$$\mathcal{L}(\lambda, \mathbf{A}) = H(\mathbf{A}) + \lambda(Q_1(\mathbf{A}) - Q_0), \quad (3.11)$$

where  $\lambda$  is the Lagrangian multiplier. The solution can be obtained by partial differentiation of  $\mathcal{L}$  in (3.11) with respect to  $a_i$  and  $\lambda$ , and equate the derivatives to zero; this generates the solution set  $\mathbf{A}$  with  $N$  variables. This solution set  $\mathbf{A}$  satisfies  $N + 1$  non-linear equations obtained as:

$$\begin{aligned} \Delta(\mathcal{L}, a_i) = 0; \quad \frac{d}{da_i}H(\mathbf{A}) + \lambda\frac{d}{da_i}Q_1(\mathbf{A}) = 0; \quad i \in [1, N], \\ \Delta(\mathcal{L}, \lambda) = 0; \quad Q_1(\mathbf{A}) = Q_0, \end{aligned} \quad (3.12)$$

where  $H$  and  $Q_1$  are substituted from (2.31) and (3.10), respectively. To find the ultimate solution of the maximization problem (3.9), it is necessary to solve the set of  $N+1$  equations written in (3.12), but it is difficult to get a close form solution out of these equations because they involve complex nonlinear terms. Therefore, we adopt a numerical method (algorithm) to find out the solution; which is presented in Section 3.3.5.2.

### 3.3.5.2 Numerical method to find Optimum turn assignment $\mathbf{A}$

As the optimization problem considered in this paper is not for an adaptive system, therefore, the complexity issue of the algorithm in numerically finding the optimal set solution is meaningless. The computational optimization algorithm is presented in Table 3.3 and for a particular  $N$ , the steps of the algorithm are described. The algorithm has seeds to initialize its variables, e.g.,  $a_i = \sqrt{2}D$ ,  $\forall i \in [1, N]$ , as  $0 < a_i \leq \sqrt{2}D$ . In each iteration, first, the turn radii is decreased by a step size  $\delta$  (a minimum permitted separation,  $g$ , between adjacent turns in the fabrication process), and second, resultant  $H$  and  $Q_1$  of the coil with new turn distribution are calculated, then, after each iteration a comparison check is performed for  $Q_1 = Q_0$  and  $H$  is maximum. Once the comparison check result is found positive, the algorithm reveals the optimized NDTC turn assignment  $\mathbf{A}$  found analytically.

TABLE 3.3: Algorithm to find optimum turn assignment **A**

```

Initialization:
 $I \Leftarrow I_0$ 
 $a_i \Leftarrow \sqrt{2}D$  (in mm),  $\forall i \in [1, N]$ 
 $\delta \Leftarrow 0.1$ 
 $g \Leftarrow 0.45$ 
B  $\Leftarrow$  A
Iteration:
while(B(1) > 0)
    B(2)  $\Leftarrow$  B(1) -  $g$ 
    while(B(2) > 0)
        B(3)  $\Leftarrow$  B(2) -  $g$ 
        while(B(3) > 0)
            .
            .
            .
        B( $N$ )  $\Leftarrow$  B( $N - 1$ ) -  $g$ 
         $Q_1 = 0$ 
        while(B( $N$ ) > 0)
            Calculate  $Q_1$  and  $H$  for set B using (2.31) and (3.10)
            if ( $Q_1$  is equal  $Q_0$ )
                Get A(optimum)  $\Leftarrow$  B with Maximum  $H$ 
            end
            B( $N$ )  $\Leftarrow$  B( $N$ ) -  $\delta$ 
        end
    end
    .
    .
    .
end
B(2)  $\Leftarrow$  B(2) -  $\delta$ 
end
B(1)  $\Leftarrow$  B(1) -  $\delta$ 
end

```

### 3.3.6 Analytical results of NDTC antenna

The analytical study of the proposed design was carried out in [90] using MATLAB. Algorithm detailed in Table 3.3 is analyzed and the numeral quantities are set as:  $D = 0.05$  m and  $S_{wire} = 0.05$  mm<sup>2</sup>, and  $a_0 = 0.07$  m,  $N_0 = 1$  and  $H_0 = H_{min} = 1.5$  A/m (rms value specified in ISO-14443 [83]) in (3.8) led to  $I_0 = 0.4$  A.

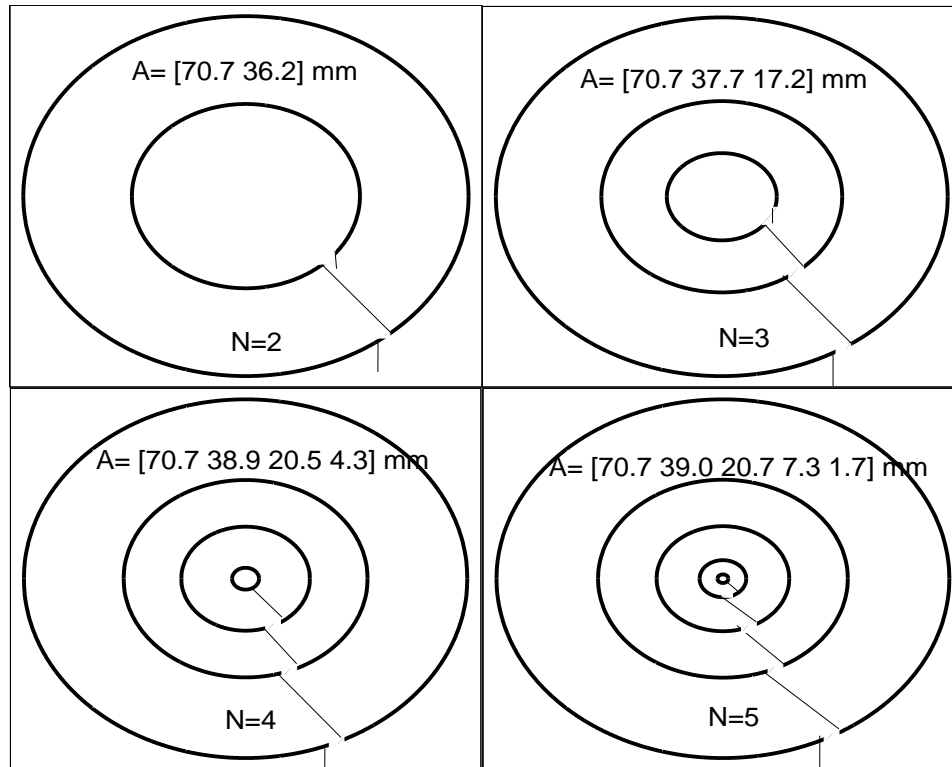


FIGURE 3.8: Revealed NDTC antennas optimized using algorithm for various  $N$ ;  $D = 0.05$  m;  $S_{wire} = 0.05$  mm<sup>2</sup>;  $I_0 = 0.4$  A.

Fig. 3.8 shows the output generated by the algorithm of Table 3.3 for various values of  $N$ ; these NDTC designs with unconstrained  $Q$  achieved the maximized  $H$ . Rest of the results of the optimized NDTC designs, e.g.,  $Q$ ,  $H$ , percentage  $H$  enhancement are listed in Table 3.4. The STC antenna ( $H = 1.5$  A/m and  $N_0 = 1$ ) results are included for comparison and show its quality factor  $Q_0 = 33.165$ ; this value is sufficiently small for reliable data transfer [79].

The key information extracted from Table 3.4 are detailed next. A significant enhancement of 72.47% in the H-field is observed for just one turn increment,  $N = 2$ ; moreover, this enhancement improves for higher values of  $N$ . NDTC

designs having  $N > 5$  are not feasible due to space limitations within the inner area of 5<sup>th</sup> turn, Fig. 3.8. Ultimately, the optimized NDTC design with  $N = 5$  shows the highest  $H$  with 118.33% improvement over the STC with similar  $Q = 33.16$ ; this is the final solution encouraged to be adopted. These results prove the significance and intelligence of NDTC design approach to enhance  $H$  without compromising with  $Q$ -factor.

TABLE 3.4: Analytical results of H-field enhancement for optimal NDTC antenna designs

Design	Q-factor	$H$ (A/m)	$\frac{(H-H_0)}{H_0}\%$
STC	33.165	1.500	0
NDTC N=2	33.162	2.587	72.47
NDTC N=3	33.162	3.017	101.13
NDTC N=4	33.164	3.207	113.80
NDTC N=5	33.164	3.275	118.33

### 3.3.7 Simulated Results of NDTC antenna

In this section, the analytical results produced in Section 3.3.6 are backed and corroborated with simulation results. The simulation study is carried out using Zeland IE3D for Near-field calculations of the NDTC antennas. The coils are drawn in the simulator editor with scale  $a_1 = 70.7$  mm and strip width 0.25 mm and strip height 0.2 mm (hence,  $S_{wire} = 0.05$  mm<sup>2</sup>). The simulation of STC

TABLE 3.5: Simulated results of H-field enhancement for optimal NDTC antenna designs

Design	Q-factor	$H$ (A/m)	$\frac{(H-H_0)}{H_0}\%$	C1 (pF)	C2 (pF)
STC	31.33	1.491	—	173.80	40.56
NDTC N=2	31.35	2.521	69.08	97.64	31.28
NDTC N=3	31.27	2.920	95.84	78.07	28.43
NDTC N=4	31.18	3.109	108.52	70.59	27.27
NDTC N=5	31.16	3.224	116.23	67.73	26.81

and NDTC antennas are performed and the results are presented in Table 3.5.

One can see that the simulation results have a fair agreement with the results produced analytically in Table 3.4, and therefore, validate the idea. The prominent observations of simulation results of Table 3.5 are detailed next. The NDTC design with  $N = 2$  has 69.08% greater  $H$  compared to STC. As found in analytical results, simulations show that the  $H$  improvement increases with greater  $N$ , e.g., with  $N = 5$  NDTC has 116.23%  $H$  enhancement. However, this  $H$  enhancement reduces with higher  $N$ , because opportunity to exploit the area beneath the inner turn reduces, consequently, comparatively a smaller new turn is added to the coil as  $N$  increases, Fig. 3.8. In addition to the performance results, Table 3.5 also includes the simulated  $C1$  and  $C2$  values for the matching network of Fig. 3.5 for consideration in the fabrication presented in next chapter.

### 3.4 Summary

In this chapter, a modeling of a RFID system was presented and the optimization process of the RFID reader coil antenna was discussed. The RFID system considered was suitable for High Frequency near field applications. A survey of various designed coil antennas for the system under review was carried out, and we explored possibility of enhancing H-field of state-of-the-art coil antennas. Essentially the RFID system bifurcated in to two different applications, one requiring a high power transfer efficiency and hence demands for a higher Q-factor, whereas, second demanding a reliable data transfer seeking some BW and constrained Q-factor. In this regard, some geometric approaches present in the literature were considered; and Distributed-Turns Coil (DTC) seemed attractive to enhance H-field for a predefined read-range of the RFID. In DTC design, by increasing the number of turns of the existing optimized coil antenna and re-arranging them with a well defined spacing between them, a significantly high H-field enhancement was achieved. To validate the new design, a fair comparison was made with a reference design having comparable Q-factor. For the first application of high  $Q$  high power efficiency, a Uniformly-Distributed-Turns-Coil (UDTC) was designed and validated by analysis and simulation; the results demonstrated the advantage by

showing an improved H-field with unconstrained inductance,  $L$  and Q-factor and indicated that the UDTC design overcame a 23.34% higher  $H$  compared to the reference design. Compared to a constant- $L$  design, the constant- $Q$  UDTC had a 3.97% higher  $H$  and a 8.92% higher  $Q$ ; a higher  $Q$  means a less lossy design.

Subsequently, for the second application demanding reliable data transfer, DTC antennas were explored to enhance H-field of an optimized coil antenna. But, the UDTC design approach showed discouragement having no proper solution for an unconstrained Q-factor. However, a Non-uniformly Distributed-Turns Coil (NDTC) was adopted for an enhanced H-field for such applications. The design algorithm of NDTC antenna follows by first, increasing the number of turns for maximizing H-field, and later optimally distribute the turns with a non-uniform separation (spacing between the turns). This NDTC antenna was validated by theoretical results and corroborated using Zeland IE3D simulator. The results showed a 116.23% higher H-field with unconstrained Q-factor compared to the reference design, encouraging its use over other coil antennas for HF-RFID reader application.

After an intensive study of the NDTC antennas by analytical and simulation modeling in this chapter, our next focus is to fabricate the NDTC antennas and corroborate the desired performance by measurements, in next chapter.

### 3.5 Chapter related publications

1. **A. Sharma**, I. J. Garcia Zuazola, A. Gupta, A. Perallos, and J. C. Batchelor, "Non-uniformly distributed-turns coil antenna for enhanced H-field in HF RFID," *IEEE Trans. Antennas Propagation*, vol. 61, no. 10, pp. 4900-4907, Oct 2013.
2. **A. Sharma**, I. J. Garcia Zuazola, A. Gupta, A. Perallos, and J. C. Batchelor, "Enhanced H-field in HF-RFID systems by optimizing the loop spacing of antenna coils," *Microwave and Optical Technology Letters*, vol. 55, Issue 4, pages 944-948, April 2013.

# Chapter 4

## Fabrication of NDTC antenna and its applications

The newly developed NDTC coil antennas in Chap. 3 to use for High-Frequency (HF) Radio Frequency IDentification (RFID) are fabricated and near-field measurement results are presented in this chapter. These coils having similar Q-factor were designed for the highest possible magnetic field (H-field) and optimized using non-uniformly distributed turns terminology [90] in Chap. 3. In this chapter, the fabricated coils are measured. The results compare the performance of the developed designs and prove that the optimized NDTC antenna achieves relatively higher H-field to corroborate with the previous analysis and simulation results. Later, the influence of various used substrate types and reflector proximities over the NDTC antenna is demonstrated and provide the matching network parameters to impedance the antenna. Finally, an application of NDTC antenna is considered, where the effective reading area of the antenna is widened using an Array of 5 NDTC antenna elements. A wider area is required in applications such as wireless data-transfer or power charging of large devices (or multiple devices).

## 4.1 NDTC Coil antenna Fabrication and Measurements

The four NDTC antennas reported in Section 3.3.5 having number of turns from 2 to 5 respectively, were optimally designed and compared with STC; all the designs were optimized for read range  $D = 0.05\text{m}$  and  $Q = 33.16$ . In this section, we performed measurements of the STC and the NDTC antennas for comparative study. The fabricated STC antenna with single turn is termed as Coil-1, whereas NDTC antennas with number of turns 2 to 5 are termed as Coil-2 to -5, respectively.

The optimized designs proposed in [90] and presented in Section 3.3.5 have sizes:  $\mathbf{A}_1 = [70.7]\text{mm}$ ,  $\mathbf{A}_2 = [70.7 \ 36.2]\text{mm}$ ,  $\mathbf{A}_3 = [70.7 \ 37.7 \ 17.2]\text{mm}$ ,  $\mathbf{A}_4 = [70.7 \ 38.9 \ 20.5 \ 4.3]\text{mm}$ ,  $\mathbf{A}_5 = [70.7 \ 39.0 \ 20.7 \ 7.3 \ 1.7]\text{mm}$ . The coils are etched on a double-sided printed circuit board (PCB) of copper (50microns) and substrate Polyamide  $E_r = 3.4$  and shown in Fig. 4.1(a). The equivalent circuit model of the coil antenna

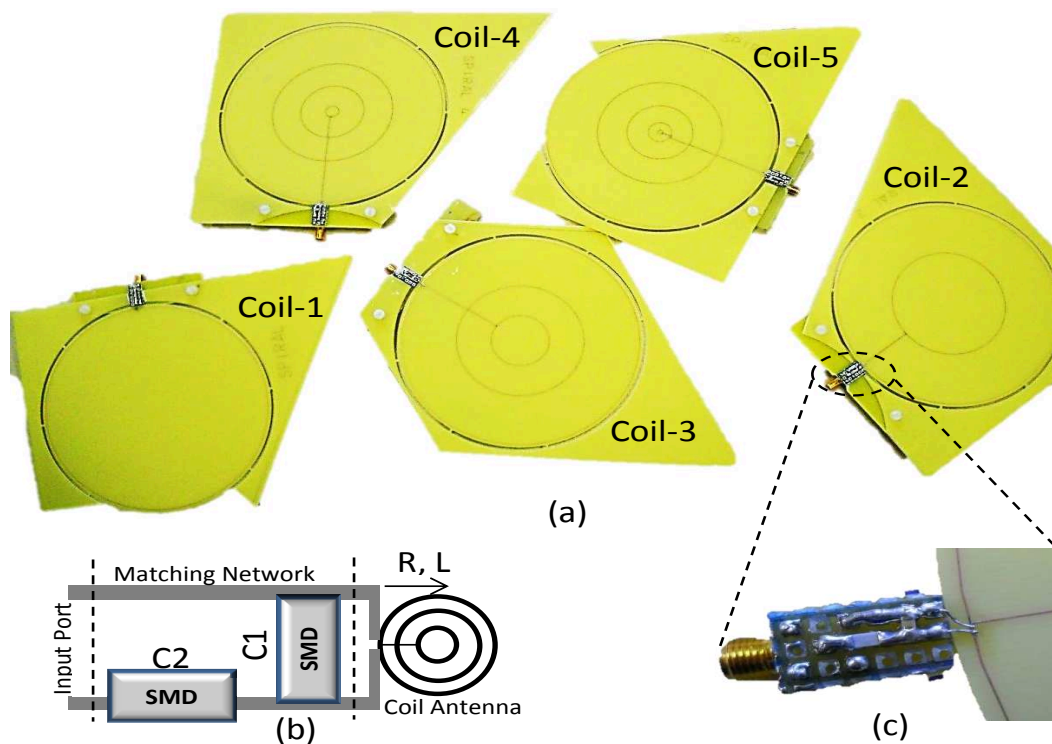


FIGURE 4.1: (a) Fabricated Coil antennas (b) Circuit Model (c) Matching assembly.

having inductance  $L$  and resistance  $R$ , includes a matching network, Fig. 4.1(b).

The in-house fabricated matching network is attached to the coil as shown in Fig. 4.1(c). The performed measurements are detailed next.

#### 4.1.1 Measurement Setup and results

In this section, the setup for the measurements is presented. The fabricated coils are first measured for  $R$ ,  $L$ , and  $Q$  using a micro probe (from Agilent 42941A Impedance Probe Kit) shown in Fig. 4.2(a).

The Coils-1 to -5 are first measured for  $R$ ,  $L$ , and  $Q$  using a micro probe (Agilent 42941A Impedance Probe Kit), Fig. 4.2(a), and a precision impedance analyzer (Agilent 4294A). The micro probe was calibrated and placed at two test points

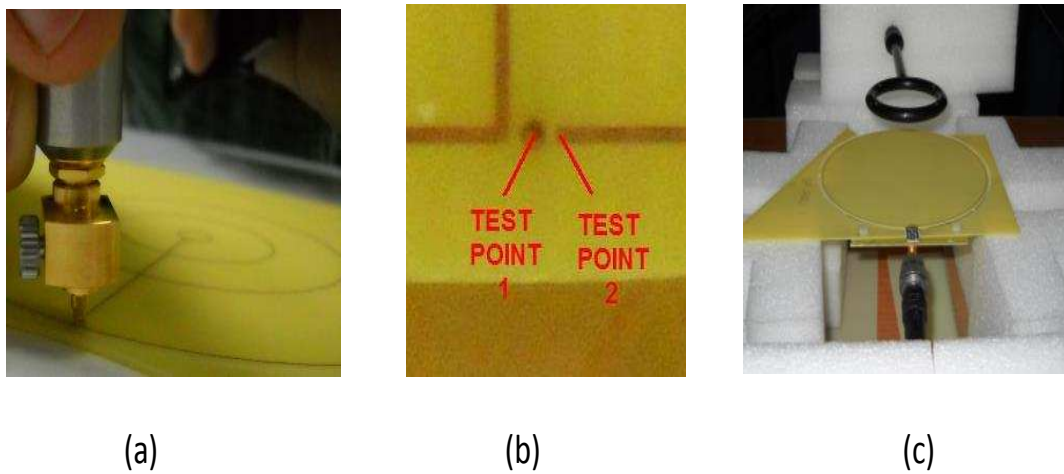
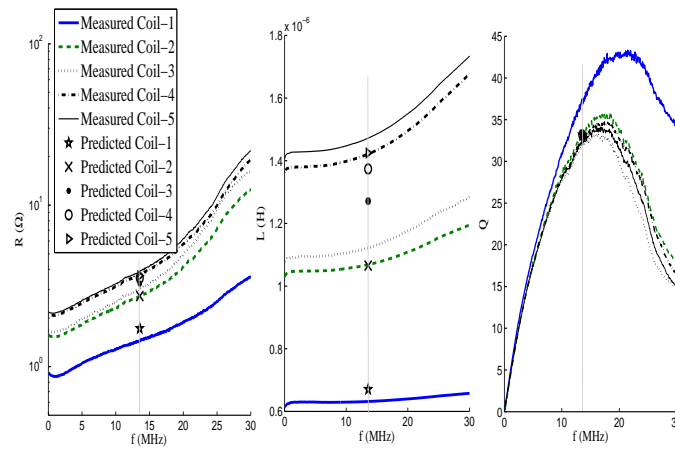


FIGURE 4.2: a) The micro probe to measure  $R$ ,  $L$ , and  $Q$  b) The test points for the probe c) Near-field probe and setup for  $H$  measurement.

of the coils exaggerated in Fig. 4.2(b). A precision impedance analyzer Agilent 4294A is used and the measured  $R$ ,  $L$ , and  $Q$  vs. frequency of Coil-1 to -5 are shown in Fig. 4.3 which includes theoretical values for comparison purposes. At the desired frequency of operation  $f = 13.56$  MHz, analytical, simulated [90], and measured  $Q$  are shown in Table 4.1 where the deviation in the measured values are observed due to manufacturing tolerances.

FIGURE 4.3: Measured  $R$ ,  $L$ , and  $Q$  variation with frequency.TABLE 4.1: The  $Q$  of the stand-alone coils.

	Coil-1	Coil-2	Coil-3	Coil-4	Coil-5
Q analytical	33.165	33.162	33.162	33.164	33.164
Q simulated	31.33	31.35	31.27	31.18	31.16
Q measured	37.50	33.38	31.89	32.52	32.16

The measured  $R$  and  $L$  are used to calculate the  $C1$  and  $C2$  for the matching network of the corresponding Coil-1 to -5, and the closest commercially available capacitances are chosen and surface-mount device (SMD) capacitor chips are purchased. Both calculated and selected capacitances are shown in Table 4.2. Once

TABLE 4.2: Calculated and commercially available capacitance

	Calculated C1 (pF)	Calculated C2 (pF)	SMD C1 (pF)	SMD C2 (pF)
Coil-1	178.90	38.75	180	39
Coil-2	98.99	30.35	100	33
Coil-3	94.86	28.98	100	27
Coil-4	70.54	26.60	68	27
Coil-5	63.38	25.72	68	27

SMDs chips are selected, the matching network is welded along with input SMA connector and attached to the fabricated coils, Fig. 4.1(c). This renders the coils ready for performance measurement.

For the return loss (S11) measurements, a PNA-X Network Analyzer from Agilent technologies was used and appropriately calibrated up to SMA connector to account for any possible cable inaccuracy. All the considered designs, Coil-1 to -5, are measured and corresponding S11 variation is depicted in Fig. 4.4. As

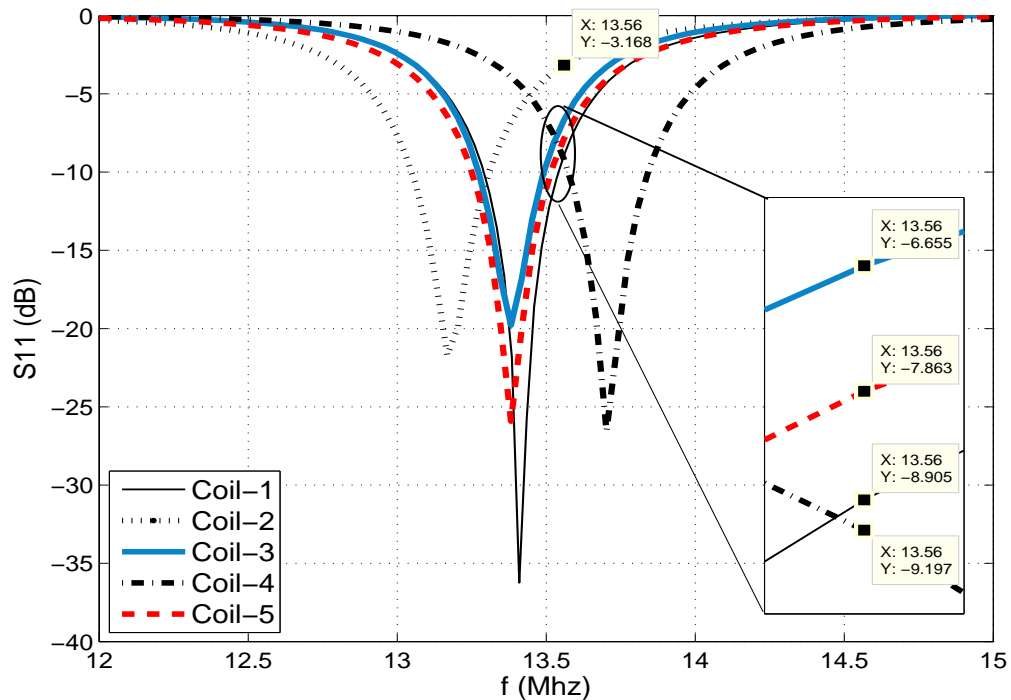


FIGURE 4.4: Measured S11 of the fabricated Coils-1 to -5.

apparent from this figure, the fabricated coils have resonating frequency deviated from desired 13.56 MHz; this is due to manufacturing tolerances of the impedance matching network. The Coil-1 to -5 resonate nearly around 13.42, 13.15, 13.14, 13.37, 13.69, and 13.34 (MHz), respectively. Furthermore, it is observed that S11 at working frequency 13.56 MHz varies for different coils as shown via data points in Fig. 4.4, where the return loss of the Coil-1 has advantage over other coils, on the contrary, Coil-2 shows worse return loss performance. Coil-1 has the highest measured  $Q$  with high deviation from its expected value given in Table 4.1. Both, the return loss advantage/disadvantage and a high  $Q$  for the Coil-1 (both are not desired for a fare comparison) are expected to reflect in the final performance comparison presented next.

The H-field of the manufactured coils are measured in the anechoic chamber and a near-field probe (ETS-Lindgren's Model 7405 Near Field Probe Set) is used which is placed  $D = 0.05\text{m}$  above the coil, as shown in Fig. 4.2(c). The signal generator (R&S SM300) is connected to the coil on the test pad and sends signal at  $f = 13.56\text{MHz}$  with generator voltage  $9.2\text{ mV}$  peak. An analyzer (Agilent PNA-X Network Analyzer) at the near-field probe measures the induced voltage,  $V_{ind}$  due to received H-field intensity. The conversion from measured  $V_{ind}$  to  $H$  for the used probe is governed by [92]:

$$H(\text{A/m}) = V_{ind}(V) + F(V) - 51.52 + Loss,$$

where  $Loss = 0.4\text{ dBm}$ , and  $F(V)$  is the probe performance factor with value  $64.8\text{dB}$ . Table 4.3 shows measured  $H$  for Coil-1 to -5, and relative enhancement

TABLE 4.3: The measured  $H$  enhancement of the coils

	Coil-1	Coil-2	Coil-3	Coil-4	Coil-5
$H$ (A/m)	1.499	1.506	1.721	1.741	1.817
$\frac{(H-H_0)}{H_0}\%$	0	0.46	14.81	16.14	21.21

compared to the Coil-1. The Coil-1 has measured  $H = 1.49\text{ A/m}$  and Coil-2 shows a poor  $H$  enhancement of  $0.46\%$  over Coil-1; this is because of a significant  $S_{11}$  difference of  $5.7\text{ dB}$  between Coil-1 and Coil-2 as shown in Fig. 4.4. Concluding remark from results is that an attractive  $21.21\%$  improvement in  $H$  is achieved by the Coil-5. The improvements shown here by the fabricated coils are significant enough to encourage the practical use of the NDTC prototypes [90] for an advanced design of the interrogator antenna for HF-RFID system.

## 4.2 NDTC Antenna over different Substrate Types and Reflector Proximities

In previous section, we have presented fabricated NDTC antenna printed on ployimide substrate, in this section, we investigate the performance of the NDTC antenna etched over various substrates with deposited conductor types and thicknesses. In addition, the NDTC antenna deployed in such applications where it encounters metallic surfaces (reflectors) nearby, gets influenced and any variation in the performance of the antenna is investigated.

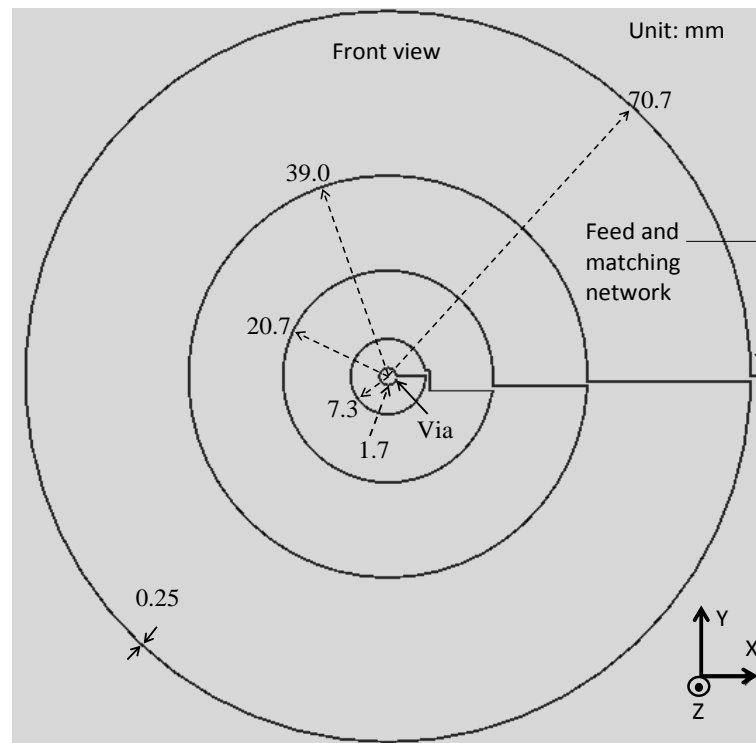


FIGURE 4.5: The NDTC antenna front view printed of various substrates

The optimized NDTC antenna, coil-5, designed for a read range of  $D = 5\text{cm}$ , is now printed on various substrates using various metal depositions, shown the front view in Fig. 4.5 and back view in 4.6. The matching network composing lumped capacitances C1 and C2 were shown in Fig. 4.1(b); the capacitors are designated to resonate the coil at  $f=13.56\text{MHz}$ .

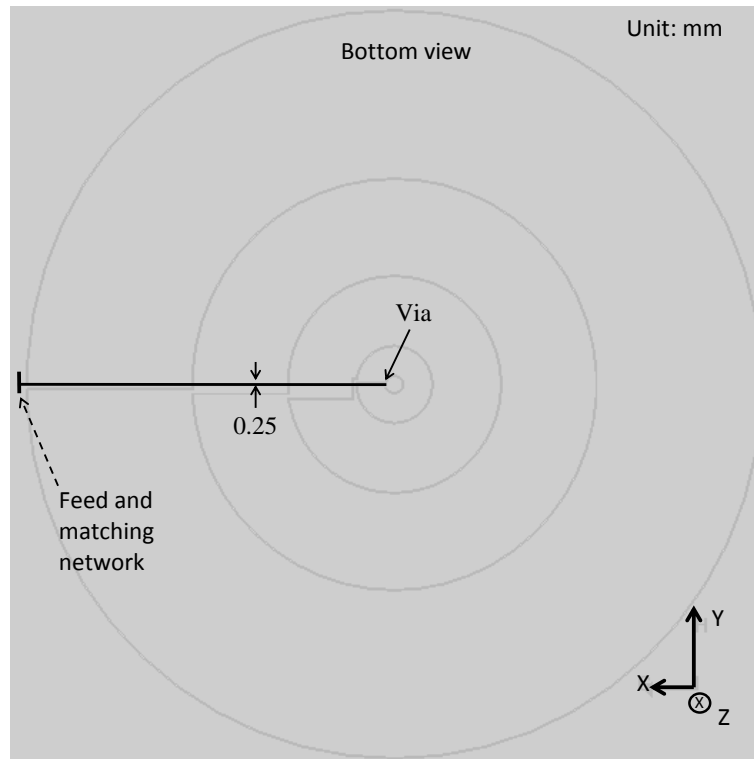


FIGURE 4.6: The NDTC antenna bottom view

### 4.2.1 Various substrates and conductor types under consideration

We have chosen some typically utilized substrates presented in [93] for the HF-RFID applications, such as the Printed Circuit Board (PCB) based on laminate FR4 and Polyamide, the Liquid Crystal Polymer (LCP), the Low Temperature Co-fired Ceramics (LTCC) and the Polyethylene Terephthalate (PET). The description of considered substrates and their corresponding conducting materials are summarized in Table 4.4. Five NDTC antennas, correspondingly built using the five configurations of Table 4.4, are simulated and their performances are compared in the following section.

TABLE 4.4: Considered substrates with corresponding conductors.

	$E_r$	$\tan\delta$	conductor	thickness
PCB FR4	4.3	0.025	copper	35
LCP	2.9	0.002	copper	18
LTCC	5.7	0.001	gold	10
PET	3.4	0.002	silver	20
PCB-Polyamide	3.4	0	copper	17.5

### 4.2.2 Simulation of NDTC antenna printed over various substrates

The five NDTC antennas with corresponding substrate/conductor types of Table 4.4 are simulated using Zeland IE3D. To calculate the corresponding matching elements C1 and C2, we first simulate the unloaded version of five NDTC antennas to get the corresponding values of  $R$  and  $L$ . Table 4.5 includes simulated results of  $R$ ,  $L$ , corresponding  $Q$ , and C1 and C2 of the five configurations considered for the investigation.

TABLE 4.5:  $R$ ,  $L$ ,  $Q$  of unloaded coils and corresponding matching network elements.

	$R(\Omega)$	$L(\mu H)$	$Q$	C1(pF)	C2(pF)
PCB FR4	2.2	1.48	58.0	73.78	19.47
LCP	3.9	1.47	32.3	67.79	26.26
LTCC	9.1	1.47	13.7	53.84	40.51
PET	3.3	1.47	37.8	69.62	24.25
PCB-Polyamide	4.0	1.47	31.3	67.22	26.62

Once the matching network parameters for all five configurations are known, the five NDTC antennas with loaded matching network can be simulated. The input signal with peak 1V was fed to all the designs. Fig. 4.7 shows simulated S11 of five configurations of the NDTC antenna, and the measured response for the PCB

Polyamide NDTC antenna, that was presented in Section 4.1, is included here to corroborate and prove correctly configured simulation setup. We now discuss the

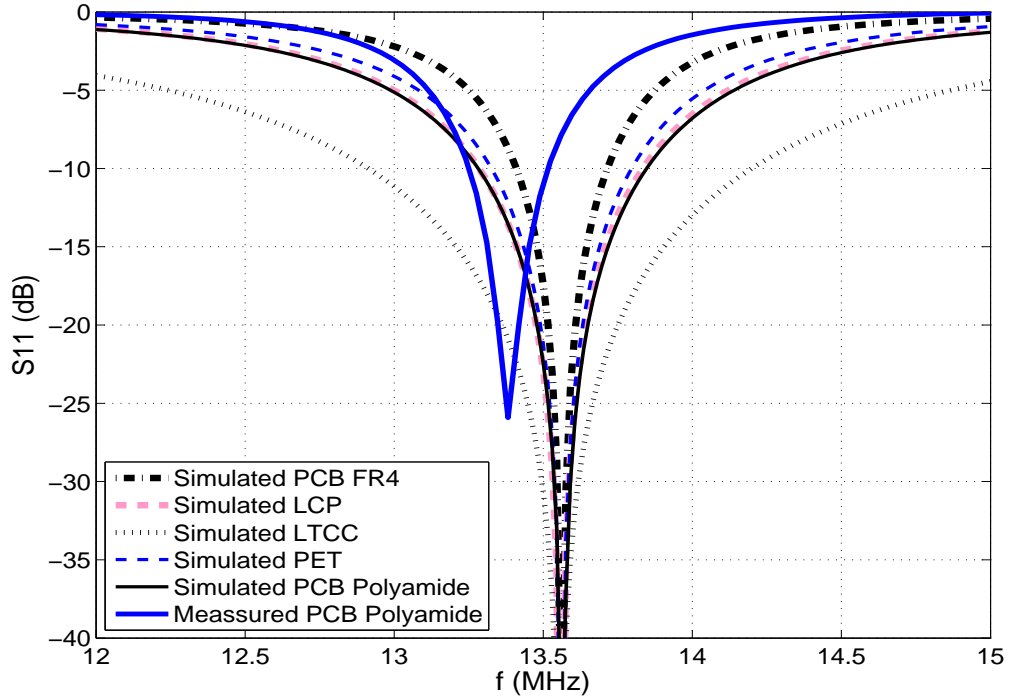


FIGURE 4.7: S11 of the loaded NDTC antenna with various substrates.

observations found from these results. It is shown that all the five NDTC antennas show a very well matched S11 response to 13.56MHz. The PCB FR4 shows the highest Q-factor of 58, hence, has maximum power efficiency, whereas, the BW shown is the lowest. The simulated  $H$  captured at  $z = D = 5\text{cm}$  out of five NDTC antennas are compared in Fig. 4.8. It shows that the highest  $H$  achieved is when NDTC is developed using the PCB FR4. For the antenna with LCP, PCB polyamide, and PET  $H$  is about 46%, 44%, and 35% lower than that using the PCB FR4. In the light of highest  $Q$  and  $H$  shown by PCB FR4, it is encouraging to use it for low-cost HF-RFID NDTC antenna realizations. In the next section, we exclusively choose the PCB FR4 substrate to investigate the influence of the reflector on the NDTC antenna.

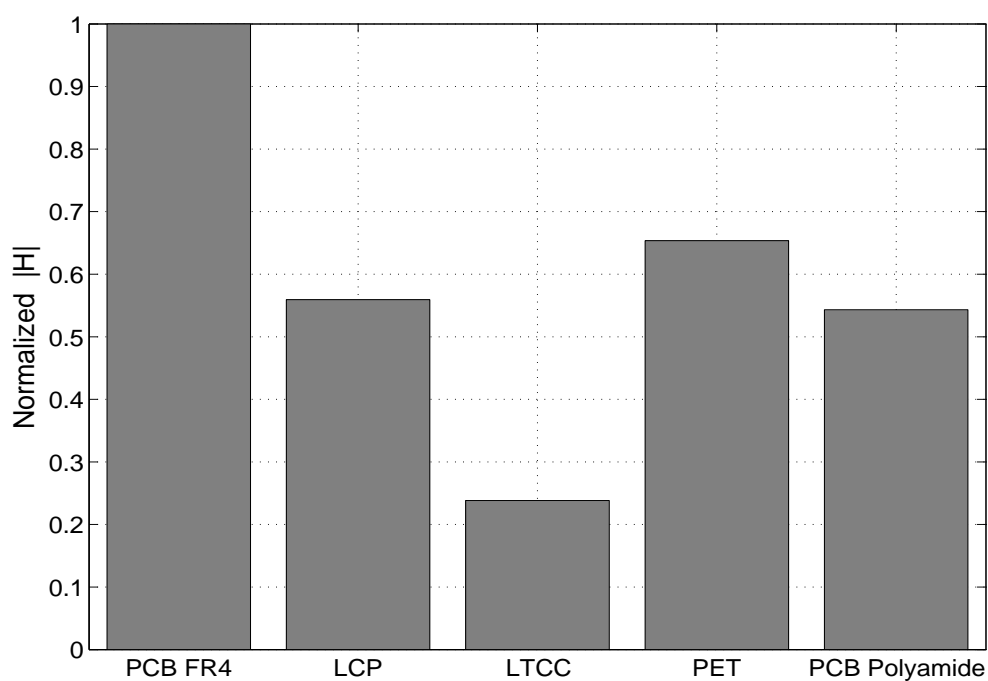


FIGURE 4.8: H-field comparison of NDTC antenna with various substrates.

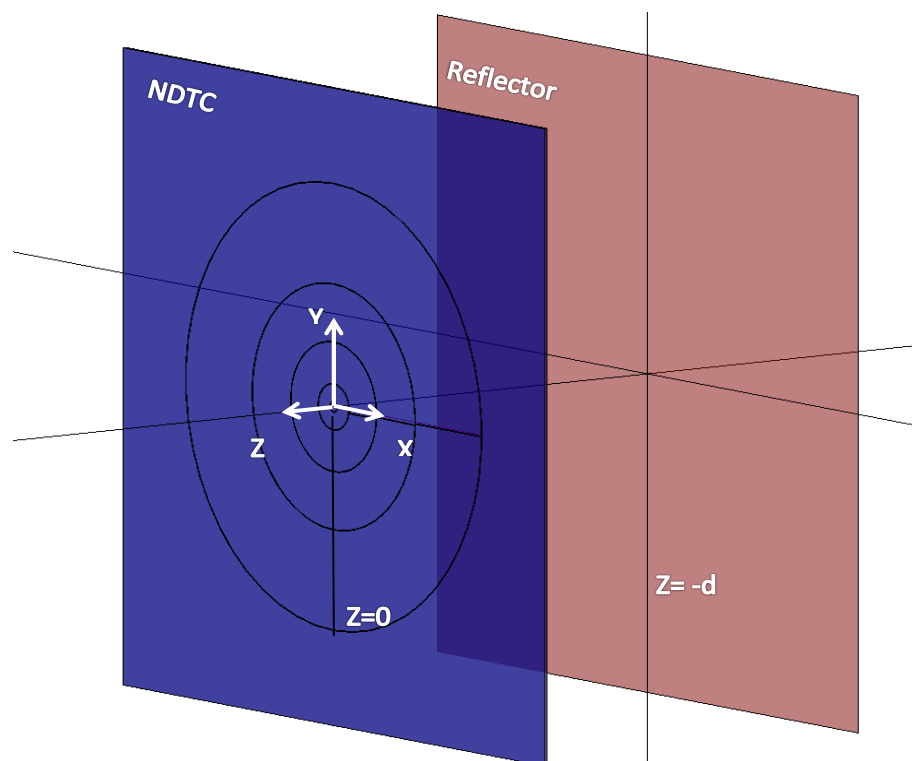


FIGURE 4.9: The NDTC antenna working in proximity to a metallic reflector.

### 4.2.3 Influence of Reflector Proximities over NDTC antenna

We consider a metallic plane, situated parallel to the NDTC antenna with PCB FR4 substrate, and placed at  $z = -d$ , hence, the separation between reflector and NDTC antenna is  $d$ , shown in Fig. 4.9. This configuration consisting of the antenna and the reflector is simulated for  $d = 1 - 11\text{cm}$  and the  $S_{11}$  responses are depicted in Fig. 4.10. It is apparent that the reflector in the vicinity detunes the

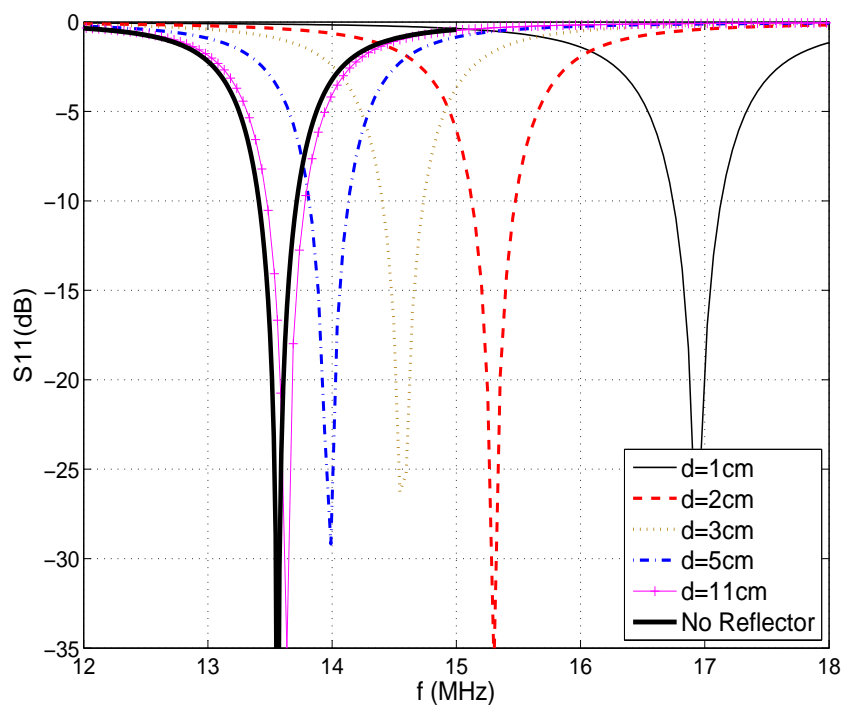


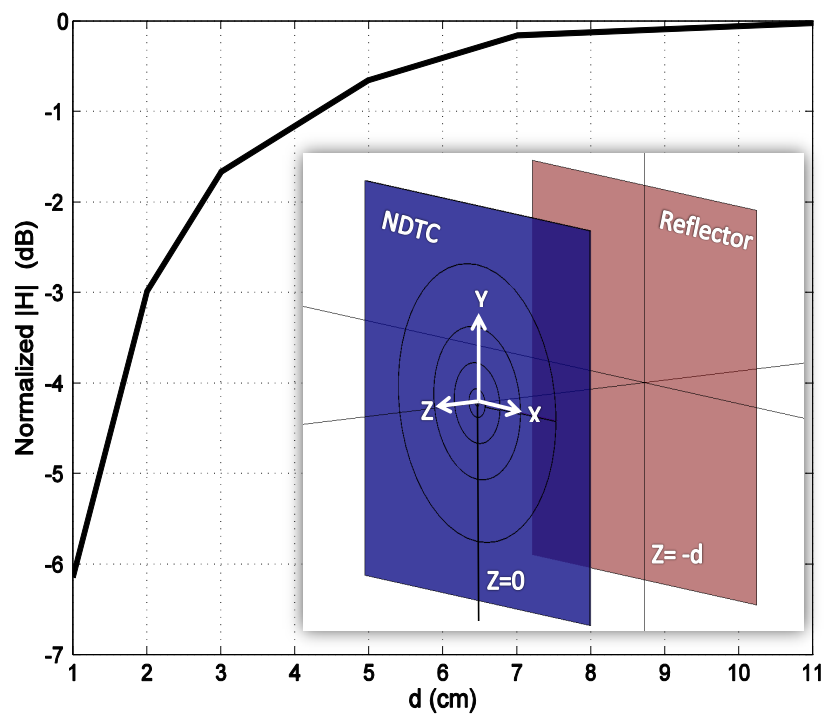
FIGURE 4.10: The simulated  $S_{11}$  response of the NDTC antenna (PCB FR4) and nearby reflector situated at  $d$  distance.

NDTC antenna but this impact dies off for higher  $d$  and becomes insignificant for  $d > 11\text{cm}$ . The antenna is re-tuned to  $f$  by reconfiguring matching network, the new  $C_1$  and  $C_2$  depending of  $d$  are evaluated and presented in Table 4.6 for  $d=1, 2, 3, 5,$  and  $11\text{cm}$ . Once the NDTC antenna is tuned back to  $f$ , we simulate it to evaluate the  $H$  at  $z = 5\text{cm}$  for several reflector separations  $d$ , the results are presented in Fig. 4.11, where normalization is performed with respect to the  $H$  without reflector. We observe that even after the antenna is re-tuned to  $f$ , the

TABLE 4.6: Recalculated matching network C1 and C2 to preserve matching.

$d$ (cm)=	1	2	3	5	11
C1 (pF)	92.67	83.46	79.40	75.77	74.14
C2 (pF)	24.56	22.05	20.97	19.99	19.56

$H$  falls down due to reverse currents in the reflector, for instance, a  $\sim 6$ dB loss in  $H$  is observed for  $d = 1$ cm. However, the effect on deterioration of  $H$  due the metallic surface becomes insignificant for  $d > 11$ cm. This suggests that the effect of contextual metallic parts in the vicinity should be considered while deploying the NDTC antenna for HF-RFID reader. The reduced  $H$  implies a decreased reading range, and to preserve the reading range to  $D = 5$ cm, the  $H$  loss should be compensated by an equal increase in input power.

FIGURE 4.11: The simulated  $H$  captured at  $z = 5$ cm of the NDTC antenna lying next to a reflector.

### 4.3 Application: Wide-spreading of the near-field

It will be demonstrated in this section that reading area of a single NDTC antenna unit is confined to the antenna size ( $\approx \pi a_1^2$ ), and for certain applications e.g., the reading/interrogating and wireless power transfer (charging mats), a significantly large reactive area can be demanded, as illustrated in Fig. 4.12. Therefore, an array using NDTC antenna is investigated to significantly extend the reading area of the antenna. The reading area is expandable (as much required by the application) by repeating the unit cell of the NDTC array. One unit cell consists five NDTC antenna elements. In this section we concentrate on design and performance evaluation of one unit cell (now onwards called NDTC array) of very large array. The NDTC array produces strong H-field in the interrogation zone with broadened reading area of  $> 4\pi a_1^2$ .

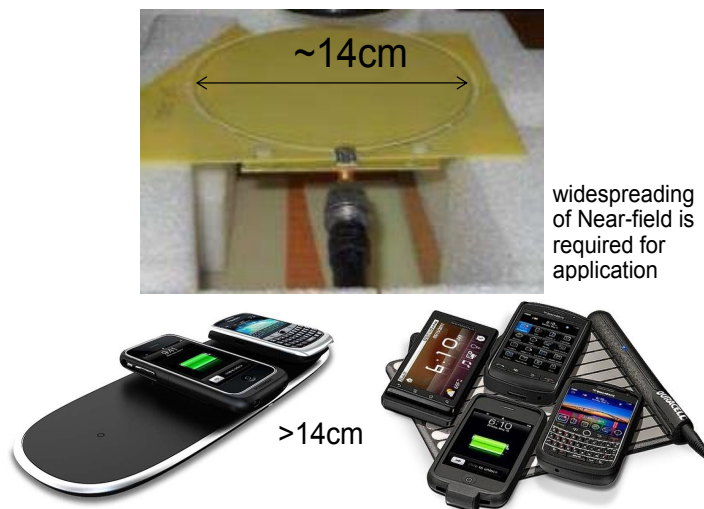


FIGURE 4.12: Applications demanding wide-spreading of the near-field (photos are for representation purpose only)

A single NDTC antenna optimized in Chap. 3 for a read range of  $D = 5\text{cm}$  at  $13.56\text{MHz}$  was used as array element whose maximum reading area (interrogation zone area,  $A$ ) was limited by the size of that NDTC antenna ( $A \approx \pi 7^2\text{cm}^2$ ). In this section, a NDTC array antenna is designed which extends  $A$  to at least four times and simulated to prove that a robust  $H$  is produced in its interrogation zone.

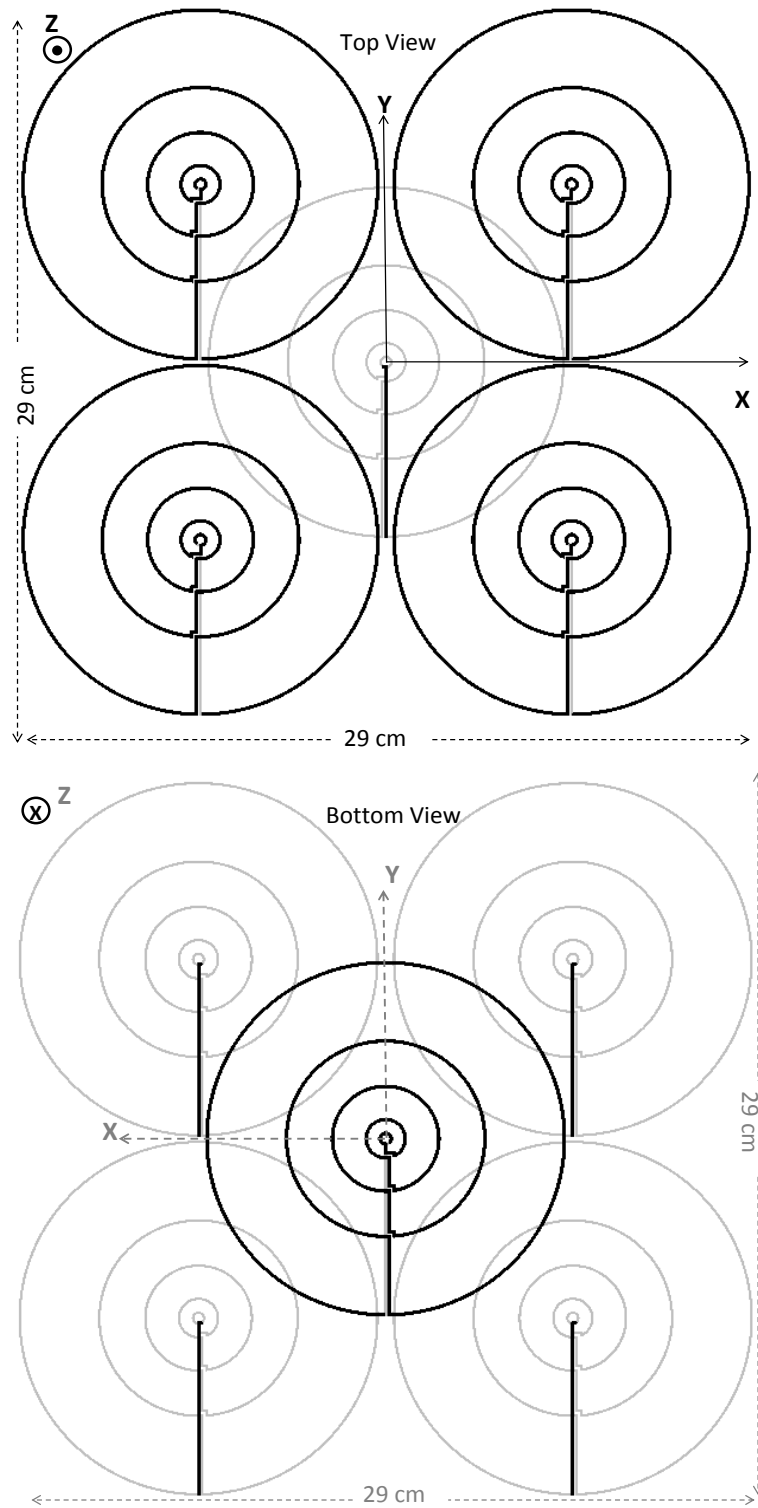


FIGURE 4.13: The NDTC array antenna.

### 4.3.1 The NDTC array antenna design

The NDTC array antenna structure is drawn in Fig. 4.13 consisting of 5 NDTC elements; each element with their respective matching networks and shown in Fig. 4.5 and Fig. 4.6. The NDTC array antenna is printed on a two-sided FR4 substrate having  $E_r = 4.8$  and  $\tan\delta = 0.02$ . As apparent from Fig. 4.13, the four NDTC elements out of five have their front sides printed on the top face of the substrate. At the beginning of the array design, only four elements were placed and this arrangement showed a void (low  $H$  spot) between the four NDTC units and was avoided by placing one more NDTC unit in the void. However, to avoid inter element touching, the fifth NDTC element was printed with its front side at the bottom of the substrate as illustrated in Fig. 4.13. The total area covered by this 5 element array is around  $29 \times 29 \text{cm}^2$ . The array elements are fed with equal power and zero phase signal, hence contributing to the H-field in extended reading area. The NDTC array antenna is simulated and its performance is evaluated in the next section.

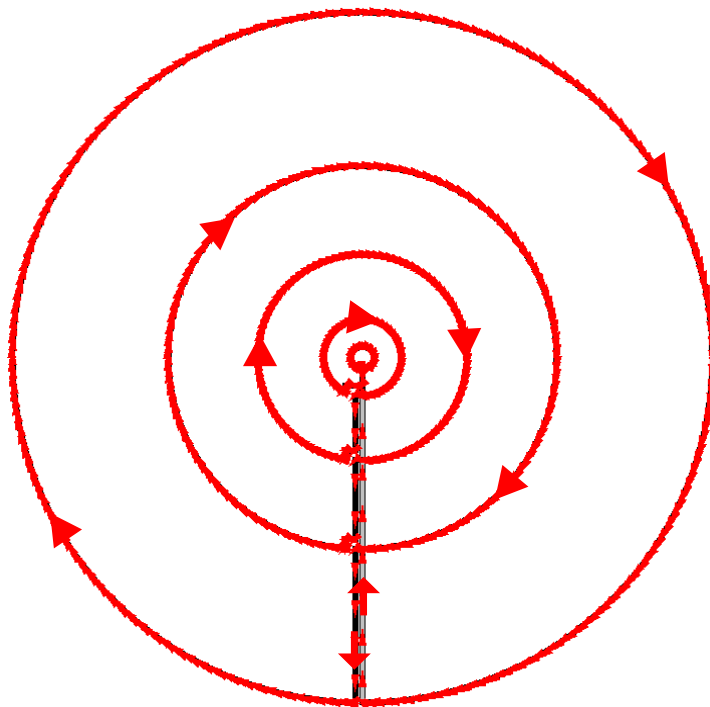


FIGURE 4.14: Current distribution in one NDTC element.

### 4.3.2 Simulation and Results

Using EM software Zeland IE3D the NDTC array antenna was simulated along with a NDTC element for comparison purposes. The current in a single NDTC element is compared with that of the final NDTC array antenna, also,  $H$  distribution in the interrogation zone of a single NDTC element is compared with the Array.

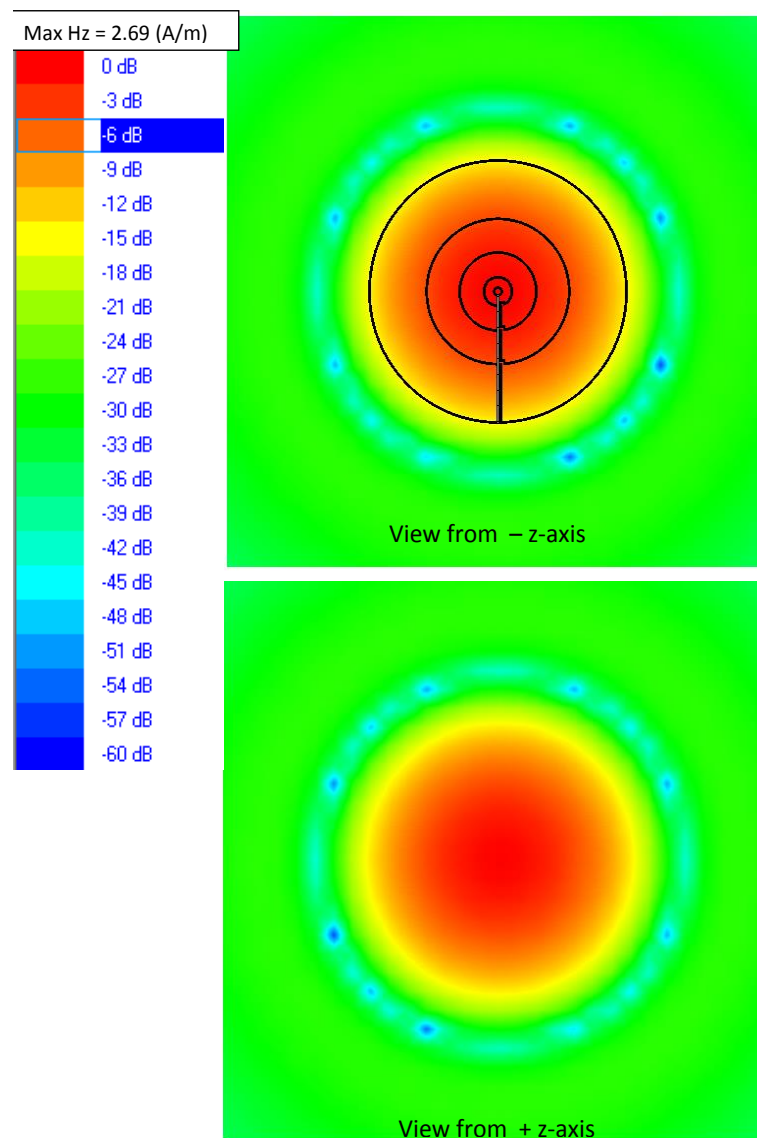


FIGURE 4.15: H-field distribution for one NDTC element at  $z = 5\text{cm}$ .

The simulated current distribution of a single NDTC element at 13.56MHz is demonstrated in Fig. 4.14. It is apparent that the current flowing in the NDTC

antenna has no phase variations due to electrically small size of the loop. Therefore, these currents contribute to the H-field constructively in the reading area (interrogation zone), and result into a strong field in the x-y plane.

The H-field distribution of the NDTC element at 13.56MHz is shown in Fig. 4.15. The 2-dimensional (x-y plane) H-field distribution of the z-component,  $H_z$ , at  $z=5\text{cm}$  of maximum magnitude  $H_z = 2.69\text{A/m}$  is shown. It is apparent that the effective field is confined only to the element area.

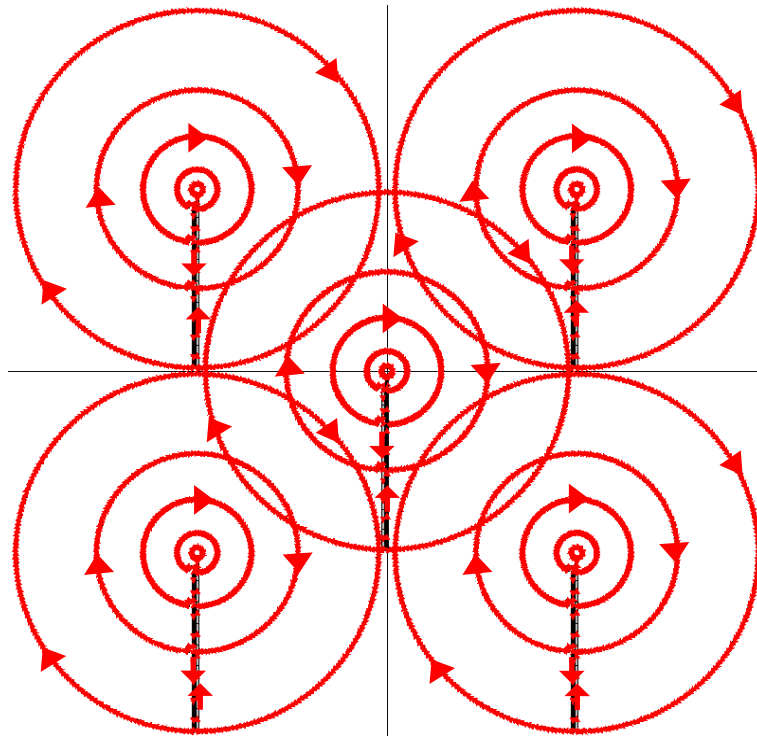


FIGURE 4.16: Current distribution in the NDTC array antenna.

The current distribution of the NDTC array at 13.56MHz is shown in Fig. 4.16 that demonstrates consistency of the current flowing in each NDTC element of the array and its same clock-wise circulation with no phase variations along the loop. Such a distribution of currents has ability to produce strong H-field and to spread the reading area to at least 4 times than that of a single NDTC element. It is demonstrated in Fig. 4.17 where the H-field ( $H_z$ ) distribution of the NDTC array is shown as a 2-dimensional (x-y plane) distribution at  $z=5\text{cm}$  and has a maximum magnitude  $H_z = 2.7\text{A/m}$ . The effective field area is broadened and this

justifies the use of NDTC array as a large antenna surface which can extend the reading area significantly.

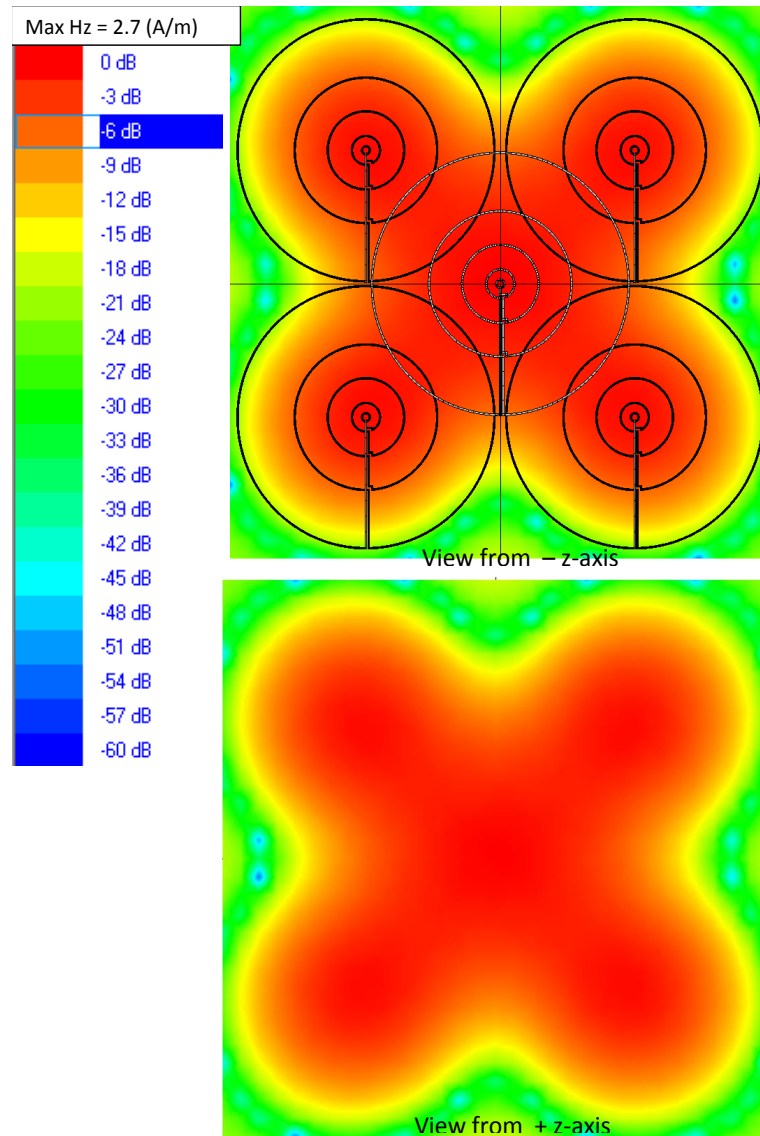


FIGURE 4.17: H-field distribution for NDTC array at  $z = 5\text{cm}$ .

## 4.4 Summary

Analytically designed NDTC antennas proposed in [90] used for HF-RFID applications were fabricated and measured in this chapter. The five coil antennas optimized in [90] having comparable Q-factor were manufactured and termed as Coil-1 to -5. The Coil impedances were measured and corresponding L-matching

network components were evaluated (at 13.56 MHz), and commercial SMD chip capacitors with closest possible capacitances were used in the matching network assembly. The final fabricated coils were measured for S11 and results showed the shifts of resonating frequency due to tolerances in matching components. The Coil-1 to -5 were experimentally validated for Q-factor with analytical and simulated values. We have observed that the optimized NDTC coils in [90] achieve considerably enhanced H-field and measured for the Coil-5 as 21.21% enhancement compared to the reference design Coil-1.

Furthermore, in this chapter, the NDTC antenna was assessed for the use on various substrates with different deposited conductors types and thicknesses and the performance degradation due to existing reflector in the vicinity of the antenna was investigated. Since a well defined matching network was designed, the S11 response of the NDTC antenna showed insensitivity to the substrate permittivity, and independence to the conductor type. However, the NDTC over PCB-FR4 had highest  $Q$  and  $H$ , its therefore seems suitable for the applications with high power efficiency. The impact of reflector situated behind the NDTC antenna was found negative when in close proximity and negligible for a reasonable separation. The compromised  $H$  can be compensated by an equal increase in input power; this would allow the antenna to be used near reflectors.

In the final section of this chapter, we investigated an array antenna developed using NDTC antenna elements. For multipurpose NF applications, e.g., the reading/ interrogating and wireless power transfer (charging mats), a wider reactive field area is demanded. The NDTC array antenna was designed for extending near-field interrogation zone at HF (13.56MHz). The maximum reading area (interrogation zone,  $A$ ) of a single NDTC element was limited to  $A \approx \pi 7^2 cm^2$ . It was expended to at least four times of  $A$  by designing an array composing five cautiously arranged NDTC elements to produce robust magnetic-field in the wider interrogation zone. Not only four-times but a much wider reading area of any size can be obtained by repeating this NDTC array unit in the antenna plane. We showed that the NDTC array antenna simulation results validate the claims and show a robust and extended  $H$ .

## ACKNOWLEDGEMENT

Thanks to Agustí Urgell, GSPK, and Diego Pérez de Diego, CATECHOM for the technical support.

### 4.5 Chapter related publications

1. **A. Sharma**, I. J. Garcia Zuazola, A. Gupta, A. Perallos, and J. C. Batchelor, “Fabricated Non-uniformly distributed-turns coil,” in *IEEE Antennas and Propagation Society International Symposium*, Memphis, USA, July 2014, pp. 1536-1537.
2. **A. Sharma**, I. J. Garcia Zuazola, A. Gupta, J. C. Batchelor, and A. Perallos, “Influence of Substrate Types and Reflector Proximities Over a NDTC Antenna,” in *Loughborough Antennas and Propagation Conference (LAPC)*, Loughborough, UK, Nov 2014, pp. 431-433.
3. **A. Sharma**, I. J. Garcia Zuazola, J. C. Batchelor, and A. Perallos, “Wide-spread near-Field with robust H-field using NDTC antennas in multipurpose Applications,” in *Twenty First National Conference on Communication (NCC-2015)*, Mumbai, India, Feb.-Mar. 2015, pp. 1-5.



# Chapter 5

## Coil antenna for UHF-RFID

In previous chapters, we studied some highly efficient and optimized coil antennas (e.g, NDTC) used for HF-RFID readers. There are also existing applications, e.g., medical products and bio-sensing, logistics, transports, tracking of pharmaceutical products, which equally demand near-field RFID operating at Ultra-High-Frequency (UHF). This chapter is intended to explore some coil antennas designed to work for UHF-RFID readers. Among these antennas, a highly efficient Segmented-line Non-uniformly Distributed-Turns Coil (SL-NDTC) antenna used for near-field UHF-RFID will be investigated. This newly developed SL-NDTC antenna, achieving a significantly improved magnetic field in the near-field zone, is compared with a conventional UHF segmented-line Coil and a conventional solid-line coil.

### 5.1 Introduction

The near-field UHF-RFID systems employ inductive coupling similar to the HF-RFID, and can adopt the conventional solid-line coils used in LF/HF-RFIDs. Those coils were electrically small loops ( $C < \lambda/10$ , where  $C$  is the total circumference of the loop and  $\lambda$  is the operating wavelength [1]), which means that the current flowing along the loop was almost in-phase making them capable of

producing strong magnetic field in the near-field region of the reader antenna [24, 25, 29]. In contrast, at UHF,  $C$  of the same coil antenna becomes comparable to  $\lambda$  [28, 30] (the loop becomes electrically large) and current distribution along the loop is no longer in-phase, even the phase inversions and current nulls are encountered. Therefore, the conventional solid-line coil used as a UHF-RFID reader antenna suffers with weak and non-uniform H-field in the interrogation zone diminishing the system performance.

The key to design electrically large coils for UHF is by dividing the coil into several segments and compensating the current phases (introduced along the line) at the end of each segment by a capacitor, such that the current in the coil appears to be in-phase. The UHF segmented-line coils presented in [37, 38] were composed of multiple pairs of a solid-line section and a fork-shaped capacitor which are distributed along the periphery of the coil. These designs are composed of only a single turn and termed as Segmented-Line Single-Turn Coils (SL-STC). Although Single-Turn Coils (STC) are widely used in HF-RFID readers, multi-turn coil (e.g., NDTC) are of major interest for coupling enhancement between the inductively coupled Reader and Tag antennas in HF-RFID. Similarly, at UHF, the segmented-line coils with multiple turns used for UHF-RFID are also intended to enhance the H-field. In the next section, a SL-STC antenna (with 75mm radius) [37] and a newly developed Segmented-Line NDTC (SL-NDTC) antenna, both used for UHF-RFID, will be investigated and compared. The SL-NDTC antenna will be designed to optimize radii of the inner turns for a maximum H-field. These designs will be compared with a UHF solid-line coil, STC antenna.

Moreover, it will be shown that the designed UHF SL-NDTC antenna not only performs in the near-field effectively, but also has an encouraging far-field radiation; this is essentially welcomed for dual-purpose applications where it can read tags in near- as well as far-field of the UHF-RFID applications.

## 5.2 Segmented-line coil antenna for UHF-RFID readers

The UHF coil antennas introduced in Section 5.1 are investigated in this section. All the designs considered in this chapter are etched over a FR4 PCB with thickness  $h = 0.8$  mm, relative dielectric constant of  $\epsilon_r = 4.4$ , loss tangent of  $\tan\delta = 0.02$ , and metal strip width 1mm and height 0.002mm. The PCB lies in  $x$ - $y$  plane with the center of printed coils coinciding with the origin of the coordinate system. For a fair comparison, all the designs are confined by a fixed maximum turn radius  $R_1 = 75$ mm, and resonating at frequency 915MHz.

### 5.2.1 The STC and the SL-STC antenna design

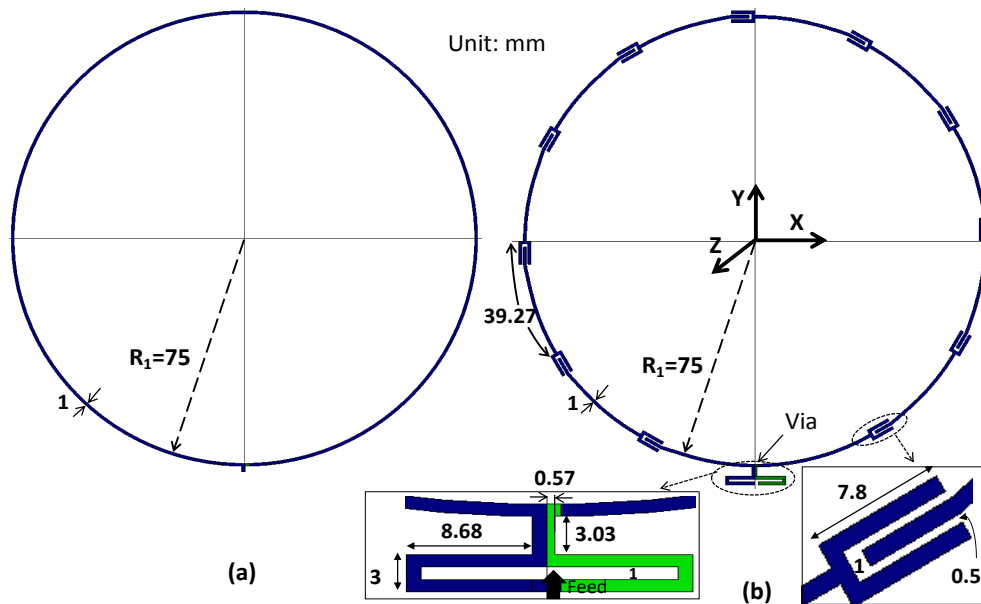


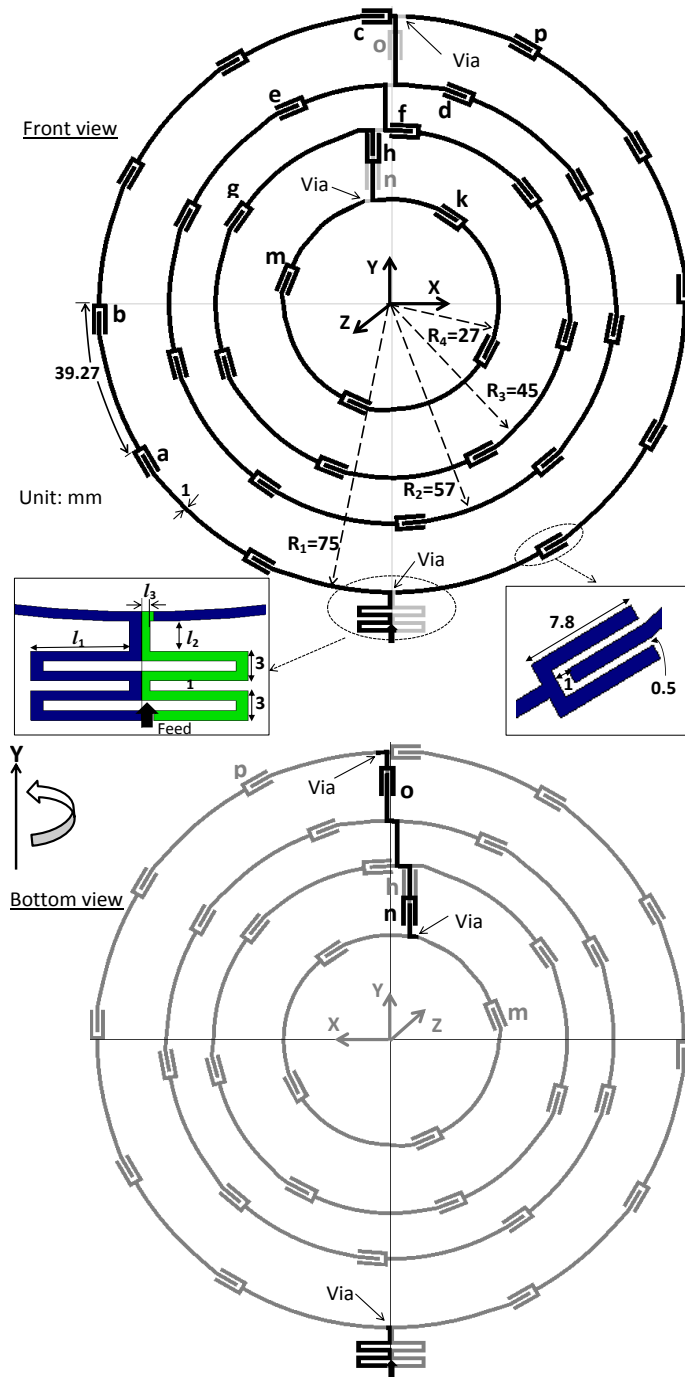
FIGURE 5.1: a) The STC and b) the SL-STC antennas for UHF-RFID.

Fig. 5.1(a) shows the printed conventional solid-line coil, STC, having total perimeter  $1.44\lambda$  (hence electrically large). The SL-STC shown in Fig. 5.1(b) has perimeter  $1.44\lambda$  similar to that of the STC, however, in addition to that it consists of fork-shaped distributed capacitors to compensate the phase delay along solid-line segments. One segment attached with a fork-shaped capacitor is 39.27 mm long, Fig. 5.1(b), and the SL-STC is realized by repeating these segments along the

coil's trace. To match the input impedances of the antennas to  $50\Omega$ , we use stub matching network printed on both sides of the PCB. Since the current along the SL-STC is expected to be unidirectional, it should provide strong H-field compared to the STC in the near-field zone of the antenna. However, to further enhance the H-field over that of the SL-STC antenna, next section presents a SL-NDTC antenna which facilitates multiple distributed turns to maximize the H-field.

### 5.2.2 The SL-NDTC antenna design

In this section, we present the design of SL-NDTC antenna introduced in Section 5.1. Similar to the SL-STC, the SL-NDTC antenna is made of several distributed segments (with one fork-shaped capacitor) shown in Fig. 5.2, but additionally, consists  $N$  turns of radii  $[R_1, \dots, R_N]$ . A similar optimization as proposed in [90] and described before in Section 3.3.5 is used for the SL-NDTC antenna to evaluate the optimal radii while maximizing the  $H_z$  along the coil axis. The rigorously performed optimization starts with  $N = 1$ , that essentially is the SL-STC, and gradually adds more turns to the current version of the antenna, and optimizes the radius of the newly added turn for a maximum  $H_z$ . An intermediate design with  $N = 2$  will be elaborated in the next paragraph for a greater understanding of the optimization procedure and parametric study. Once the full optimization terminates, it yields  $N = 4$ ,  $R_1 = 75\text{mm}$ ,  $R_2 = 57\text{mm}$ ,  $R_3 = 45\text{mm}$ , and  $R_4 = 27\text{mm}$ , and final version of SL-NDTC is shown in Fig. 5.2. The connecting strips between two turns are such that the segment length =  $39.27\text{mm}$  is maintained for the proper phase cancellation. In Fig. 5.2, (front view) the length  $cd = ef = gh = hk = 39.27\text{mm}$ . Point  $m$  is connected at the via to the bottom view, such that length  $mn$  and  $no = 39.27\text{mm}$ . Finally point  $o$  is connected by via to the front view so that length  $op = 39.27\text{mm}$ . The antenna was matched to  $50\Omega$  and the matching network parameters are evaluated as  $l_1 = 8\text{mm}$ ,  $l_2 = 3\text{mm}$ , and  $l_3 = 0.67\text{mm}$ .



All adjacent capacitors ab, cd, ef, gh, hk, mn, no, op, etc. have total segment length 39.27 mm between them.

FIGURE 5.2: The SL-NDTC antenna for UHF-RFID reader.

During the optimization, the Segmented Line-Dual Turn Coil (SL-DTC) with the geometry shown in Fig. 5.3 came as an intermediate result between the SL-STC and the SL-NDTC. The SL-DTC was obtained by an iterative procedure to establish appropriate separation between the turns. Starting with STC antenna

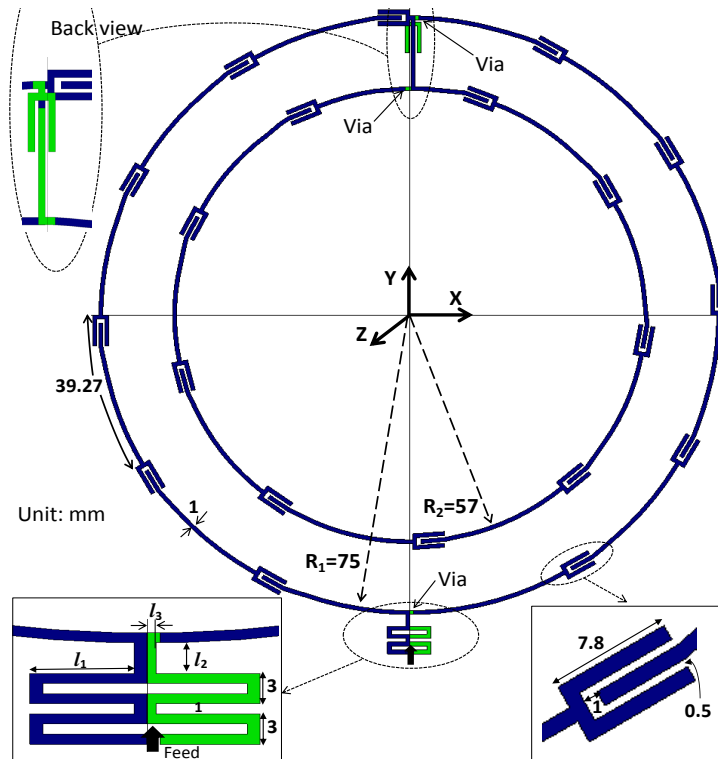
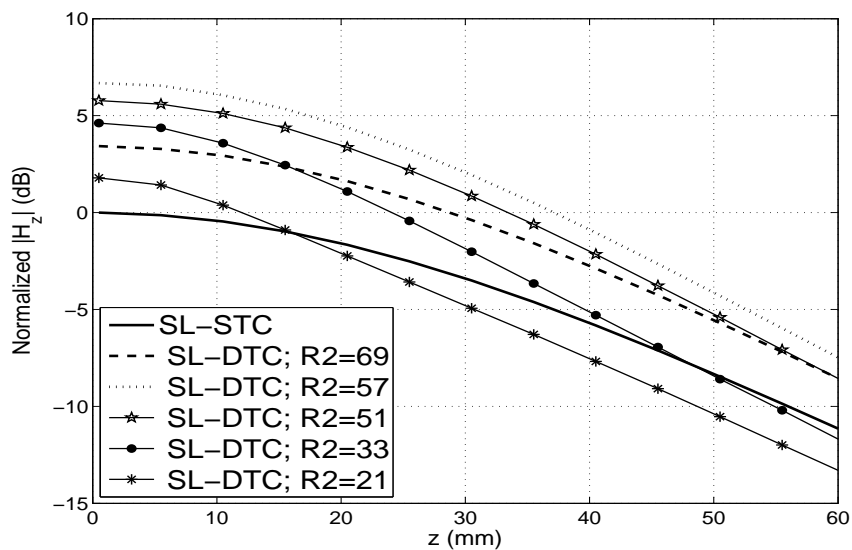


FIGURE 5.3: The intermediate design: SL-DTC antenna.

FIGURE 5.4: Assessing the optimal radius  $R_2$  of the SL-DTC antenna.

with  $R_1 = 75\text{mm}$ , the radius of the second turn was found by optimization from the iterative radii shown in Fig. 5.4. The radius of second turn is chosen giving maximum  $H_z$ , by observation from Fig. 5.4, the response for  $R_2 = 57\text{mm}$  was chosen to proceed for next step in the optimization. Further turns were added to

the intermediate coil and distributed for a maximum  $H_z$  leading to the final SL-NDTC design. For the SL-DTC design, the required stub matching circuit (Fig. 5.3 inset) was found by iteration and reveals values  $l_1 = 4.48\text{mm}$ ,  $l_2 = 3.04\text{mm}$ , and  $l_3 = 0\text{mm}$ .

### 5.3 Simulations and results

The UHF coil antennas, STC, SL-STC, SL-DTC, and SL-NDTC, are now simulated and results are compared. All the antennas were fed with the same input power, 1Watt, and simulated for their corresponding S11 variation, as depicted in Fig. 5.5.

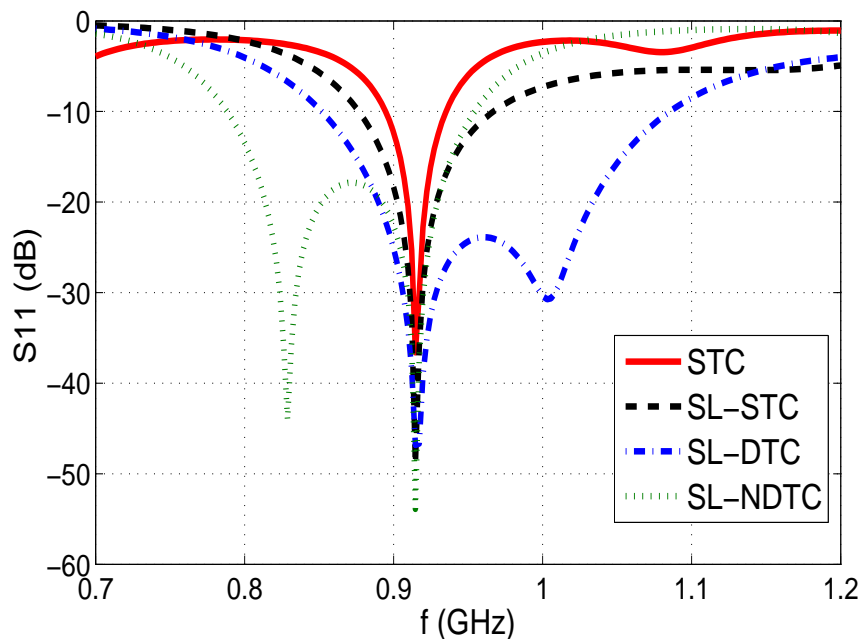


FIGURE 5.5: Simulated S11 of the UHF-RFID coil antennas.

The -10dB Bandwidths (BW) are summarized in Table 5.1 for the operating frequency of 915MHz. Results indicate that wide fractional bandwidths between 18 and 25% can be obtained for the multi-turn segmented designs which are 5-7 times greater than the STC design. The achieved bandwidths are influenced by the double stub matching networks (inset Fig. 5.2 and 5.3) meaning that the quoted values

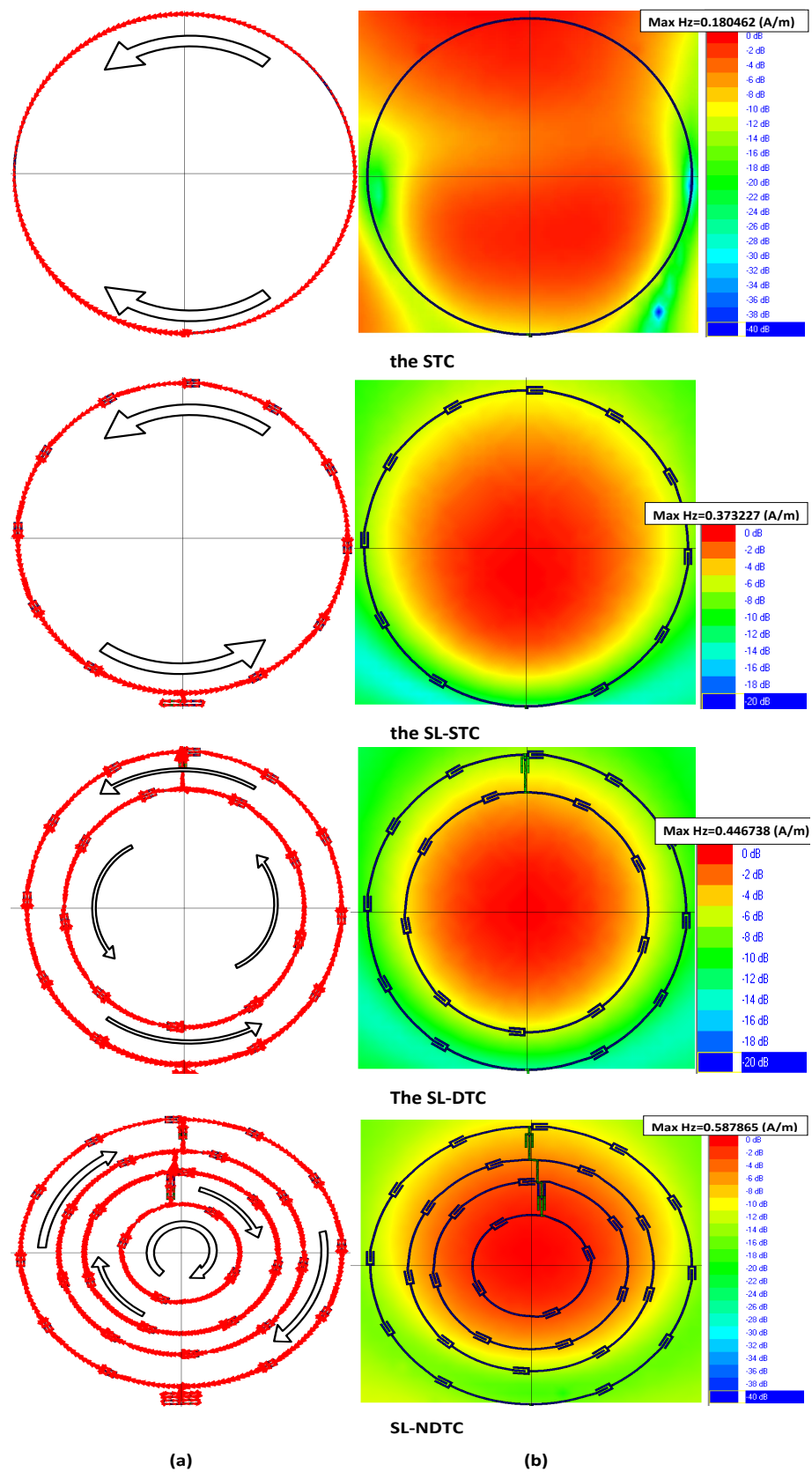
TABLE 5.1: Simulated bandwidths of the UHF coil antennas.

	-10dB S11 BW (MHz)	Fractional BW for 915MHz	Normalized BW with respect to STC
STC	34	3.7%	1
SL-STC	89	9.7%	2.6
SL-DTC	233	25%	6.8
SL-NDTC	165	18%	4.9

may not be the maximum obtainable in each case. However, further improvement was not deemed necessary because the proposed SL-NDTC fully covers the 865-868 MHz (Europe) and 902-928 MHz (North America) UHF industrial, scientific and medical (ISM) radio bands,.

The simulated currents and H-field distributions of the coils at 915MHz are compared in Fig. 5.6(a) and (b), respectively. The 2-dimensional (x-y plane) H-field distribution of the z-component,  $H_z$ , at z=50mm plane is shown. It is apparent from Fig. 5.6 that the current flowing in the solid-line coil antenna faces phase inversions due to electrically large size of the loop. Therefore, these currents essentially do not contribute to the H-field constructively in the interrogation zone, and result into a weak field in x-y plane of maximum magnitude  $H_z = 0.18\text{A/m}$ . Whereas, a higher  $H_z = 0.37\text{A/m}$  is produced by the SL-STC antenna because of the equal phased currents flowing along the traces of the coil, even though the coil is electrically large. For the SL-DTC design, the current flow in the inner turn has a same direction as of the outer turn, contributing constructively such that the  $H_z$  becomes 0.45 A/m which is 1.2 times greater than the SL-STC. Fig. 5.6 also shows that the current distribution in the SL-NDTC antenna is ensured to flow in-phase by the use of segmented-line configuration, and it effectively works for multiple turns as well. The constructive contribution of the currents in the SL-NDTC antenna enhances H-field in the central portion of the interrogation zone and results in the maximum  $H_z = 0.58\text{A/m}$  which is 1.3, 1.57 and 3.3 times higher than the SL-DTC, SL-STC and the STC, respectively.

Fig. 5.7 shows simulated H-field distribution along the coil axis (z-axis) for the

FIGURE 5.6: Simulated (a) currents and (b)  $H$  distribution of the coils.

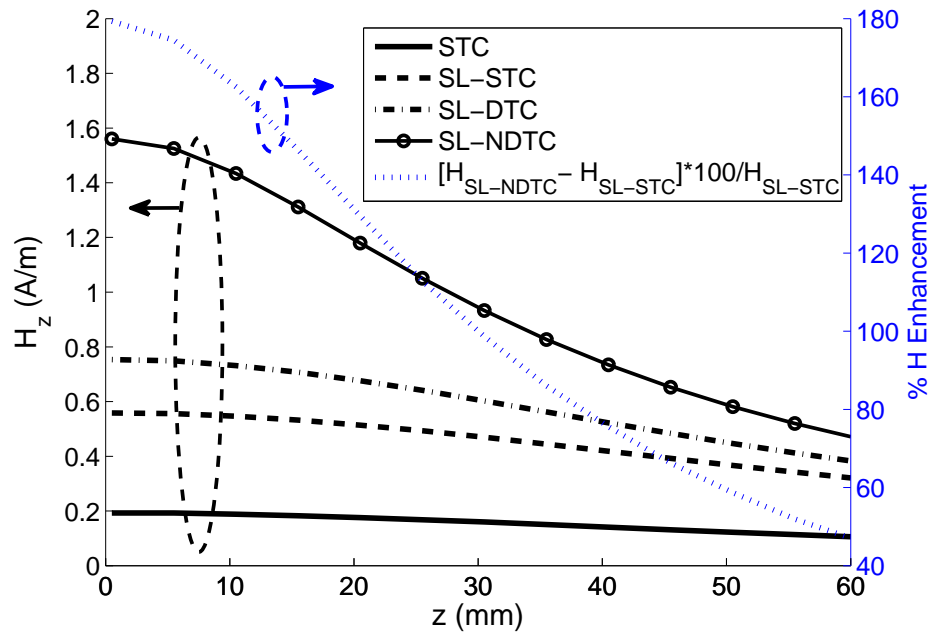


FIGURE 5.7: Simulated H-field distribution along z-axis and percentage  $H$  enhancement by the SL-NDTC antenna.

three designs, and relative enhancement by the SL-NDTC compared to the SL-STC is presented. For an equal power input to all the designs, a weaker H-field is produced by the conventional solid-line coil throughout the z-axis. Whereas, an enhancement in  $H$  is achieved by the proposed SL-NDTC over the SL-STC antenna; that is 2.3, 5.8 and 0.3 times with respect to the STC, the SL-STC, and the SL-DTC, which is significant enough to encourage the use of the SL-NDTC configuration in the advanced design of reader antennas for UHF-RFID applications.

### 5.3.1 Far-field simulation results

The SL-NDTC is now investigated for its use in far-field UHF RFID applications. The simulated far-field radiation patterns are shown in Fig. 5.8 and the efficiency and gain are plotted against frequency in Fig. 5.9. The observations extracted from the far-field results are as follows. The SL-NDTC antenna has a gain of  $\sim 1.44$  dBi, and an efficiency of  $\sim 80\%$ . A reasonably flat gain response across 840-960 MHz with a slight variation of  $\pm 0.05$  dBi is observed. Quite similar radiation patterns

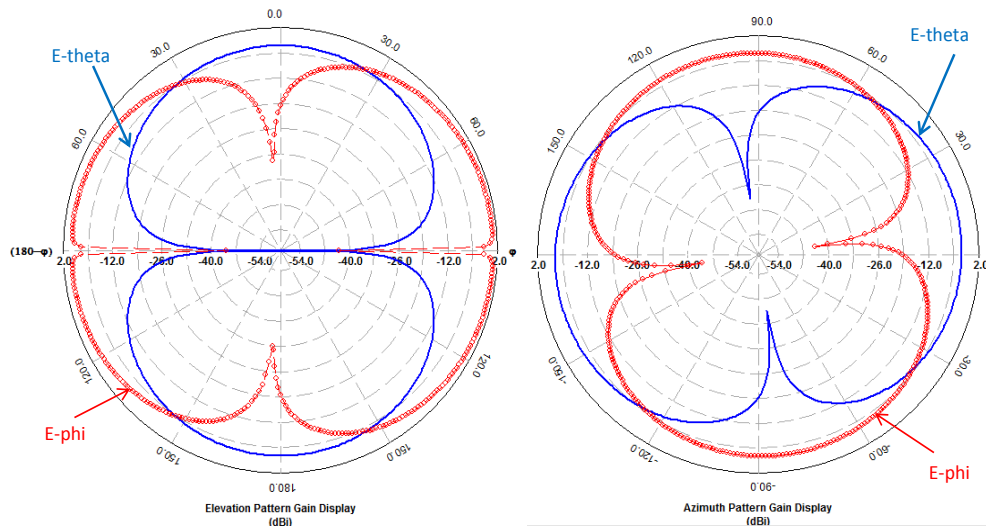


FIGURE 5.8: Simulated radiation pattern of the SL-NDTC antenna

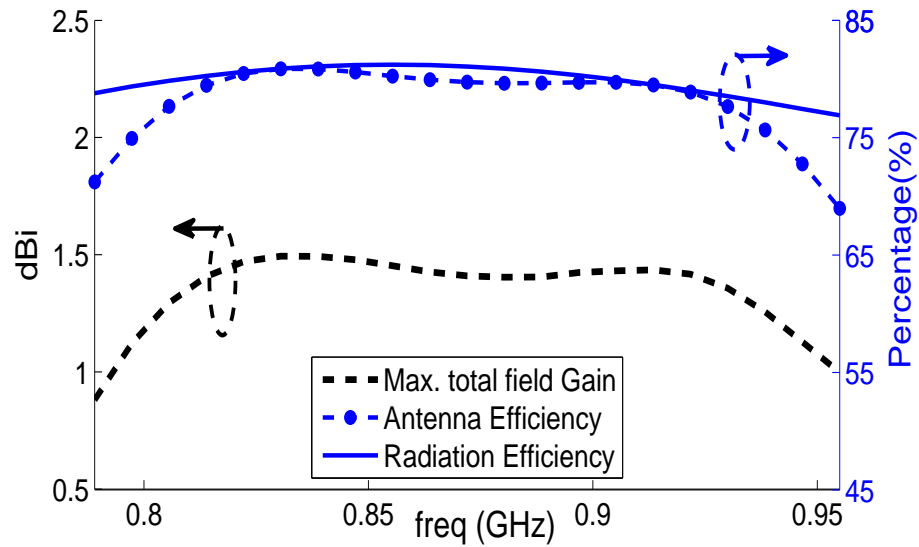


FIGURE 5.9: Simulated efficiency and gain of the SL-NDTC antenna.

in E-theta and E-phi of the Elevation and Azimuth planes are observed and shows a good omnidirectionality (E-total) for reading tags of any orientation.

## 5.4 UHF antenna fabrication and measurements

The STC, the SL-STC, and the SL-NDTC antennas were fabricated and shown in Fig. 5.10(a). To measure the reflection coefficient (S11) of the antenna, an Agilent PNA-X Network Analyzer (connectors and cables appropriately calibrated)

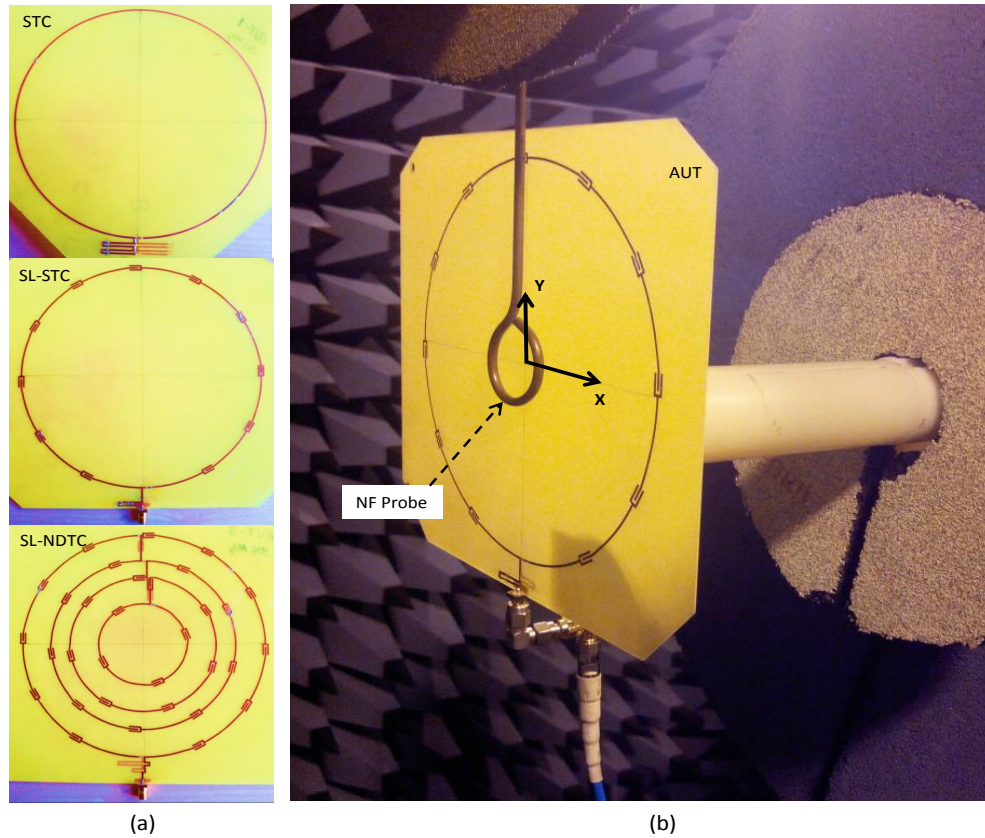


FIGURE 5.10: a) Fabricated antennas b) setup for measurement

was used. The  $S_{11}$  responses are shown in Fig. 5.11. The deviation of  $S_{11}$  responses from operating frequency 915MHz can be attributed to manufacturing tolerances. The fabricated antennas are now measured for their near- and far-field performances, presented next.

#### 5.4.1 Measurement results

The  $H$  of the antennas were measured in an anechoic chamber. The measurement setup is shown in Fig. 5.10(b) where the fabricated antennas were fixed as a transmitter (AUT) and fed with 10dB input power. A near-field probe (small loop antenna as a receiver) was placed at a distance  $z = 50\text{mm}$  away from the AUT and moved to scan the x-y plane. A Network Analyzer was connected to the near-field probe and the measured received power (representing  $H$ ) distributions are presented in Fig. 5.12. The results show that the maximum received power from the STC is -46.68dB, whereas, the SL-STC shows 4.45dB higher power than the

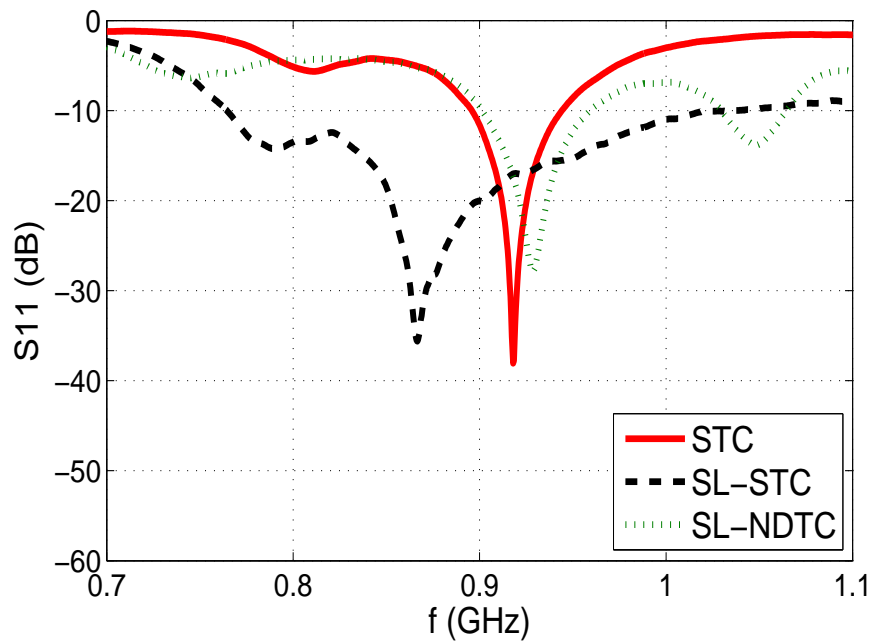


FIGURE 5.11: Measured  $S_{11}$  of the UHF-RFID coil antennas.

STC. The SL-NDTC enhances the maximum received power by 2.21dB over that of the SL-STC which is equivalent to 29.9% enhancement in magnitude. These results encourage the practical use of the prototype for advanced interrogator antennas in Near-field UHF-RFID systems. The SL-NDTC was also measured for far-field radiation patterns and the results are depicted in Fig. 5.13. The directive gain pattern in H-plane and E-plane are showing good omnidirectionality. The measurements corroborated the simulations and showed the SL-NDTC with enhanced magnetic field in near-field zone and decent radiations in far-field zone of the antenna; this proves it as a suitable option for Dual-purpose near- and far-field UHF-RFID applications.

## 5.5 Summary

The circular segmented-line coil antennas used for UHF near- and far-field RFID applications are studied. The traditional solid-line coil shows weak magnetic field (H-field) due to currents facing phase inversions and nulls since the coil is electrically large at UHF 915MHz. Instead, Segmented-Line Single-Turn Coil (SL-STC)

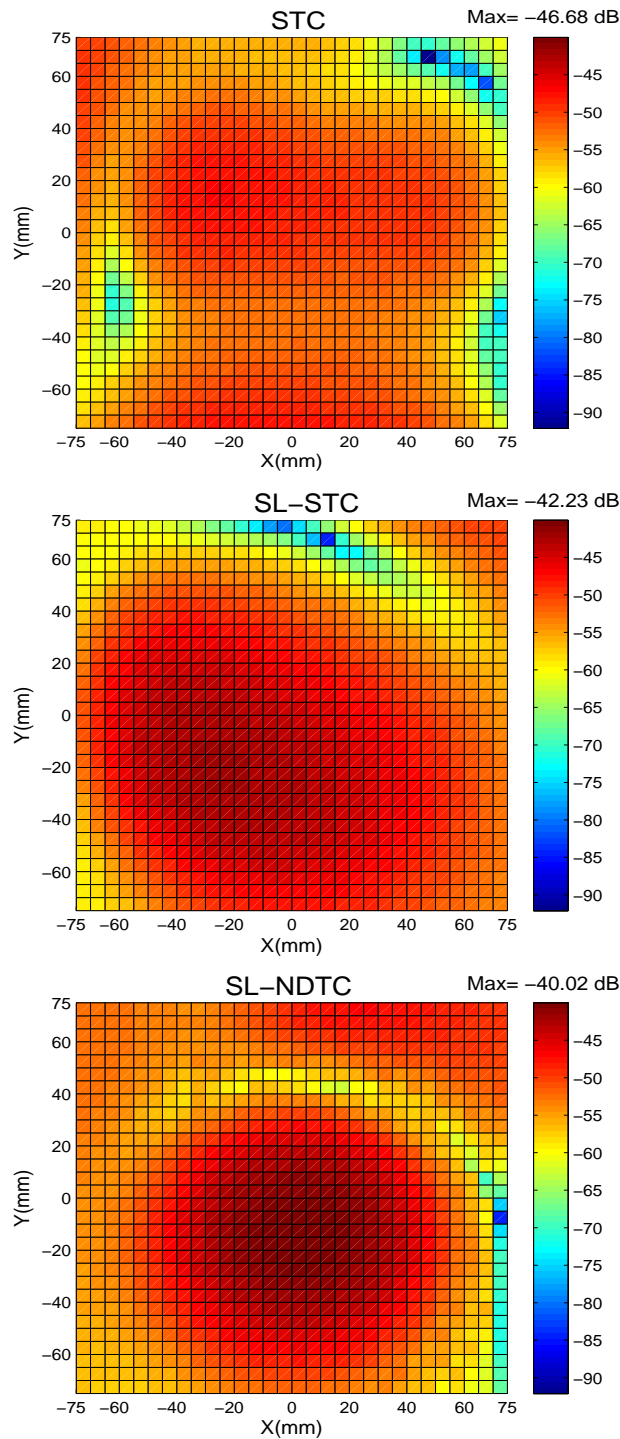


FIGURE 5.12: Measured  $H$  of the UHF-RFID coil antennas at  $z = 50\text{mm}$ .

antenna is usually used (incorporating solid-line sections along with distributed capacitors to compensate current phases along the traces of the coil) to produce strong and uniform H-field even though the coil is electrically large. The use of multi-turn coil was proved to enhance the performance over the SL-STC. For this

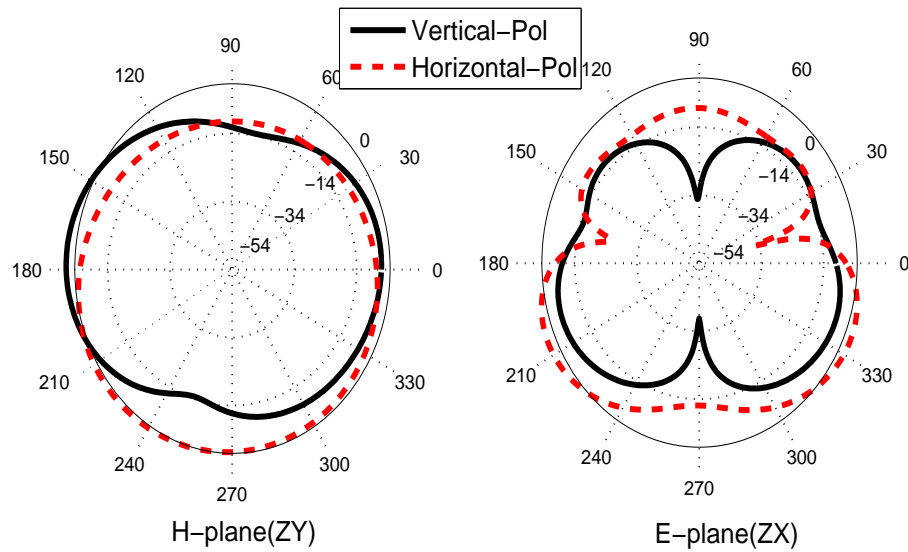


FIGURE 5.13: SL-NDTC measured normalized radiation pattern.

purpose, an optimized Segmented-line Non-uniformly Distributed-Turns Coil (SL-NDTC) antenna at UHF was presented. The radii of inner turns of the SL-NDTC coil antenna were optimized using non-uniformly distributed turns terminology for a maximum H-field in the interrogation zone. The simulations backed my measurements of the solid-line coil, SL-STC, and SL-NDTC yield the results which proved that the optimized SL-NDTC design achieves significant enhancement in H-field compared to the other two antennas. The percentage H-field enhancement achieved by the SL-NDTC over the SL-STC was 162.6% at 10mm and 58.7% at 50mm distance from the coil center. Along with the near-field results, the far-field radiation patterns were encouraging and this shows the SL-NDTC as a Dual-purpose near- and far-field UHF-RFID reader antenna.

## 5.6 Chapter related publications

- **A. Sharma**, I. J. Garcia Zuazola, A. Gupta, A. Perallos, and J. C. Batchelor, “Dual purpose near- and far-field UHF RFID Coil Antenna with Non-uniformly Distributed-Turns,” *IEEE Letters on Antennas and Propagation*, vol. 14 , pp. 1342-1345, Feb. 2015.



# Chapter 6

## Switchable Multiband antennas

In preceding chapters, RFID reader antennas were designed to work for a certain frequency of operation, such as HF(13.56MHz) or UHF (915MHz). Those can be designated as single band antennas working for either HF-RFID or a UHF-RFID. In this chapter, novel multiband antennas are investigated with emphasis to deployments in various RFID systems which current standards can be met using only a single radiating unit; this is attractive for compactness (single unit vs. multiple units) and its related cost reduction. The frequency of operation of the targeted antenna can be switched among various frequency bands assigned for RFIDs; this incorporates frequency reconfigurability into the system. In addition to the multiband switching ability, it will be fascinating to design a antenna which facilitates both the near- and the far- field operations for a multi-purpose use. This would lead to a multi-purpose near- far-field switched multiband reader antennas for RFID applications.

In this regard, two switched multiband antennas are investigated in this chapter. First, in Section 6.1, a dual-band antenna which evolves form the previously optimized single band NDTC antenna (Chapters 3, 4) is designed and successively in Section 6.2, a novel dual-purpose near- and far-field tri-band reader antenna for RFID applications is proposed and presented.

## 6.1 Switchable dual-band NDTC antenna

Several dual-band RFID antennas have been reported in the literature and reviewed in Chapter 1. For instance, the one presented in [74] was designed to operate in near-field at HF (13.56MHz) and far-field at UHF (920MHz). However, the one reported in [94] benefits from a previously optimized near-field performance at HF. To maximize the  $H$  using multi-turn coil antenna, the NDTC design [90] at HF has already been presented in Chapters 3, 4. The design [94] investigated in this section evolved from NDTC antenna to operate at 13.56MHz in near-field or 866.6MHz in far-field and switches between two frequencies of operation using two Micro ElectroMechanical System (MEMS) switches. To evaluate the switched dual-band operation, the design is simulated using ideal switch model as well as equivalent circuit model. The initial NDTC antenna with incorporated switches yields robust reactive and radiated performance, leading to a dual-band near-far-field antenna in a single unit; this is subsequently presented.

### 6.1.1 Design description of dual-band NDTC antenna

Similar to the NDTC antenna of Section 3.3.5, the switched dual-band NDTC (DB-NDTC) antenna was defined by a radius vector  $\mathbf{A} = [a_1, a_2, a_3, a_4, a_5]$  where  $a_i$  is the radius of  $i^{th}$  turn of the coil as shown in Fig. 6.1. The radiative elements were etched on a double-sided printed circuit board (PCB) of copper (50microns) and substrate(FR4 with  $E_r = 4.8$  and  $\tan\delta = 0.02$ ) having thickness  $h = 0.8$  mm. The front surface (printed turns) of the PCB lies in x-y plane with the center of the printed coils coinciding with the origin.

To obtain multiband operation, two switches, SW1 and SW2, with position parameters  $\theta_1$  and  $d_1$  respectively, are incorporated within the design as shown in Fig. 6.1. Depending on the states (ON or OFF) of SW1 and SW2, the antenna switches its frequency of operation to one out the two bands. The switching states with correspondingly selected bands are listed in Table 6.1 and detailed in subsequent section.

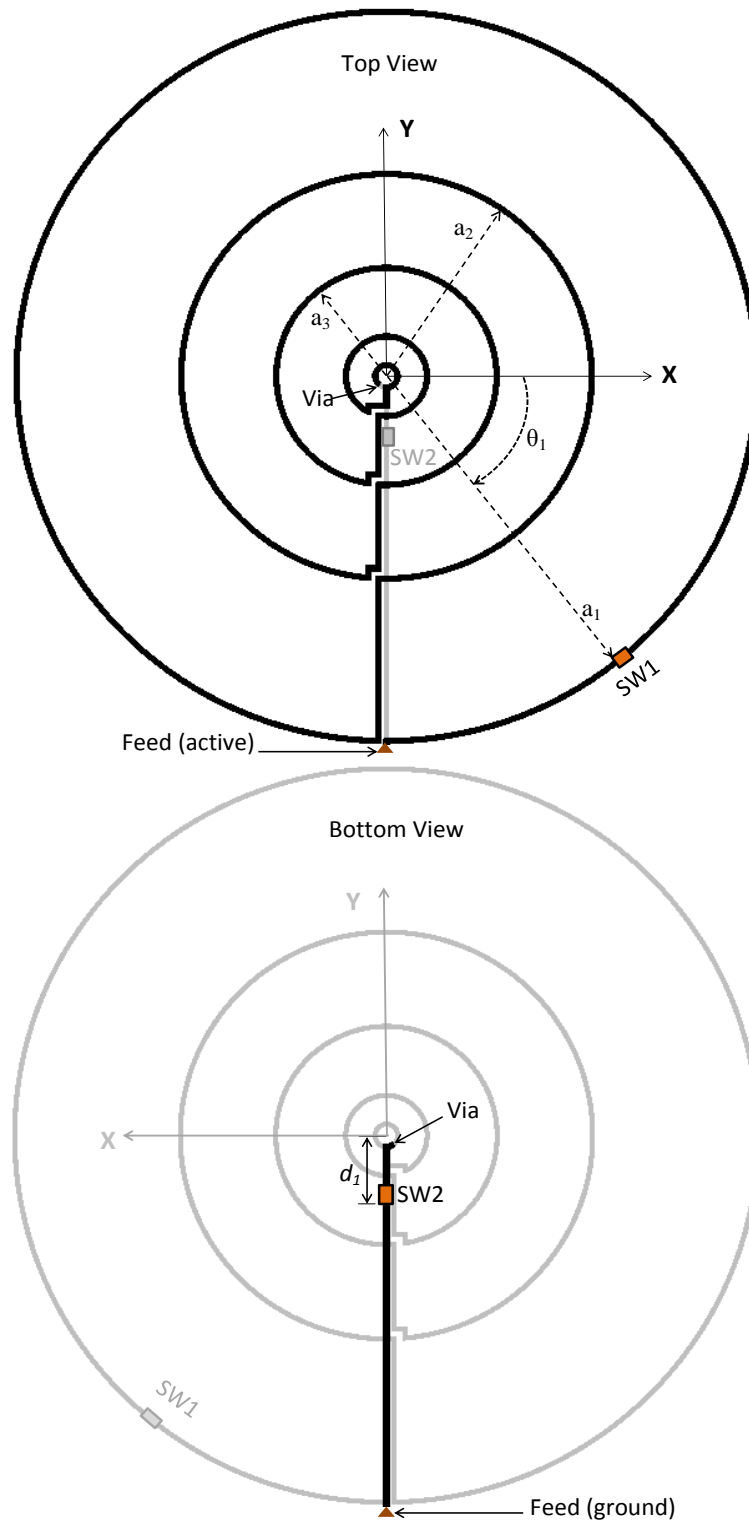


FIGURE 6.1: The switched DB-NDTC antenna.

TABLE 6.1: The DB-NDTC antenna switching

State: band	SW1	SW2
State-1: HF	ON	ON
State-2: UHF	OFF	OFF

### 6.1.1.1 State-1: Near-Field HF band

The State-1 of the switches in Table 6.1, essentially, defines the DB-NDTC antenna as a NDTC antenna which was designed for near-field at operational frequency  $f_1 = 13.56\text{MHz}$  and optimized for a read range of  $D = 0.05\text{m}$  and  $Q = 33.16$ , having resultant optimal radii  $\mathbf{A} = [70.7, 39.0, 20.7, 7.3, 1.7]$  mm. The equivalent circuit model of the coil and the matching network has been presented in Fig. 3.5; the coil had inductance  $L$ , resistance  $R$ , and matched using L-matching network made of lumped capacitances C1 and C2. The capacitors were selected to resonate the coil at 13.56 MHz.

### 6.1.1.2 State-2: Far-field UHF band

The State-2 of the antenna in Table 6.1 corresponds to the UHF band where the DB-NDTC antenna is designed to perform in the far-field at operational frequency  $f_2 = 866.6\text{ MHz}$ . The switch position parameters ( $\theta_1$  and  $d_1$ ) of SW1 and SW2 are optimized using Zeland IE3D to match the antenna to  $50\Omega$  at  $f_2$ ; this gives  $\theta_1 = 49.2^\circ$  and  $d_1 = 17\text{mm}$ . The final design of the DB-NDTC is depicted in Fig. 6.1.

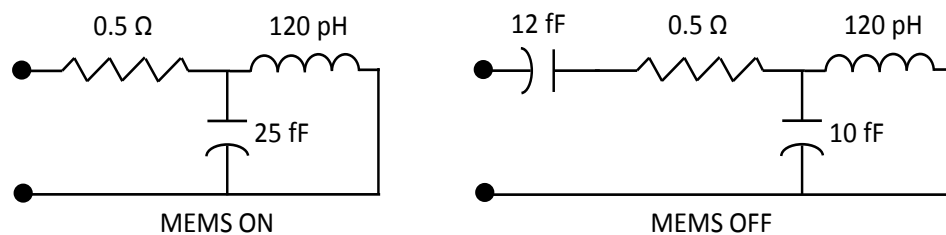


FIGURE 6.2: MEMS equivalent circuit model for ON-OFF states.

### 6.1.2 RF MEMS switch modeling

For simulating the switches incorporated in the designs, we have considered two equivalent switch models: 1) ideal switch model 2) MEMS equivalent circuit model. In the ideal switch model, the OFF state of the switch is represented by an open circuited (no metal) line, whereas, the ON state of the switch is represented by a short circuited (galvanic connection with metal strip) line. This represents the simplest switch model which can be considered. In contrast, the MEMS equivalent circuit model is sophisticated and includes switch's internal capacitance/reactance in the simulations; this is done by using equivalent circuits with lumped LCR elements. In this study we adopted a MEMS equivalent circuit model reported in [95], and redrawn the ON and OFF states in Fig. 6.2. Considering these two switch models in the simulations, the DB-NDTC is simulated using Zeland IE3D and results are presented in the next section.

### 6.1.3 Simulation and measurement: Results

#### 6.1.3.1 State-1: Near-Field HF band

When the switches were in configuration of State-1, the DB-NDTC was measured for  $R$ ,  $L$ , and  $Q$  using a mini probe (Agilent 42941A Impedance Probe Kit) and a precision impedance analyzer (Agilent 4294A). The values measured were  $R = 3.89\Omega$  and  $L = 1.47\mu H$  at  $f_1$ . The  $Q$  of the stand-alone coil antenna (without the matching network) was measured at the  $f_1$  and found to be 31.16 and 32.16, simulated and measured, respectively. The deviation between the measured and predicted results can be attributed to manufacturing tolerances. The measured  $R$  and  $L$  at the  $f_1$  were used to calculate the required  $C1 = 63.38\text{pF}$  and  $C2 = 25.72\text{pF}$  and the most appropriate commercially available SMD capacitors  $C1 = 68\text{pF}$  and  $C2 = 27\text{pF}$  were chosen.

Once the DB-NDTC antenna switched into State-1 and ready to be simulated and measured, the  $S_{11}$  responses are gathered. The DB-NDTC antenna was simulated

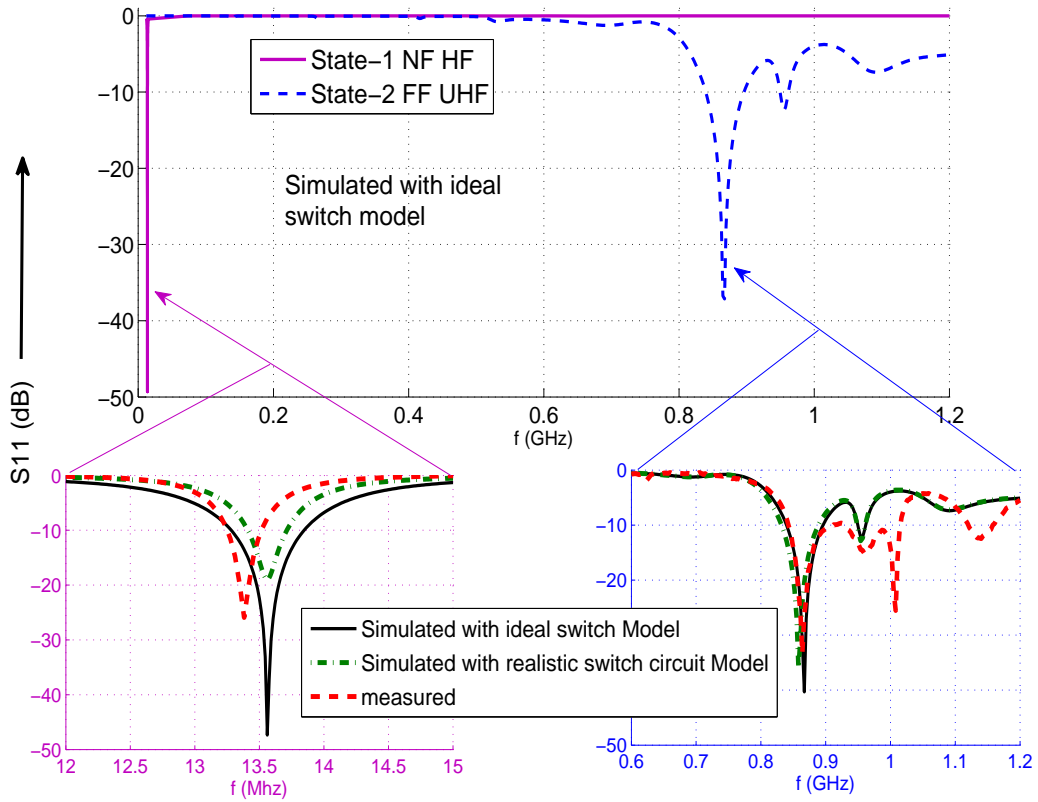


FIGURE 6.3: Simulated and measured S11 of the switched DB-NDTC antenna.

with both the ideal switch model and the equivalent switch models as described in Section 6.1.2, in addition, the fabricated antenna was measured. All the corresponding S11 responses are shown in Fig. 6.3 where a zoomed version of the plot is also shown in inset for clarity. By observations we see that, using both switch models in simulations, the antenna resonates around  $f_1$ , however, realistic switch model shows a degraded return loss performance, but that is acceptable. Whereas, the measured S11 shows a deviation from  $f_1$  due to manufacturing tolerance, which can be mitigated by adjustments during fabrication process.

The  $H$  of the DB-NDTC in State-1 were measured in an anechoic chamber using a near-field probe (ETS-Lindgren's Model 7405 Set) which was placed at a distance  $D = 5\text{cm}$  above the coil. A signal generator (R&S SM300) was connected to the coil and sent a sine wave signal of 9.2 mV peak at  $f_1$ . The  $H$  of the coil antenna at was measured to be 1.817A/m which is a sufficiently large value to read the tags from a distance  $D$ .

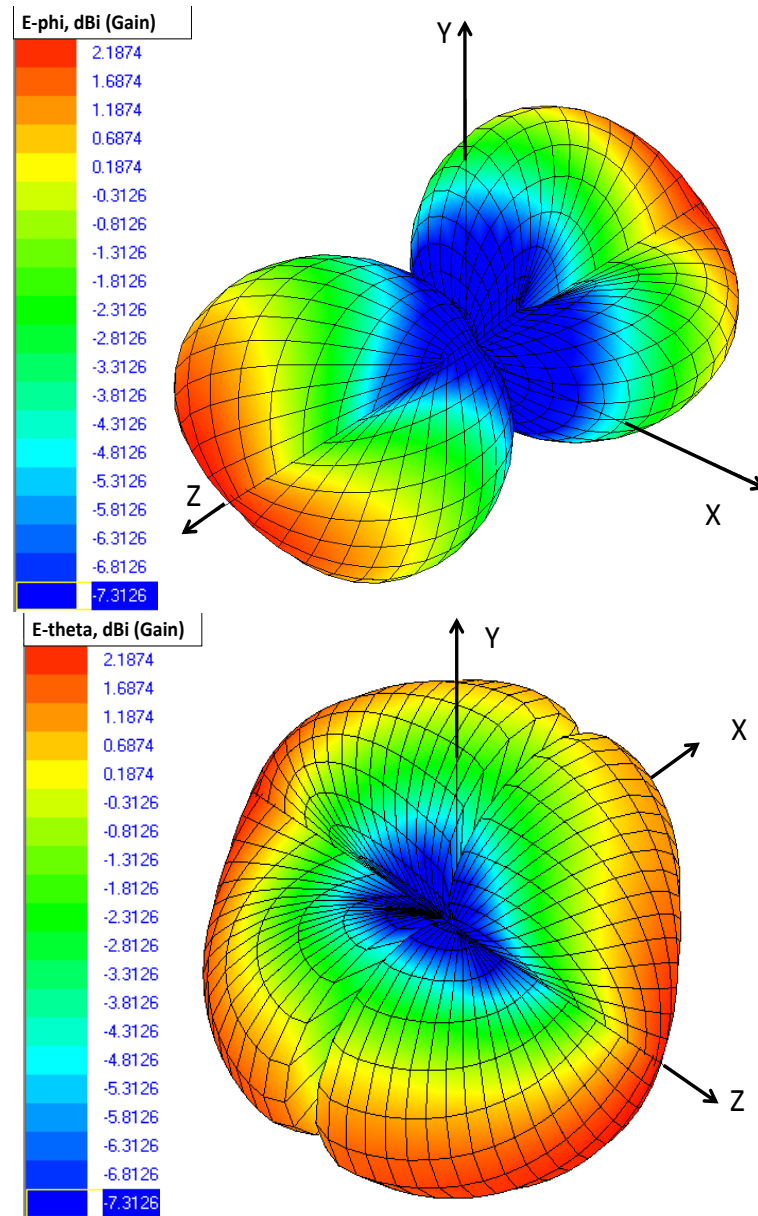


FIGURE 6.4: Simulated radiation pattern of the switched DB-NDTC antenna.

### 6.1.3.2 State-2: Far-field UHF-band

In State-2 of the switches, the DB-NDTC was simulated using two switch models, and corresponding S11 plots are depicted in Fig. 6.3. It is observed that the antenna resonated around  $f_2$  without significant deviation. Moreover, the measured S11 response is included in the figure and matches with the simulations with insignificant deviation. By calculation from Fig. 6.3, the 10dB (return loss) bandwidth of the antenna is 54.7MHz (841.2-895.9MHz) which includes UHF RFID band 865.6-867.6 MHz in Europe. To assess far-field performance, the simulated

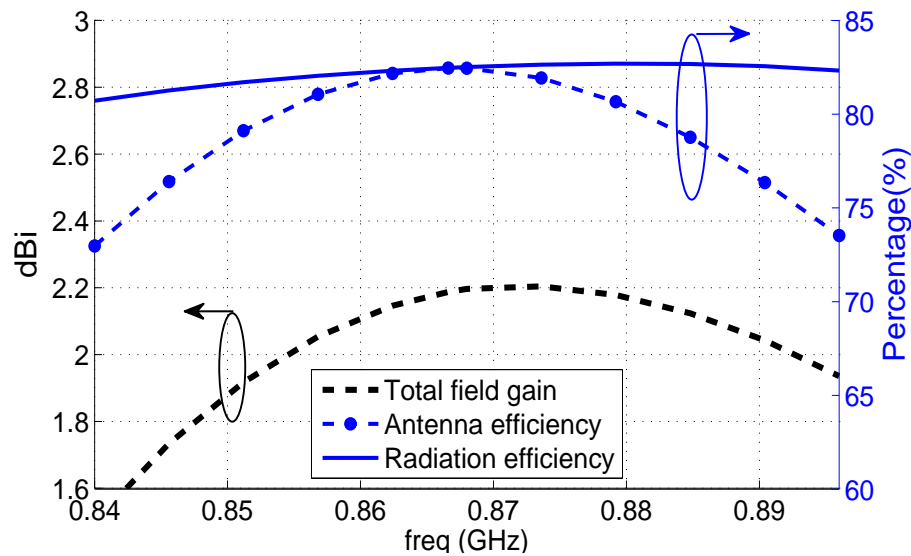


FIGURE 6.5: Simulated efficiency and gain of the switched DB-NDTC antenna.

far-field radiation patterns are shown in Fig. 6.4 while the efficiency and gain are plotted against frequency in Fig. 6.5. The simulated far-field results showed that the DB-NDTC antenna switched into state-2 had a gain of  $\sim 2.2$  dBi, and an efficiency of  $\sim 82.5\%$  at  $f_2$ , with relatively wide E-total coverage.

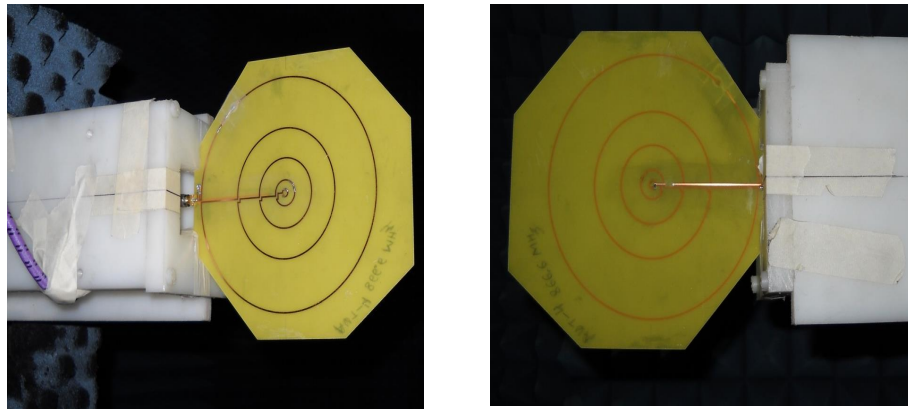


FIGURE 6.6: Fabricated switched DB-NDTC antenna in anechoic chamber.

To support the results produced by far-field simulations, the fabricated DB-NDTC antenna while switched into State-2 was measured in an anechoic chamber as shown in Fig. 6.6. In ideal switch model was replicated on the fabricated antenna, and the far-field radiation patterns were measured at 866.6 MHz. The measured radiation pattern of the DB-NDTC are shown in Fig. 6.7 where normalized gain in E-plane and H-plane are plotted in both vertical and horizontal polarization of

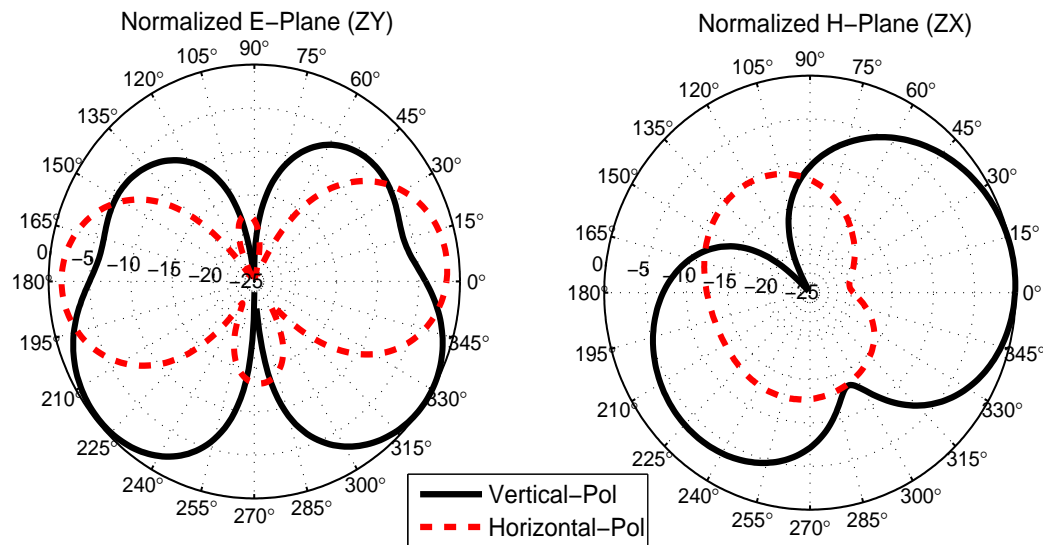


FIGURE 6.7: Measured radiation pattern of the switched DB-NDTC antenna.

tags. The maximum gain measured was  $\sim 2.71$  dBi at  $f_2$  which corroborated the simulation results.

The simulated and measured results showed a highly efficient near- (at HF) and far- (at UHF) field antenna with switching capability for dual band operation, this encourages the use of switched DB-NDTC antenna in dual-purpose RFID applications.

## 6.2 Multi-purpose switched multi-band antenna

In previous section, we have investigated a switched dual-band coil antenna working in near-field at HF and far-field at UHF. Low-cost multipurpose antennas having both near-field and far-field operations in their respective frequency of operation and capable of switching between the operating frequencies of a multi-band design is very attractive. For this, a switched multi-band antenna is realized in this section. The proposed antenna is designed to switch its operating frequency between 915 MHz, 2.45 GHz, and 5.8 GHz using RF switches which leads to a multi purpose near- and far-field antenna. The proposed antenna, which is etched on a single-sided PCB, incorporates four RF switches to reconfigure the resonance

frequency of the antenna. The simulated results will show the H-field (NF) and radiation pattern (FF) generated at each switching state of the antenna to prove the usefulness of the design for NF and FF RFID applications.

Essentially, the antenna investigated in this section, will be shown to include bands at center frequencies 354MHz (348-360MHz) and 915MHz (900-930MHz) and 2.45GHz (2.42-2.49GHz) and 3.72GHz (3.5-3.93GHz) and 5.8GHz (5.59-5.93GHz), for a penta-band antenna realization. However, since in this study we are concentrating only on reader antennas for RFID applications, therefore, only three bands 915MHz, 2.45GHz, and 5.8GHz, which has been reported in the literature for RFID applications will be considered in the analysis presented subsequently.

### 6.2.1 Design of a switched multi-band antenna

The switched multiband NF-FF antenna was designed by incorporating a coil with non-uniformly distributed turns as shown in Fig. 6.8. The radiative elements were etched on a single-sided PCB of copper (50microns) and substrate (FR4 with  $E_r = 4.8$  and  $\tan\delta = .02$ ) having thickness  $h = 0.8$  mm, maximum size of the antenna is  $98 \times 98 \times 0.8$  mm<sup>3</sup>. The front surface (printed turns) of the PCB lies in x-y plane with its center at the origin and printed with a strip width 0.25 mm and height 0.002 mm. The antenna was optimized using CST MW studio software and consisting of three turns with radii 47.6mm, 14.8mm, and 7.0mm to achieve targeted three frequency resonances which can be switched using four RF switches SW1-4. The chip resistances shown in Fig. 6.8 are selected to resonate the antenna at desired frequencies. Depending on the states (ON or OFF) of SW1-4, the antenna operation is switched between the three bands. The switching states along with correspondingly selected modes are detailed in Table 6.2 and described subsequently.

The antenna is fed at the center as shown in the Fig. 6.8. We first describe the operation in mode-3 which is selected when SW1 and SW2 are OFF. This means that the inner most turn will no longer be in contact with other outer

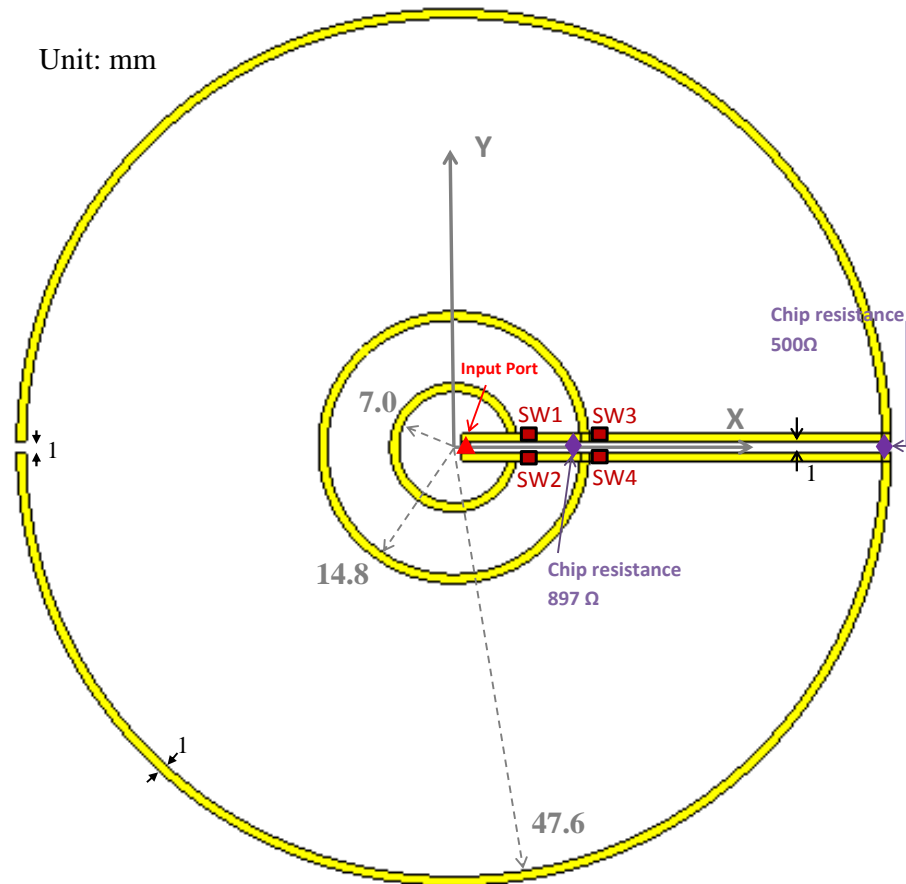


FIGURE 6.8: Multipurpose switched multiband antenna.

turns, therefore, the smallest active element shows resonance at higher frequency and the antenna resonates at 5.8GHz. Since circular loop design produces robust reactive field in the near-field zone, the choice for this design is justified. The circular loop provides a sufficient  $H$  for inductive coupling between the reader and the tag coils in near-field region. In mode-2, when SW1, SW2 are ON and SW3, SW4 are OFF, the innermost turn connects with the middle turn but outermost turn is still disconnected, the antenna resonance switches to 2.45GHz, in this case both the inner turns will contribute to near-field  $H$  as well as far-field radiations. In mode-1, when all the switches are ON, all the three turns get connected and contribute to near-field  $H$  and far-field radiation, and the antenna's resonating frequency switches to 915MHz. For mode-1, the largest turn is divided by a cut of 1mm in left side to achieve the highest area of the coil (for a maximum reading area) while maintaining the uni-directional circulation of the currents.

TABLE 6.2: Switching modes of multi-band antenna

mode: band	SW1	SW2	SW3	SW4
mode-1: 915 MHz	ON	ON	ON	ON
mode-2: 2.45 GHz	ON	ON	OFF	OFF
mode-3: 5.80 GHz	OFF	OFF	OFF	OFF

### 6.3 UHF antenna fabrication and measurements

The antenna were fabricated and shown in Fig. 6.9(a). The coils are etched on an FR4 substrate of thickness,  $h = 0.8\text{mm}$ , relative dielectric constant  $\epsilon_r = 4.4$ , and loss tangent  $\tan\delta = 0.02$ . The coil lies in the x-y plane with its center at the coordinate origin and consists of copper tracks of width  $d = 1\text{mm}$ . To measure the

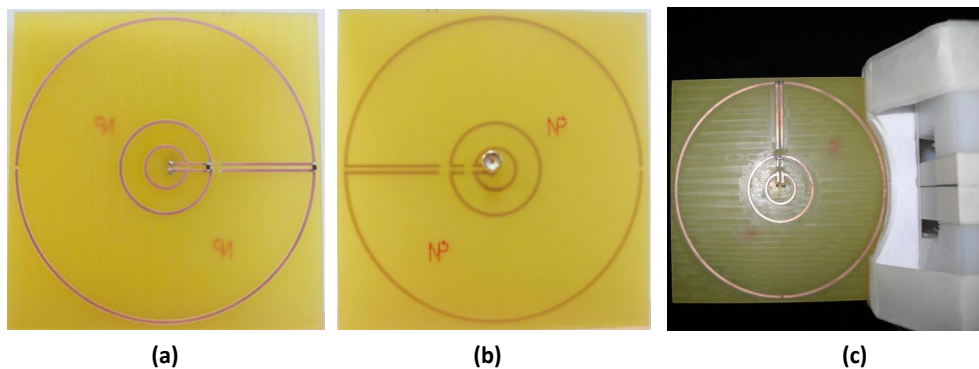


FIGURE 6.9: Fabricated antenna a) front b) back c) in anechoic chamber

reflection coefficient ( $S_{11}$ ) of the antenna, an Agilent PNA-X Network Analyzer (connectors and cables appropriately calibrated) was used. The  $S_{11}$  responses are included in Fig. 6.10 for comparisons.

#### 6.3.1 Results

In this section, the antenna presented in Fig. 6.8 is simulated using CST MW studio. We have considered only ideal switch model for simulating the antenna, where the OFF state is represented by an open circuit (no metal) and the ON state by a short circuit (galvanic connection with metal strip). The antenna performance is evaluated in each mode of operation and simulated  $S_{11}$  responses are shown in

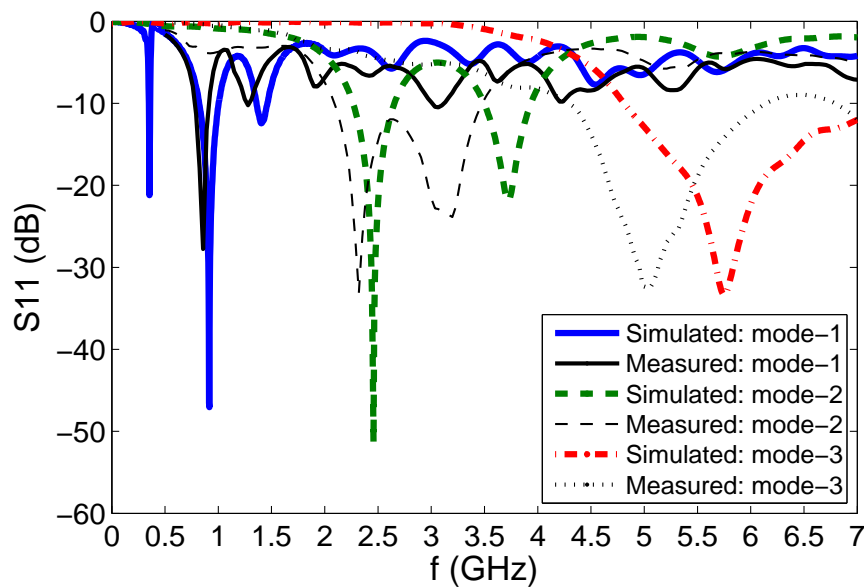


FIGURE 6.10: S11 of the switched multiband antenna.

Fig. 6.10. As apparent from figure, the antenna resonates around 915MHz in mode-1, 2.45GHz in mode-2, and 5.8GHz in mode-3 achieving targeted RFID frequencies. The bandwidth corresponding to 25dB return loss is 30MHz (900-930MHz) in mode-1, 70MHz (2.42-2.49GHz) in mode-2, and 340MHz (5.59-5.93GHz) in mode-3. The deviation of S11 responses from operating frequency can be attributed to manufacturing tolerances.

For each mode, the antenna is simulated to evaluate  $H_z$  ( $z$ -component of  $H$ ) in the near-field and radiation pattern in the far-field, the results are subsequently presented.

### 6.3.1.1 mode-1: UHF 915 MHz near- and far-field results

In mode-1, all the three turns composing the antenna get connected and antenna resonates around 915MHz. The current distribution in the antenna at 915MHz is depicted in Fig. 6.11. At 915MHz, the largest turn has a perimeter of the order of one wavelength, therefore, no current inversions are observed and a unidirectional current flow is observed given the cut introduced in the outer turn of the design. The clock-wise current flow in all the three turns favors a robust near-field reactive

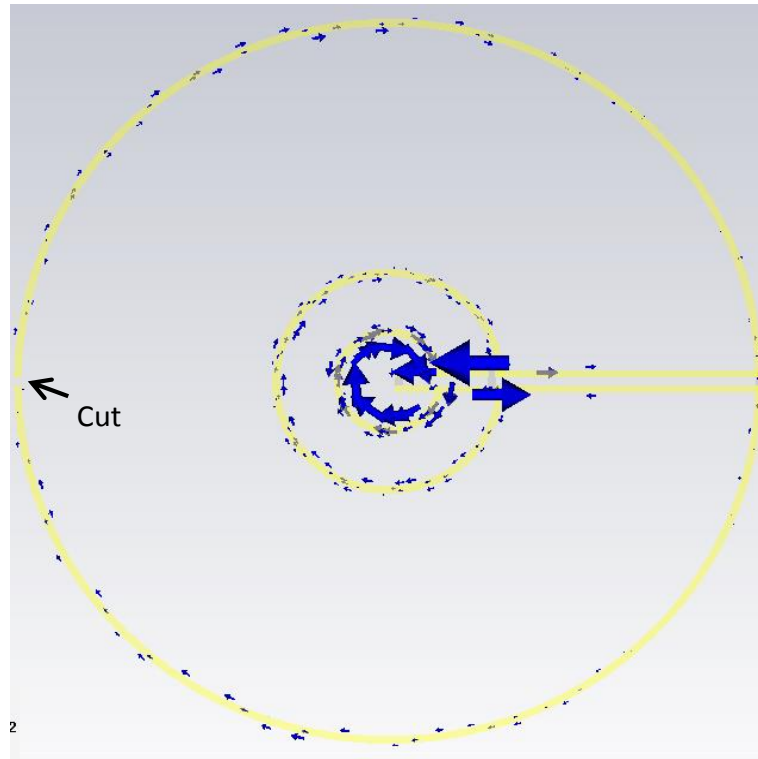


FIGURE 6.11: Simulated current at 915MHz in switching mode-1.

energy and a contributing  $H_z$ . The simulated  $H_z$  distribution of the antenna at 915MHz is shown in Fig. 6.12(i) which was captured at  $z=10\text{mm}$  plane. A peak magnitude 1.12 A/m of  $H_z$  is observed. This corroborates that the designed antenna produces effective reactive field in the near-field zone of the antenna, and hence, suitable for interrogating the magnetically coupled Tags; this encourages the antenna to be used for the near-field RFID applications for 915 MHz.

To assess FF performance, the radiation patterns are evaluated in both the planes, Azimuth and Elevation. The polar plots of simulated E-theta and E-phi in azimuth and elevation cuts are depicted in Fig. 6.12(ii). The results show that the proposed antenna in mode-1 has a maximum gain of  $\sim 1\text{dBi}$  in elevation plane at 915MHz. A relatively wide E-total coverage was observed indicating a potential for interrogation of tags in any direction allowing additionally the use of the proposed antenna for far-field RFID applications at UHF.

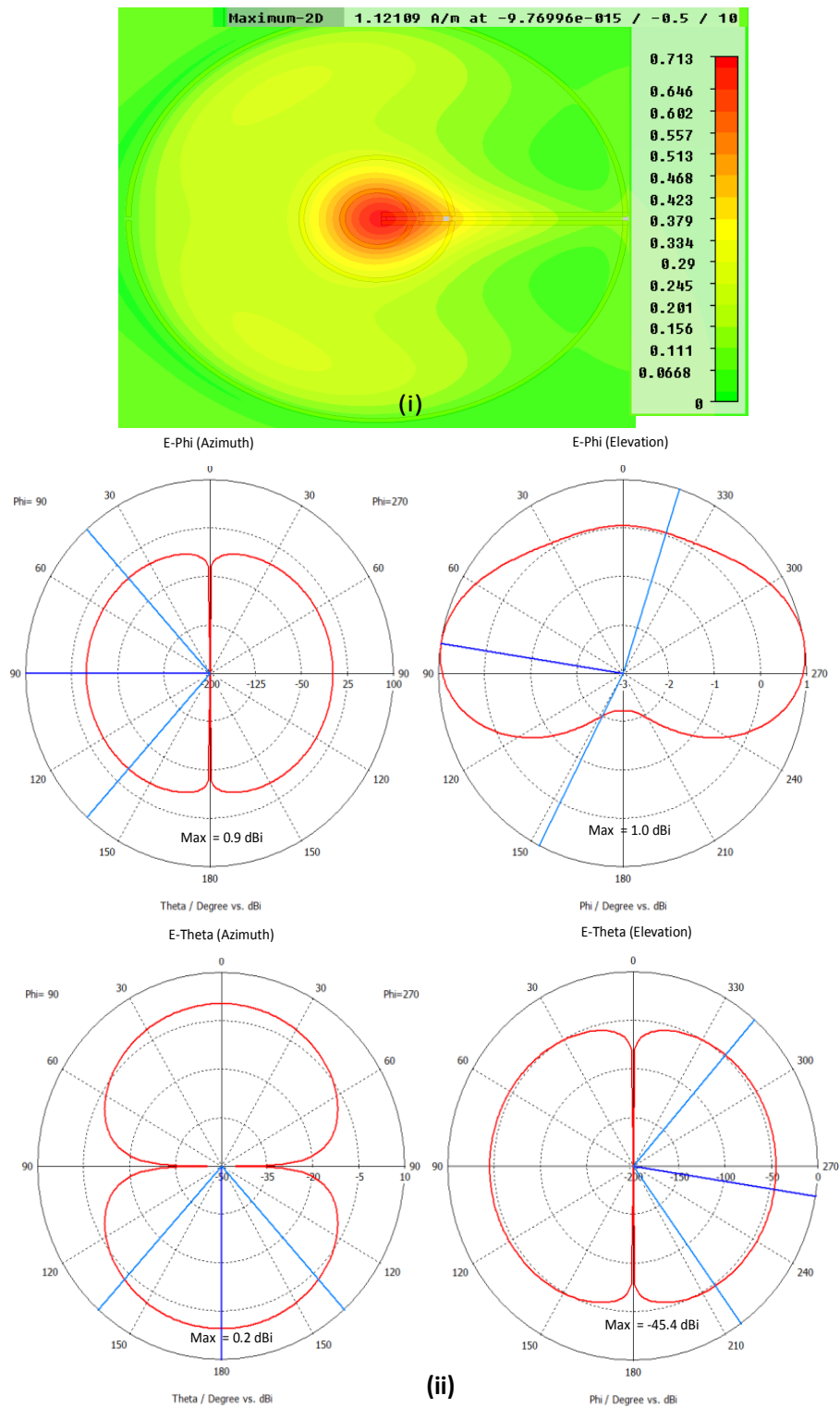


FIGURE 6.12: mode-1: (i) simulated  $H_z$  in near-field (ii) far-field radiation patterns at 915MHz.

### 6.3.1.2 mode-2: 2.45GHz near- and far-field results

In mode-2, the antenna is simulated at 2.45GHz for its current distribution, near-field and far-field evaluation. The current distribution of the antenna is shown in Fig. 6.13. As apparent from this figure, since only two inner turns are con-

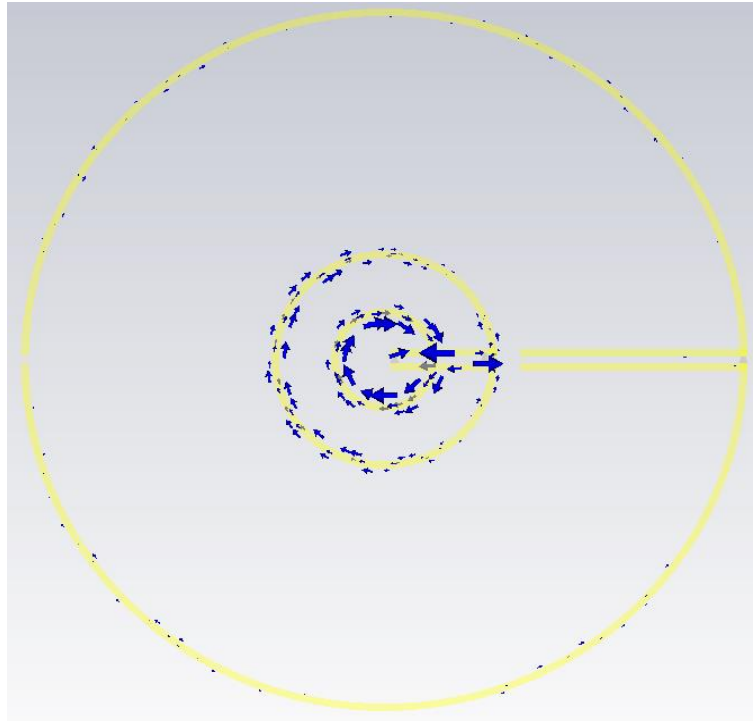


FIGURE 6.13: Simulated current at 2.45GHz in switching mode-2.

nected to feed, currents mostly flow in those two inner turns only, and contribute to  $H_z$  dominantly; the outermost turn has negligible currents to affect the  $H_z$  in near-field. Moreover, since the perimeter of the second turn is of the order of wavelength at 2.45GHz, the current flows in same direction throughout its perimeter. A clock-wise circulation of currents was observed in the two inner-turns, therefore, contributing to the resultant  $H_z$  in the near-field zone. Fig. 6.14(i) shows the simulated  $H_z$  distribution of the antenna in the  $z=10\text{mm}$  plane, where the maximum  $H_z$  magnitude is 0.82 A/m. This shows that the antenna is suitable for near-field reader RFID applications at 2.45GHz.

The FF simulation of the antenna at 2.45GHz in mode-2 is performed to evaluate the radiation patterns in azimuth and elevation planes and shown in Fig. 6.14(ii).

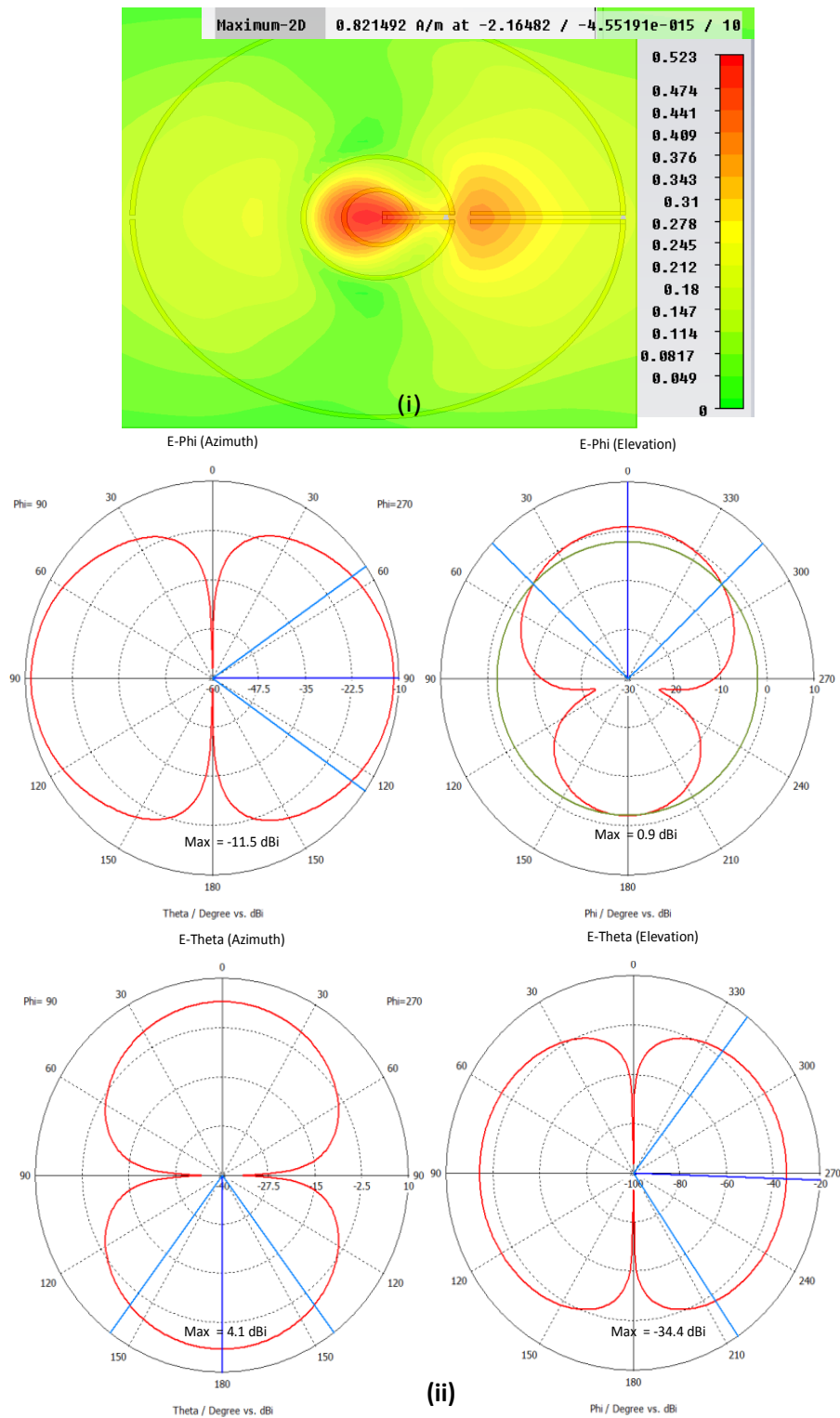


FIGURE 6.14: mode-2: (i) simulated  $H_z$  in near-field (ii) far-field radiation patterns at 2.45MHz.

It can be observed from the results that the proposed antenna has relatively wide E-total coverage for the tags to be read from any direction. Moreover, a maximum gain of  $\sim 4.1$  dBi in azimuth plane is observed, thereby, a high gain performance

for the use in far-field RFID application is justified.

### 6.3.1.3 mode-3: 5.8GHz near- and far-field results

Similarly, the proposed design in mode-3 is simulated at 5.8GHz. The current distribution of the antenna is shown in Fig. 6.15, which shows that the inner turn has

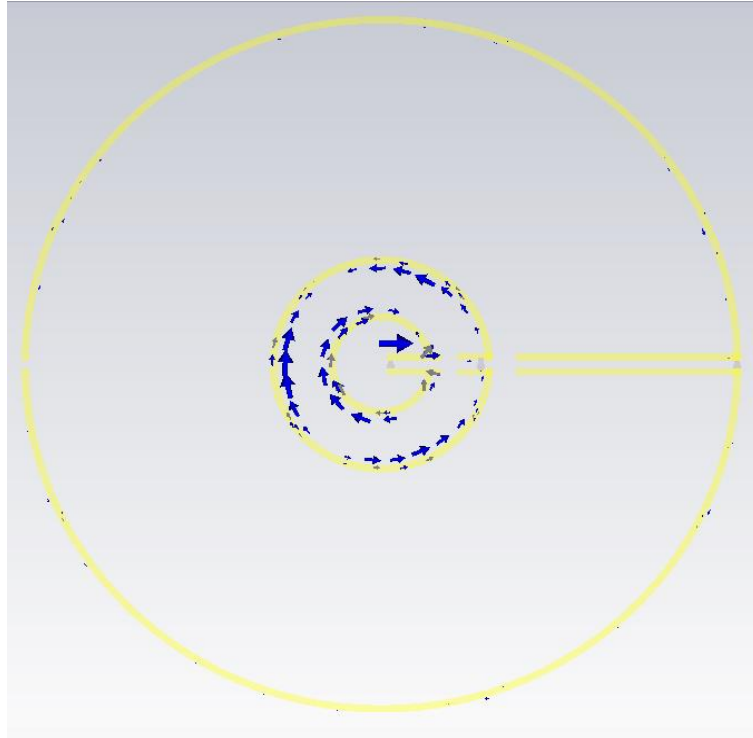


FIGURE 6.15: Simulated current at 5.8GHz in switching mode-3.

a clock-wise circulation of currents to contribute towards near-field  $H_z$ . In contrast, since the middle turn perimeter is electrically large, it has induced currents which are non-uniform with certain nulls; this is non-supporting a enhanced  $H_z$ . Although the induced currents in the middle turn are unfavorable for near-field, it can favor far-field radiation gain and the inner turn current flow shows dominant effects in  $H_z$ . The  $H_z$  distribution of the antenna in the  $z=10\text{mm}$  plane is shown in Fig. 6.16(i) and maximum achieved  $H_z$  has magnitude 0.98 A/m. Therefore, the proposed antenna can be used for near-field RFID applications at 5.8GHz additionally.

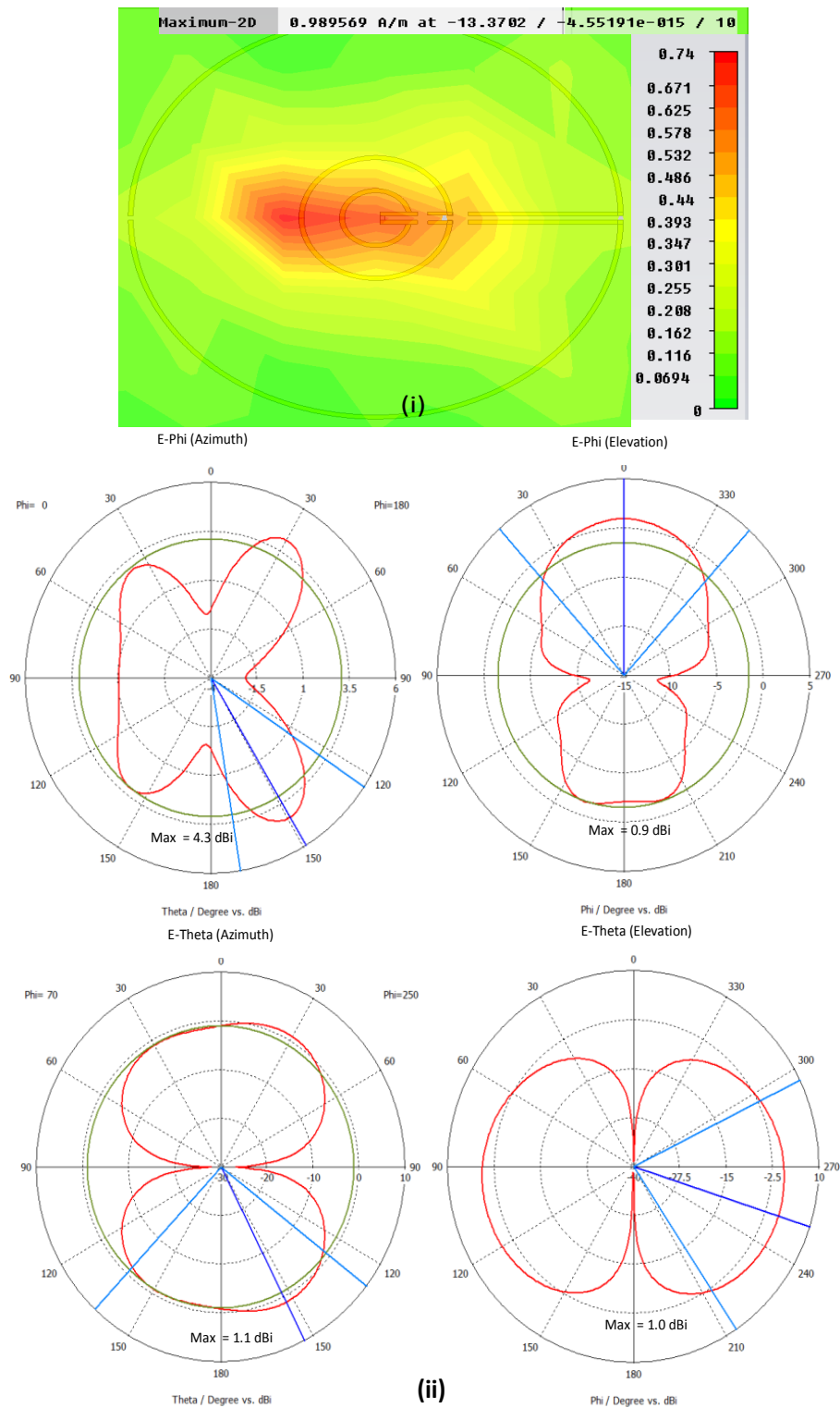


FIGURE 6.16: mode-3: (i) simulated  $H_z$  in near-field (ii) far-field radiation patterns at 5.8GHz.

For the antenna in mode-3, the simulated FF radiation patterns at 5.8GHz of the E-theta and E-phi are presented in Fig. 6.16(ii). The results show an encouraging gain of  $\sim 4.3$  dBi in azimuth plane and corroborate the additional applicability of

the proposed antenna for far-field RFIDs at 5.8GHz applications.

## 6.4 Summary

In this chapter, we have investigated, designed and presented multiband antennas with frequency switching ability and suitable for near- and far-field RFID applications. Various frequency bands have been adopted in the literature for RFID as well as for either a near-field or a far-field. The near-field antennas are aimed to produce sufficient magnetic field  $H$  because the working principle of the system is based on inductive coupling, whereas, the far-field antennas are aimed for high gains and wide radiation patterns so that it can read tags from any direction. For the accomplishment the following antennas were proposed.

First, a switched Dual-Band NDTC (DB-NDTC) antenna [94] was presented; this antenna was optimized to function for near-field in HF and far-field in UHF. These two modes of operations were switched by using two MEMS switches; while both the switches ON, the DB-NDTC antenna maintained all the features of the HF NDTC design [90] and a robust magnetic-field ( $H$ ) in the interrogation zone, while both switches OFF, the DB-NDTC antenna operational frequency shifts to UHF and provided a far-field radiation. The presented antenna is of interest for RFID applications where a greater coverage (extended interrogation zones) is sought. Simulations validated the design and measurements supported the argument.

Second, a multi-purpose switched multiband antenna used for near- and far-field RFID applications was presented. The antenna incorporated frequency reconfigurability by switching between three frequency bands of RFID using four RF switches. Depending upon the states of the switches, one out of three modes-1-3 of operation was selected with corresponding resonating frequency 915MHz, 2.45GHz, and 5.8GHz, respectively. The circular loop shape adopted in the design supported effective generation of reactive field (H-field,  $H_z$ ) in the interrogation zone; this works for near-field RFID applications. Whereas, non-uniform currents along the loop advantageously resulted in far-field radiation making the antenna

suitable for far-field RFID applications. The claims were supported by the simulations which showed a decent  $H_z$  achieved in the near-field zone and radiation gain in the far-field zone for all the three frequency modes of operation. This demonstrates the suitability of the proposed antenna for RFID applications willing to exploit multiple zones (near- and far-field) and multiband behavior using frequency reconfigurability (switching technology).

## 6.5 Chapter related publications

- **A. Sharma**, I. J. Garcia Zuazola, J. C. Batchelor, and A. Perallos, “Switched Non-uniformly Distributed-Turns Coil Antenna for Dual-band operation”, *in 9th European Conference on Antennas and Propagation (EuCAP)*, Lisbon, Portugal, April 2015, pp. 1-4.
- **A. Sharma**, I. J. Garcia Zuazola, J. C. Batchelor, and A. Perallos, “Multi-purpose near- far-field switched multiband coil antenna for 915MHz/2.45/5.8GHz RFIDs,” *shall be communicated in IEEE Journal*, 2015.



# Chapter 7

## Applications

This chapter presents three novel applications of antennas; although the antennas might not be exactly those reported in preceding chapters, these application concepts can be generalized to all. First application investigates the possibility of attaining a highly focused field in the NF region of 5.8GHz RFID. Second application uses current ink-jet printing technology for antenna fabrication and reports a RFID Tag antenna developed using conducting ink sprayed over food/beverage can. Third application investigates a novel technique for the possibility of achieving a highly efficient antenna for in-car wireless communications.

### 7.1 Near-field focusing for RFID applications

RFID technology has well emerged for the applications of tracking, packaging, intelligent transport, and authentication and management systems. For instance, for assets identification in conveyor belts, the reader antenna is desired to be well focused in the near-field region with low Side-Lobe-Levels (SLL) [41, 42]. A highly focused antenna results in high gain with increased efficiency of the reader and the low SLLs are welcomed for accuracy and reduced cross-talk systems. To achieve this, an array specifically designed for Near-Field Focusing (NF-F) can be the choice [43, 49, 96–100]. By adjusting the corresponding phases of the array

elements, the NF-F effect can be obtained, this means forcing radiated fields of every element to contribute constructively at the focus. The array elements can be printed as microstrips with corresponding feeding-network for the excitation of every element [96–98].

A focus agile (tunes/re-configures the focal distance) antenna can empower RFID systems with rapid reconfigurability of the energy confinement of a reader. The focus agility in rectangularly-configured arrays [43] was performed by having adequate phase shifts per array element, but since several phase shifters (one for each element) are required, it results into a highly complex feeding network. In contrast, a circularly-configured array [45, 101] shows reduced complexity, because of the circular distribution of the array elements, the array elements belonging to the same circle will be equidistant from the focus, and therefore, just one phase shifter per circle is required.

Following this idea, a Near-Field Focused Circular Array (NF-FCA) antenna for 5.8GHz RFID reader applications was proposed in [45]. The NF-FCA is made of 24 array elements distributed along the periphery of 3 co-centric circles (8 elements per circle), and uses planar printed dipoles as radiating elements which are preferred due to their mathematical tractability. The corresponding phases of circles are adjusted to confine the radiating energy at the focus. The array whose dipole element orientations (direction of the current flow with respect to the center of the array) are aligned radially will be validated using vector projections in Section 7.1.1.1 and used as the base for the studies; this is termed as initial design.

The Electric fields (E-fields) generated by every dipole are modeled analytically in a 3-D coordinate system. Using this model, we compute the beneficial contribution of E-field vectors at the focus for several dipole orientations (only 2 cases of dipole orientation will be presented for brevity, the radial and the co-linear [102]), and the constructive effect of the resulted E-field magnitude will be given. It will be shown that although the E-fields from radially oriented dipoles [45] combine at the focus constructively, they spread in 3-D near the focus and are some what likely to

cancel each other showing a drawback. As a result, the total E-field magnitude is not maximized and a final design proposed in [102] is constructed and optimized for enhancement. This is performed by reorienting the printed dipoles adequately for maximum E-field response, and redefining the internal circle radii to control SLL. This yields an improved energy confinement at the focus using the latter design compared to the initial design.

### 7.1.1 The optimization process using vector projections

Vector projections in a 3-D coordinate system are used to model the NF-FCA antenna as reported in [102]. The vector projections are used for the optimal estimation of the focalization and the resultant E-field magnitude from the array antenna when adequate dipole orientations are found. The possible vector projections in the 3-D coordinate system is given in Fig. 7.1(a). We use planar-printed half wavelength dipoles for the array antenna; adequate phases are selected for the constructive E-fields. The antenna-array plane is denoted in Fig. 7.1(a) by the X-Y plane, and the location of focus by the Z-axis with coordinates  $(0, 0, F)$ . The array is made of  $C$  concentric circular rows (circles) of radii  $R^v, \forall v \in [1, C]$ , where a number,  $N$ , of dipoles are distributed per circle. Hence, the array is made of total  $NC$  dipoles. For the phased-array analysis and the individual E-fields that originate from dipoles, we will show how the antenna system is modeled in 3-D using vector projections on coordinates X, Y, and Z and respective unit vectors  $\hat{x}$ ,  $\hat{y}$ , and  $\hat{z}$ .

#### 7.1.1.1 Customized 3-D vector projection analytical model

In this section, the final contribution of the individual E-fields out of each element of the NF-FCA is modeled and we use 3-D vectors to represent the possible rays launched by the antenna, Fig. 7.1. The spacial location of a dipole  $u$  in a circle  $v$  is denoted by a vector  $\vec{S}_u^v$  and mathematically given by:

$$\vec{S}_u^v = (R^v \cos \phi_u) \hat{x} + (R^v \sin \phi_u) \hat{y} + 0\hat{z}, \quad (7.1)$$

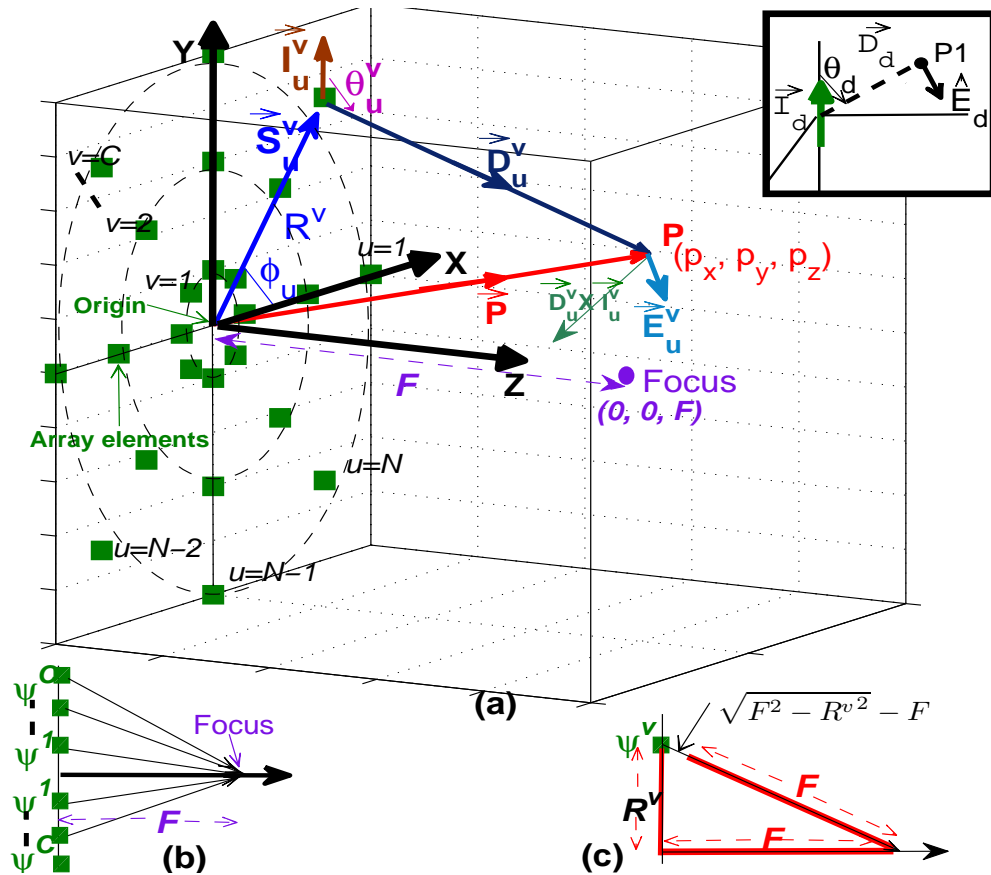


FIGURE 7.1: (a) The NF-FCA antenna E-field vector projections in a 3-D rectangular coordinate system. (b) A 2-D representation of the array elements (phases  $\psi$ ) in regard to the focus and (c) Geometric evaluation of the  $\psi^v$  corresponding to a circle  $v$ .

where  $u \in [1, N]$ ;  $v \in [1, C]$ , and  $\phi_u$  is the angular position of dipole  $u$  with respect to the X-axis. Equation (7.1) formulates the spacial vectors locating the dipoles, but it does not consider the dipole's orientation ( $0^\circ - 360^\circ$ ) which defines the direction of individual E-fields at the focus. To follow this, the current flowing in dipole  $u$  of the circle  $v$  is defined by a vector  $\vec{I}_u^v$  whose direction,  $\hat{I}_u^v$ , and magnitude,  $I_u^v$ , represent the orientation and the current magnitude, respectively. Since the NF-FCA is designed such that the individual E-fields originated from each of the array elements contribute constructively at the focus, the current phases,  $\psi^v$  are adjusted accordingly to compensate unequally distant dipoles, Fig. 7.1(b). Typically, the dipoles in a shared circle are equally distant from the focus, as a result, the phases need to be equal for each dipole of a shared circle. In contrast, a phase difference is inserted between two group of dipoles of two different circles; this means  $C - 1$  phase-shifters are required. To account for the phase differences,

we assume that a phase  $\psi^v$  is inserted to each dipole of the circle  $v$ , Fig. 7.1(b). To determine  $\psi^v$ , a geometrical evaluation is performed Fig. 7.1(c), and calculated [45] as:

$$\psi^v = -k_0 \left( \sqrt{F^2 + R^{v^2}} - F \right), \quad (7.2)$$

where  $k_0 = \frac{2\pi}{\lambda}$  is the free space wave number and  $\lambda$  is the wavelength. If the total current,  $I_0$ , fed to the antenna-array is known, and the necessary phase shifts,  $\psi^v$ , given by (7.2), then  $I_u^v$  can be calculated as:

$$I_u^v = \frac{I_0}{NC} \left( e^{-jk_0\psi^v} \right), \quad \forall u \in [1, N]; v \in [1, C]. \quad (7.3)$$

We note from (7.3) that, the  $I_u^v$  is independent of  $u$  for a given  $v$  because of an equal  $\psi^v$  used for each of the dipole in the circle  $v$ .  $\hat{I}_u^v$  is found by the orientation of the dipoles in the array. The NF-FCA antenna can be fully represented by the parameters:  $N$ ,  $C$ ,  $R^v$ ,  $\phi_u$ ,  $\vec{S}_u^v$ , and  $\vec{I}_u^v$ . For a designed NF-FCA antenna, the resultant E-field due to  $NC$  dipoles at a point P, Fig. 7.1(a), is subsequently formulated. The vector location,  $\vec{P}$ , of point P is given by  $\vec{P} = p_x\hat{x} + p_y\hat{y} + p_z\hat{z}$  and the vector distance,  $\vec{D}_u^v$ , between the dipole  $u$  (of the circle  $v$ ) and the point P, is given by:

$$\vec{D}_u^v = \vec{P} - \vec{S}_u^v. \quad (7.4)$$

Since, the resultant E-field occurring at point P is the sum of all the individual E-fields (denoted as vectors, Fig. 7.1), we first compute the E-field due to every dipole.

The near-field distance,  $l$ , in the Fresnel region is defined [1] by  $l = 2d^2/\lambda$ , where  $d$  is the antenna linear dimension; any value greater than  $l$  would lay in the far-field. The considered 5.8 GHz NF-FCA antenna is of  $d = 1$  m and  $l = 38.69$  m and every dipole  $d = \frac{\lambda}{2} = 2.58$  cm and  $l = 2.58$  cm. Therefore, because the focal distance of the antenna-array is  $0.4 \leq F \leq 2$  m, it lays in the Fresnel region, however, for every dipole ( $l = 2.58$  cm) in the Far-field. Thus the E-field vector of a each dipole in isolation, Fig. 7.1(a) (inset), is expressed [1] in a local spherical

coordinate system as:

$$\vec{E}_d = \frac{j\eta I_d e^{-jk_0 D_d}}{2\pi D_d} \left( \frac{\cos\left(\frac{\pi}{2} \cos\theta_d\right)}{\sin\theta_d} \right) \hat{E}_d, \quad (7.5)$$

where  $\eta = 120\pi$ ,  $\theta_d$  is the angle between the dipole current vector,  $\vec{I}_d$  with respect to  $\vec{D}_d$  (distance vector to P1); note that the quantities in the dipole local coordinate system are denoted with the subscript  $d$ .

The resultant direction of  $\vec{E}_d$  is shown in Fig. 7.1(a) (inset), however, since we have considered a rectangular coordinate system instead, (7.5) is arranged to define  $\vec{E}_u^v$  (the E-field vector projected at P due to a dipole  $u$  of the circle  $v$ ), as:

$$\vec{E}_u^v = E_u^v \hat{E}_u^v, \quad (7.6)$$

where  $E_u^v$ , and  $\hat{E}_u^v$  are (for a dipole  $u$  of a circle  $v$ ) the magnitude, and the direction of the E-field, respectively.  $E_u^v$  is calculated using (7.5), where  $D_d$  is substituted by the magnitude  $D_u^v$  from (7.4), and  $\theta_d$  is substituted by  $\theta_u^v$ , Fig. 7.1(a), which is computed by the cosine law as:

$$\theta_u^v = \cos^{-1} \left( \frac{\vec{D}_u^v \cdot \vec{I}_u^v}{D_u^v I_u^v} \right). \quad (7.7)$$

Using (7.4),  $D_u^v$  and (7.7),  $\theta_u^v$ , we derive  $E_u^v$  from (7.5) as:

$$E_u^v = \frac{j\eta I_u^v e^{-jk_0 D_u^v} \cos\left(\frac{\pi}{2} \cos\theta_u^v\right)}{2\pi D_u^v \sin\theta_u^v} (e^{-jk_0 \psi^v}), \quad (7.8)$$

where  $e^{-jk_0 \psi^v}$  is the phase shift required to co-phase E-fields at the focus. Since it can be observed from the inset of Fig. 7.1(a),  $\hat{E}_u^v$  must be normal to  $\vec{D}_u^v$  and parallel to the plane consisting of  $\vec{D}_u^v$  and  $\vec{I}_u^v$ , this must satisfy using vector cross products:

$$\hat{E}_u^v = \frac{\vec{D}_u^v \times (\vec{D}_u^v \times \vec{I}_u^v)}{|\vec{D}_u^v \times (\vec{D}_u^v \times \vec{I}_u^v)|} = \frac{\vec{D}_u^v (\vec{D}_u^v \cdot \vec{I}_u^v) - \vec{I}_u^v D_u^{v2}}{|\vec{D}_u^v (\vec{D}_u^v \cdot \vec{I}_u^v) - \vec{I}_u^v D_u^{v2}|}. \quad (7.9)$$

Finally, since all E-field vectors,  $\vec{E}_u^v \forall u \in [1, N]; v \in [1, C]$  (7.6), are found by substituting  $E_u^v$  and  $\hat{E}_u^v$  from (7.8) and (7.9), the overall E-field,  $\vec{E}$ , at P is calculated as:

$$\vec{E} = \sum_{v=1}^C \sum_{u=1}^N \vec{E}_u^v = \sum_{v=1}^C \sum_{u=1}^N E_u^v \hat{E}_u^v. \quad (7.10)$$

### 7.1.1.2 Initial NF-FCA antenna design

Based on [45], the initial design consists of 3 circles,  $C = 3$ , having 8 dipoles uniformly separated per circle,  $N = 8$ , and the circle radii  $R^1 = 10$  cm,  $R^2 = 30$  cm, and  $R^3 = 50$  cm, hence, the array is made of  $N \times C = 24$  dipoles, and is printed on the X-Y plane of Fig. 7.1(a). The dipoles angular positions  $\phi_u = \frac{2\pi(u-1)}{N}$  of vectors,  $\vec{S}_u^v$ , are calculated using (7.1). We considered radially-oriented [45] dipoles for  $\hat{I}_u^v$ , which is defined as  $\hat{I}_u^v = s \cdot \hat{S}_u^v$ , where  $s = -1$  for  $u > 5$  and  $s = 1$  otherwise. To compensate for the phase difference of the array, two phase shifts are required and calculated using (7.2). We use the same feeding network as presented in [45] to feed the array. The total E-field distribution of the initial design in the proposed scenario is calculated from (7.10).

Although the E-fields are embraced to contribute in-phase at the focus, vector components with same magnitude and opposite direction cancel each other - this limits the practical E-field. Preliminary results were used to calculate the  $\hat{E}_u^v$  delivered to the focus using (7.9) and corroborated this statement. Subsequently, rather than using radially-oriented dipoles for the array, a unidirectional configuration for mitigated cancellations of E-fields and enhanced performance is presented.

### 7.1.1.3 Final NF-FCA antenna design

Using the customized 3-D vector projection analytical model, the most prominent orientation of dipoles are found for best focalization at the focus. Initially, the vector projections were analyzed for several dipole orientations, whose expected E-field directions  $\hat{E}_u^v$  were computed using (7.9), and depicted in Fig. 7.2(a). We found that certain vectors were the image of those initializing and therefore

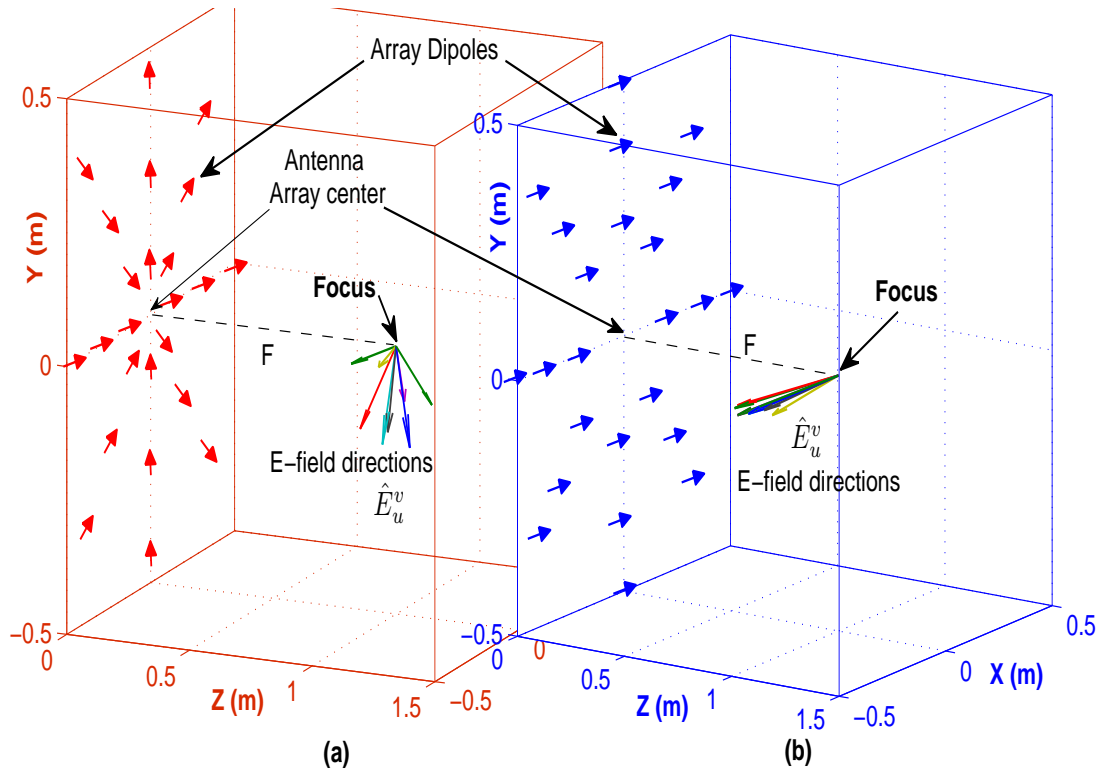


FIGURE 7.2: Optimal E-field vectors to adequately direct in a more concentrated fashion at focus and due to (a) radially oriented dipoles (initial design), (b) co-linearly oriented dipoles (final design).

canceled by a mirroring effect, but a right orientation of dipoles aligned the  $\hat{E}_u^v$  more efficiently, minimized cancellations, and as a result, more concentrated E-field vectors led to an enhanced focused response, Fig. 7.2(b). Moreover, to improve the FLL and the SLL over that of the initial design, the radii,  $R^v$ , Fig. 7.1(a), were redefined.

Hence, the optimization process was having two stages. In first stage, we found the optimal dipole orientations to maximize the summation of the E-Field at the focus (results into an intermediate design ID-1), however, Forward-Lobe-Levels (FLLs) and SLLs were compromised. In second stage, we suppressed the side lobes in the focal plane without compromising the focalization performance (results into final design). In the first stage, it was found that least cancellation of  $\hat{E}_u^v$  occurred when all dipoles were aligned in parallel (co-linearly oriented). In the second stage, the compensation for the poor FLLs and SLLs of ID-1 is done by re-calculating  $R^1$  and  $R^2$  by iteration  $0 < R^2 < R^3$  and  $0 < R^1 < R^2$ . Ultimately, the shared

design parameters of the initial and the final designs are: 24 dipoles,  $N = 8$ ,  $C = 3$ , and  $\phi_u$ ; while the new set of optimized  $R^v$  is:  $R^1 = 22\text{cm}$ ,  $R^2 = 37\text{cm}$ , and  $R^3 = 50\text{cm}$  (maximum antenna size). For comparison, another intuitive design, ID-2, will be included in investigation results; ID-2 has same dipole orientations as initial design but the  $R^1$  and  $R^2$  values from the final design are used. All the designs are analytically evaluated and compared in next section.

## 7.1.2 Analytical Results

First, we validate the customized 3-D vector projection analytical model presented in Section 7.1.1.1 using MATLAB. Initially, the E-field analysis of the initial antenna is performed and the results, later given in this Section, were in line with [45] validating the model. In addition, the model is used for the ID-1, -2 and the final designs to compare their performances with the initial design. We first start by calculating the E-fields received at every point of the scenario, Fig. 7.1(a), in near-field using (7.10) and the necessary phase shifts  $\psi^v$  of the array for a desired focal distance  $F$  using (7.2).

For  $F = 1\text{m}$ , the calculated  $\psi^v$  at each circle  $R^1$ ,  $R^2$ , and  $R^3$  of the array were respectively,  $0.92\pi$ ,  $2.56\pi$ ,  $4.56\pi$ , for the initial and ID-1 designs, and  $0.19\pi$ ,  $1.70\pi$ ,  $4.56\pi$ , for the final and ID-2 designs. The expected field strength (normalized  $|E|$ ) distribution in the focal plane ( $z = F = 1\text{m}$ ) for the initial and final designs is presented in Fig 7.3(a) and (b), respectively. Compared to the initial design, the final version provides a higher  $|E|$  at the focus ( $x = 0\text{m}$ ,  $y = 0\text{m}$ ,  $z = 1\text{m}$ ), with lower SLLs.

The following expressions analyze the focus properties of all considered antennas including, the  $|E|$  at focus, beam-width (BmW), focal depth, SLL, and FLL

$$\text{BmW} = \Delta \left[ \text{arg}_{(x,y)}(|E|_{dB}^{(x,y,F)} = |E|_{dB}^{(0,0,F)} - 3) \right],$$

$$\text{focal depth} = \Delta \left[ \text{arg}_{(z)}(|E|_{dB}^{(0,0,z)} = |E|_{dB}^{(0,0,F)} - 3) \right],$$

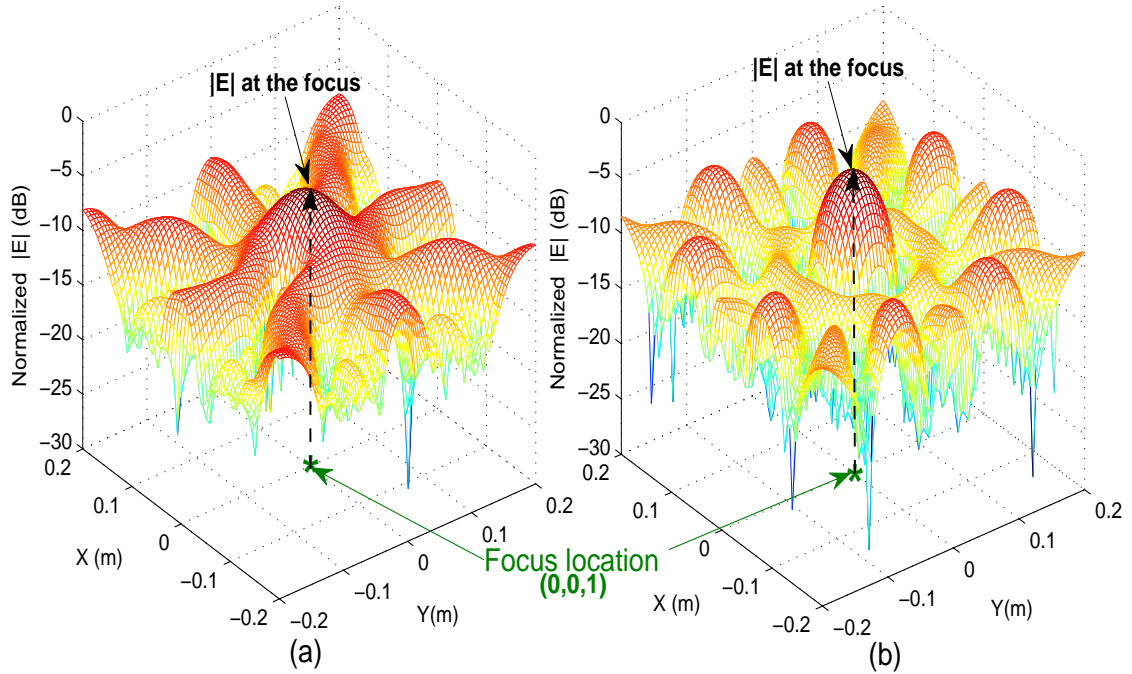


FIGURE 7.3: Normalized  $|E|$  in the focal plane when  $F = z = 1$  m (a) initial design (b) final design.

$$\text{SLL} = |E|_{dB}^{(x_0, y_0, F)} - |E|_{dB}^{(0, 0, F)},$$

$$\text{FLL} = |E|_{dB}^{(0, 0, z_0)} - |E|_{dB}^{(0, 0, F)},$$

where  $\Delta[p]$  is the distance between two possible solution points  $p$ , and  $(x_0, y_0, z_0)$  are the coordinates of the lobe nearest to the focus.

The normalized  $|E|$  for all the designs in Cartesian form for two transversal cuts of the main beam is depicted in Fig 7.4. Following observations can be extracted from the results. The ID-1 achieves a higher  $|E|$  as compared to initial design, but the SLLs are compromised (the final design compensates this by optimizing  $R^1$  and  $R^2$ ). whereas, the ID-2 shows similar  $|E|$  levels to the initial design, but increased SLL along the Y-axis. In contrast, a higher  $|E|$  of  $\approx 4$  dB in favor of the final design is achieved; this is measured at the peak center of the focus, with lower SLL along the X-axis (SLL-X) and along the Y-axis (SLL-Y). The BmW along the X-axis (BmW-X) is narrower for the final design and similar in the Y-axis (BmW-Y), Fig 7.4.

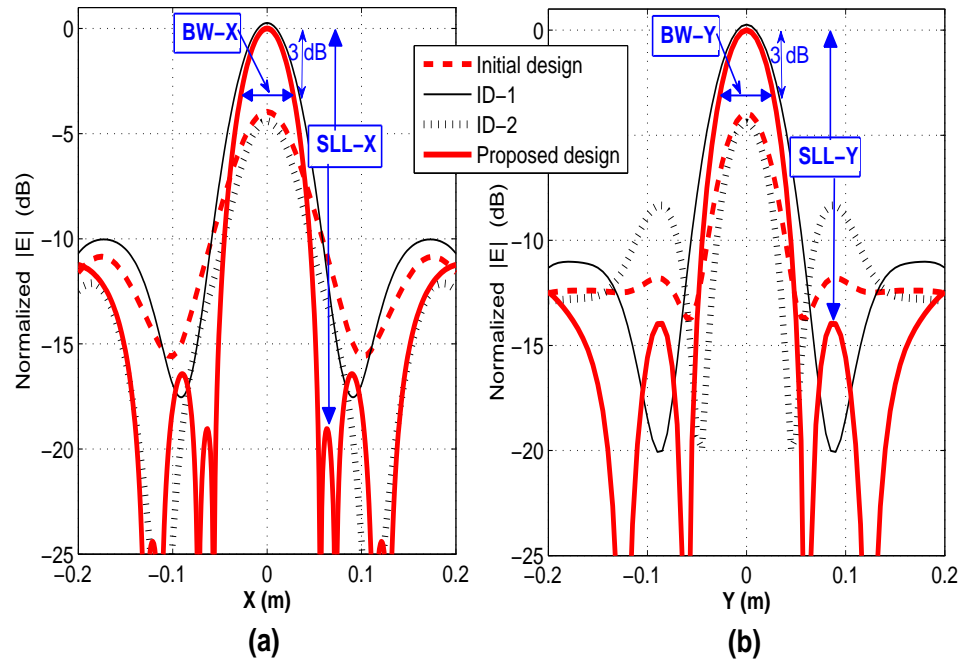


FIGURE 7.4: The normalized  $|E|$  (analytical) for two transversal cuts of the main beam,  $z = F = 1$  m along the (a)X-axis (b)Y-axis.

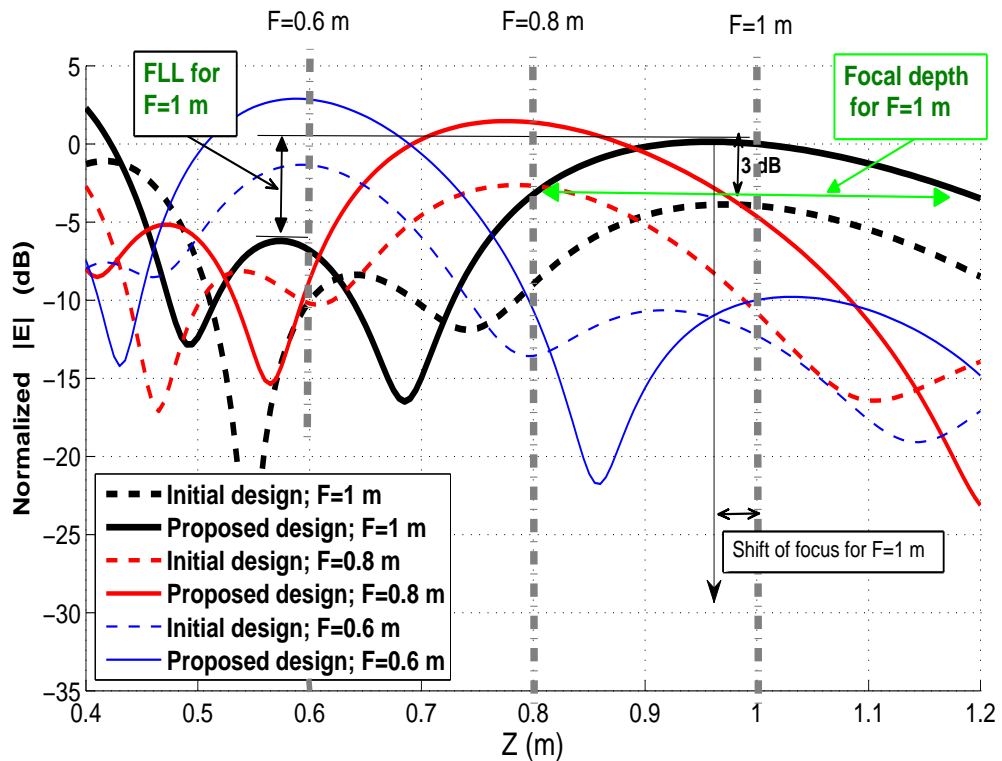


FIGURE 7.5: Focus agility comparison of the initial and the final design along the Z-axis ( $x = 0, y = 0$ ) for various  $F$ .

The focus agility of the final design is now investigated. Fig 7.5 shows the normalized  $|E|$  distributed along the Z-axis  $x = y = 0$  for  $F = 0.6, 0.8,$  and  $1$  m for

the initial and final designs. Compared to the initial design, the final design shows higher,  $|E|$ , and lowers FLLs for the three  $F$  cases without a focus displacement in the X and Y axis.; this defines an efficient focused agile antenna.

An in-depth comparison between the designs is presented in Table 7.1. The results

TABLE 7.1: focus properties of the initial design vs. the final design

focal length, $F \rightarrow$	0.5 m	0.6 m	0.8 m	1 m
Initial design:-				
BW-X (cm)	5.10	5.50	6.50	7.70
BW-Y (cm)	3.30	3.70	4.50	5.50
SLL-X (dB)	-7.35	-7.19	-7.01	-6.89
SLL-Y (dB)	-7.90	-7.89	-7.86	-7.82
SLL-Max (dB)	-2.27	-2.29	-3.08	-3.14
FLL (dB)	-5.85	-6.27	-5.54	-4.50
Focal depth (cm)	13.30	16.10	23.50	31.70
% shift of the focus	0.4	0.6	2.0	3.6
Proposed design:-				
BW-X (cm)	3.32	4.24	4.56	5.42
BW-Y (cm)	3.12	3.55	4.42	5.32
SLL-X (dB)	-14.28	-15.37	-17.36	-19.04
SLL-Y (dB)	-9.83	-11.06	-12.81	-13.91
SLL-Max (dB)	-3.91	-3.89	-3.81	-3.80
FLL (dB)	-5.45	-6.17	-6.23	-6.35
Focal depth (cm)	15.20	20.15	26.75	36.75
% shift of the focus	1.6	2.0	2.8	4.2
E-field enhancement (dB)				
$ E _{\text{proposed}} -  E _{\text{initial}}$	4.29	4.22	4.10	4.02

give confidence of improved focus agility for the final design. Concluding remarks reveal (compared to the initial design), 1) A final design with  $\approx 4$  dB enhanced  $|E|$  for all values of  $F$ . 2) Narrower BmW-X and similar BmW-Y. 3) Lower SLL-X and SLL-Y, and SLL-Max (the maximum SLL at the focal plane) with similar and lower FLLs when  $F < 0.6$  m and  $F > 0.6$  m respectively. 4) Higher focal depths (3 dB beam width along Z-axis) of  $\approx 4$  cm. The focal depth of the final design was

10-15% higher than initial design and is deemed acceptable for the antenna-array application.

The maximum peak intensity of the beam is seen slightly shifted in regard to the focus, Fig 7.5, that is, the peak intensity lies at a shorter distance than  $F$ , and is naturally always present as reported in [45, 98, 103]. The calculated shifts measured in percentage (%) ( $\frac{\text{shift}(m)}{F(m)} \times 100$ ) is included in Table 7.1; they provide an insight of focus displacements to be intentionally compensated prior prototyping.

## 7.2 Ink-jet printing of antennas using conductive ink

Since antennas are essential in a communication system, their effective and optimized designs are necessary for an overall system efficiency, in addition, for an adequate system cost minimization, their manufacturing is deemed intended cost effective. For instance, planar antenna structures are encouraged over 3-D, because the 3-D structures present a higher difficulty for integration with existing electronics and RF stages which prefer more compact antennas. Therefore, the solution adopted here is the planar antennas with simplified structures, for example, circular, elliptical or trapezoidal shapes [104, 105]. Apart from choosing printed planar antennas from design point of view, the cost effective and easy techniques for antenna manufacturing are also sought. Nowadays, the fabrication of printed antennas, by reflecting metal patterns on substrates, is done by selective masking and etching, and from decades the most popular technology for that is photolithography [106].

The photolithography process involves multiple steps to fabricate the intended antenna design. From copying the antenna shape (designed using some CAD software or EM software designing tool) over a mask while maintaining the real antenna dimensions for physical realization, to transferring the shape over the

silicon wafer, etching and electroplating, all steps are time consuming and resource-inefficient. Moreover, the use of substrates is limited due to solvent used for etching and e.g., the low cost tags printed over paper material cannot be realized. Therefore, the photolithography does not represent an optimum solution for a cost and resource effective manufacturing of the antennas [21, 107].

On the other hand, a low cost low complexity technique can be used for flexible applications; that is inkjet printing technology, which resembles to a most common method of printing on paper using home computers and printers. The most attractive feature provided by the inkjet printing is the direct printing of the CAD shapes over the substrates; this reduces manufacturing time drastically by skipping many of the steps involved in photolithography. The evolution of ink-jet printing opened a new path of cost effective and novel applications for consumer electronics by development of various Nano-technology based conductive inks suitable for printing over various substrates including paper [21]. This attracted the ink-jet printing technology for new applications such as, printed solar panel and cells, sensors, flexible displays, RFIDs, and antennas. Although it is an attractive technique to use conductive ink to spray the pattern over a substrate, there are many printer parameters needed to be carefully controlled while fabricating RF components, since the sprayed conductor ink will eventually define the RF properties of the printed shape. Hence, inkjet printing poses challenges in using it for RF applications, and a precise control of the ink deposition is required. The controlling parameters for inkjet printing include physical and chemical properties of the conductive ink, pressure/temperature of the jet and orifice size to spray, substrate properties, etc. Once these parameters are precisely controlled, ink-jet printing becomes a promising technology to empower the antenna manufacturing.

The ink-jet printing technology also found its utility in RFID applications. The RFID antennas fabricated using conductive paint and ink-jet printing technology were reported in [22, 108]. A UHF RFID printed antenna was developed in [22], where the conductive paint was sprayed over a car body to develop the antenna, and a coating layer was used to make the antenna suitable for in-car hidden applications. In [108], a novel application of RFID-WLAN at 5.8GHz was demonstrated

by printing a tag antenna over a can body; this is potentially useful for RFID applications with hidden tags pasted on food and beverage cans and metal-based containers. As the tag antenna was sprayed using copper conductive paint, a low-cost and compact tag was realized having reasonable gain and a range of input impedance for various Tag ICs. A summary of the sprayed antenna reported in [108] is presented next.

### 7.2.1 Sprayed antenna on cans for WLAN-RFID tags

In this section, we briefly introduce/study the RFID tag antenna, reported in [108], sprayed over a beverage can. The frequency band chosen for the design is 5.8 GHz because the antenna designed at this frequency will be less affected by reflector in close proximity, and a compact and conformal structure can be designed. Using conductive paint, the antenna pattern is sprayed onto a can body and Tag IC can be attached at the input port of the design. How the integration of Tag antenna with metallic body of the can affects the Tag's performance was analyzed, and parametric study to tune the antenna for various possible Tag ICs was presented.

#### 7.2.1.1 Sprayed antenna structure

The can used for investigation is shown in Fig. 7.6, it has a cylindrical shape with 115.5mm height and 32.9mm radius of circular bottom face. The metallic can body when purchased generally has a sprayed color paint of thickness 0.127mm, which works like a substrate and prevents contact of printed tag with can metal. The antenna was first designed in CAD and its formed of two layers; radiating layers and resonating layers. First resonating layer is sprayed over can, then a layer of color paint is sprayed over it. Finally the radiating layer is sprayed over color paint, hence, forming a top layer which has a non-conductive gap to connect Tag IC between two strips: inner, of length  $b$ , and outer, of length  $a$ . By adjusting the inner strip length  $b$ , the input impedance of the gap is adjusted to match with the Tag IC impedance.

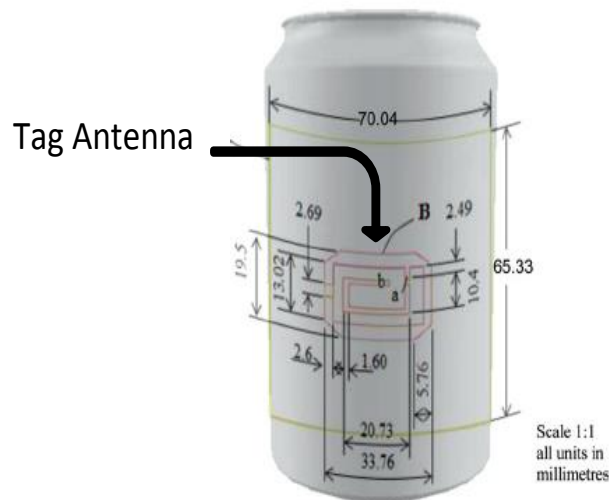


FIGURE 7.6: Sprayed Tag antenna on a can.

### 7.2.1.2 Results

The sprayed tag antenna over can was simulated and measured, and the results were presented in [108]. For the measurements of the can with sprayed tag antenna, a  $50\Omega$  coaxial probe was connected with the gap (rather IC), and precisely arranged to not let it contact with the can body. The return loss (RL) of the sprayed antenna was simulated and measured and showed that the antenna resonated around 5.8GHz, any discrepancy in the simulated and measured S11 results were attributed to manufacturing tolerances. The S11 result showed a -10dB bandwidth of 785MHz for the sprayed antenna. Also, it was found that there was not any significant effect of an extra layer of color paint (over radiating layer) over S11 performance, therefore, such antenna is also suitable for hidden application.

The parametric study revealed that adjustment in the inner strip length  $b$  can provide a fine tuning of the input impedance at the gap for Tag IC while maintaining almost the same S11 characteristics (resonating frequency). A highly capacitive Tag IC impedance should be conjugately matched to the impedance at the gap between the strips of antenna for full power transfer. Therefore, a highly inductive with low real part of impedance at the gap of antenna is intended and achieved by trimming inner strip  $b$ .

For far-field performance evaluation, the can with sprayed tag antenna was measured in an anechoic chamber. The far-field results showed that the antenna was radiating in all the directions for both elevation as well as azimuth planes, and had a measured gain of 3.04dBi. Overall results encouraged the use of this new technique and color painted sprayed tag antenna for hidden tagging applications.

## **7.3 Antenna customization for In-vehicle UWB MB-OFDM Communications**

For in-vehicle high-speed wireless communications, Ultra-Wide Band (UWB) Multi-Band Orthogonal Frequency Division Multiplexing (MB-OFDM) is a suitable technology, because of its high performance, low-power and low-cost characteristics. To optimize the UWB MB-OFDM system design, an antenna can be customized to provide improved Bit-Error-Rate (BER) performance at all the passenger locations inside the vehicle. To achieve this, a step-by-step process of channel-based antenna synthesis, which includes full in-car channel profile measurements, BER profile simulations, pattern synthesis, and source construction, is realized and presented in this section. The channel is first measured using a standard antenna and based on the experiments is set-up to measure the distribution of impulse responses (IRs) and signal-to-noise ratios (SNRs) in the vehicle's Passenger Plane (PP). The measured and simulated data is used in the synthesis process to customize a new antenna having optimized radiation pattern to improve BER performance in the passenger plane. The optimum radiation pattern shows a remarkable improvement of BER over the commercial antenna used in the measurements.

### **7.3.1 Introduction**

In-vehicle wireless connectivity is attractive to reduce the cost associated with wiring, and to provide mobility to portable devices which is highly demanded as a user point of view. The challenges for the realization would be: the solution should

be low cost, suitable for unlicensed use, and capable of providing high data rates; the coverage range of operation is not stringent for in-vehicle communication due to the small vehicle volumes. In 2002, the US Federal Communications Commission (FCC) allocated the frequency band 3.1 - 10.6 GHz for unlicensed operation of UWB radios [109] having a maximum allowed power spectral density of -41.3 dBm/MHz. Such a low power is only suitable for applications limiting for a short range ( $< 10\text{m}$ ) but a wider bandwidth (BW) can be supported for a high data rate  $\sim 480\text{Mbps}$ . Therefore, UWB has emerged as a promising technology for short-range high data rate wireless communication [110]. For instance in-vehicle applications, *the UWB technology showed the potential to deliver high data rate and spatial capacity, with multipath immunity* [111] along with low power, low cost solution.

The MultiBand Orthogonal Frequency-Division Multiplexing (MB-OFDM) has been a strong candidate for standardization for UWB applications [112, 113]. To develop an alternative physical layer based on UWB signaling, the IEEE 802.15 standardization group organized a task group 3a [114] who proposed physical layer specification for MB-OFDM UWB system [115, 116]. In another place, MB-OFDM has been recently accepted in a standard European Computer Manufacturers Association (ECMA) [117]. For in-vehicle communication, the MB-OFDM system was adopted in [111] for its slightly more immune to Gaussian noise [118]. Whereas, in [119], the performance of MB-OFDM is shown to be inferior than its competitor Direct Sequence UWB (DS-UWB) for intra vehicle communication, but the paper concludes the advantage of MB-OFDM due to its comparatively low complexity. The MB-OFDM system design parameters optimized for realistic UWB channel environment is presented in [120] and various blocks of the UWB MB-OFDM PHY architecture are described. The system performance was evaluated for the UWB channel models developed under IEEE 802.15.3a work group consisting CM1, CM2, CM3, and CM4, for several line of sight (LOS) and non-line of sight (NLOS) situations [120, 121] based on the clustering effects reported in [122]. Whereas, in the investigation presented in this examines the UWB MB-OFDM system functions under in-vehicle channel.

For in-vehicle propagation, the characteristics of the received signals reflected from vehicle body, windows, seats, etc., are very complex to be modeled inside the vehicle. Therefore, the distribution of the received envelope caused by in-vehicle multipath propagation requires a new set of measurements for its proper understanding.

In the literature, various studies [123–129] are dedicated to in-vehicle channel measurements and modeling and various kind of vehicles were considered. All of the aforementioned works adopt application specific transceiver deployment and measurements were taken only at those few deployed locations. Moreover, many were deployed just to provide wireless connectivity to static locations without any mobility feature desired for the passenger devices. Furthermore, the antennas used were omni-directional without any intelligence incorporated to optimize the performance in-vehicle. The preferred location of the Access Point (AP) antenna inside vehicles had being set in the middle of the ceiling of the car [130] to ensure good power distribution intending high bit rates to likely mobile equipment (ME) locations within the car. In this regard, the experimental channel measurements with preferable AP location were carried out in [111] for an specific car. Still, the antenna used was omni-directional and only a set of locations were measured in the passenger plane. Whereas, the system with omni directional antenna may not be an optimal choice for system design point of view. If a new antenna is customized specifically to optimize the system, then new measurements will be required for all the possible locations of ME in the passenger plane.

To optimize UWB system for in-vehicle application, along with the channel characteristic in the passenger plane, the behavior of various UWB antennas including the directional one should be investigated. The UWB antenna behavior study for in-vehicle provides an idea to customize a new antenna which is optimal for UWB MB-OFDM system deployed inside the vehicle. The UWB antennas have vast literature dedicated and having different characteristics and various types; from 3-D structures to planar and from plate/slot to printed monopole antennas [41, 104, 105, 131–134]. But, they all have limitations including size, bandwidth,

inability of integration with an integrated circuit. The drawback limits their practical use for specific applications and a lot of efforts have been put to improve the performance of the UWB antennas for particular applications. For instance, [135] presented several UWB antennas for wireless communications and detection applications working from 3.5 GHz to 9.9 GHz. Since the UWB antennas designed covering whole UWB spectrum suffer from interference by licensed user, e.g., WLAN, the implementation of MB-OFDM systems prefers antennas with BPF like response. Thereby, some band-notched UWB antennas were designed in [132, 135].

These UWB antennas have several concerns. None of the aforementioned UWB antennas were designed for optimal performance while deploying inside the vehicle. They were not customized to provide uniform BER performance throughout the passenger plane. Moreover, their radiation pattern is such that the received SNR will not be uniform in the passenger plane and certainly will have unacceptable SNR at some locations (blind-areas: defined for BERs  $> 10^{-5}$ ). To minimize the deeply faded blind-areas of the passenger plane, the antenna's radiation pattern can be customized such that a higher power is radiated towards deeply faded locations, and brings-up the received SNR level to match with a minimum acceptable SNR for target BER. To achieve this aim, we need many parameters to be defined, measured, simulated, and processed together to finally develop an antenna with desired optimum radiation characteristics. Thereby, in this section, we investigate a step-by-step process of channel-aware source synthesis to design an optimized antenna which minimizes blind-areas and achieves target End-to-end BER performance. This channel-aware antenna synthesis process includes full in-car channel profile measurements, BER profile simulations, pattern synthesis, and source construction, all detailed next.

### 7.3.2 In-vehicle UWB connectivity in the passenger plane: Problem description

For the model, dimension of the vehicle and location of the transmitter (Tx) and Receiver (Rx) systems are shown in Fig. 7.7. The access point (AP=Tx) being set in the middle of the ceiling of the car and is the preferred location in vehicles [130] to ensure high bit rates by ensuring a good power distribution to likely Mobile Equipment (ME=Rx) locations within the car. Both Tx and Rx are equipped with UWB MB-OFDM systems. The measurements were therefore taken at 0.8 m below the ceiling, “*This is the most likely location for the ME/fixed equipment while minimizing field exposure to occupants*” [111]. The in-car environment is assumed to be static, using a closed-environment (complete shielded vehicle) scenario and a motionless vehicle.

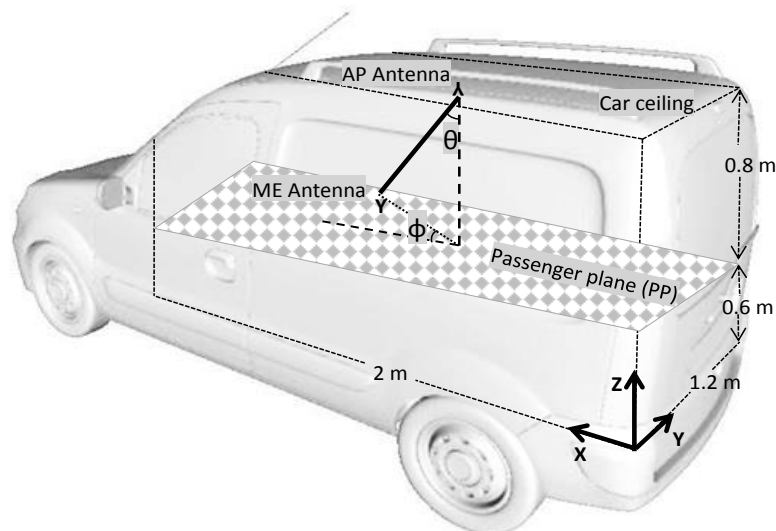


FIGURE 7.7: The in-vehicle system configuration.

According to the coordinate system shown in Fig. 7.7, the Passenger Plane (PP) is defined by  $z = 0.6m$ , whereas, the location  $(x, y, 0.6)m, \forall x \in (1, 2)m; y \in (0, 1.2)m$ , of the UWB receiver can be anywhere in the PP. The location of the Rx with respect to the Tx essentially determines the channel (impulse response and received SNR) between them. This is why the channel profiles will be varying for the various locations in the PP, and so the End-to-End BER performance

at the receiver. Since Rx is assumed existing anywhere in the PP, the BER is determined at each location  $(x, y, 0.6)m$  with profile,  $BER(x, y)$ . The  $BER(x, y)$  distribution also depends on the radiation pattern of the antenna used inside the vehicle. In general, the commercial UWB Tx antenna having omni directional pattern would have  $BER(x, y)$  profile with many deeply faded areas in the PP. At these deeply faded locations,  $BER(x, y)$  is unacceptably lower than the target BER,  $BER_{target} = 10^{-5}$ , and they are called blind-areas. The ultimate performance measure of the UWB antenna in-vehicle is given by %Blind-Area, which is defined as:

$$\%Blind\text{-Area} = \frac{\text{total PP area with } BER > BER_{target}}{\text{total PP area}} 100 \quad (7.11)$$

Ideally, the %Blind-Area should be zero, but it is not true for the commercial antenna. Therefore, to improve the performance, an antenna is customized particularly for in-vehicle channel. The ultimate aim should be the synthesis of an antenna which achieves an acceptable BER at each location of the passenger plane, hence,

$$\left\{ \begin{array}{l} \text{Synthesize antenna with customized pattern} \\ \text{such that} \\ \text{\%Blind-Area is minimized} \end{array} \right. \quad (7.12)$$

The actual  $BER(x, y)$  using ordinary antenna does not follow (7.12). To achieve the desired BER distribution in the PP, a process is desired to customize the antenna pattern by utilizing the channel knowledge. Thereby, we propose the channel-aware synthesis process of designing customized antenna which solves the problem defined in (7.12).

### 7.3.3 Channel-aware source synthesis process

In this section, a systematic process, to be followed to design the antenna specifically customized for the in-vehicle application, is presented as a solution of (7.12).

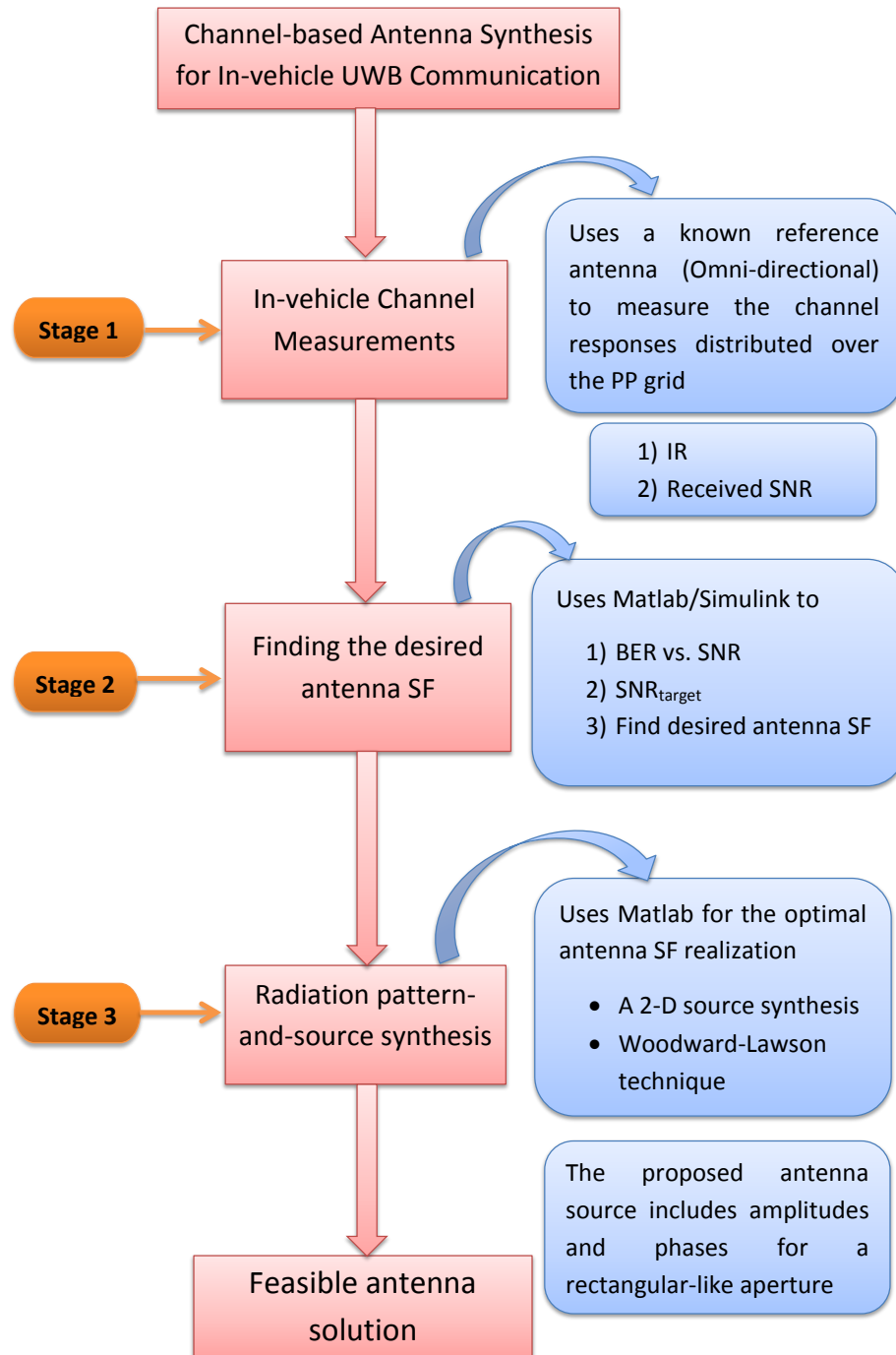


FIGURE 7.8: Steps for the channel-aware process of antenna design for in-vehicle UWB connectivity.

Fig. 7.8, shows the steps of the channel-based antenna synthesis process to obtain the final antenna design. We elaborate each step involved in the process, subsequently.

### Step-1 : In-vehicle channel measurements

Since in-vehicle channel is a multi-path scenario, BER of the communication system working in-vehicle depends on the received Signal-to-Noise Ratio,  $SNR_{Rcv}$ , and the impulse response (IR),  $h(t)$ . Since the channel property changes depending on the location of the Rx, the SNR and the IR should be location dependent and are related by [136]:

$$BER(x, y) = f[SNR_{Rcv}(x, y), h(t, x, y)], \quad (7.13)$$

where  $f[\cdot]$  is the complex relation which transforms the channel parameters into the system performance, and depends on the properties of various blocks of the MB-OFDM system. To evaluate  $BER(x, y)$ , we need to know channel profiles  $h(t, x, y)$  and  $SNR_{Rcv}(x, y)$ . Using known omni-antenna, the channel profiles  $h^0(t, x, y)$  and  $SNR_{Rcv}^0(x, y)$  were measured inside the vehicle. For the channel measurement set-up, a PNA-X Network analyzer from Agilent technologies, two UWB antennas (commercial) from Wisair Ltd, and connecting cables were used, Fig. 7.9. Both the commercial antennas are monopole antennas with 2 dBi gains [111]. The transmitter emits power spectral density (PSD) of -42 dBm/MHz containing the WiMedia/ MBOA group 1 sub-band (3.168 - 4.752 GHz).

### Step-2 : Finding the desired antenna space-factor

Once the channel profiles  $SNR_{Rcv}^0(x, y)$  and  $h^0(t, x, y)$  are measured at all the points of the passenger plane, the  $BER^0(x, y)$  in case of the known omni-antenna is obtained by simulating the UWB MB-OFDM system corresponding to  $f[\cdot]$  used in (7.13). The MATLAB Simulink model of UWB MB-OFDM system is presented in Fig. 7.10 where the building blocks of the MB-OFDM Tx and Rx [115, 116] are shown. The UWB channel block includes antenna front end responses which were measured and feed in terms of channel profiles  $SNR_{Rcv}(x, y)$  and  $h(t, x, y)$ . This way, the channel block can represent the real radiation pattern as well as the path impairments.

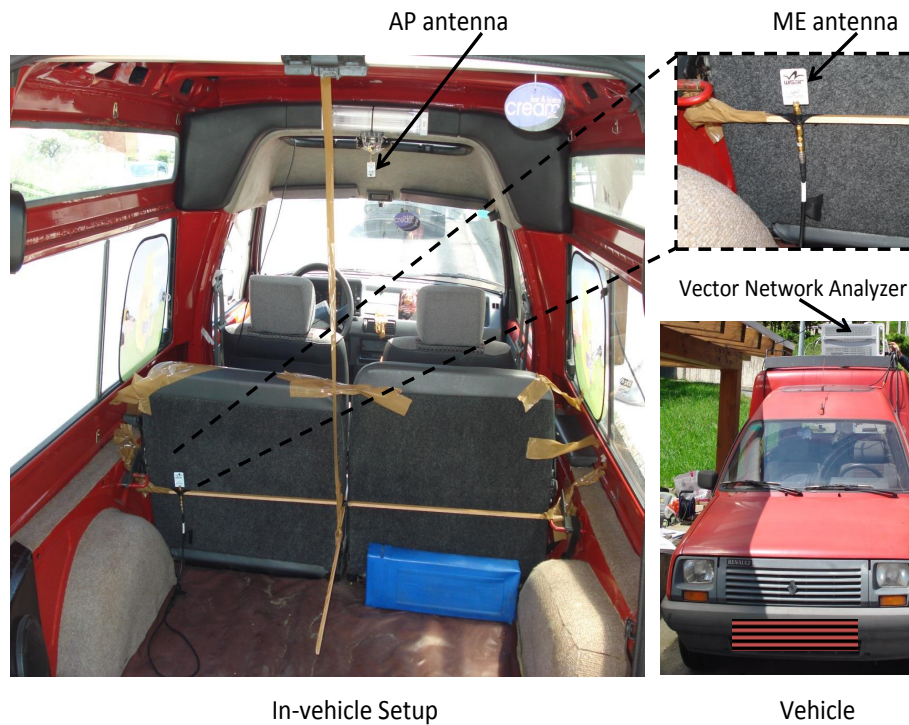


FIGURE 7.9: Measurements of the in-car UWB channel scenario.

The BER simulations for commercial antenna shows that there are certain locations in the passenger plane where the BER is unacceptable. To improve the BER, the  $SNR_{Rcv}(x, y)$  should be redistributed by customizing the antenna radiation pattern. This problem is known as antenna pattern synthesis for which the desired antenna radiation pattern is first evaluated. To do that, we simulate the BER-SNR variation of the UWB MB-OFDM system using measured IR  $h^0(t, x, y)$ , this is to find the targeted minimum SNR,  $SNR_{target}$  that corresponds to the target  $BER_{target}$ . This manual search is performed as:

$$\begin{aligned}
 &\text{For } \forall x \in (1, 2); y \in (0, 1.2) \\
 &\quad \left\{ \begin{array}{l} \text{find } snr > 0 \text{ such that} \\ f[snr, h^0(t, x, y)] = BER_{target} \end{array} \right. \quad (7.14) \\
 &SNR_{target}(x, y) \Leftarrow snr
 \end{aligned}$$

The target SNR profiles,  $SNR_{target}(x, y)$ , calculated using (7.14), is the desired SNR, whereas, the  $SNR_{Rcv}^0$  is the real measured SNR using omni-antenna. Using

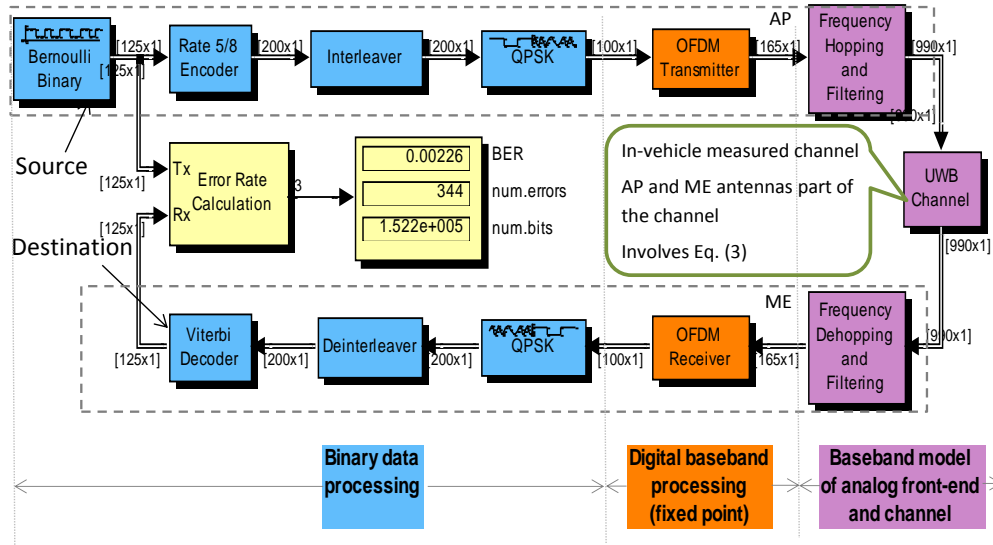


FIGURE 7.10: MATLAB Simulink model of UWB MB-OFDM system.

these two quantities we can evaluate the desired radiation pattern  $SF_d(x, y)$  for the synthesized source using following equation.

$$SF_d(x, y) = \sqrt{\frac{SNR_{target}(x, y)}{SNR_{Rcv}^0(x, y)}}. \quad (7.15)$$

The  $SF_d(x, y)$  obtained using (7.15) is subsequently used in Step-3 to synthesize the source having desired radiation pattern.

### Step-3 : Radiation Pattern and Source Synthesis

The antenna pattern and source synthesis process is invoked to obtain the desired SF. For instance, we have considered rectangular aperture source of dimension  $l_x \times l_y$ . The source dimension and the local coordinate system  $(x', y', z')$  is demonstrated in Fig. 7.11. As a result,  $SF_d(x, y)$  takes the form of  $SF_d(\theta, \phi)$  to account for the spherical coordinate system of the antenna whose aperture (effective area) is predominantly related to the PP dimensions, Fig. 7.7, and  $\theta$  and  $\phi$  are given

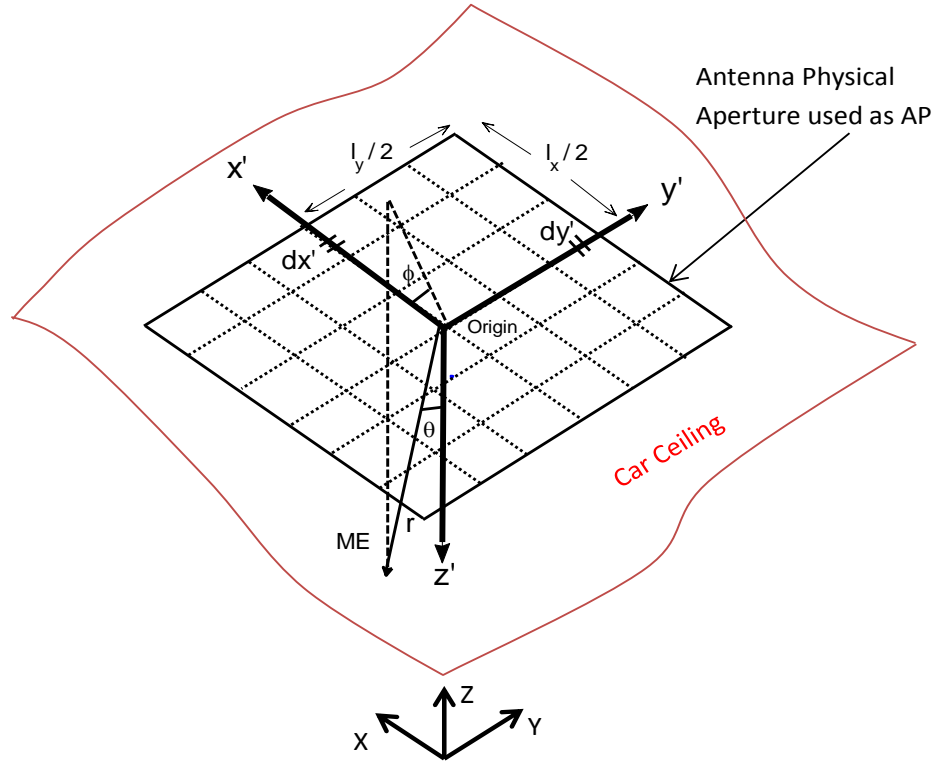


FIGURE 7.11: The geometry of the antenna physical aperture used as AP.

by the following transformation equations and calculated geometrically as,

$$\theta = \tan^{-1} \left[ \frac{\sqrt{(x - 1.0)^2 + (y - 0.6)^2}}{0.8} \right], \quad (7.16)$$

$$\phi = \tan^{-1} \left[ \frac{(0.6 - y)}{(1.0 - x)} \right].$$

The origin of the antenna aperture (Fig. 7.11) is the center of the AP (Fig. 7.7) with coordinates  $x=1\text{m}$ ,  $y=0.6\text{m}$  and  $z=1.4\text{m}$ . Hence,  $x = x' + 1$ ;  $y = y' + 0.6$ ;  $z = 1.4 - z'$ . The general form of  $SF(\theta, \phi)$  for a continuous source (a single source also applies) is given by [1], Chap. 7, as,

$$SF(\theta, \phi) = \int_{-l_y/2}^{l_y/2} \int_{-l_x/2}^{l_x/2} I(x', y') \times e^{j(kx' \sin\theta \cos\phi + ky' \sin\theta \sin\phi + \Phi(x', y'))} dx' dy', \quad (7.17)$$

where  $l_x$  and  $l_y$  are the linear dimensions along the  $x'$  and  $y'$  directions,  $I(x', y')$  is the source amplitude,  $\Phi(x', y')$  is the phase distribution of the antenna for a rectangular-like physical aperture, and  $\forall x' \in (-\frac{l_x}{2}, \frac{l_x}{2})$ ;  $y' \in (-\frac{l_y}{2}, \frac{l_y}{2})$ . The

$SF_d(\theta, \phi)$  is then given by substituting (7.17) as,

$$SF_d(\theta, \phi) \approx \int_{-l_y/2}^{l_y/2} \int_{-l_x/2}^{l_x/2} I_{fin}(x', y') \times e^{j(kx' \sin\theta \cos\phi + ky' \sin\theta \sin\phi + \Phi_{fin}(x', y'))} dx' dy'. \quad (7.18)$$

where the required source coefficients, amplitude  $I_{fin}(x', y')$  and phase  $\Phi_{fin}(x', y')$  for the desired radiation pattern are reflected in (7.18). To solve the inverse problem (7.18) with unknowns  $I_{fin}(x', y')$ ,  $\Phi_{fin}(x', y')$  and known  $SF_d(\theta, \phi)$ , we used the Method of Moments (MoM) and the Woodward Lawson synthesis. These numerical solution techniques are used for the pattern synthesis and source construction, and the details of these standard methods could be found in [1] but omitted in this dissertation for brevity.

#### Step-4 : Feasible antenna solution

The theoretically obtained desired source with amplitude and phase distributions is reflected as antenna hardware using some antenna fabrication technology. It is highly complex to exactly reflect theoretical current amplitude and the phase coefficients on continuous antenna aperture, whereas, array as the solution could be inefficient for in-car application due to confined size issues. The discretization of the continuous sources (e.g., discrete source) is another possibility which gives an approximate radiation pattern to the desired pattern. The permitted difference between the desired and the approximate radiation pattern will depend on the final BER performance in the passenger plane. For sampling of continuous sources, the root-matching, and perturbation techniques [137] can be used but all have their own limitations of accuracy. For shaping the antenna's radiation pattern, the use of dielectric lenses and domes [138] is also an attractive approach and we suggest to investigate them for channel-based antenna synthesis, this is intended to provide an ideal antenna solution with dispersive gain.

### 7.3.4 Results

In this section, the final results of BER distribution for the optimum source produced by channel-aware synthesis process is presented. The  $BER^{fin}(x, y)$  distribution in the passenger plane is calculated by the optimized source ( $I_{fin}(x', y')$  and  $\Phi_{fin}(x', y')$ ) given in (7.18). A comparison is done with  $BER^0(x, y)$  of the commercial antenna. Both  $BER^0(x, y)$  and  $BER^{fin}(x, y)$  were calculated and the results are shown in Fig. 7.12. We observe from Fig. 7.12(a) that the BER performance for the commercial antenna in passenger plane is not consistent, and there exists many blind locations (BLUE grids) where the targeted BER is not achieved. Whereas, it is apparent from Fig. 7.12(b) that, the optimized final source drastically reduces the blind locations as compared to that of the commercial antenna.

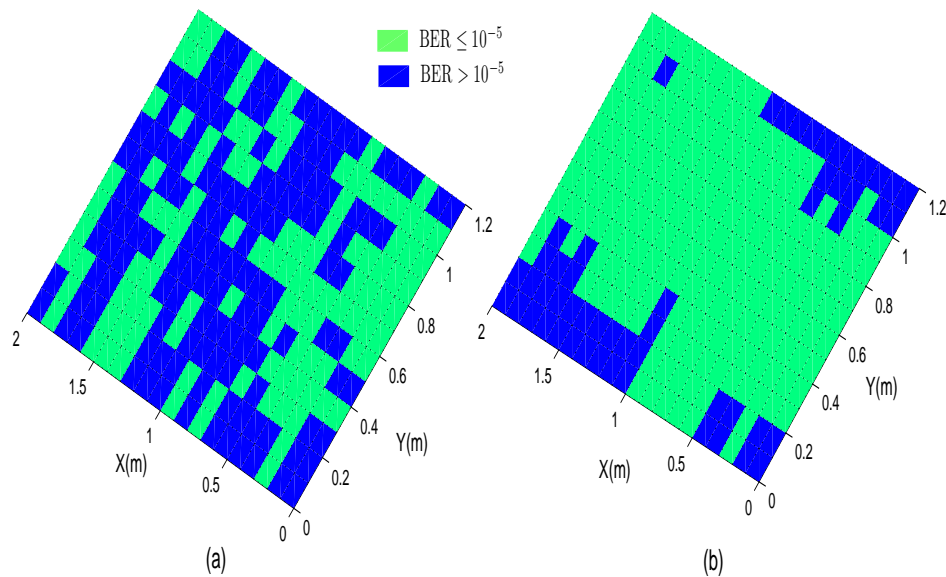


FIGURE 7.12: BER distribution in the passenger plane (a)  $BER^0$  for the commercial antenna (b)  $BER^{fin}$  for the customized optimum source

Using the results of Fig. 7.12, the blind-area (in percentage) is computed for comparison between the responses when the customized and the standard antennas were used as AP. The %Blind-Area is compared in Table 7.2, where the customized optimum source reduced the %Blind-Area to 17.72% as compared to 55.45% of the commercial antenna. Hence, the investigated optimum source shows great

advantage of the channel-aware synthesis process for improving the performance of UWB-OFDM communications inside the vehicle.

TABLE 7.2: Performance comparison of the optimized antenna vs. the standard antenna used as AP.

	% Blind Area
Standard Antenna	55.45%
Proposed Antenna	17.72%

## 7.4 Summary

In this chapter, a near-field focusing, a printed antenna technology and a customization of an antenna for in-car applications have been proposed, investigated and presented.

First, we investigated a Near-Field Focused Circular Array (NF-FCA) antenna designed for 5.8 GHz RFID applications. The antenna array was carefully modeled in 3-D for maximum focalization and field strength at the focus in near-field. Using the customized 3-D vector projection analytical model, the resulting E-field vectors were optimally found to direct in a more concentrated fashion while minimizing their cancellation from imaging. The effects of the E-fields contributing at the focus due to possible dipole orientations were studied. The model affirmed that dipoles oriented unidirectionally (final design) are favored over those oriented radially (initial design), and the corresponding necessary parameters for the final design customization were given. The final design showed (compared to the initial design) a higher field strength, a more focused beam with improved beam-width and side-lobe levels, and enhanced focus agility.

Second, we presented a short review on ink-jet printing technology used as a cost and resource effective antenna manufacturing. The advantages of the ink-jet printing over traditional photolithography were presented, where the latter is more laborious, time consuming and involves many steps to fabricate the antennas. One antenna design for 5.8GHz RFID tagging application was studied and presented,

where the tag antenna was sprayed over a cylindrical can. The antenna was fabricated by using a copper paint, and a color paint coating. The results encouraged its use for hidden tagging applications and showed a good return loss, gain, and omni radiation patterns for the azimuth as well as the elevation planes.

Third, we investigated a channel-aware source synthesis process of designing optimally an antenna to specifically customize it for inside vehicle applications of UWB MB-OFDM system. We showed that using commercial antenna there exist deeply faded locations (blind-areas) in the passenger plane where the BERs are unacceptably high. The radiation pattern of the antenna under investigation was customized to improve the blind-areas in the passenger plane. For the process, a new set of in-vehicle channel measurements (channel profiles) were taken. The BER-SNR characteristics were simulated using a MATLAB/Simulink model, where the measured in-vehicle channel profiles were utilized. Using measured in-vehicle channel profiles, we evaluated the desired antenna pattern and synthesized optimally the corresponding source (rectangular aperture) amplitude and phase profiles. The optimal source profiles had shown a potentially reduced blind area to 17.72% in the passenger plane as compared to the 55.45% using the commercial antenna, hence, it is very welcome for the UWB MB-OFDM system in in-vehicle applications.

## 7.5 Chapter related publications

- **A. Sharma**, I. J. Garcia Zuazola, R. Martinez, J. C. Batchelor, A. Perallos, and L. de-Haro Ariet, “Optimal E-field vector for a highly-focused antenna-array”, *IEEE Letters on Antennas and Propagation*, vol. 13, pp. 392-395, Feb. 2014.
- I.J. Garcia Zuazola, **A. Sharma**, J.C. Batchelor, I. Angulo, A. Perallos, W.G. Whittow, J.M.H. Elmirghani, and R. Langley, “Radio frequency Identification miniature interrogator antenna sprayed over an in-vehicle chassis”,

---

*IET Microwaves, Antennas and Propagation*, Volume 6, Issue 15, pp. 1674-1680, Dec. 2012.

- I.J. Garcia Zuazola, **A. Sharma**, J.C. Batchelor, I. Angulo, A. Perallos, and J.M.H. Elmirghani, “Sprayed antenna on cans for WLAN-RFID tags”, *Wiley - Microwave and Optical Technology Letters*, Volume 55, Issue 4, pp. 773-775, April 2013.
- **A. Sharma**, I.J. Garcia Zuazola, R. Martinez, A. Perallos, and J. C. Batchelor, “Channel-based Antenna Synthesis for Improved In-vehicle UWB MB-OFDM Communications”, *submitted for review in IEEE Transaction on Vehicular Technology*.
- I.J. Garcia Zuazola, L. Azpilicueta, **A. Sharma**, H.Landaluce, F.Falcone, I. Angulo, A.Perallos, W.G.Whittow, J.M.H. Elmirghani, and J.C. Batchelor, “Bandpass filter-like antenna validation in an ultra-wideband in-car wireless channel”, *IET Communications*, Volume 9, Issue 4, pp. 532-540, Mar. 2015.

# Chapter 8

## Conclusion and Future Open Problems

### 8.1 Concluding remarks

In this dissertation we have investigated the advancement of antennas used for Radio-Frequency Identification (RFID) applications. In general, the RFID finds its application individually in Near-Field (NF) and Far-Field (FF) zones of the reader antenna designed to operate at a single RFID frequency. The bands adopted in the literature for RFID applications are LH, HF, UHF, 2.45GHz, and 5.8GHz, where each band can be utilized for NF and FF applications. In this work, we developed a 'multi-purpose NF and FF switched multiband RFID reader antenna' which through a single antenna unit performs both NF and FF operations and incorporates multiple RFID bands with switching facility. The elaborated antenna was as a result of several intermediate designs, each introducing novel properties for advancement, and presented as UDTC, NDTC, SL-NDTC, and DB-NDTC.

Initially, we presented optimization of HF-RFID reader antenna to enhance H-field by targeting the following two criterion. First, we optimized the coil antenna for a high power transfer efficiency (hence a high Q-factor) using a Uniformly-Distributed-Turns-Coil (UDTC) approach. By analysis and simulation results, it

was demonstrated that a significant enhancement in H-field can be achieved using UDTC antenna, that is a 23.34% improvement over a reference design. Subsequently, the coil was optimized for the second criteria of a high data transfer rate; a Non-uniformly Distributed-Turns Coil (NDTC) was proposed. The design algorithm of the NDTC antenna was presented to maximizing H-field by optimally distributing the multiple turns in the inner area of the coil. Theoretical study and simulation of NDTC antenna showed a 116.23% higher H-field with unconstrained Q-factor compared to the reference design. Furthermore, the NDTC antenna was fabricated and measured, and the corresponding H-field enhancement from the measured results was 21.21%, this encourages the use of NDTC antenna over others for HF-RFID reader applications. Moreover, an assessment of the NDTC antenna was performed for use on various substrates with different deposited conductors types and thicknesses and the performance degradation due to existing reflector in the vicinity of the antenna was investigated. The results proved that the NDTC over PCB-FR4 had highest  $Q$  and  $H$ , and therefore, most suitable for the applications seeking high power efficiency. It was also found that reflector in vicinity affects negatively when very close to the NDTC antenna, however, the effect diminishes for a reasonable separation. The compromised  $H$  can be compensated by an equal increase in input power; this would allow the antenna to be used near reflectors. Although the NDTC antenna exhibited a robust performance in NF zone, applications such as the reading/interrogating and wireless power transfer (charging mats) demands for a wider reactive field area. Therefore, an array antenna was also developed composing five cautiously arranged NDTC elements to produce robust and extended H-field in the interrogation zone. It was validated through simulations and demonstrated a proposed array capable of expanding the interrogation zone to at least four times of that of a single NDTC antenna.

Since the NDTC antenna was developed for NF applications it does not serve any FF purpose. To fulfill that, a multi-purpose antenna serving both NF and FF operations was developed for 915MHz UHF-RFID readers. In the design process, circular segmented-line coil antennas were studied. The traditional solid-line coil showed weak H-field because of the currents facing phase inversions and nulls and

is due to the electrically large coil at UHF 915MHz. Instead, a Segmented-Line Single-Turn Coil (SL-STC) antenna is proposed (incorporating solid-line sections along with distributed capacitors to compensate current phases along the traces of the coil) to produce strong and uniform H-field even though the coil is electrically large. An optimized Segmented-line Non-uniformly Distributed-Turns Coil (SL-NDTC) antenna at UHF was designed to expand/improve the SL-STC antenna for a maximum H-field in the interrogation zone. The simulations backed by corroborated measurements proved a significant enhancement in H-field achieved by SL-NDTC over SL-STC, that was in percentage 162.6% at 10mm and 58.7% at 50mm distant from the coil center. The FF radiation pattern results were encouraging to use the SL-NDTC as a dual-purpose NF and FF UHF-RFID reader antenna.

Although, the SL-NDTC antenna served dual-purpose, however, it was designed to operate at a single RFID frequency. In the view of this constraint, and to further move a step ahead towards the ultimate goal, we designed a Dual-Band NDTC (DB-NDTC) antenna with frequency switching capability, and optimized it to operate in NF when switched to 13.56MHz and in FF when switched to 915MHz. The simulation and measurement results showed a DB-NDTC antenna with a robust H-field in the NF zone when switched to HF, and a wide FF radiation pattern of gain  $\sim 2.2$  dBi and  $\sim 82.5\%$  efficiency when switched to UHF. This design is welcome for RFID applications where an extended and distinguished interrogation zones are sought. Ultimately, a multi-purpose switched multiband antenna was customized for providing multiple switched bands. The antenna incorporated frequency reconfigurability by switching between three frequency bands of RFID operation using four RF switches. Depending upon the states of the switches, one out of three modes-1-3 of operation can be selected with corresponding resonating frequency 915MHz, 2.45GHz, and 5.8GHz, respectively. The non-uniformly distributed circular shape was adopted in the design to support effective generation of H-field in the NF zone which advantageously also resulted in FF radiation. The results proved the claim with decent H-field in the NF zone and radiation gain in the FF zone for each individually switched frequency. This demonstrated

the suitability of the proposed RFID reader antenna for multiple zones (NF and FF) and multiband applications using switching (frequency reconfigurability) for multi-purpose use.

In this dissertation, novel applications for the antennas has also been covered, e.g., near-field focusing using antenna-array, ink-jet printed antennas, and customization of antenna for in-car applications. In this regard, we have presented a Near-Field Focused Circular Array (NF-FCA) antenna made of dipoles for 5.8 GHz RFID applications and carefully modeled using a customized 3-D vector projection analytical model. The E-field contributions from dipole elements were optimized in such a way that the resulting field strength at the focus was maximized by producing a more focused beam with improved (narrower) beam-width and lower side-lobe levels with an enhanced focus agility. Another application reported a cost effective design technology; a 5.8GHz RFID/WLAN antenna was designed by spraying the conductive paint over a cylindrical can with a color paint coating. The design was encouraging for hidden tagging applications and showed a good return loss, gain, and omni radiation patterns for the azimuth as well as the elevation planes. Latest application reports a channel-aware UWB antenna synthesis process for in-vehicle applications utilizing MB-OFDM system, where results demonstrated an antenna customized using the proposed specific synthesis to effectively reduce deeply faded areas of signals inside the vehicle, hence, a suitable choice for the UWB MB-OFDM system in in-vehicle applications.

## 8.2 Scope for future research

The research work performed in this dissertation can be further extended in the following directions:

- The final design presented in this dissertation for RFID reader antenna was developed for three RFID switchable bands, e.g., 915MHz, 2.45GHz, 5.8GHz. It is motivating to extend the idea to also include LF and HF bands in

the same design to ultimately get an universal RFID reader antenna. Of course, it must be challenging, because the final antenna should perform equally good in near-field and far-field at all the selected frequencies. Also, impedance matching of the antenna at multiple frequencies is another issue.

- The number of RF switches used in universal design should be minimized for an optimal system point of view.
- The interrogation area in the near-field zone for microwave 2.45/5.8GHz RFID readers is small and future studies should investigate the possibility of extending this area particularly for higher frequencies while maintaining a robust and intensive H-field.
- Only RFID reader antennas were considered in this work, therefore, in future, tag antennas should be developed targeting multi-purpose multi-band designs.
- In this dissertation, the reader antennas were developed on PCB, whereas, the effects of novel approaches for antenna fabrication, e.g., spray painted antenna technology should be investigated for printing the reader antenna cost effectively over flexible surfaces while maintaining the multi-purpose switchable multiband.
- In future studies, one target to extend the multi-purpose multiband antenna is optimizing the multiband design to achieve a band-pass-filter like response for each switched band of operation.
- Since the effect of reflector proximity over reader antenna exhibited certain limitations, a new design technique to make the antenna insensitive to such proximities should be developed. The use of ferrite cores is among the proposed options.



# Bibliography

- [1] C. A. Balanis, *Antenna Theory Analysis and Design*, 2nd ed. Wiley, 1997.
- [2] J. S. Seybold, *Introduction to RF Propagation*. John Wiley & Sons, 2005.
- [3] Y. Lee. (2003) Antenna Circuit Design for RFID Applications. <http://ww1.microchip.com/downloads/en/appnotes/00710c.pdf>. Microchip Technology Inc. [Online]. Available: <http://ww1.microchip.com/downloads/en/appnotes/00710c.pdf>
- [4] Z. Tang, Y. He, Z. Hou, B. Li, and Z. Tang, “The Effects of Antenna Properties on read Distance in Passive backscatter RFID Systems,” in *Proc. Int. Conf. on Networks Security, Wireless Communications and Trusted Computing (NSWCTC)*, Wuhan, China, April 2009, pp. 120–123.
- [5] H. Zhang and X. Lv, “Antenna Circuit Design and Simulation for the Reader of 125 KHz RFID,” in *International Conference on Computer Science and Service System (CSSS)*, Nanjing, Aug. 2012, pp. 507–510.
- [6] K. Wang, A. Diet, S. A. Chakra, C. Conessa, M. Grzeskowiak, T. Bouaziz, S. Protat, D. Delcroix, L. Rousseau, G. Lissorgues, and A. Joisel, “Detecting range and coupling coefficient tradeoff with a multiple loops reader antenna for small size RFID LF tags,” in *IEEE International Conference on RFID - Technologies and Applications (RFID - TA)*, Nice, Nov. 2012, pp. 154 – 159.
- [7] F. Z. Fazrul, M. S. Anuar, P. J. Soh, and S. A. Aljunid, “125 KHz Ubiquitous RFID Tag Signal Detector System,” in *International Conference on Intelligent and Advanced Systems*, Kuala Lumpur, Nov. 2007, pp. 418–421.

- [8] C. Phongcharoenpanich, R. Pansomboon, T. Lertwiriyaprapa, and S. Kawdungta, "Fishing Net Antenna for LF-RFID Reader of Cuboid Aquarium Applications," in *IEEE International Conference on Wireless Information Technology and Systems (ICWITS)*, Maui, HI, Nov. 2012, pp. 1–4.
- [9] B. Dakic, M. Damnjanovic, L. Zivanov, A. Menicanin, N. Blaz, and M. Kistic, "Design of RFID Antenna in Ink-Jet Printing Technology," in *IEEE 10th Jubilee International Symposium on Intelligent Systems and Informatics*, Subotica, Serbia, Sept. 2012, pp. 429–432.
- [10] *Identification Cards-Contactless Integrated Circuit(s) Cards-Proximity Cards-Part 3: Initialization and Anticollision*, Int. Std. ISO/IEC 14443-3, ISO/IEC/JTC1 Inf. Technol, ISO/IEC/JTC1 Inf. Technol Std., 1999. [Online]. Available: <http://www.waazaa.org/download/fcd-14443-3.pdf>
- [11] B. Jiang, J. R. Smith, M. Philipose, S. Roy, K. Sundara-Rajan, and A. V. Mamishev, "Energy Scavenging for Inductively Coupled Passive RFID Systems," *IEEE Tran. on Instruments and Measurement*, vol. 56, no. 1, pp. 118–125, Feb. 2007.
- [12] N.-G. Choi, H.-J. Lee, and S.-H. Lee, "A 13.56 Mhz RFID System," in *Proc. Asia-Pacific conference on applied electromagnetics (APACE)*, Johar, Malaysia, Dec. 2005, pp. 289–292.
- [13] L. Qiwei, "Research and Design on Radio Frequency Identification Reader," in *Proc. IEEE International Workshop on Anti-counterfeiting, Security, Identification*, Xiamen, China, April 2007, pp. 356–359.
- [14] Y.-C. Choi, M.-W. Seo, Y.-H. Kim, and H.-J. Yoo, "A Multi-standard 13.56MHz RFID reader system," in *Proc. The 23rd Int. Technical Conf. on Circuits/Systems, Computer and Comm. (ITC-CSCC)*, Yamaguchi, Japan, July 2008, pp. 1073–1076.

- [15] J. Kim, H. Kim, J. Kim, J. Cho, G. Kim, and S. Kim, "13.56 MHz RFID reader SiP with embedded Antenna," in *Electrical Design of Advanced Packaging and Systems Symposium (EDAPS)*, Seoul, South Korea, Dec. 2008, pp. 186–189.
- [16] S. S. Basat, L. Kyutae, J. Laskar, and M. M. Tentzeris, "Design and modeling of embedded 13.56 MHz RFID antennas," in *Proc. Antennas and prop. society Intl. Symposium*, 2005.
- [17] K. Fotopoulou and B. W. Flynn, "Optimum antenna coil structure for inductive powering of passive RFID tags," in *Proc. IEEE intl. conf. on RFID*, Grapevine, Tx, USA, Mar. 2007, pp. 71–77.
- [18] F. Ohnimus, I. Ndip, S. Guttowski, and H. Reichi, "Design and analysis of a bent antenna-coil for a HF-RFID transponder," in *Proc. 38th European Microwave Conf.*, Amsterdam, Netherlands, Oct. 2008, pp. 75–78.
- [19] U.-M. Jow and M. Ghovanloo, "Design and Optimization of Printed Spiral Coils for Efficient Transcutaneous Inductive Power Transmission," *IEEE Trans. on biomedical circuits and systems*, vol. 1, no. 3, pp. 193–202, Sept. 2007.
- [20] N. Rueangsri and A. Thanachayanont, "Coil design for optimum operating range of magnetically coupled RFID system," in *Proc. Intl. Symp. on Comm. and Info. Tech. ISCIT*, 2006, pp. 1199–1202.
- [21] J. Mei, M. R. Lovell, and M. H. Mickle, "Formulation and Processing of Novel Conductive Solution Inks in Continuous Inkjet Printing of 3-D Electric Circuits," *IEEE Tran. on Electronics Packaging Manufacturing*, vol. 28, no. 3, pp. 265–273, July 2005.
- [22] I. J. Garcia Zuazola, A. Sharma, J. Batchelor, I. Angulo, A. Perallos, W. Whittow, J. Elmirghani, and R. Langley, "Radio frequency IDentification miniature interrogator antenna sprayed over an in-vehicle chassis," *IET Microwaves, Antennas and Propagation*, vol. 6, no. 15, pp. 1674–1680, Dec 2012.

- [23] X. Chen, W. G. Yeoh, Y. B. Choi, H. Li, and R. Singh, "A 2.45-GHz near-field RFID system with passive on-chip antenna tags," *IEEE Trans. on Microwave theory and techniques*, vol. 56, no. 6, pp. 1397–1404, June 2008.
- [24] W. Aerts, E. D. Mulder, B. Preneel, G. A. E. Vandenbosch, and I. Verbauwhede, "Dependence of RFID reader antenna design on read out distance," *IEEE Trans. on Antenna and Propagation*, vol. 56, no. 12, pp. 3829–3837, Dec. 2008.
- [25] C. M. Zierhofer and E. S. Hochmair, "Geometric approach for coupling enhancement of magnetically coupled coils," *IEEE Trans. on Biomedical Engineering*, vol. 43, no. 7, pp. 708–714, July 1996.
- [26] X. Jian, X. Zeng, and L. Zhang, "An Innovative Semicircular Spiral Antenna for On-Metal Passive RFID Applications," *IEEE Tran. on Antennas and Propagation*, vol. 61, no. 3, pp. 1026–1031, Mar. 2013.
- [27] H. W. Son and C. H. Park, "Loop antenna producing uniform horizontal magnetic fields over plane for HF RFID applications," *Electronics Letters*, vol. 50, no. 17, pp. 1186–1188, Aug. 2014.
- [28] X. Qing and Z. N. Chen, "UHF near-field RFID antennas," in *International Workshop on Antenna Technology (iWAT)*, Lisbon, March 2010, pp. 1–4.
- [29] A. Sharma, I. J. G. Zuazola, A. Gupta, A. Perallos, and J. C. Batchelor, "Enhanced H-field in HF-RFID systems by optimizing the loop spacing of antenna coils," *Wiley Microwave and Optical Technology Letters*, vol. 55, no. 4, pp. 944–948, April 2013.
- [30] X. Qing, C. K. Goh, and Z. N. Chen, "A broadband near-field UHF RFID antenna," *IEEE Trans. Antennas and Propagation*, vol. 58, no. 12, pp. 3829–3838, Dec. 2010.
- [31] D. M. Dobkin, S. M. Weigand, and N. Iye, "Segmented magnetic antennas for near-field UHF RFID," *Microwave Journal*, vol. 50, no. 6, pp. 96–102, June 2007.

- [32] R. A. Oliver, “Broken-loop RFID reader antenna for near field and far field UHF RFID tags,” U.S. design patent D570, 337 S, June 3, 2008.
- [33] —, “Broken-loop RFID reader antenna for near field and far field UHF RFID tags,” U.S. design patent D574, 369 S., Aug. 5, 2008.
- [34] —, “Broken-loop RFID reader antenna for near field and far field UHF RFID tags,” U.S. design patent D570, 337 S, June 3, 2008.
- [35] Z. N. Chen, C. K. Goh, and X. Qing, “Loop antenna for UHF near-field RFID reader,” in *Proc. 4th European Conference of Antenna and Propagation (EuCAP)*, Barcelona, Spain, April 2010, pp. 1–4.
- [36] X. Qing, Z. N. Chen, and C. K. Goh, “UHF near-field RFID reader antenna with capacitive couplers,” *IET Electron. Lett.*, vol. 46, no. 24, pp. 1591–1592, Dec. 2010.
- [37] —, “A UHF near-field/far-field RFID metamaterial-inspired loop antenna,” in *IEEE Antennas and Propagation Society International Symposium (APSURSI)*, Chicago, IL, July 2012, pp. 1–2.
- [38] Y. S. Ong, X. Qing, C. K. Goh, and Z. N. Chen, “A segmented loop antenna for UHF near-field RFID,” in *IEEE Antennas and Propagation Society International Symposium (APSURSI)*, Toronto, ON, July 2010, pp. 1–4.
- [39] J. K. Pakkathillam, M. Kanagasabai, C. Varadhan, and P. Sakthivel, “A Novel Fractal Antenna for UHF Near-Field RFID Readers,” *IEEE Antennas and wireless propagation letters*, vol. 12, pp. 1141–1144, Sept. 2013.
- [40] X. M. Ding, K. Zhang, H. Yu, L. Zhu, C. N. Feng, and Q. Wu, “A Novel Magnetic Coupling UHF Near Field RFID Reader Antenna Based on Multilayer-Printed-Dipoles Array,” *IEEE Trans. on magnetics*, vol. 50, no. 1, Jan. 2014.
- [41] K. Chen, S. Zhong, X. Tang, and Z. Sun, “Low-sidelobe circularly-polarized microstrip array for RFID reader applications,” in *Proc. IET Conf. Wireless, Mobile and Sensor Networks*, Shanghai, China, Dec. 2007, pp. 482–484.

- [42] X. T. S. Zhong, Z. Sun and K. Chen, "Circularly-polarized microstrip array with low-sidelobe for RFID application," in *Proc. Asia Pacific Microwave Conf.*, Hong Kong, Dec. 2008, pp. 1–4.
- [43] A. Buffi, A. A. Serra, P. Nepa, H.-T. Chou, and G. Manara, "A focused planar microstrip array for 2.4 GHz RFID readers," *IEEE Trans. Antennas Propag.*, vol. 58, no. 5, pp. 1536–1544, May 2010.
- [44] A. Buffi, P. Nepa, and G. Manara, "Design criteria for near-field-focused planar arrays," *IEEE Antennas and Propagation Magazine*, vol. 54, no. 1, pp. 40–50, Feb. 2012.
- [45] R. Siragusa, P. Lematre-Auger, and S. Tedjini, "Tunable near-field focused circular phase-array antenna for 5.8-ghz rfid applications," *IEEE Antennas and Wireless Propagation Letters*, vol. 10, pp. 33–36, 2011.
- [46] R. Hasse, V. Demir, W. Hunsicker, D. Kajfez, and A. Elsherbeni, "Design and Analysis of Partitioned Square Loop Antennas," *ACES JOURNAL*, vol. 23, no. 1, pp. 1054–4887, Mar. 2008.
- [47] R. Hasse, W. Hunsicker, K. Naishadham, A. Z. Elsherbeni, and D. Kajfez, "Analysis and Design of a Partitioned Circular Loop Antenna for Omnidirectional Radiation," in *IEEE Antennas and Propagation Society International Symposium (APSURSI)*, Toronto, ON, July 2011, pp. 1379–1382.
- [48] V. V. Yem, B. Journet, P. V. Chi, V. T. Tu, N. V. Duc, P. V. Tien, and N. T. Duc, "Novel High Gain and Broadband CPW-Fed Antennas With EBG for ITS Applications," in *International Conference on Advanced Technologies for Communications (ATC'13)*, Ho Chi Minh City, Oct. 2013, pp. 451–456.
- [49] S. M. R. N. C. Karmakar and M. S. Ikram, "Development of smart antenna for rfid reader," in *Proc. IEEE Int. Conf. RFID*, Las Vegas, Nevada, USA, May 2008, pp. 65–73.

- [50] N. C. Karmakar, P. Zakavi, and M. Kumbukage, "Development of a phased array antenna for universal UHF RFID reader," in *IEEE Antennas and Propagation Society International Symposium (APSURSI)*, Toronto, ON, July 2010, pp. 1–4.
- [51] P. Salonen and L. Sydiinheimo, "A 2.45 GHz digital beam-forming antenna for RFID reader," in *IEEE Vehicular Technology Conference (VTC Spring)*, May 2002, pp. 1766–1770.
- [52] T. Deleruyelle, P. Pannier, E. Bergeret, and S. Bourdel, "Dual Band UHF and Microwave RFID Antenna," in *Proceedings of the 38th European Microwave Conference*, Amsterdam, The Netherlands, Oct. 2008, pp. 342–345.
- [53] C. Phongcharoenpanich and R. Suwalak, "Dual-Band RFID-Reader Antenna using Annular Plate with Curved and Rectangular Slots," in *International Conference on Electromagnetics in Advanced Applications (ICEAA)*, Sydney, NSW, Sept. 2010, pp. 633 – 636.
- [54] J. R. Panda and R. S. Kshetrimayum, "A Printed 2.4 GHz/5.8 GHz Dual-band Monopole Antenna for WLAN and RFID Applications with a Protruding Stub in the Ground Plane," in *National Conference on Communications (NCC)*, Bangalore, Jan. 2011, pp. 1–5.
- [55] A. T. Mobashsher, M. T. Islam, and N. Misran, "A Novel High-Gain Dual-Band Antenna for RFID Reader Applications," *IEEE Antennas and Wireless Propagation Letters*, vol. 9, pp. 653–656, July 2010.
- [56] Y.-C. Lee, J.-S. Sun, M.-H. Hsu, and R.-H. Chen, "A New Printed Slot Loop Antenna With Tunable Strips for 2.4- and 5-GHz Wireless Applications," *IEEE Antennas and Wireless Propagation Letters*, vol. 8, pp. 356–358, May 2009.
- [57] F. Y. Zulkifli, S. F. Siddiq, and E. T. Rahardjo, "Multiband Microstrip Antenna for RFID Application," in *Proc. IEEE Asia-Pacific Conference on Applied Electromagnetics (APACE)*, Port Dickson, Nov. 2010, pp. 1–4.

- [58] J. Ni, S. Yan, and M. Zhang, "A Triple-band Meandered Dipole Antenna With Bandwidth improved For RFID Tag," in *International Conference on Electronics, Communications and Control (ICECC)*, Ningbo, Sept. 2011, pp. 1857 – 1859.
- [59] C. Varadhan, J. K. Pakkathillam, M. Kanagasabai, R. Sivasamy, R. Natarajan, and S. K. Palaniswamy, "Triband Antenna Structures for RFID Systems Deploying Fractal Geometry," *IEEE Antennas and Wireless Propagation Letters*, vol. 12, pp. 437–440, Mar. 2013.
- [60] X. Lai, Z. Xie, and X. Cen, "COMPACT LOOP ANTENNA FOR NEAR-FIELD AND FAR-FIELD UHF RFID APPLICATIONS," *Progress In Electromagnetics Research C*, vol. 37, pp. 171–182, Feb. 2013.
- [61] L. X. zheng, X. Zeming, and C. Xuanliang, "A Compact RFID Reader Antenna for UHF Near-Field and Far-Field Operations," *Hindawi International Journal of Antennas and Propagation*, pp. 1–5, July 2013.
- [62] W. Li, Y. Yao, J. Yu, and X. Chen, "Compact and planar near-field and far-field reader antenna for handset," in *Proceedings of the International Symposium on Antennas & Propagation (ISAP)*, Nanjing, Oct. 2013, pp. 133 – 135.
- [63] B. Shrestha, A. Elsherbeni, and L. Ukkonen, "UHF RFID Reader Antenna for Near-Field and Far-Field Operations," *IEEE Antennas and Wireless Propagation Letters*, vol. 10, pp. 1274–1277, Nov. 2011.
- [64] A. C. de Souza, Y. .Duroc, T. P. Vuong, A. Luce, and J. Perdereau, "A near-field and far-field antenna for UHF RFID applications," in *IEEE-APS Topical Conference on Antennas and Propagation in Wireless Communications (APWC)*, Torino, Sept. 2013, pp. 1240–1243.
- [65] C. K. Goh, X. Qing, and Z. N. Chen, "A Slotted Circularly-polarized Patch Antenna for Near-field and Far-field UHF RFID Applications," in *IEEE Antennas and Propagation Society International Symposium (APSURSI)*, 2012.

- [66] A. L. Borja, A. Belenguer, J. Cascon, and J. R. Kelly, "A Reconfigurable Passive UHF Reader Loop Antenna for Near-Field and Far-Field RFID Applications," *IEEE Antennas and Wireless Propagation Letters*, vol. 11, pp. 580–583, May 2012.
- [67] K. S. Leong, M. L. Ng, and P. H. Cole, "Miniaturization of Dual Frequency RFID Antenna with High Frequency Ratio," in *IEEE Antennas and Propagation Society International Symposium*, Honolulu, HI, June 2007, pp. 5475 – 5478.
- [68] M. Hirvonen, N. Pesonen, O. Vermesan, C. Rusu, and P. Enoksson, "Multi-system, multi-band RFID antenna: bridging the gap between HF- and UHF-based RFID applications," in *Proceedings of the 1st European Wireless Technology Conference*, Amsterdam, The Netherlands, Oct. 2008, pp. 346–349.
- [69] L. W. Mayer and A. L. Scholtz, "A Dual-band HF /UHF Antenna for RFID Tags," in *IEEE 68th Vehicular Technology Conference Fall*, Calgary, BC, Sept. 2008, pp. 1–5.
- [70] T. Deleruyelle, P. Pannier, J. Alarcon, M. Egels, and E. Bergeret, "Multi-Standard mono-chip HF-UHF RFID tag antenna," in *Proceedings of the 40th European Microwave Conference*, Paris, France, Sept. 2010, pp. 1094–1097.
- [71] Z. L. Ma, L. J. Jiang, J. Xi, and T. T. Ye, "A Single-Layer Compact HF-UHF Dual-Band RFID Tag Antenna," *IEEE Antennas and wireless propagation letters*, vol. 11, pp. 1257–1260, Nov. 2012.
- [72] Y. Nishioka, K. Hitomi, H. Okegawa, T. Mizuno, T. Fukasawa, H. Miyashita, and Y. Iida, "Design and Evaluation of HF/UHF Dual-Band RFID Tag Utilizing HF-Coil as UHF Antenna Conductor," in *IEEE-APS Topical Conference on Antennas and Propagation in Wireless Communications (APWC)*, Palm Beach, Aug. 2014, pp. 225 – 228.

- [73] K. Yi, H. Kim, J. Kim, J. Kim, J. Cho, K. An, and S. Kim, "Implementation of HF/UHF multiband RFID reader SiP with Package-on-Package technology," in *Electrical Design of Advanced Packaging and Systems Symposium*, Seoul, Dec. 2008, pp. 65 – 68.
- [74] W. I. Son, K. S. Oh, W. S. Lee, H. S. Tae, and J. W. Yu, "Dual-frequency antenna for HF/UHF handheld RFID reader," in *IEEE MTT-S International Microwave Workshop Series on Intelligent Radio for Future Personal Terminals (IMWS-IRFPT)*, Daejeon, Aug. 2011, pp. 1–2.
- [75] R. L. Haupt and M. Lanagan, "Reconfigurable Antennas," *IEEE Antennas and Propagation Magazine*, vol. 55, no. 1, pp. 49–61, Feb. 2013.
- [76] D. M. Pozar, *Microwave Engineering*, 2nd ed. John Wiley, 1998.
- [77] Y. Huang and K. Boyle, *Antennas: From Theory to Practice*. John Wiley & Sons, 2008.
- [78] C. A. Balanis, "Antenna Theory: A Review," *Proceedings of the IEEE*, vol. 80, no. 1, pp. 7–23, Jan. 1992.
- [79] C. Reinhold, P. Scholz, W. John, and U. Hilleringmann, "Efficient antenna design of inductive coupled RFID-systems with high power demand," *Journal of communications*, vol. 2, no. 6, pp. 14–23, Nov. 2007.
- [80] R. J. Cameron, R. Mansour, and C. M. Kudsia, *Microwave Filters for Communication Systems: Fundamentals, Design and Applications*, 1st ed. Wiley-Interscience, July 2007.
- [81] I. J. Garcia Zuazola, L. Azpilicueta, A. Sharma, H. Landaluce, F. Falcone, I. Angulo, A. Perallos, W. G. Whittow, J. M. H. Elmirghani, and J. C. Batchelor, "Ultra-wide band in-car wireless channel using a customised bpf-like antenna," *IET Communications (submitted for review)*, 2013.
- [82] T. I. Inc. (2003, Sept.) HF Antenna Design Notes. <http://www.ti.com/rfid/docs/manuals/appNotes/HFAntennaDesignNotes.pdf>.

- [Online]. Available: <http://www.ti.com/rfid/docs/manuals/appNotes/HFAntennaDesignNotes.pdf>
- [83] (1999) Identification Cards-Contactless Integrated Circuit(s) Cards-Proximity Cards-Part 3: Initialization and Anticollision. Int. Std. ISO/IEC 14443-3, <http://www.waazaa.org/download/fcd-14443-3.pdf>. ISO/IEC/JTC1 Inf. Technol. [Online]. Available: <http://www.waazaa.org/download/fcd-14443-3.pdf>
- [84] K. Finkenzeller, *RFID Handbook*, 2nd ed. New York: Wiley, 2003.
- [85] D. Staelin, A. Morgenthaler, and J. Kong, *Electromagnetic Waves*. New York: Prentice-Hall Int., 1994.
- [86] D. Wang, L. Xu, H. Huang, and D. Sun, "Optimization of Tag Antenna for RFID System," in *Proc. Int. Conf. on Info. Technology and Computer Science*, Kiev, Ukraine, July 2009, pp. 36–39.
- [87] S. Salleh, K. Salleh, M. F. Hashim, and Z. A. Majid, "Design and Analysis of 13.56MHz RFID Antenna Based on Modified Wheeler Equation: A Practical Approach," in *Proc. Int. Conf. on Electronic Devices, Systems and Applications (ICEDSA)*, Kuala Lumpur, Malaysia, April 2010, pp. 326–330.
- [88] X. Qing and Z. N. Chen, "Characteristics of a Metal-Backed Loop Antenna and its Application to a High-Frequency RFID Smart Shelf," *IEEE Antennas and Propagation Magazine*, vol. 51, no. 2, pp. 26–38, April 2009.
- [89] J. Nummela, L. Ukkonen, L. Sydneimo, and M. Kivikoski, "13,56 MHz RFID Antenna for Cell Phone Integrated Reader," in *IEEE Antennas and Propagation Society International Symposium*, Hawai'i, USA, June 2007, pp. 1088–1091.
- [90] A. Sharma, I. J. G. Zuazola, A. Gupta, A. Perallos, and J. C. Batchelor, "Non-uniformly Distributed-turns Coil Antenna for Enhanced H-field in HF RFID," *IEEE Trans. on Antenna and Propagation*, vol. 61, no. 10, pp. 4900–4907, Oct. 2013.

- [91] C. Bowick, *RF Circuit Design*. Burlington, MA: Newnes, 1997.
- [92] (2013, May) Model 7405 Near-Field probe set user manual. ETS-Lindgren Inc. [Online]. Available: <http://www.ets-lindgren.com/manuals/7405.pdf>
- [93] G. Tarapata, H. T. Hui, J. Weremczuk, R. Jachowicz, C. W. P. Shi, and X. Shan, "Comparison of performance of four RFID sensor antennas fabricated on different substrates," in *Asia Pacific Microwave Conference APMC*, Suntec City, Singapore, Dec. 2009, pp. 614–617.
- [94] A. Sharma, I. J. Garcia Zuazola, J. C. Batchelor, and A. Perallos, "Switched Non-uniformly Distributed-Turns Coil Antenna for Dual-band operation," in *accepted in 9th European Conference on Antennas and Propagation*, Lisbon, April 2015.
- [95] D. E. Anagnostou, M. T. Chryssomallis, B. D. Braaten, J. L. Ebel, and N. Sepveda, "Reconfigurable UWB Antenna With RF-MEMS for On-Demand WLAN Rejection," *IEEE Trans. on Antenna and Propagation*, vol. 62, no. 2, pp. 602–608, Feb. 2014.
- [96] M. Bogosanovic and A. G. Williamson, "Microstrip antenna array with a beam focused in the near-field zone for application in noncontact microwave industrial inspection," *IEEE Trans. on Instrumentation and Measurement*, vol. 56, no. 6, pp. 2186–2195, Dec. 2007.
- [97] —, "Antenna array with beam focused in near-field zone," *Electron. Lett.*, vol. 39, no. 9, pp. 704–705, May 2003.
- [98] S. Karimkashi and A. A. Kishk, "Focused microstrip array antenna using a DolphChebyshev near-field design," *IEEE Trans. Antennas Propag.*, vol. 57, no. 12, pp. 3813–3820, Dec. 2009.
- [99] A. Buffi, A. Serra, P. Nepa, G. Manara, and M. Luise, "Near field focused microstrip arrays for gate access control systems," in *Proc. IEEE APSURSI*, Charleston, SC, USA, June 2009, pp. 1–4.

- [100] S. H. Zainud-Deen, H. A. Malhat, and K. H. Awadalla, "Dielectric resonator antenna phased array for fixed RFID reader in near field region," in *Proc. Japan-Egypt Conference on Electronics, Communications and Computers*, Alexandria, Egypt, Mar. 2012, pp. 102–107.
- [101] R. Siragusa, P. Lemaitre-Auger, and S. Tedjini, "Near field focusing circular microstrip antenna array for RFID applications," in *Proc. IEEE APSURSI*, Charleston, SC, USA, June 2009, pp. 1–4.
- [102] A. Sharma, I. J. G. Zuazola, R. Martinez, J. C. Batchelor, A. Perallos, and L. de Haro Ariet, "Optimal E-Field Vector Combination for a Highly Focused Antenna-Array," *IEEE Antennas and Wireless Propagation Letters*, vol. 13, pp. 392–395, Feb. 2014.
- [103] J. W. Sherman, "Properties of focused aperture in the fresnel region," *IRE Trans. Antennas Propag*, vol. 10, no. 4, pp. 399–408, Jul. 1962.
- [104] H. Deng, X. He, S. Liu, and Y. Xie, "A Novel Ultra Wideband Planar Antenna," in *Global Symposium on Millimeter Waves, GSMM*, 2008, pp. 288 – 290.
- [105] Z. shunshi, L. Xianling, and Y. Xiaorong, "UWB planar antenna technology," *Chinese Journal of Radio Science*, vol. 22, no. 2, pp. 308–315, April 2007.
- [106] M. W. Jawitz, *Printed Circuit Board Materials Handbook*. New York-McGraw-Hill, 1997.
- [107] H. P. Le, "Progress and trends in inkjet printing technology," *J. Imaging Sci. Techno.*, vol. 42, no. 1, pp. 49–62, 1998.
- [108] I. J. Garcia Zuazola, A. Sharma, J. Batchelor, I. Angulo, A. Perallos, and J. Elmirghani, "Sprayed antenna on cans for WLAN-RFID tags," *Wiley - Microwave and Optical Technology Letters*, vol. 55, no. 4, pp. 773–775, April 2013.

- [109] “First report and order, revision of part 15 of the commissions rules regarding ultra-wideband transmission systems,” FDD, Tech. Rep. ET Docket 98-153, Feb. 2002.
- [110] S. Roy, J. Foerster, V. Somayazulu, and D. Leeper, “Ultrawideband radio design: the promise of high-speed, short-range wireless connectivity,” *Proc. IEEE*, vol. 92, no. 2, pp. 295–311, Feb. 2004.
- [111] I. J. Garcia Zuazola, J. M. H. Elmirghani, and J. C. Batchelor, “High-speed ultra-wide band in-car wireless channel measurements,” *IET Communications*, vol. 3, no. 7, pp. 1115 – 1123, July 2009.
- [112] A. Batra and et al., “Multiband OFDM physical layer specification,” Wi-Media Alliance, Release 1.1, July 2005.
- [113] V. S. Somayazulu, J. R. Foerster, and S. Roy, “Design challenges for very high data rate UWB systems,” in *Asilomar on Systems, Signals, and Computation*, Nov 2002, pp. 717 – 721.
- [114] IEEE 802.15 WPAN High Rate Alternative PHY Task Group 3a (TG3a). [Online]. Available: <http://www.ieee802.org/15/pub/TG3a.html>
- [115] A. Batra and et .al., “TI physical layer proposal for IEEE 802.15 task group 3a,” IEEE P802.15-03/142r2-TG3a, March 2003.
- [116] —, “Multi-band OFDM physical layer proposal,” IEEE P802.15-03/268r0-TG3a, July 2003.
- [117] *ECMA-368*, Std., December 2008. [Online]. Available: <http://www.ecma-international.org/publications/standards/Ecma-368.htm>
- [118] S. H. Kratzet, “MB-OFDM and DS-UWB ultra-wideband design using SystemView by Elanixw,” Eagleware-Elanix App Note AN-24B, March 2005.
- [119] G. Khuandaga, A. Iqbal, and K. S. Kwak, “ Analysis of Modulation Schemes in Intra Vehicle Communications (IVC) Channel,” in *13th International Conference on Advanced Communication Technology (ICACT)*, Feb. 2011, pp. 725–729.

- 
- [120] A. Batra, J. Balakrishnan, G. R. Aiello, J. R. Foerster, and A. Dabak, "Design of a Multiband OFDM System for Realistic UWB Channel Environments," *IEEE Transaction on Microwave theory and Techniqtues*, vol. 52, no. 9, pp. 2123–2138, Sept. 2004.
- [121] J. Foerster, "Channel modeling sub-committee report final," *IEEE, P802.15-02/368r5-SG3a*, 2002.
- [122] A. Saleh and R. Valenzuela, "A statistical model for indoor multipath propagation," *IEEE Journal on selected areas in communication*, vol. 5, no. 2, pp. 128–137, Feb. 1987.
- [123] P. C. Richardson, W. Xiang, and W. Stark, "Modeling of Ultra-Wideband Channels Within Vehicles," *IEEE Journal on selected areas in communication*, vol. 24, no. 4, pp. 906–912, april 2006.
- [124] Y. Katayama, K. Terasaka, K. Higashikaturagi, I. Matunami, and A. Kajiwara, "Ultra-Wideband Impulse-Radio Propagation for In-Vehicle Wireless Link," in *64th IEEE Vehicular Technology Conference, VTC Fall*, Montral, Qubec, Canada, 25-28 September 2006.
- [125] W. Niu, J. Li, and T. Talty, "Intra-vehicle UWB channels in moving and staionary scenarios," in *IEEE MILCOM*, Oct. 2009, pp. 1–6.
- [126] J. Mar, Y.-C. Yeh, and C.-C. Kuo, "Novel UWB In-Vehicle Channel Measurement Approach Based on Chirp Pulse Sounding Signal," in *International Symposium on Intelligent Signal Processing and Communication Systems (ISPACS 2009)*, Dec. 2009.
- [127] Y. Jin, D. Kwak, and K. S. Kwak, "Performance Analysis of Intra-vehicle Ultra-Wide Band Propagation in Multi-user Environments," in *IEEE 1st International Workshop on Vehicular Communications, Sensing, and Computing (VCSC)*, June 2012.

- [128] D. W. Matolak and A. Chandrasekaran, "5 ghz intra-vehicle channel characterization," in *IEEE Vehicular Technology Conference (VTC Fall)*, 2012, pp. 1–5.
- [129] C. U. Bas and S. C. Ergen, "Ultra-wideband Channel Model for Intra-vehicular Wireless Sensor Networks Beneath the Chassis: From Statistical Model to Simulations," *IEEE Transaction on Vehicular Technology*, vol. 62, no. 1, pp. 14–25, Jan. 2013.
- [130] T. Kayser, J. V. Hagen, and W. Wiesbeck, "Optimisation of antenna locations for wireless incar communication," in *URSI Int. Symp. Electromagnetic Theory*, Pisa, Italy, May 2004.
- [131] M. A. Peyrot-Solis, G. Galvan-Tejada, and H. Jardon-Aguilar, "State of the art in ultra-wideband antennas," in *2nd International Conference on Electrical and Electronics Engineering (ICEEE) and XI Conference on Electrical Engineering (CIE)*, Mexico City, Mexico, September 7-9 2005, pp. 101–105.
- [132] W.-S. Lee, D.-Z. Kim, K.-J. Kim, and J.-W. Yu, "Wideband Planar Monopole Antennas With Dual Band-Notched Characteristics," *IEEE Transactions on Microwave Theory and Techniques*, vol. 54, no. 6, pp. 2800–2806, June 2006.
- [133] D. Valderas, J. Legarda, I. Gutierrez, and J. I. Sancho, "Design of UWB Folded-Plate Monopole Antennas Based on TLM," *IEEE Transactions on Antennas and Propagation*, vol. 54, no. 6, pp. 1676–1687, June 2006.
- [134] S. Adnan, R. A. Abd-Alhameed, S. Jones, H. I. Hraga, M. S. Bin-Melha, and E. A. Elkhazmi, "A modified printed monopole antenna for ULTRA-WIDEBAND applications," in *Proceedings of the Fourth European Conference on Antennas and Propagation (EuCAP)*, April 2010.
- [135] A. A. Kishk, X. H. Wu, and K. S. Ryu, "UWB Antenna for Wireless Communication and Detection Applications," in *IEEE International Conference on Ultra-Wideband (ICUWB)*, Sept. 2012, pp. 72–76.

- 
- [136] A. Goldsmith, *Wireless Communications*. Cambridge University Press, NY, 2005.
- [137] R. S. Elliott, “On discretizing continuous aperture distributions,” *IEEE Transaction on Antennas and propagation*, vol. 25, no. 5, pp. 617–621, Sept. 1977.
- [138] N. T. Nguyen, A. V. Boriskin, A. Rolland, L. L. Coq, and R. Sauleau, “Shaped Lens-Like Dome for UWB Antennas With a Gaussian-Like Radiation Pattern,” *IEEE Transaction on antennas and propagation*, vol. 61, no. 4, pp. 1658–1664, April 2013.









